

**DOCTORAL THESIS**

# Characterization of Silicon Carbide (SiC) and Graphene-Based Novel Semiconductor Devices

Muhammad Haroon Rashid

TALLINN UNIVERSITY OF TECHNOLOGY  
DOCTORAL THESIS  
6/2021

**Characterization of Silicon Carbide (SiC)  
and Graphene-Based Novel  
Semiconductor Devices**

MUHAMMAD HAROON RASHID



TALLINN UNIVERSITY OF TECHNOLOGY

School of Information Technologies

Thomas Johann Seebeck Department of Electronics

This dissertation was accepted for the defense of the degree in 22/12/2020

**Supervisor:**

Prof. Dr. Ants Koel  
Thomas Johann Seebeck Department of Electronics  
Tallinn University of Technology  
Tallinn, Estonia

**Co-supervisor:**

Prof. Dr. Toomas Rang  
Thomas Johann Seebeck Department of Electronics  
Tallinn University of Technology  
Tallinn, Estonia

**Opponents:**

Prof. Dr. Márta Rencz  
Department of Electronic Devices  
Budapest University of Technology and Economics  
Budapest, Hungary

Prof. Dr. Serge Dos Santos, Hab. Dir. Rech  
INSA Centre Val de Loire, Blois Campus, France  
Department of Industrial Systems, IEEE Senior Member,  
U1253 iBrain “Imaging and Brain” Inserm-University of  
Tours, France

**Defense of the thesis:** 01/02/2021 Tallinn

**Declaration:**

Hereby, I declare that this doctoral thesis, my original investigation, and achievement, submitted for the doctoral degree at Tallinn University of Technology has not been submitted for a doctoral or equivalent academic degree.

Muhammad Haroon Rashid

-----  
signature



European Union  
European Regional  
Development Fund



Investing  
in your future

Copyright: Muhammad Haroon Rashid, 2021

ISSN 2585-6898 (publication)

ISBN 978-9949-83-658-1 (publication)

ISSN 2585-6901 (PDF)

ISBN 978-9949-83-659-8 (PDF)

Printed by Koopia Niini & Rauam

TALLINNA TEHNIKAÜLIKOOL  
DOKTORITÖÖ  
6/2021

# Ränikarbiidil (SiC) ja grafeenil põhinevate uudsete pooljuhtstruktuuride karakteriseerimine

MUHAMMAD HAROON RASHID





# Contents

List of publications .....	9
Author's contribution to the publications .....	11
Abbreviations .....	13
List of Figures .....	14
Organization and graphical abstract of the thesis .....	16
Introduction and motivation .....	17
Problem statement and research questions .....	20
Contribution of the thesis .....	21
Claims about the novelty of the thesis .....	22
1 Numerical simulations of Silicon Carbide based hetero-structure devices.....	23
1.1 SiC and its different forms.....	23
1.2 Heterostructures of SiC.....	24
1.2.1 Bandgap alignment at the heterojunction interface.....	24
1.2.2 State-of-the-art fabrication techniques for SiC heterostructures.....	25
1.2.3 Novelty of SiC related work of this Ph.D. thesis.....	26
1.3 Methodology of simulated SiC based heterostructures .....	27
1.3.1 Why SILVACO TCAD and QuantumWise Atomistix Toolkit (ATK-VNL) .....	28
1.3.2 Computational procedure of SILVACO TACD and QuantumWise Atomistix Toolkit (ATK-VNL) .....	28
1.3.3 Exchange-correlation Functionals for DFT based simulations .....	30
1.3.4 Microscale simulations of SiC based heterostructure diodes .....	30
1.3.5 Nanoscale simulations of SiC based heterostructure diodes .....	32
1.3.6 Geometry optimization of simulated SiC based heterostructures in ATK-VNL.....	32
1.4 Results and discussion on simulated SiC based heterostructures .....	33
1.4.1 Differences in nano- and micro-scale simulation results .....	35
1.5 Validation and comparison of results related to SiC based hetero-structures .....	36
1.6 Conclusions from the simulations of SiC based heterostructures .....	36
1.7 Challenges in the prospective physical fabrication of simulated Devices.....	37
1.8 Overview of publications related to the numerical analysis of SiC-based heterostructures .....	37
2 Numerical simulations of graphene-based gas sensors.....	40
2.1 Introduction to Graphene .....	40
2.1.1 Derivatives of carbon-based nanomaterials .....	41
2.1.2 State-of-the-art of gas sensing technology .....	42
2.1.3 Types of interactions between graphene and target molecules .....	43
2.1.4 Novelty of graphene-based gas sensors related work of Ph.D. thesis .....	43
2.1.5 Methodology adopted for graphene-based gas sensors related work of the Ph.D. thesis .....	44
2.1.6 Geometry optimization of graphene and CNT based simulated devices in ATK-VNL..	45
2.1.7 Graphene-based simulated structures for the detection of a wide range of molecules .....	46
2.2 Results and discussion on simulated graphene-based gas sensors .....	46
2.2.1 Geometry optimization of simulated graphene-based field-effect transistor .....	47

2.2.2 Density of states of simulated graphene-based field-effect transistor (FET).....	47
2.2.3 IV-characteristics of simulated FET .....	48
2.3 Validation of results of graphene-based simulated sensors (surfaces) .....	52
2.4 Conclusions from graphene-based gas sensors simulations.....	52
2.5 Challenges in the prospective physical fabrication of proposed gas/molecule sensors .	54
2.6 Overview of publications related to the numerical simulations of graphene-based molecule detectors .....	54
Limitations of DFT based Simulations .....	56
Limitations of SILVACO TCAD based Simulations.....	57
Summary of conclusions of Ph.D. work.....	58
Prospective work.....	60
References .....	61
Acknowledgements.....	73
Abstract.....	74
Lühikokkuvõte.....	76
Appendix A.....	79
Appendix B .....	83
Appendix C.....	87
Appendix D.....	91
Appendix E .....	95
Appendix F .....	101
Appendix G.....	117
Appendix H.....	123
Appendix I .....	135
Appendix J.....	155
Appendix K .....	171
Curriculum vitae.....	174
Elulookirjeldus.....	175

## ***Dedication***

*I dedicate this work to my parents, sisters, nephews, and fiancée*



## List of publications

The list of author's publications, based on which this thesis has been prepared is:

- A. **M. H. Rashid**, A. Koel, T. Rang, "Simulations of heterostructures based on 3C-4H and 6H-4H silicon carbide polytypes," *Mater. Sci. Forum*, vol. 924, pp. 302–305, 2018. **(Published in 1.1)**
- B. **M. H. Rashid**, A. Koel, and T. Rang, "Nano and microscale simulations of the Si/4H-SiC and Si/3C-SiC NN-heterojunction diodes," *Mater. Sci. Forum*, vol. 963, pp. 357–361, 2019. **(Published in 1.1)**
- C. **M. H. Rashid**, A. Koel, and T. Rang, "Nano- and Micro-scale Simulations of Ge/3C-SiC and Ge/4H-SiC NN-heterojunction Diodes," *Mater. Sci. Forum*, vol. 1004, pp. 490–496, 2020. **(Published in 1.1)**
- D. **M. H. Rashid**, A. Koel, and T. Rang, "Effects of the inclusion of armchair graphene nanoribbons on the electrical conduction properties of NN-heterojunction 4H-6H/SiC diodes," *Mater. Sci. Forum*, vol. 962, pp. 29–35, 2019. **(Published in 1.1)**
- E. **M. H. Rashid**, A. Koel, and T. Rang, "Phenol and methanol detector based on pristine graphene nano-sheet: A first-principles study," In Proc. Baltic Electronics Conference, Tallinn, Estonia, October 8–10, 2018. **(Published in 3.1)**
- F. **M. H. Rashid**, A. Koel, and T. Rang, "First-Principles Simulations of Phenol and Methanol Detector Based on Pristine Graphene Nanosheet and Armchair Graphene Nanoribbons," *Sensors Journal*, vol. 19, no. 2713, June, pp. 1–14, 2019. **[impact factor: 3.031] (Published in 1.1)**
- G. **M. H. Rashid**, A. Koel, and T. Rang, "Simulations of methane and acetone detector based on pristine graphene nano-sheet over intrinsic 4H-SiC substrate," In Proc. 19<sup>th</sup> IEEE Nano Conference, Macau, China, July 22–26, 2019. **(Published in 3.1)**
- H. **H. Rashid**, A. Koel, and T. Rang, "Simulations of Propane and Butane Gas Sensor Based on Pristine Armchair Graphene Nanoribbon," in Proc. of International Conference on Smart Engineering Materials, Romania, March 2017. **(Published in 3.1)**
- I. **M. H. Rashid**, A. Koel, and T. Rang, "Simulations of Graphene Nanoribbon Field Effect Transistor for the Detection of Propane and Butane Gases: A First-Principles Study," *Nanomaterials*, vol. 10, no. 98, 2020. **[impact factor: 4.034] (Published in 1.1)**

## Other related publications

- J. **M. H. Rashid**, A. Koel, T. Rang, and M.H. Ziko, "Simulations of Benzene and Hydrogen-sulfide Gas Detector based on Single-Walled Carbon Nanotube over Intrinsic 4H-SiC Substrate," *Micromachines*, vol. 11, 2020. **[Impact fact:2.530] (Published in 1.1)**
- K. **M. H. Rashid**, A. Koel, T. Rang and H. Mehmood, "Modelling and Simulations of 4H-SiC/6H-SiC/4H-SiC Single Quantum-well Light Emitting Diode Using Diffusion Bonding Technique," *Materials*, 2020. **[impact factor: 2.98] (under-review in 1.1)**

- L. **H. Rashid**, A. Koel, T. Rang, R. Gähwiler, M. Grosberg, and R. Jõemaa, “Nanoscale And Microscale Simulations Of NN-Junction Heterostructures Of 3C-4H Silicon Carbide,” *WIT Transactions on Engineering Sciences*, vol. 116, June, pp. 235–248, 2017. **(Published in 3.1)**
- M. M. H. Ziko, A. Koel, T. Rang and **M. H. Rashid**, “Investigation of Barrier Inhomogeneities and Electronic Transport on Al-Foil/p-Type-4H-SiC Schottky Barrier Diodes Using Diffusion Welding,” *Crystals*, vol. 10, no. 8, 2020. **[impact factor: 2.404]**  
**(Published in 1.1)**

## Author's contribution to the publications

Author's contributions to the published papers are:

- A.** The author proposed a novel design of *nn*-heterostructure diodes based on two different combinations of silicon carbide polytypes i.e. 3C-4H/SiC and 6H-4H/SiC considering the diffusion bonding approach. He simulated the device structures at nano- and micro-scale. He also drafted the full manuscript and published the paper under the guidance of his supervisors.
- B.** The author proposed novel *nn*-heterojunction diodes based on Si, 4H-SiC, and 3C-SiC. He simulated his proposed diodes both at the nanoscale and at microscale considering the diffusion bonding technique. He characterized these simulated structures in simulators and drafted the whole manuscript.
- C.** In this article, the author proposed another novel combination of Ge/3C-SiC and Ge/4HSiC-based *nn*-heterojunction diodes. He simulated both proposed devices at the micro-level with a novel technique called diffusion welding. He also simulated these structures in a nanoscale semiconductor device simulator; QuantumWise Atomistix Toolkit. The author drafted the full manuscript and published it.
- D.** The author simulated a novel nanoscale *nn*-heterojunction diode based on 4H-6H/SiC and deposited armchair graphene nanoribbon over this simulated structure. The author investigated the effect of the inclusion of graphene on the electrical conduction properties of 4H-6H/SiC diode by depositing graphene at a different location on the diode. The author wrote the first draft of the paper and published it.
- E.** The author proposed another device based on graphene nano-sheet for the detection of flammable and toxic organic compounds; phenol and methanol. He did all the simulations and wrote the whole draft of the manuscript.
- F.** This is the extended version of **Paper E**. The author extended his previously published work by simulating armchair graphene nanoribbon based phenol and methanol detector. In this article, he proposed a novel molecule detection mechanism (change in photo-current) and did all the simulations.
- G.** In this paper, the author proposed a novel structure based on a pristine graphene nano-sheet over an intrinsic 4H-SiC substrate for the detection of methane and acetone molecules. He simulated this structure in QuantumWise Atomistix Toolkit software, wrote the manuscript, and published it.
- H.** The author proposed a gas sensor based on armchair graphene nanoribbon for the leakage detection of flammable household gases; propane and butane. He simulated the proposed structure of the sensor in a nanoscale semiconductor device simulator; QuantumWise Atomistix Toolkit software. The author also drafted the manuscript and published it with the guidance of his supervisors.
- I.** In this article, the author simulated a novel graphene-based field-effect transistor for the detection of propane and butane gases. This proposed device has not been reported yet in literature for the detection of propane and butane gases. The author drafted the whole manuscript and published it in a reputed journal.

## **Other related publications**

- J.** In this work, the author proposed a novel gas detection mechanism (change in photo-current) for the detection of hazardous gases; hydrogen-sulfide and benzene using carbon nanotubes. He did all the simulations, drafted the whole manuscript, and published it.
- K.** The author proposed a novel SiC-based LED and simulated it in SILVACO TCAD software. The prospective fabrication of the proposed 4H-SiC/6H-SiC/4H-SiC LED with diffusion bonding of wafers will significantly reduce the device fabrication cost and complications. The manuscript is under review in a reputed journal.

## Abbreviations

AC	Alternative current
ATK-VNL	QuantumWise Atomistix Toolkit Software
AGNR	Armchair Graphene Nanoribbon
BRR	Bulk Rigid Relaxation
CBO	Conduction Band Offset
CNT	Carbon Nanotube
DC	Direct Current
DFT	Density Functional Theory
DOS	Density of States
EAM	Electron Affinity Model
EMI	Electromagnetic Interference
FET	Field Effect Transistor
FF2D	FastFourier2D
GGA	Generalized Gradient Approximation
HPC	High-Performance Computing
HUMO	Highest Occupied Molecular Orbital
LCAO	Linear Combination of Atomic Orbitals
LDA	Local Density Approximation
LED	Light Emitting Diode
LUMO	Lowest Occupied Molecular Orbital
MEMS	Micro Electro Mechanical System
MOSFET	Metal Oxide Semiconductor Field Effect Transistor
PBE	Perdew-Burke-Ernzerhof
PPM	Parts Per Million
SBD	Schottky Barrier Diode
VBO	Valence Band Offset
WBG	Wide Band Gap
ZGNR	Zigzag Graphene Nanoribbon

## List of Figures

<b>Figure 1:</b> Organization of Ph.D. thesis.....	16
<b>Figure 2:</b> Graphical abstract of the thesis. ....	16
<b>Figure 3:</b> Materials properties of Silicon and Silicon carbide [6]. ....	18
<b>Figure 4:</b> Different crystalline forms of Silicon carbide (a) Single crystal; (b) 3C-SiC; (c) 4H-SiC; (d) 6H-SiC [42-43]. ....	23
<b>Figure 5:</b> Different types of semiconductor heterostructures based on the band alignments at junction interface [61].....	24
<b>Figure 6:</b> Energy band alignment of 3C/4H-SiC based heterostructure.....	25
<b>Figure 7:</b> (a)A schematic of the physical vapor deposition process; (b) resultant structure after epitaxial growth [80]. ....	26
<b>Figure 8:</b> (a)The basic process of diffusion bonding; (b) schematic of the experimental setup for direct bonding of wafers [82]. ....	27
<b>Figure 9:</b> (a) Diffusion welding realization in SILVACO TCAD software; (b) schematic of microscale simulated <i>nn</i> -junction diodes. ....	31
<b>Figure 10:</b> Two probe atomic-scale model of nanoscale simulated devices in ATK-VNL software [119].....	32
<b>Figure 11:</b> Nanoscale simulated (a) Si/3C-SiC and Si/4H-SiC based <i>nn</i> -heterojunction diodes[123]; (b) 3C-6H/SiC and 4H-6H/SiC based <i>nn</i> -heterojunction diodes [124]; (c) Ge/3C-SiC and Ge/4H-SiC based <i>nn</i> -heterojunction diodes [125]. ....	33
<b>Figure 12:</b> (a) ATK view of <i>nn</i> -heterojunction 4H-6H/SiC; (b) pristine armchair graphene nanoribbon device; (c) diode with nanoribbon layer deposited over the whole device; (d) <i>nn</i> -junction diode with nanoribbon layer deposited partially over the device [126].	33
<b>Figure 13:</b> (a) Forward; (b) reverse IV-characteristics of microscale and nanoscale 3C-4H/SiC devices (for actual current values *current axis x10 <sup>-5</sup> **current axis x10 <sup>-9</sup> ) [124]. ....	34
<b>Figure 14:</b> (a) Forward; (b) reverse IV-characteristics of microscale and nanoscale 4H-6H/SiC devices (for actual current values *current axis x10 <sup>-5</sup> **current axis x10 <sup>-9</sup> ) [124]. ....	34
<b>Figure 15:</b> (a) graphene honeycomb lattice structure; (b) stacks of graphene layer connected with Van der Waals forces; (c) sigma and pi bonding in graphene [132]. ....	40
<b>Figure 16:</b> Formation of the electronic cloud around the graphene layer due to the presence of $\pi$ -bonds [134]. ....	41
<b>Figure 17:</b> (a) Multiwall carbon nanotube; (b) zigzag graphene nanoribbon (c) armchair graphene nanoribbon [136-137]. ....	41
<b>Figure 18:</b> (a) Bandgap vs. the number of carbon atoms in AGNR; (b) bandgap vs. the number of carbon atoms having an even number of electrons (curve1) and an odd number of electrons (curve2) of ZGNR [138]. ....	42
<b>Figure 19:</b> Schematic of proposed graphene-based gas detection mechanism for better accuracy and selectivity of graphene-based sensors. ....	44
<b>Figure 20:</b> Simulated graphene-based gas sensors for the detection of a wide range of gases and organic/inorganic molecules in ATK-VNL software. ....	47
<b>Figure 21:</b> Geometry of graphene-based FET for the detection of butane molecules [185]. ....	48
<b>Figure 22:</b> Geometry of graphene nanoribbon based field-effect transistor for the detection of propane and butane molecules [185]. ....	48
<b>Figure 23:</b> Change in the density of states (DOS) of simulated field-effect transistor in presence of (a) propane gas molecules; (b) butane gas molecules; (c) both propane and butane gas molecules [185]. ....	49

**Figure 24:**  $V_{ds}$  and  $I_{ds}$  curves of the simulated field-effect transistor in the presence propane and butane gases at (a)  $V_{gate}=0V$ ; (b)  $V_{gate}=-0.1V$ ; (c)  $V_{gate}=-0.3V$ ; (d)  $V_{gate}=-0.5V$  [185]. ..... 49

**Figure 25:**  $V_{ds}$  and  $I_{ds}$  curves of the simulated field-effect transistor at  $-0.1V$  gate voltage in the presence of (a) only water and oxygen molecules; (b) propane, water, and oxygen molecules; (c) butane, water and oxygen molecules [185]. ..... 50

## Organization and graphical abstract of the thesis

This Ph.D. thesis is divided into two chapters. Chapter 1 covers the work related to SiC-based heterostructures. This chapter includes the introduction of SiC, a detailed discussion on heterostructures of SiC, state-of-the-art of SiC heterostructures, the novelty of this Ph.D. work, the methodology adopted for simulations of SiC heterostructures, discussion on results and conclusions.

Chapter 2 covers the introduction to graphene and its derivatives, state-of-the-art of gas sensing technology, the novelty of this Ph.D. work, the methodology adopted for the simulations of graphene-based gas sensors, discussion on simulation results and conclusions. At the end of chapter 2, overall conclusions drawn from this Ph.D. work have been stated. In the end, the appendices section includes all related publications.

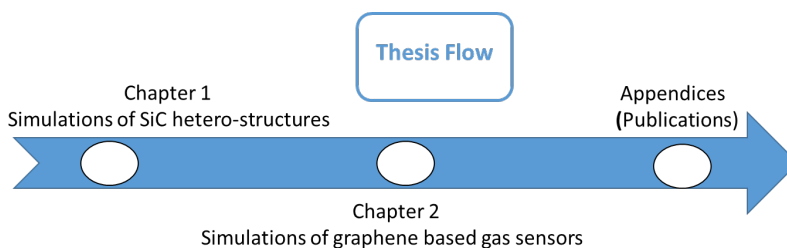


**Figure 1:** Organization of Ph.D. thesis.

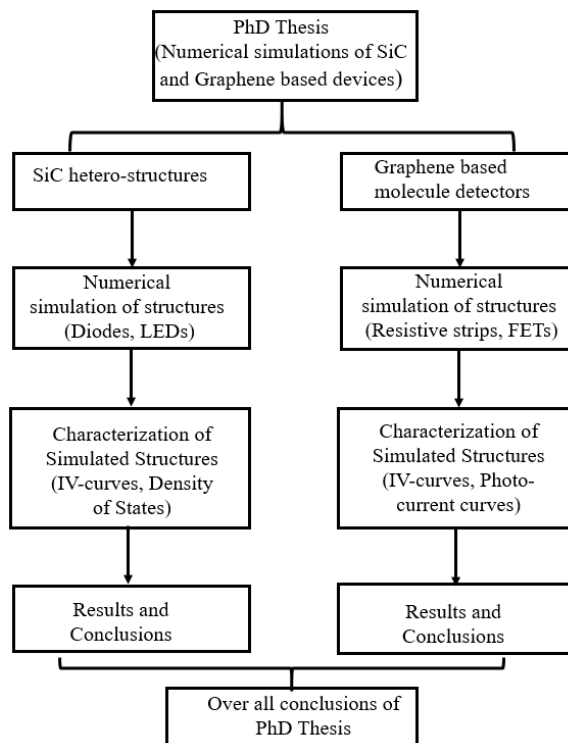


**Figure 2:** Graphical abstract of the thesis.

## Introduction and motivation

The goal of this thesis was to work in two different regimes for the development of Silicon carbide (SiC) and graphene-based novel semiconductor devices for power electronics and gas sensing applications, respectively. The first task was to work on the simulations of novel SiC-based heterostructure diodes for power electronics applications. The second task was to work on the simulations of graphene-based sensors for the detection of a wide range of organic and inorganic compounds. Therefore, the introduction and motivation part of the thesis contains the literature for both SiC and graphene-based devices, respectively.

As mentioned above, the first goal of this Ph.D. thesis was to target the simulations of novel SiC-based heterostructure diodes considering diffusion bonding/welding technique for power electronics applications. During the last few decades, power electronic devices have gained significant importance due to their tremendous applications in power converting and controlling circuits. Power electronic devices are being widely used as power converters to modify the alternating current (AC), as well as direct-current (DC), obtained from hydropower, solar, wind, coal, and other power generation systems. The power converters are used to convert the electricity from AC or DC mains to useable lower AC or DC supplies. These power converters are based on power electronics components. The power electronic-based control circuit must be highly efficient and cheap to optimize the energy conversion process [1-2].

Power electronics devices based on conventional semiconductor materials like silicon (Si) are approaching their limits in terms of power conversion efficiency, cost, and size [3-4]. Si-based power electronic devices have reached their theoretical limits to handle high operating voltages and high frequencies [5]. The maximum voltage handling capability of the Si-based transistor is 6.5kV and it cannot tolerate temperature above 200°C [6]. The constituent semiconductor materials of the converter circuitry cause a major portion of power losses in energy converters. Wide bandgap (WBG) materials have emerged as promising candidates to replace conventional Si-based power electronic devices.

The WBG materials can be used to cope with the challenges of low power conversion efficiency, cost, and size. SiC has been accepted as a potential candidate for power electronics applications due to its tremendous exceptional physical and electrical attributes. SiC can tolerate very high temperatures, high voltages, and high frequencies compared to that of Si [7]. Commercially available SiC-based discrete devices can handle voltages between 650V to 1700V with a current rating of 120Ampere. For example, 4H-SiC (a crystalline form of SiC) is highly suitable to handle extremely high voltages (above 10kV) in modern power electronic devices. The SiC-based chips of power electronic devices are smaller in size due to the low specific resistance of SiC compared to that of Si. The small value of specific resistance results in low parasitic capacitance in SiC-based devices. Therefore, such devices have a high switching speed compared to their counterpart Si-based devices [8-11]. Ultimately, SiC-based power electronic devices can operate at very high temperatures due to its inherent high thermal conductivity, which allows it to transfer heat to its surrounding environment [12-13]. Recent studies have shown that SiC-based metal-oxide field-effect transistors (MOSFETs) can operate above 200°C without degraded performance [14-15]. The main reason of SiC-based devices to tolerate high temperatures is its wide bandgap that reduces the generation of electron-hole pairs by thermal activation, even at elevated temperatures [16]. A summary

of the properties of Si and SiC for high temperature, high voltage, and high-frequency applications has been given in Fig. 3. It can be seen in this figure that SiC is dominating in all three domains i.e. high temperature, high voltage, and high-frequency applications.

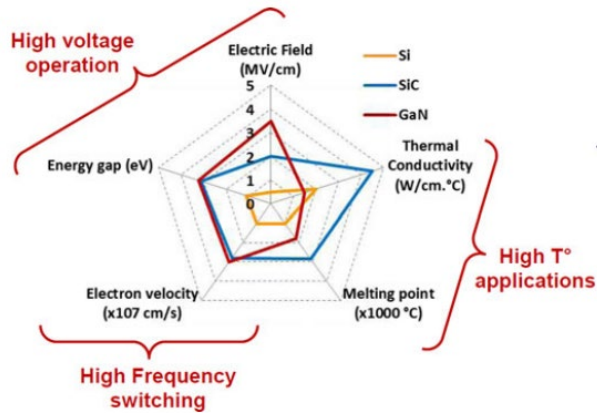


**Figure 3:** Materials properties of Silicon and Silicon carbide [6].

Moreover, state-of-the-art research on SiC-based devices covers different types of devices including SiC diodes, metal-oxide-semiconductor field-effect transistors (MOSFETs), thyristors, and SiC switches. SiC Schottky barrier diodes (SBDs) have high on/off speed due to the absence of reverse recovery current that makes it superior over Si PIN diodes. SiC SBD also has less electromagnetic interference (EMI) and oscillation. As opposed to Si-based diodes, SiC SBDs have a positive thermal coefficient (i.e. increase with an increase in temperature) allowing more parallel connections to handle high current values. SiC MOSFETs have been widely used as switches and highly suitable for industrial applications. They have extremely low switching loss compared to that of Si-based devices [17-18]. The recent research trend in the field of SiC-based devices includes: (a) design of devices to handle high temperatures; (b) minimization of parasitic inductance for gate loop and power loop; (c) Optimization of switching operations and better handling of EMI noise; (d) reducing defects of SiC substrates; (e) reduction of weight and size of the devices by reducing passive components (i.e. capacitors and inductors); (f) decreasing forward voltage degradation by reducing stacking faults and (g) reduction in the cost of devices [19-25]. The main hurdles in the fast commercialization of SiC-based devices are cost and reliability. The work presented in this thesis contributes to the major challenge of cost reduction of SiC-based devices by proposing a new fabrication technique (diffusion bonding) for SiC-based devices.

The second part of this thesis contains the simulations of graphene-based gas sensors. Gas detection and monitoring have been significant for household safety, environmental monitoring, medical diagnosis of diseases, aerospace, and military applications [26]. Although, solid-state gas sensors based on conventional semiconductor materials have some advantages like low cost, low power consumption, and small size. They play a crucial role in the monitoring and detection of hazardous and toxic compounds in industrial as well as household environments. But there are some challenges associated with these sensors related to accuracy/reproducibility in measurements and the long term stability of the device components like electrodes, sensing materials itself, and electrolytes [27-28].

The ultimate target of gas sensing technology is to obtain a gas sensor with high resolution and high accuracy. Even with the state-of-the-art solid-state gas sensors, it is not possible to detect very low concentrations of gases [29-30]. The issue of the low resolution of solid-state gas sensors comes from their intrinsic noise caused by the thermal motion of charge carriers. This noise reduces the ability of such sensors to detect a very low concentration of gases and other chemicals [31]. Therefore, there is a need to develop efficient and robust gas sensors to detect very low concentrations of chemicals. To meet these requirements, several efforts have been made to modify the conventional constituent materials of the solid-state gas sensors [27].

Nanomaterials have emerged as exceptional candidates to overcome the issues of low resolution, high sensitivity, and stability of the devices. The sensitivity of a gas-sensing device depends upon the surface-to-volume ratio of the sensing material. The high surface-to-volume ratio of the gas sensing material enables it to adsorb the target molecules effectively and efficiently [32]. Among the gas sensing nanomaterials, graphene has become a prominent material due to its several outstanding electrical and physical properties compared to that of conventional solid-state gas sensing materials [33-35]. Graphene-based sensors detect the presence of a wide range of organic and inorganic molecules more effectively compared to that of solid-state devices. Due to very low intrinsic noise, a very low concentration of the target molecules can be easily detected by graphene-based gas sensors [36-39].

## Problem statement and research questions

As stated in the introduction, this Ph.D. work has been divided into two parts. The first part is based on the numerical simulations of SiC power electronics devices and the second part is focussed on the numerical simulations of graphene-based gas sensors. SiC heterostructures are of great interest for high temperatures and high power electronics applications. The state-of-the-art techniques that are being used for the fabrication of SiC-based heterostructure devices are complicated and require a high level of expertise to handle the related fabrication equipment. Despite all this care and high fabrication cost, the fabricated structures may have defects in them. The focus of the first part of this Ph.D. work is to reduce the complexity of the fabrication process and investigate the feasibility of different combinations of SiC-based materials for the physical fabrication of power electronics devices. For this purpose, a semiconductor device simulator has been used to simulate SiC-based novel heterostructure devices considering a novel technique; diffusion bonding/welding. Prospective fabrication of SiC-based devices with this direct bonding of wafers (diffusion bonding) will reduce the complexity in the fabrication process as well as the fabrication cost. By using this direct bonding approach, defects at the hetero-junction interfaces of SiC-based heterostructure devices can be avoided.

Furthermore, the aim of the second part of this Ph.D. work is to investigate graphene-based structures for gas sensing applications. As the state-of-the-art solid-state gas sensors have some limitations in terms of stability and ability for the detection of very low concentration of gases. Graphene has emerged as an extraordinary nanomaterial for gas sensing applications. Therefore, in this Ph.D. work, the feasibility of graphene-based materials has been investigated for gas sensing applications. For this purpose, a nanoscale semiconductor device simulator QuantumWise Atomistix Toolkit (ATK-VNL) is used to simulate graphene-based sensors for the detection of a wide range of hazardous and flammable compounds.

Overall, this Ph.D. work focuses on the following research questions:

1. Investigation of circumstances for the realization of SiC-based polytypic hetero-structure with direct bonding?
2. What are the main characteristics and the behavior of the structures realized with a direct bonding technique?
3. What would be the most advanced possible combinations of SiC-based polytypic heterostructures that could be realized?
4. Can graphene-based devices detect very low concentrations of target gases and compounds?
5. How the target molecules affect the conductivity of different graphene-based materials after adsorption on the graphene surface?
6. Can the changes in photocurrent in the proximity of target gases be used as a novel mechanism for gas detection?

## Contribution of the thesis

As stated before; this Ph.D. work covers two regimes. The first aim is to investigate the feasibility of SiC-based heterostructures with the diffusion bonding approach of wafers. Whereas, the goal of the second part is to investigate the possibility of using graphene-based structures for gas sensing applications. The main contributions of this Ph.D. thesis are:

- I. Microscale simulations of SiC polytypes, Si, and Ge have been done considering the diffusion bonding of wafers. The simulation results revealed that theoretically, it is possible to develop the polytypic hetero-junction structures with the diffusion bonding of wafers.
- II. Diffusion bonding of all combinations of SiC polytypes itself as well as with Si and Ge do not give rectifying behavior of the resultant devices. A suitable combination of materials is required to get the rectifying behavior of the resultant devices. It has been concluded from the numerical simulations that electron affinity values of the constituent materials of heterostructures play a crucial role in defining the electrical behavior and barrier height at the heterojunction interface of the device. If there is no significant difference in electron affinity values of the constituent materials, then the realized heterostructure device shows resistive behavior. Therefore, the proper choice of materials is important to get rectifying behavior of the heterostructure devices.
- III. A large variety of hazardous and toxic organic/inorganic compounds has been detected with graphene-based devices in this Ph.D. work. The numerical simulation results revealed that it is possible to detect a very low concentration of gases (even a few molecules) with graphene nanoribbons, nano-sheets, and carbon nanotubes.
- IV. A novel gas/molecule detection mechanism (change in photocurrent) for graphene-based sensors has been demonstrated with simulation in this Ph.D. work. This proposed mechanism can be integrated with any state-of-the-art gas detection mechanisms in physical sensors to improve the device accuracy and selectivity for desired target gases/molecules.

The above-mentioned contributions are related to the research papers listed in the list of publications. These publications are available in full in appendices (**Paper A-K**).

## Claims about the novelty of the thesis

On the bases of the research questions mentioned earlier, some claims have been made about the novelty of this Ph.D. research work. These claims correspond to the contributions I to IV that are mentioned above. In the forthcoming chapters of this Ph.D. thesis, the following claims have been proved and defended:

**Claim 1:** Theoretically, it is possible to develop SiC-based polytypic or with other materials heterostructures with a direct bonding technique. Direct bonding of SiC-SiC wafers can be a promising fabrication technique for SiC polytypic heterostructures to reduce the fabrication cost, complexity, and improve the performance of the resultant devices.

**Claim 2:** The electrical behavior (either resistive or rectifying) of the SiC-based hetero-structures depends on the constituent polytypes. Therefore, a suitable combination of constituent polytypes of SiC must be chosen to get the desired electrical attributes of the resultant heterostructures.

**Claim 3:** A large variety of hazardous and toxic organic/inorganic compounds/gases can be detected with graphene-based devices. Even a very low concentration of target molecules (one or two molecules) can be detected with graphene-based sensors (with the use of activated surface) due to the low intrinsic electronic noise and high surface state activity of the graphene compared to the other solid-state gas sensing materials.

**Claim 4:** The change in photocurrent in the proximity of desired target molecules can be used as a novel molecule detection mechanism for graphene-based gas sensors to improve sensor accuracy and selectivity. This mechanism can be integrated with any other state-of-the-art molecule/gas detection mechanism for graphene-based sensors.

# 1 Numerical simulations of Silicon Carbide based hetero-structure devices

This chapter covers the following topics:

- A brief introduction to Silicon carbide (SiC) and its different crystalline forms
- SiC heterostructures and their fabrication techniques
- Novelty and methodology of SiC-based heterostructures that have been simulated in this Ph.D. thesis
- Conclusions drawn from the numerical simulations of SiC-based hetero-structure devices

Moreover, the target of the work that has been presented in this chapter is to investigate the electrical properties of novel SiC-SiC, SiC-Si, and SiC-Ge heterostructures using numerical experiments. Numerical simulations of heterostructure devices have been done both at the micro- and nano-levels by choosing novel combinations of SiC, Si, and Ge. Diffusion bonding/welding of SiC, Si, and Ge wafers has been proposed as a novel and prospective fabrication technique to build micro-scale SiC heterostructures.

## 1.1 SiC and its different forms

During the last decade, SiC has emerged as exciting material for high temperature, high power, and high-frequency applications [40]. It has become an exciting material for a wide range of electronic and optoelectronic applications due to its several distinct properties. SiC exists in different forms, including single crystalline, polycrystalline and amorphous forms. In a basic single crystalline form of SiC, a silicon atom is bonded with four carbon atoms or vice versa to form a tetrahedral structure, as shown in Fig. 4(a) [41-42].

Among different polycrystalline forms of SiC, the most popular polytypes are 3C-SiC, 4H-SiC, and 6H-SiC due to their promising physical and electrical characteristics. 3C-SiC is called beta silicon carbide ( $\beta$ -SiC), while 4H-SiC and 6H-SiC are called alpha-SiC ( $\alpha$ -SiC).  $\alpha$ -SiC and  $\beta$ -SiC have different and unique stacking sequences of silicon and carbon atoms that are represented with Ramsdell notations, as shown in Fig. 4(b), (c) and (d).

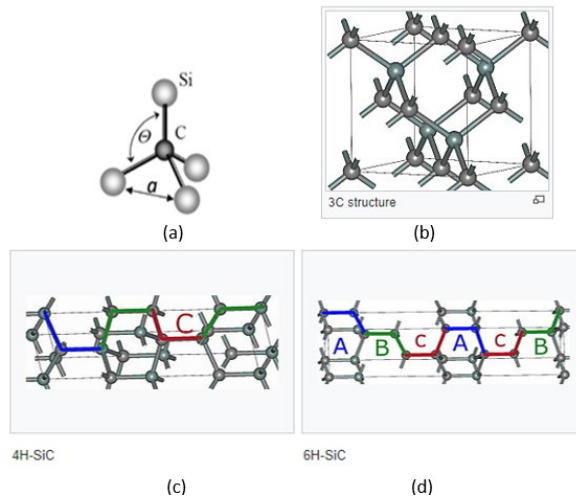


**Figure 4:** Different crystalline forms of Silicon carbide (a) Single crystal; (b) 3C-SiC; (c) 4H-SiC; (d) 6H-SiC [42-43].

In Ramsdell notation, each number like 3, 4, and 6 with 3C-SiC, 4H-SiC, and 6H-SiC respectively indicate the number of layers and the letter indicates Bravais lattice, as shown in Fig. 4. Elements AB do not change the orientation of the bilayer, whereas the element C twist the lattice by  $60^\circ$  degrees. The stacking sequences of 3C-SiC, 4H-SiC, and 6H-SiC are ABC, ABCB, and ABCACB respectively, as shown in Fig. 4.

## 1.2 Heterostructures of SiC

The heterostructure is a junction between two different semiconductor materials having different bandgaps [44]. They are the most essential components of modern electronics and optoelectronics devices due to their several interesting properties [45-46]. One of the major advantages of these devices is precise control of the motion of charge carriers that is controlled during the device design phase. By choosing appropriate materials during the design phase, the device performance can be customized [46]. Heterostructures based on the most prominent polytypes of SiC are being fabricated for a wide range of electronic and optoelectronic applications [47]. Devices based on 4H-SiC and 6H-SiC polytypes have high mobility of holes and high breakdown voltage. Whereas the main advantage of 3C-SiC based devices is that, it allows the inversion at lower electric fields [48-49]. The high-quality growth of epilayers of the constituent semiconductor materials is required to realize heterostructure devices. The Schottky barrier height (difference in energy levels at the heterojunction interface) dictates the flow of charge carriers across the heterojunction devices [44].

Furthermore, SiC heterostructures with other semiconductors like Si, GaN, InAlGaN, AlN, and Barium Ferrite (BaM) have been reported in the literature using epitaxial growth techniques [50-58] and SiC/Si heterostructures with activated direct bonding technique [59]. But SiC-SiC heterostructures with diffusion bonding/welding techniques have not been reported in the literature. In this Ph.D. work, SiC-SiC, SiC-Si, and SiC-Ge heterostructures have been proposed considering a rarely used technique; diffusion bonding or diffusion welding to make semiconductor-semiconductor interfaces.

### 1.2.1 Bandgap alignment at the heterojunction interface

As mentioned above that the heterojunction is formed by joining two dissimilar semiconductors having different band gaps. The discontinuity at the heterojunction interface gives rise to interesting properties and controls the motion of charge carriers in the resultant heterostructures devices. The Interface quality, valence band offset (VBO), and conduction band offset (CBO) play a significant role in defining the performance of the heterostructure device [60]. Based on the bandgap alignment, heterostructures can be categorized into three types, i.e., (a) Straddling gap (type-I); (b) Staggered gap (type-II); and (c) Broken gap (type-III), as shown in Fig. 5 [61].

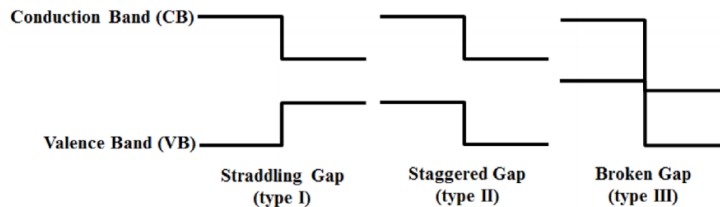


**Figure 5:** Different types of semiconductor heterostructures based on the band alignments at junction interface [61].

Different parameters of the constituent materials of heterojunction devices like work function, band gaps, and electron affinity control the properties of the resultant devices. The most famous model to define the barrier height at the heterojunction interface is the electron affinity model (EAM) [62]. According to EAM, the electron affinities of the constituent materials of a heterojunction device define the barrier height at the junction interface. According to EAM, the conduction band offset at the heterojunction interface is equal to the difference in the electron affinities of the constituent semiconductor materials. The shape of the energy bands at the junction interface is also dictated by the electron affinities. Consequently, the motion of the charge carrier through the device is controlled by the electron affinities. The energy band profile of a heterostructure based on 3C-SiC and 4H-SiC has been shown in Fig. 6. In this figure,  $E_{g1}$ ,  $E_{c1}$ ,  $E_{v1}$ , and  $\chi_1$  are the bandgap, conduction band, valence band, and electron affinity of 3C-SiC, respectively. Whereas  $E_{g2}$ ,  $E_{c2}$ ,  $E_{v2}$ , and  $\chi_2$  are the bandgap, conduction band energy, valence band energy, and electron affinity of 4H-SiC respectively [63-64].

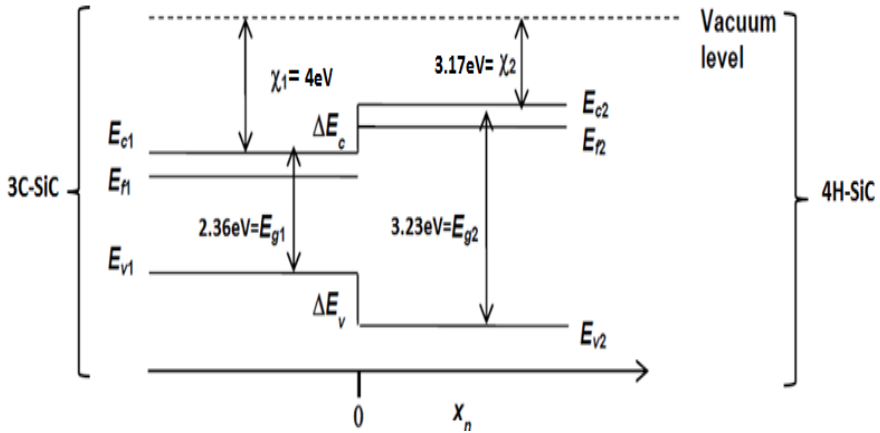


**Figure 6:** Energy band alignment of 3C/4H-SiC based heterostructure.

According to EAM, the conduction band offset and valence band offset can be calculated with the following equations:

$$\Delta E_c = q(\chi_2 - \chi_1) \quad (1)$$

$$\Delta E_v = (E_{g1} - E_{g2}) - \Delta E_c = \Delta E_g - \Delta E_c \quad (2)$$

### 1.2.2 State-of-the-art fabrication techniques for SiC heterostructures

SiC-SiC heterostructures are being fabricated with sublimation epitaxy techniques [65-66], chemical vapor deposition [67], and molecular beam epitaxy [68]. Epitaxial growth has been widely reported in the literature for the fabrication of SiC-based structures [69-79]. The epitaxial growth gives rise to defects in the resultant devices [47,76]. The physical vapor deposition technique is the simplest epitaxial growth technique to fabricate heterostructures. In this technique, one thick wafer of SiC polytype is used as a substrate and another polytype of SiC is evaporated to deposit its thin layer over the other SiC wafer. The simplest setup to realize the epitaxial growth process has been shown in Fig. 7(a). This process is called physical vapor deposition. It can be observed in this figure that one type of material (shown with yellow color) is being used as a substrate. Whereas

the other material (shown with green color at the top) is evaporated, so-called sputtering target. The whole process is carried out in a vacuum chamber, in the presence of Argon gas. The evaporated material makes its thin layer after accumulating onto the substrate, as shown in Fig. 7(b).

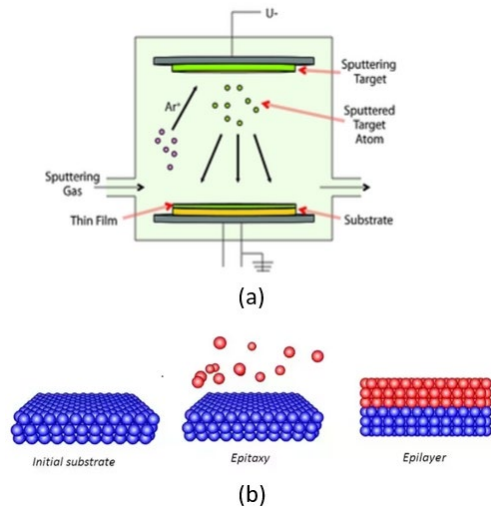


**Figure 7:** (a) A schematic of the physical vapor deposition process; (b) resultant structure after epitaxial growth [80].

SiC can tolerate very high temperatures as discussed in previous sections. This makes it very difficult to bond SiC-SiC wafers directly [81]. Epitaxial growth is a complex and costly fabrication process that demands highly sophisticated expertise to handle the tools. Diffusion bonding (direct bonding) of different SiC polytype wafers to fabricate heterostructure devices could be a promising approach to reduce the device cost and simplify the fabrication process. This process is being widely used to make metal-metal and metal-semiconductor junctions. The diffusion bonding process allows us to join two dissimilar materials directly with each other under high pressure. This process also preserves the constituent material's properties even after making a bond with the other material. This process is cheap and less time consuming [82]. The concept of diffusion welding can be realized in Fig. 8. Another advantage of using a diffusion bonding process is that the lattice mismatch issues and defects at the junction interface can be avoided [83]. Up to date, diffusion welding for making SiC-SiC heterojunction has not been successful due to the ability of SiC to resist very high temperatures [84].

### 1.2.3 Novelty of SiC related work of this Ph.D. thesis

The direct bonding of SiC-to-SiC wafers to develop the polytypic heterostructures has not been successful yet. Therefore, the main goal of this Ph.D. work is to investigate firstly the feasibility of SiC-to-SiC and secondly SiC-to-other materials heterostructures by direct bonding of wafers of these materials. In the Ph.D. work, SiC-SiC, SiC-Ge, and SiC-Si heterostructures have been numerically investigated considering the diffusion bonding/welding technique. These numerical simulations could be a pathway to the fabrication of novel SiC-based heterostructures by choosing appropriate materials. Our research group at Thomas Johann Seebeck Department of Electronics, Tallinn University of Technology, Estonia has been working to fabricate SiC-SiC heterojunctions with the direct bonding of the wafers [85-87]. The bonding of SiC-SiC wafers is quite tricky

technology. One must know the optimized pressure, temperature, and other diffusion bonding related parameters for the successful bonding of wafers. The surface treatment of the wafers also plays a crucial role in facilitating the diffusion bonding process. For better adhesion of wafer and get the smoother surface of the wafer, chemical etching could be a promising technique [88]. The catalytic etching is another feasible technique that can be used to polish SiC wafers. It is intended to use these polishing techniques for wafers that can give much better results in terms of the direct bonding of wafers [89].

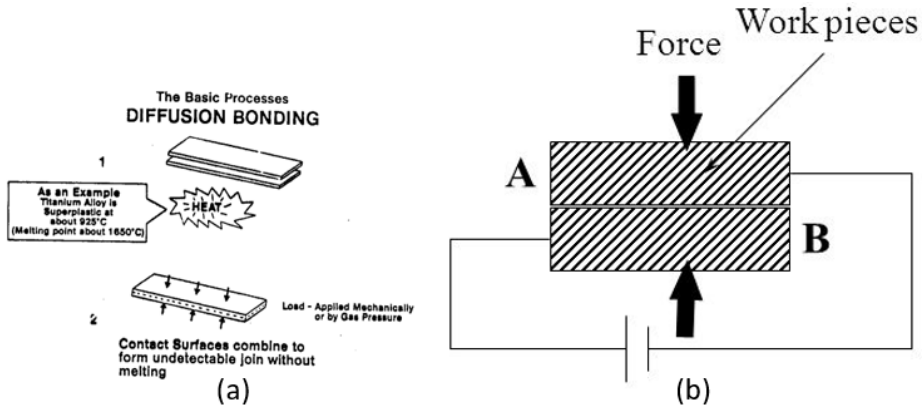


**Figure 8:** (a) The basic process of diffusion bonding; (b) schematic of the experimental setup for direct bonding of wafers [82].

### 1.3 Methodology of simulated SiC based heterostructures

This section includes comprehensive detail about the adopted methodology of the simulated devices. Micro- and nano-scale devices have been simulated with SILVACO TCAD [90] and QuantumWise Atomistix Toolkit (ATK-VNL) [91] softwares, respectively. SILVACO TCAD is a commercially available software package that is used to simulate micro-scale semiconductor devices based on the basic semiconductor equations [92]. These equations are based on statistics describing relatively large material volumes. Here, large material volume means that the dimensions (thickness) of the materials are in the range of micrometers (for example 300 $\mu\text{m}$  in **Paper A, B, and C**). These equations are only valid for those materials having dimensions in the range of micrometers. This statement is also valid for the sub-models (mobility, recombination, generation, etc.) accurately describing the physics applicable to volumes, where Fermi statistics could be applied. For the devices having dimensions comparable to the mean free path of electrons (i.e. ballistic transportation of the charge carriers), the duality of particles starts to play its major role. Therefore, the basic semiconductor equation set does not remain applicable to such nano-level devices. In such type of nano-scale devices, it becomes more crucial to calculate the surface and nano-level effects. Therefore, another type of mathematical equations (i.e. Schrödinger equations and DFT approximations) depicting nano-level physics correctly is needed. ATK-VNL software package is the best available commercial software package based on mathematical equations that are valid for nano-scale devices. Therefore, two different software packages have been used for numerical simulations of proposed micro- and nano-scale devices to get a better insight into the electrical attributes of the simulated structures.

### 1.3.1 Why SILVACO TCAD and QuantumWise Atomistix Toolkit (ATK-VNL)

In semiconductor materials and devices research, a particular approach is followed. Therefore, firstly, the semiconductor structures are simulated, and their characteristics are comprehensively analyzed. This analysis could include the investigation of the electronic properties, thermal properties, and current distribution mechanisms. TCAD software is being widely used in the industries for physics-based modeling of semiconductor devices. This software is used to optimize the semiconductor device fabrication process. As mentioned above, this software is based on differential equations that are a modified version of Maxwell's equations [93]. The results obtained from this software are accepted worldwide in the semiconductor community. A large number of reputed published articles, based on the use of SILVACO TCAD simulation tools, can be found, as it is shown for example in [94]. This justifies that SILVACO TCAD software is used for the modeling of the proposed microscale devices in the thesis. Furthermore, for nanoscale simulations, Quantumwise Atomistix Toolkit (ATK-VNL) software has been used in this thesis. This software is developed by world-leading nano-electronics researchers and experts. This software is being widely used in the nanoscale semiconductor industry for atomic-scale modeling of devices. This tool provides highly accurate and realistic results. A large number of reputed published articles based on ATK-VNL software can be found at this reference [95].

### 1.3.2 Computational procedure of SILVACO TACD and QuantumWise Atomistix Toolkit (ATK-VNL)

The calculation methodology adopted by SILVACO TACD software is based on semiconductor physics and related equations. A large range of suitable material's related physical models and parameters are defined in the code using different commands during simulation of the device. Comprehensive detail of all these models and related equations are given in the SILVACO user manual [96]. The detail of used physical models and their related equations for proposed SiC-based devices have been given in subsection 1.3.4. Computational details and related theoretical background for ATK-VNL is given as:

ATK-VNL software models the electronic attributes of the quantum system within the framework of density functional theory (DFT). This DFT theory is based on a "linear combination of atomic orbitals (LCAO)". ATK-VNL software simulates semiconductor devices using "non-equilibrium Green's function (NEGF)" [97]. ATK has several in-built calculators to calculate the electronics properties of the simulated nano-structures. For the calculation of the electronic properties of simulated devices, an in-built DFT calculator has been used. This calculator calculates the electronic structure of the simulated device based on "single-particle wave functions". This calculator allows fast and accurate calculation of results compared to that of other calculators [98]. The density matrix is the most important parameter in self-consistent calculations to determine the electron density. Afterward, this electron density function is used to derive the effective potential. Subsequently, this calculated effective potential is used to obtain Kohn-Sham Hamiltonian as shown in Eq.3:

$$H_{electron} = -\frac{\hbar^2}{2m} \nabla^2 + V^{eff}[n](r) \quad (3)$$

The first term in Eq. 3 is the kinetic energy and the second term is the potential energy of the electron moving in the presence of applied external voltage. After that, the one-electron Schrödinger equation is used to formulate the Eigen-functions of

Kohn-Sham Hamiltonian. Then, one-electron Schrödinger equation is solved to obtain “one-electron Eigen-functions of the Kohn-Sham Hamiltonian ( $\Psi_\alpha$ )” as shown below:

$$H_{\text{electron}} \Psi_\alpha(r) = \varepsilon_\alpha \Psi_\alpha(r) \quad (4)$$

Then, Eq. 4 is resolved by expanding the “Eigen-functions  $\Psi_\alpha$ ” as given below:

$$\Psi_\alpha(r) = \sum_i c_{\alpha i} \phi_i(r) \quad (5)$$

Finally, a matrix equation can be developed to get “expansion coefficients,  $C_{\alpha i}$ ” as:

$$\sum_j H_{ij} c_{\alpha j} = \varepsilon_\alpha \sum_j S_{ij} c_{\alpha j} \quad (6)$$

Where  $H_{ij}$  indicates the Hamiltonian matrix and  $S_{ij}$  designates the “overlap matrix” in Eq. 6. In the next step, the eigenstates of the Kohn-Sham Hamiltonian are used to get the electron density of the many-electron system as shown below:

$$n(r) = \sum_\alpha f_\alpha |\Psi_\alpha(r)|^2 \quad (7)$$

In Eq. 7,  $f_\alpha$  stands for the occupation of a level that has been denoted by  $\alpha$ . In the next step, the electron density is written in terms of density matrix:

$$n(r) = \sum_{ij} D_{ij} \phi_i(r) \phi_j(r) \quad (8)$$

Electron density matrix ( $D_{ij}$ ) in Eq. 8 can be given by:

$$D_{ij} = \sum_\alpha f_\alpha C_{\alpha i}^* C_{\alpha j} \quad (9)$$

After obtaining a density matrix, several transport properties of the simulated device including the transmission spectrum can be calculated. Afterward, the transmission spectrum is used to obtain the electric current. Transmission amplitude “ $t_k$ ” is used to define the scattering states “ $k$ ” propagating through the device. The transmission coefficient is obtained as:

$$T(\varepsilon) = \sum_k t_k^* t_k \delta(\varepsilon - \varepsilon_k) \quad (10)$$

In Eq. 10,  $\varepsilon$  is the energy of the transmission coefficient at which all transmission amplitudes are summed up [99]. Then to obtain IV-curves, the transmission spectrum of the simulated device is calculated in ATK-VNL [100]. The electric current can be calculated from transmission coefficients as:

$$I(V_L, V_R, T_L, T_R) = \frac{e}{h} \sum_\sigma \int T_\sigma(E) \left[ f\left(\frac{E - \mu_R}{k_B T_R}\right) - f\left(\frac{E - \mu_L}{k_B T_L}\right) \right] dE \quad (11)$$

In Eq. 11,  $T_{L/R}$  are “left/right electrode temperatures”,  $T_\sigma(E)$  is “transmission coefficient”,  $f$  is “Fermi-level” and  $\mu_{R/L}$  are “chemical potentials of right/left electrode” [101]. The calculated transmission spectrum and transmission coefficient at each bias point can be viewed using the Transmission Analyzer plugin of ATK-VNL. This plugin shows the “average transmission spectrum as a function of energy” [102-104].

### 1.3.3 Exchange-correlation Functionals for DFT based simulations

The exchange-correlation function is used to approximate electron-electron interaction in the DFT method. ATK supports many exchange-correlation functions such as “local density approximation (LDA)” and “Generalized-gradient approximation (GGA)”. LDA considers all quantum system homogeneous in terms of electric field distribution. But the real systems are highly inhomogeneous in this respect [98]. GGA functionals are better in terms of accuracy and reliability for calculation of ground-state properties such as equilibrium crystal structures, total energy, and cohesion energies [105-106]. PBE-GGA is less time consuming and reduces the computation time as well [107]. DFT calculations of carbon-based nano-materials sensors using GGA have also been reported in the literature [108-111]. That is why GGA exchange-correlation has been used in these simulations. For PBE-GGA exchange-correlation, SG15 pseudopotential [112] is the latest and recommended in the Quantumwise user manual. For SG15 Pseudopotential medium basis set is the default, which is enough for most of the applications. That is why a medium basis set is used in these simulations. In DFT simulations, there is no specific rule about the validity range of complex functionals for any system. The usual practice is to test all the available functionals for simulated systems and then validate them with the available experimental results [97]. However, there are several other calculators with different exchange and correlation approximation available in ATK-VNL. There might be a slight difference in the results due to different calculation methodology and accuracy level of each calculator. The main focus of this work is not to investigate the differences in results due to different calculators. This could be considered as future work to investigate the effect of different hybrid approximation on the electronic properties of the simulated devices [113].

### 1.3.4 Microscale simulations of SiC based heterostructure diodes

The microscale SiC-based heterojunction diodes have been simulated in SILVACO TCAD software. The schematics of all microscale-simulated devices have been shown in Fig. 9. Different combination of materials like 3C-4H/SiC [Paper A], 4H-6H/SiC [Paper A], Si/4H-SiC [Paper B], Si/3C-SiC [Paper B], Ge/4H-SiC [Paper C], Ge/3C-SiC [Paper C] have been used to simulate *nn*-heterostructures. In each heterostructure diode, two wafers have been joined with each other considering the diffusion bonding technique, as shown in Fig. 9(a). The geometry of each simulated device is shown in Fig. 9 (b). The thickness of each wafer is 300 $\mu\text{m}$  and the surface area is 1x1 $\mu\text{m}^2$ . Donor doping concentrations in all materials have been kept 10<sup>18</sup>cm<sup>-3</sup> to get the ohmic electrodes at the top and bottom of the simulated structures. SILVACO TCAD allows adding several in-built material's related parameters and physical models to get more realistic results from the simulations. The following physical models have been used for the microscale simulations of the heterostructure diodes.

- **Charge carrier mobility models for SiC-based devices**

Several mobility-related physical models are implemented in these simulations. To add the anisotropic mobility of charge carriers in SiC, an in-built anisotropic mobility model proposed by Lindefelt [114] and Lades [115] has been implemented. They introduced the tensor properties in the drift-diffusion equation that are written as:

$$\mu = \begin{pmatrix} \mu_1 & 0 & 0 \\ 0 & \mu_1 & 0 \\ 0 & 0 & \mu_2 \end{pmatrix} \quad (12)$$

In Eq. 12,  $\mu_1$  is the mobility of charge carriers (holes and electrons) in one plane and  $\mu_2$  is the mobility in the second plane. Analytical low field mobility model proposed by Caughey-Thomas [116] is used to specify temperature and doping dependent low field mobilities of the charge carriers in SiC. This model along with the parallel field mobility model has also been implemented in these simulations. To add the influence of carrier-carrier scattering in simulated structures, the Conwell carrier-carrier scattering model [117] has been used. The effect of incomplete ionization has also been added by using an incomplete ionization model in TCAD.

- **Recombination models for SiC**

The recombination of charge carriers occurs due to the trap centers and direct recombination. The first process of recombination is called Shockley-Read-Hall (SRH) recombination and the second one is called Auger recombination. SRH model has been implemented to realize the emission and suppression of charge carriers by traps. The SRH model is implemented by using the following equation [118]:

$$R_{SRH} = \frac{np - n_i^2}{\tau_p(n + n_i) + \tau_n(p + n_i)} \quad (13)$$

In Eq. 13,  $\tau_p$  and  $\tau_n$  are charge carrier lifetime of holes and electrons, respectively. SiC is an indirect bandgap material, so the probability of band-to-band recombination is very low but cannot be neglected. Auger recombination is given by the following equation [118]:

$$R_{AUGER} = (np - n_i^2)(C_n n + C_p p) \quad (14)$$

In Eq. 14,  $C_n$  and  $C_p$  are coefficients representing the interaction between charge carriers. The current-voltage (IV)-curves of all microscale-simulated devices are calculated in SILVACO TCAD by using its graphical user interface module; TONYPLOT. The IV-characteristics of microscale-simulated devices have been compared with their nanoscale counterpart structures.

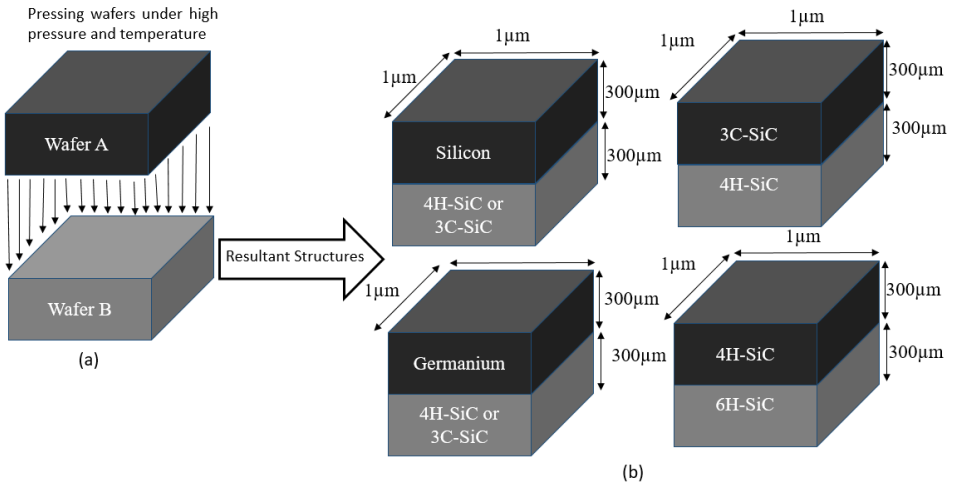


**Figure 9:** (a) Diffusion welding realization in SILVACO TCAD software; (b) schematic of microscale simulated nn-junction diodes.

### 1.3.5 Nanoscale simulations of SiC based heterostructure diodes

The same material combinations mentioned in the previous subsection are used to simulate nanoscale *nn*-heterojunction diodes. All the nanoscale simulations have been

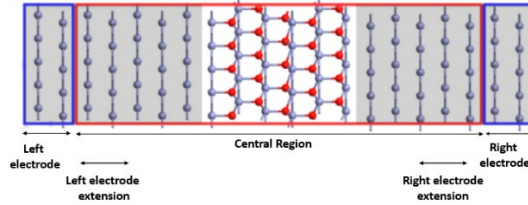


**Figure 10:** Two probe atomic-scale model of nanoscale simulated devices in ATK-VNL software [119].

done in a nanoscale semiconductor device simulator; QuantumWise Atomistix Toolkit (ATK-VNL). A wide range of nanoscale devices can be simulated in ATK-VNL. Two probe configuration model has been adopted (also suggested in the ATK-VNL user manual) for the simulation of atomic-scale heterostructures, as shown in Fig. 10. In this configuration, extreme right and left sides of the device are used to define periodic electrodes of the device. These periodic electrodes are then connected with the non-periodic region, called the central region of the device. The central region is also called the scattering region because the scattering of charge carriers occurs in this region as they travel from one electrode to the other through the device.

All simulated nanoscale *nn*-heterojunction diodes have been shown in Fig. 11. 3C-SiC, 4H-SiC, 6H-SiC, Si, and Ge have been cut in (111), (0001), (0001), (100) and (001) orientations respectively to build heterojunctions [Paper A, B, C]. These nanoscale simulated heterojunction devices are quasi-two-dimensional structures, as shown in Fig. 11. To study the effect of lattice mismatch problems at the heterojunction interface, defects have been introduced at the heterojunction interface by rotation each semiconductor atoms by 12 degrees with respect to the other, as shown in Fig. 11.

In Fig. 11(b), polytype-1, and polytype-2 are 3C-SiC and 6H-SiC respectively for the *nn*-junction 3C/4H-SiC device. Whereas polytype-1 and polytype-2 are 4H-SiC and 6H-SiC for the *nn*-junction 4H/6H-SiC device. The donor doping concentration in all nanoscale materials is kept at  $10^{18}\text{cm}^{-3}$ . Semiconductor materials themselves have been used as electrodes rather than depositing metallic electrodes to avoid Schottky barrier formation at the electrodes. This approach also reduces the computation time in the simulator.

ATK-VNL software toolkit uses several in-built calculators to calculate a wide range of electronic properties of the simulated structures. In the presented work, for the calculations of IV-curves of simulated devices, the ATK-DFT calculator has been used [120]. All the nanoscale simulations have been run in a high-performance computing environment (HPC) [121].

### 1.3.6 Geometry optimization of simulated SiC based heterostructures in ATK-VNL

In this Ph.D. work, geometry optimization of simulated heterostructure diodes (two probe models) is done using the "Bulk Rigid Relaxation (BRR) Method". In BRR, two probe configuration is simulated from relaxed electrodes. Then, the central region of the device is relaxed with "Rigid Constraints" using **Atomic Constraint Editor** of **OptimizeGeometry Block**. After relaxing the central region, device is reassembled. A comprehensive detail about geometry optimization using the BRR method in ATK-VNL can be found at this reference [122].

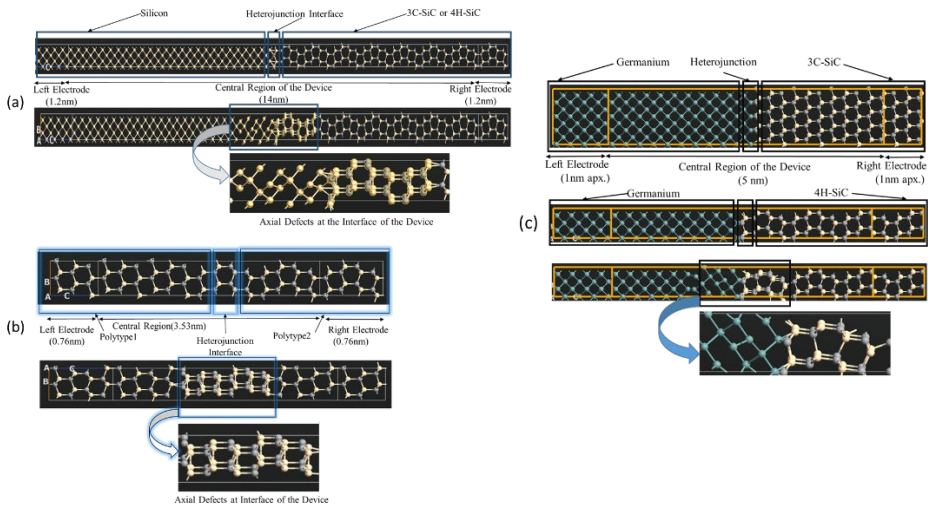


**Figure 11:** Nanoscale simulated (a)  $\text{Si}/3\text{C-SiC}$  and  $\text{Si}/4\text{H-SiC}$  based  $nn$ -heterojunction diodes [123]; (b)  $3\text{C-6H/SiC}$  and  $4\text{H-6H/SiC}$  based  $nn$ -heterojunction diodes [124]; (c)  $\text{Ge}/3\text{C-SiC}$  and  $\text{Ge}/4\text{H-SiC}$  based  $nn$ -heterojunction diodes [125].

Furthermore, in another set of simulations, the effect of the inclusion of graphene nanoribbons on the electrical conduction properties of  $nn$ -heterojunction  $4\text{H-6H/SiC}$  diodes have been studied [Paper D]. Graphene nanoribbon has been deposited on a quasi-two-dimensional diode in two different configurations, as shown in Fig. 12 (c), (d). The IV-characteristics of all simulated structures of Fig. 12 have been calculated and compared with each other.

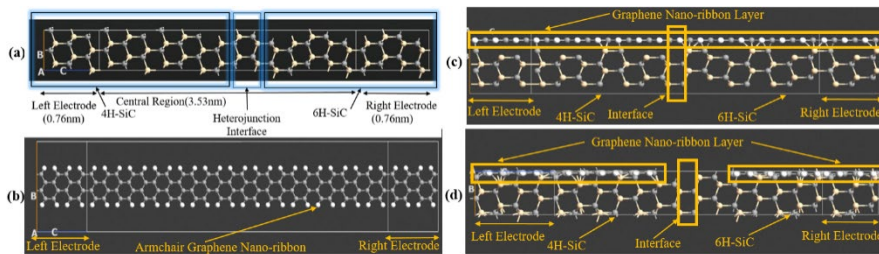


**Figure 12:** (a) ATK view of  $nn$ -heterojunction  $4\text{H-6H/SiC}$ ; (b) pristine armchair graphene nanoribbon device; (c) diode with nanoribbon layer deposited over the whole device; (d)  $nn$ -junction diode with nanoribbon layer deposited partially over the device [126].

## 1.4 Results and discussion on simulated SiC based heterostructures

The structures shown in the previous section have been numerically characterized to investigate their electrical parameters and characteristics. The focus of the results presented in this section is to prove the claim about the prospective fabrication of SiC-based heterostructures with the diffusion bonding approach [Claim 1]. Whereas, the next focus is to prove that the electrical behavior (either resistive or rectifying) of the SiC-based heterostructures strongly depends on the constituent materials [Claim 2]. The IV-characteristics of all micro- and nano-scale devices have been calculated and compared with each other. These results demonstrate that theoretically, it is possible to build SiC heterostructures with the diffusion welding technique. The IV-curves of the

simulated devices also show that the resistive or rectifying behavior of the SiC heterostructures is steered by the constituent polytypes. As an example, the simulation results of **Paper A** have been shown in Fig. 13 and Fig. 14. In these figures, the current is taken in arbitrary units (a.u.). The scaling factors are given in the figure captions of the respective figures to get the actual current values.

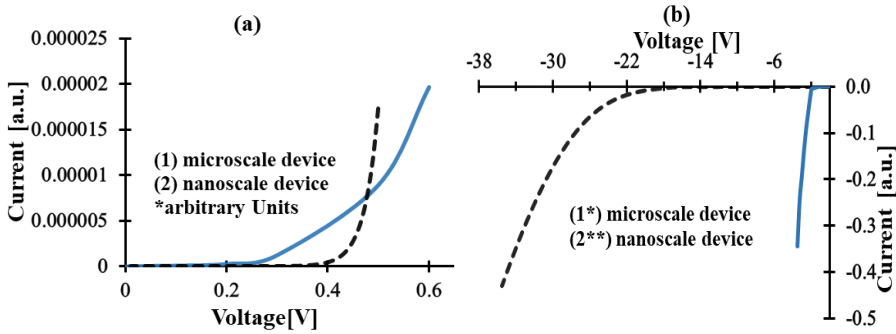


**Figure 13:** (a) Forward; (b) reverse IV-characteristics of microscale and nanoscale 3C-4H/SiC devices (for actual current values \*current axis  $\times 10^{-5}$  \*\*current axis  $\times 10^{-9}$ ) [124].

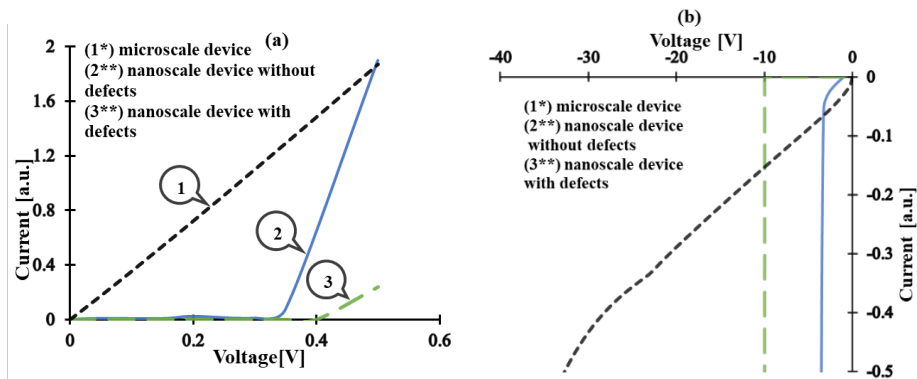


**Figure 14:** (a) Forward; (b) reverse IV-characteristics of microscale and nanoscale 4H-6H/SiC devices (for actual current values \*current axis  $\times 10^{-5}$  \*\*current axis  $\times 10^{-9}$ ) [124].

The simulation results of **Paper A** reveal that the forward and reverse IV-characteristics of *nn*-heterojunction 3C-4H/SiC are similar to conventional *pn*-junction diodes, as shown in Fig. 13 (a). Whereas, the reverse break down in simulated microscale device occurred due to the joint influence of tunneling and impact ionization process. No charge carriers have been observed in absence of tunneling model that could participate in provoking the avalanche breakdown process. This confirms that in this simulated device, reverse breakdown occurs due to the joint influence of tunneling and impact ionization processes. The reason for the small values of the turn-on forward voltage and reverse breakdown voltages in the nanoscale-simulated device is its small dimensions that are comparable to the mean free path of the constituent SiC polytypes. For example, the mean free path of 4H-SiC is approximately 23 Å [127], and the central region of the simulated 4H-6H/SiC device is 35Å. Due to these small dimensions, the electrons undergo fewer collisions as they travel through the device from one electrode to the other.

Furthermore, a low reverse breakdown voltage has been observed in nanoscale-simulated devices compared to that of microscale devices. It seems that in the nanoscale

device, the reverse breakdown is caused by the Zener effect (i.e. transition of electrons from the valence to the conduction band due to the applied electric field). The effects of lattice mismatch defects in 4H-6H/SiC based nanoscale simulated devices have been studied by introducing axial displacements at the heterojunction interface, as shown in Fig. 11(a). It has been observed that lattice mismatch defects reduce the forward current through 4H-6H/SiC device, as shown in Fig. 14(a). The defects in the device provoke the scattering phenomenon. In the defective device, electrons are deflected from their intended path under the influence of ionized impurities due to the impact of Coulomb-forces. Defects also play a role in changing the wave function of electrons [128-129]. In the reverse-bias regime, an increase in reverse breakdown voltage has been observed in the nanoscale defective device, compared to that of the nanoscale device without defects, as shown in Fig. 14 (b).

Finally, it can be concluded that the results of **Paper A** are proving **Claim 1** and **2**. The numerically analyzed heterostructures prove the claim that it is possible to develop SiC-SiC heterostructure with diffusion bonding/welding technique (**Claim 1**). The analysis of 3C-4H/SiC heterostructures shows the rectifying behavior for full current-voltage characteristics, as shown in Fig. 13. This rectifying behavior is due to the significant difference in electron affinities of 3C-SiC and 4H-SiC polytypes that creates a potential barrier at the hetero-junction interface. Whereas, 4H-6H/SiC heterostructures behaving as a resistor due to very small difference in electron affinities of 4H-SiC and 6H-SiC arising from the relatively low barrier height, as shown in Fig. 14 (**Claim 2**).

#### **1.4.1 Differences in nano- and micro-scale simulation results**

The nano- and micro-scale simulation results exhibited obvious differences in terms of IV- characteristics. The main reasons for these differences are:

1. The simplification techniques (building and forming the sub-models, and determination of the model parameters as well) used for micro- and nano-scale simulators are different. Therefore, the results could differ because of that scaling down.
2. Definitely charge carrier's transport mechanism and the factor influencing them are different for both types of devices. In nanoscale devices, the motion of charge carriers is almost ballistic. The mean free path of electrons is comparable to the length of such devices. The charge carriers undergo fewer collisions and hence do not so much deflect from their intended paths as they travel from one electrode to the other in the device.
3. For the micro-scale device, the charge carrier's transport mechanisms and governing physics are different. The dimensions of the devices are not comparable to the mean free path of electrons in such devices. Therefore, the motion of charge carriers does not remain ballistic. The choice of physical models and materials parameters in the SILVACO TCAD simulator are crucial factors that can influence the results.
4. The difference in nano- and micro-scale device simulations can be addressed by using several approaches. For the simulations of microscale devices in SILVACO TCAD, such differences can be minimized by tuning of material's parameter for used physical models. A significant difference in reverse IV- characteristics of nano- and micro-scale devices have been observed. This could be due to the non-idealization of impact ionization and tunneling models of SILVACO TCAD. Whereas, for nano-scale simulations, such differences can be minimized by proper sizing of the devices (i.e. by

increasing their length). Physical experiments are recommended to resolve and get more insight into such differences.

Therefore, in a majority of the cases, the microscale simulation is used for the general characterization of the structures and if some simulated characteristics differ strongly from the experimentally measured results after realization of the devices, then the nano-scale simulation is used for clarification of the situation to understand the physical mechanisms influencing the deviation of characteristics.

## 1.5 Validation and comparison of results related to SiC based heterostructures

The research results presented in this chapter are fully simulation-based. As discussed in previous sections, the heterostructures of SiC with direct bonding of wafers have not been reported yet in the literature. The proposed idea and structures are novel. Furthermore, it is difficult to compare such type of semiconductor materials based simulation results with other results from literature because the device characteristics change with the material parameters and used physical models. For validation and comparison of the results, physical experiments have been proposed. At this stage, no experimental results are available for comparison. However, some experiments related to this Ph.D. work are in process at Thomas Johann Seebeck Department of Electronics, Tallinn University of Technology, Estonia.

## 1.6 Conclusions from the simulations of SiC based heterostructures

In this chapter simulations of the novel, *nn*-heterojunction diodes have been accomplished. Micro- and nano-scale structures have been analyzed. The results revealed that the electron affinities of the constituent semiconductor materials of simulated diode structures play an important role in defining the barrier height at the heterojunction interfaces. It has been observed that there should be a significant difference between electron affinities of semiconductor materials, which are forming heterojunctions. Otherwise, the barrier height might be so low that the interface will show resistive rather than rectifying behavior. Since the difference in electron affinities of 4H-SiC and 6H-SiC is less compared to that of 3C-SiC and 4H-SiC, therefore 4H-6H/SiC-based *nn*-heterojunction structures behave like a resistor [Paper A]. Similar resistive behavior has been observed in Si/3C-SiC based *nn*-heterojunction diode [Paper B]. Ge/3C-SiC based device also behaving like a resistor due to a small difference in electron affinities of Ge and 3C-SiC [Paper C].

Furthermore, the lattice mismatch defects also have a strong influence on the IV-characteristics of the devices. These defects provoke the scattering phenomenon in the resultant device and degrade their performance. This can be concluded from the simulation results that the need for a proper choice of materials is crucial in defining the rectifying behavior of the resultant devices. The 3C-4H/SiC [Paper A], Si/4H-SiC [Paper B], and Ge/4H-SiC [Paper C] based devices are the most suitable combinations of materials to develop diodes. Theoretically, it is possible to develop SiC-based hetero-structures by direct bonding of the wafers that will reduce the manufacturing cost and simplify the fabrication process. The manufacturing of analyzed devices requires specific wafer polishing to get better adhesion and more precise optimization of diffusion bonding parameters (i.e. pressure, temperature, etc.).

Finally, the following novel results have been achieved out of this part of Ph.D. work that also justifies the claims that have been made at the start of the thesis:

1. It has been demonstrated that theoretically, it is possible to develop SiC-based heterostructure diodes with a novel direct bonding technique. In this Ph.D. work, the direct bonding of wafers has been proposed for the very first time as a prospective fabrication technique for SiC-based heterostructure devices [Paper A-D and K].
2. It has been demonstrated that a suitable combination of constituent materials must be chosen to develop a heterostructure diode based on SiC. A considerable difference in electron affinities of the constituent materials is mandatory to avoid resistive behavior of the resultant device. Therefore, the right choice of the materials and fabrication conditions play a crucial role in defining the electrical behavior of the resultant heterostructure devices [Paper A-D].

## **1.7 Challenges in the prospective physical fabrication of simulated Devices**

In this chapter results of nano- and micro-scale simulation of SiC with other semiconductors (Si, Ge) have been presented using the diffusion bonding technique. The simulation results revealed interesting electrical properties of the simulated devices. These results show that theoretically, it is possible to develop SiC polytypic heterostructure with a direct bonding technique. But the physical fabrication of such structure is challenging due to the extreme hardness of SiC wafers and their ability to resist high temperatures. Catalytic etching has been suggested for the polishing of SiC to get a smoother surface for the direct bonding of the wafers. Finding the optimized temperature, pressure, and other diffusion bonding related parameters are also crucial for the successful bonding of wafers. Physical experiments have been suggested to get more insight and successful development of proposed SiC heterostructures.

## **1.8 Overview of publications related to the numerical analysis of SiC-based heterostructures**

This section of the thesis explains how this Ph.D. work helped in answering the research questions that had been raised about SiC-based heterostructures at the start of the thesis.

### **Paper A**

In this paper, micro- and nano-scale simulations of *nn*-heterojunction diodes based on 3C-4H/SiC and 6H-4H/SiC are done. The effects of non-ideal bonding at the heterojunction interface of the heterostructure devices due to lattice misplacements have been investigated for nano-scale simulated devices. It has been concluded from these simulations that the forward IV-characteristics of micro- and nano-scale devices are quite similar to each other. Whereas the reverse IV-characteristics of both types of devices differ from each other. Such types of differences could be addressed by the material's parameter tuning of impact ionization and tunneling models for micro-scale devices and appropriate sizing of the nano-scale devices. It is concluded that the axial defects at the heterojunction interface of the devices contribute to

provoke the scattering phenomena, which ultimately reduce the forward-current and increase the reverse break-down voltage. However, theoretically, it is possible to fabricate the proposed devices with diffusion bonding technique (Answer to research question 1).

#### **Paper B**

In this paper, micro- and nano-scale simulations of Si/4H-SiC and Si/3C-SiC based *nn*-heterojunction diodes have been done. The simulation results revealed that the forward IV-characteristics of simulated Si/3C-SiC are similar to a resistor due to very small differences in electron affinity values between Si and 3C-SiC. Since electron affinity values define the conduction band-offset at the hetero-junction interface. In Si/4H-SiC based simulated device, a turn-on knee can be observed in forward bias-regime due to relatively a large difference in electron affinity values between Si and 4H-SiC. As opposed to Si/3C-SiC based simulated device, in Si/4H-SiC based device a complete reverse-break down can be observed at higher voltages. Si/4H-SiC based simulated device gives a rectifying behavior whereas Si/3C-SiC based device shows a resistive behavior. Si/4H-SiC based *nn*-heterojunction device is suitable for the prospective fabrication of power diodes. Whereas, Si/3C-SiC based device is simply an expensive resistor and hence not recommended for physical fabrication. Furthermore, it is concluded from these simulations that axial defects provoke the scattering phenomena in the hetero-structure devices (Answer to research question 1-3).

#### **Paper C**

In this paper, micro- and nano-scale simulations of Ge/3C-SiC and Ge/4H-SiC are done. These simulation results reveal that in forward bias regime, the IV-characteristics of both Ge/3C-SiC and Ge/4H-SiC are similar to a typical *pn*-junction diode. Whereas in the reverse bias regime the IV-characteristics are quite different from a *pn*-junction diode. These differences in reverse IV-curves can be minimized by parameter tuning of impact ionization and tunneling models in micro-scale devices. Whereas in the nano-scale devices such differences can be minimized by proper sizing of the devices. These simulation results showed that theoretically, it is possible to develop Ge/3C-SiC and Ge/4H-SiC device with diffusion bonding approach (Answer to research question 1-3).

#### **Paper D**

In this paper, nano-scale simulations are done to study the effect of the inclusion of graphene nano-ribbon on the electrical conduction properties of *nn*-heterojunction 4H-6H/SiC diodes. The simulation results revealed that the inclusion of graphene nanoribbons significantly improved the electrical conductance of the simulated diodes. The proposed configurations of 4H-6H/SiC diodes with armchair graphene nanoribbon can be used to develop diodes and field-effect transistors for nano-electronics applications (Answer to research question 1-2).

#### **Paper K**

In this paper, simulations of a novel design of 4H-SiC/6H-SiC/4H-SiC double hetero-structure single quantum-well edge light-emitting diode have been done considering the diffusion welding approach. All the simulations have been done in SILVACO TACD software. Current-voltage characteristics, luminous power, and power spectral density curves have been calculated. The simulated LED showed promising results in terms of luminous power efficiency and external quantum efficiency. The luminous power efficiency of 25%

and the external quantum efficiency of 16% have been achieved for the simulated LED. This type of LED is used as a light source in fiber optic communication links. The device performance can be optimized by choosing suitable constituent semiconductor materials to get the light emission in the desired wavelength range. The prospective physical fabrication of this proposed device with diffusion bonding technique will reduce the fabrication cost (Answer to research question **1-3**).

## 2 Numerical simulations of graphene-based gas sensors

The goal of the work presented in this chapter is to investigate novel graphene-based chemical and gas sensors. This chapter includes the following contents:

- Introduction to graphene and its derivatives
- State-of-the-art of gas/chemical sensors
- Novelty and methodology of this Ph.D. work on graphene-based gas sensors
- Conclusions of this Ph.D. work

### 2.1 Introduction to Graphene

Graphene is a single-layered two-dimensional sheet of  $sp^2$ -bonded carbon atoms in a hexagonal arrangement. Graphene and its derivatives exist in one-dimensional nanotubes and zero-dimensional fullerenes. Graphene exhibits exceptional electrical, mechanical, and thermal properties due to the long-range of  $\pi$ -conjugation in its structure [130]. Graphene was isolated first time from graphite in 2004 [131]. Intrinsic graphene has semi-metallic or metallic nature due to its zero bandgap. Graphene structure has been shown in Fig. 15 (a). There are two  $\pi$ -bonds and one  $\sigma$ -bond in graphene, as shown in Fig. 15(c). The  $\pi$ -bonds are available above and below of graphene layer, and can overlap with the neighboring carbon atoms. Whereas,  $\sigma$ -bonds are tightly bonded and they do not play any significant role in the electrical conductivity of graphene [132].

Furthermore, graphene is a smart material that responds to any physical change in its surrounding environment [133]. The presence of  $\pi$ -bonds above and below of the graphene layer form an electronic cloud around graphene. This electronics cloud enables electrons to move freely around the graphene layer rather than sticking to a specific atom. This property makes graphene highly conductive. The formation of the electronic cloud around the graphene layer has been shown in Fig. 16 [134]. Being a smart material, graphene is very sensitive to any stimuli like the presence of gas/biomolecules, mechanical strain, pH value change, and thermal/optical excitations. In the proximity of gas/biomolecules, graphene resistance is changed. It has been found that the adsorbed gas molecules change the charge carrier concentration in graphene and consequently its electrical conductivity is changed. Schedin et al. [135] used the same working principle for the detection of adsorbed molecules on graphene.

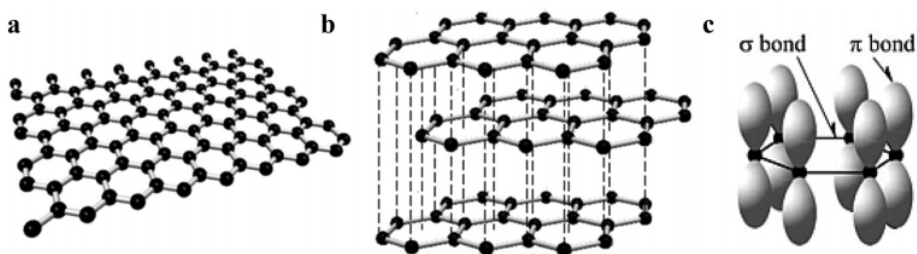


**Figure 15:** (a) graphene honeycomb lattice structure; (b) stacks of graphene layer connected with Van der Waals forces; (c) sigma and pi bonding in graphene [132].

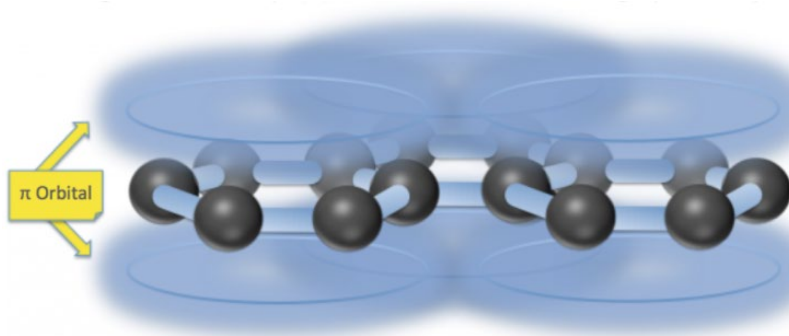


**Figure 16:** Formation of the electronic cloud around the graphene layer due to the presence of  $\pi$ -bonds [134].

### 2.1.1 Derivatives of carbon-based nanomaterials

The most popular carbon-based nanomaterials (can be considered as modified structures of graphene) are carbon nanotubes (CNTs) [136], graphene armchair, and zigzag nanoribbons [137]. CNTs can be single-walled or multiple walled (i.e. more than one wall). A double-walled CNT has been shown in Fig. 17(a). The unzipping of CNT gives rise to two types of nanoribbons i.e. armchair graphene nanoribbon (AGNR) and zigzag graphene nanoribbon (ZGNR). These names are given on the base of the shape of the termination edge of the ribbon. ZGNR termination edge shape is zigzag and the AGNR termination edge looks like an armchair, as shown in Fig. 17 (b), (c).

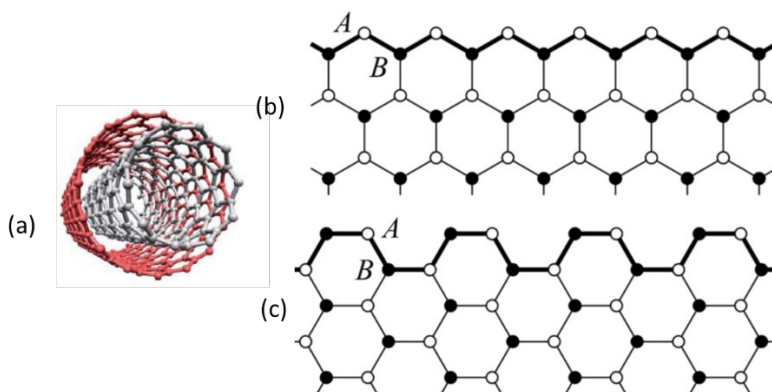


**Figure 17:** (a) Multiwall carbon nanotube; (b) zigzag graphene nanoribbon (c) armchair graphene nanoribbon [136-137].

Moreover, each type of nanoribbon has its unique electronic attributes. The change in the bandgap of AGNR versus the number of carbon atoms has been shown in Fig. 18(a). It can be seen that with an increase in the number of carbon atoms; the bandgap is decreasing for AGNRs. Whereas in ZGNR, the change in bandgap is different for even and odd number of electrons in the structure. For both cases, the bandgap decreases gradually, as shown in Fig. 18(b). Doping of boron and nitrogen may be the results of this change in the bandgap that changes the ionization energy of the ribbons [138].

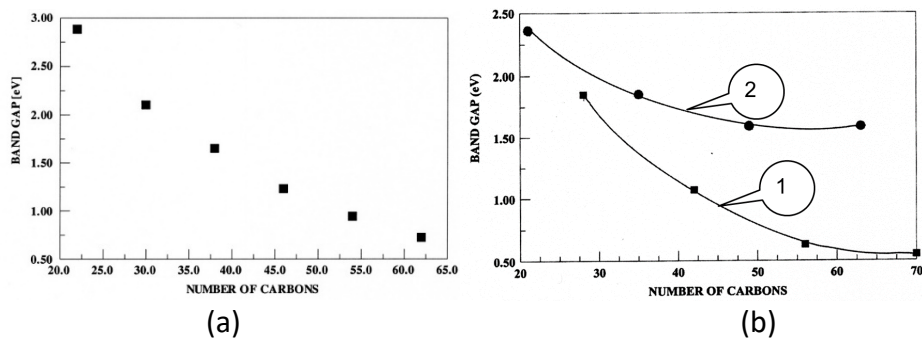


**Figure 18:** (a) Bandgap vs. the number of carbon atoms in AGNR; (b) bandgap vs. the number of carbon atoms having an even number of electrons (curve1) and an odd number of electrons (curve2) of ZGNR [138].

### 2.1.2 State-of-the-art of gas sensing technology

Gas sensing has been an important field for a wide range of applications such as environment monitoring, medical diagnosis, military, and industrial applications. The leakage detection of hazardous, toxic, and flammable gases is very crucial to avoid serious accidents in the household as well as industrial environments. There is a need for some tool to detect the leakage and presence of a large variety of such gases [139-140]. The final goal of gas detection technology is to detect the desired target gases effectively and efficiently with high resolution. The gas detectors must be able to detect even very low concentrations of hazardous gases. However, unfortunately, high-resolution gas sensing for the detection of very low concentrations of gases has not been achieved yet even with state-of-the-art solid-state gas sensors [28-30]. The abrupt fluctuation of charge carriers due to the heating effect produces noise in solid-state devices. Due to this noise, their resolution is degraded that makes it difficult to detect individual gas molecules [31].

The state-of-the-art solid-state gas sensors can be divided into different groups based on their working principles. The most popular types of gas sensors are impedance type, resistive type, and electrolyte based sensors. In resistive gas sensors, the resistance of the constituent semiconductor material changes in the presence of the target gases. This change in resistance is used as a detection signal to detect their presence [141]. Impedance type gas sensors are based on alternating current measurements in which the frequency response of the sensors changes in the presence of target gases [142]. In electrolyte based gas sensors, the conductivity of the electrolyte material changes due to the transfer of holes or electrons from the target gas to the electrolyte materials. This change in the conductivity of electrolyte material is used as a detection signal [143]. Although solid-state gas sensors are very crucial for a wide range of gas detection applications but there are also some challenges associated with such sensors like selectivity, sensibility for very low concentrations, long term stability, and accuracy. In such sensors, the electrolyte, gas sensing materials, and electrodes also degrade with time [27].

Therefore, there is a need to develop highly sensitive and robust gas sensors with low operating temperatures for the detection of very low concentrations of hazardous gases. Several efforts are being made to improve the performance of the conventional solid-state gas sensors by modifying the shape and orientations of the constituent semiconductor materials [144]. Nanomaterials have emerged as exceptional candidates

to cope with these challenges and fill the technology gap. Nanomaterials based gas sensors have low operating temperatures as well as low power consumption. The main parameter of a gas sensing material that defines the sensitivity of the sensor is its surface-to-volume ratio. Nanomaterials have high surface-to-volume ratios that enhance their capability to adsorb a wide range of organic/inorganic molecules efficiently and effectively [32]. Graphene has emerged as an extraordinary nanomaterial due to its exceptional electrical, optical, mechanical, and thermal properties. It has a high surface area [145-146] that makes it suitable for gas sensing applications [147].

### **2.1.3 Types of interactions between graphene and target molecules**

Different types of interaction may happen at the exposure of graphene-based materials to the target gases. These interactions depend on the composition of the exposed molecules. Some molecules (like water molecules) do not introduce any localized impurity states at their exposure to graphene. They just redistribute the electron in graphene and change its conductivity. Whereas, chemically active target molecules act as donor or acceptor of charge carriers for graphene. Consequently, charge concentration changes its electric conductivity. Such molecules make weak bonds with graphene. Some molecules make covalent bonds with graphene (for example H and OH radicals). Therefore, it is not mandatory that only Van der Waals interactions are possible between graphene and adsorbate molecules. The interaction is dependent on the composition of adsorbate molecules. In this Ph.D. work, all such interactions have been taken into account during the simulations of graphene and CNT based molecule sensors [148].

### **2.1.4 Novelty of graphene-based gas sensors related work of Ph.D. thesis**

As discussed in the previous subsection that the large surface-to-volume ratio of graphene makes it highly suitable for gas sensing applications. Graphene has inherently very low electronic noise. Therefore, a very small change and fluctuation of electrons around graphene cause a noticeable change in the electrical conductivity of graphene [149-151]. Graphene-based gas sensors can detect an extremely low concentration of gases even in the range of parts per million (ppm) [152]. Therefore, they can be promising candidates to replace solid-state gas sensors [33-34]. Graphene-based gas sensors can be categorized on the base of gas detection mechanisms. The most popular methods are the resistive method, micro-electromechanical system (MEMS) based method, and field-effect transistor (FET) based method. In the resistive method of gas detection, the electrical resistance of graphene changes in the presence of adsorbed target gas molecules. This change in resistivity is used as a detection signal to detect the presence of target gas [153]. In MEMS methods, mechanical and electrical components are integrated into a chip. Any physical change (i.e. presence of gas molecules) is translated into an electrical signal in MEMS-based sensors [154]. In FET based methods, change in source-to-drain current in the proximity of target gases is used as a detection signal [155-156].

In this Ph.D. work, the feasibility of graphene and its derivatives to detect toxic, flammable, and hazardous gases/compounds have been investigated with the help of density functional theory (DFT) based simulations in ATK-VNL software. To improve the selectivity and accuracy of graphene-based gas sensors, a novel gas detection mechanism (i.e. change in photocurrent) along with a state-of-the-art mechanism (change in electric current) has been proposed in this Ph.D. work. A schematic of proposed gas detection mechanisms has been shown in Fig. 19.

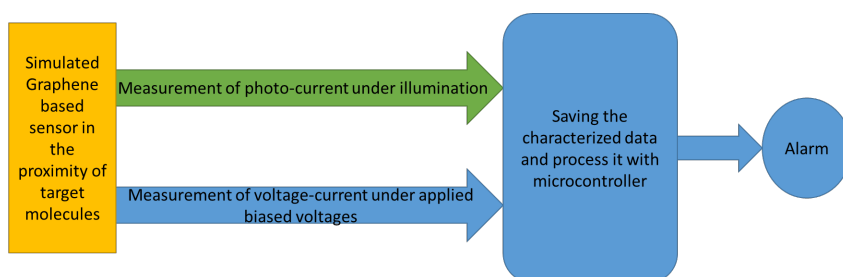


**Figure 19:** Schematic of proposed graphene-based gas detection mechanism for better accuracy and selectivity of graphene-based sensors.

It has been shown in this figure that the change in photocurrent, as well as electric current, are being used simultaneously for the detection of desired gas molecules. The change in these both parameters (i.e. photocurrent and electric current) can be fed to a microcontroller for further processing. These simulated devices have been illuminated by AM1.5 in-built solar spectrum [157] in ATK-VNL software and photocurrent curves have been calculated.

However, due to some limitations of the used simulator in controlling the polarization of incident light and other optical parameters, high values of photocurrent could not be achieved in this work. Since the generation of photocurrent in carbon-based nano-materials also depends on the polarization of incident light [158-159] and activation of hybrid plasmon-phonon coupling mode [160-161]. Still, the potential of the proposed gas detection mechanism cannot be neglected. Because carbon-based nanomaterials have been recognized as active photo-responsive material. They have several promising optical attributes like infrared absorption, ultraviolet absorption, and polarization selectivity [162-165]. High internal quantum efficiencies have been reported for graphene-based physically fabricated optoelectronic devices [166].

### 2.1.5 Methodology adopted for graphene-based gas sensors related work of the Ph.D. thesis

The QuantumWise Atomistix Toolkit (ATK-VNL) has been used for the simulations of graphene-based gas sensors. This software is a tool to simulate gas sensors [167-171]. As discussed in Section 1.3.5, the two-probe model is adopted for the simulation of electronic devices. The same model is also adopted for the simulations of graphene-based gas sensors. ATK-VNL allows to simulate a wide range of nano-electronic devices. It has several in-built calculators to calculate a wide range of electronic properties of simulated devices. Out of which, the ATK-DFT calculator [120] is used to calculate the electronic properties of the simulated sensors. The computation methodology of the ATK-DFT calculator and other related details have been given in Section 1.3.2. The same methodology is adopted for calculating IV-curves for graphene-based devices. In this Ph.D. work, photocurrent has been proposed as a novel gas/molecule detection mechanism for graphene-based sensors. ATK-VNL uses first-order perturbation theory to calculate photocurrent. A comprehensive theory about the implementation of photocurrent calculation in ATK-VNL is given in these references [172-173]. Linear combination of atomic orbitals (LCAO) basis set is used for the calculation of photocurrent [174]. In these simulations, the same basis set has been used for the calculation of photo-current. In ATK-VNL, the methodology for photocurrent

calculation is given in [175]. In this method, a modification to the Hamiltonian containing electron and light interaction has been added as:

$$\hat{H} = \hat{H}_o + \frac{e}{m_o} A \cdot \hat{p} \quad (15)$$

In Eq. 15,  $\hat{H}_o$  is “Hamiltonian without electron-light interaction”,  $m_o$  is “free electron mass”,  $e$  is “electron charge”,  $A$  is electromagnetic vector potential”, and  $p$  is “momentum operator”. For “single-mode monochromatic light source” we can write:

$$\hat{A} = \left( \frac{\hbar \sqrt{\mu_r \epsilon_r}}{2N\omega \epsilon c} I_\omega \right)^{\frac{1}{2}} \left( a b e^{-i\omega t} + a^* \hat{b} e^{i\omega t} \right) \quad (16)$$

In the above equation,  $a$ ,  $\epsilon_r$ ,  $\epsilon$ ,  $\mu_r$ ,  $c$ , and  $\omega$  are polarization vector, relative dielectric constant, dielectric constant, relative magnetic susceptibility, speed and frequency of light, respectively. Whereas,  $I_\omega$  is “photon flux” which is given by “number of photons (N) per time per unit area” as:

$$I_\omega = \frac{N_c}{V \sqrt{\mu_r \epsilon_r}} \quad (17)$$

Now, the first-order coupling matrix can be written as:

$$M_{ln} = \frac{e}{m_o} \left( \frac{\hbar \sqrt{\mu_r \epsilon_r}}{2N\omega \epsilon c} I_\omega \right)^{\frac{1}{2}} \left\langle l \left| \hat{p} \cdot a \right| n \right\rangle \quad (18)$$

In Eq. 18  $|n\rangle$  is “LCAO basis function”. Now, 1<sup>st</sup> Born electron-phonon self energies” can be written as:

$$\sum_{ph}^> = \left[ NM^\dagger G_0^>(E^+)M + (N+1)MG_0^>(E^-)M^\dagger \right] \quad (19)$$

$$\sum_{ph}^< = \left[ NMG_0^<(E^-)M^\dagger + (N+1)M^\dagger G_0^<(E^+)M \right] \quad (20)$$

Finally, first-order Green’s Function considering electron-phonon interaction can be written as:

$$G^{\nearrow/\leftarrow} = G_0^r \left( \sum_L^{\nearrow/\leftarrow} + \sum_R^{\nearrow/\leftarrow} + \sum_{ph}^{\nearrow/\leftarrow} \right) G_0^a \quad (21)$$

In Eq. 21,  $G_0^{r,a,\leftarrow,\nearrow}$  are non-interacting Green’s Functions and  $\sum_{L,R}^{\nearrow/\leftarrow}$  are greater and lesser self-energies due to electrode coupling. Finally, the photocurrent in the electrode  $\alpha$  (right or left) with “spin”  $\sigma$  is calculated as:

$$I_{\alpha,\sigma} = \frac{e}{\hbar} \int \frac{dE}{2\pi} \sum_k T_\alpha(E, k, \sigma) \quad (22)$$

## 2.1.6 Geometry optimization of graphene and CNT based simulated devices in ATK-VNL

In this Ph.D. work, the geometry optimizations of individual CNT and graphene nanoribbon based devices are done by following the steps given at this reference [176-177]. After that, these simulated devices are exposed to the target molecules to detect their presence. Then, graphene and CNT based molecule sensors (including target molecules) have been optimized using the ATK-DFT calculator. GGA-PBE exchange-correlation has been used

along with FastFourier2D (FF2D) Poisson solver for geometry optimization of simulated structures. Geometry relaxation of the simulated system/sensor has been done in two steps. In the first step, rigid constraints for target gas molecules and fixed constraints for adsorbent surfaces (graphene sheet, nanoribbon, and CNT) have been chosen using **Atomic Constraint Editor of OptimizeGeometry Block** of ATK-VNL. Rigid body constraints move the selected atoms like a rigid body during the optimization process. In the second step, the final relaxation of the simulated systems has been done. In this step, fixed atomic constraints are chosen for only adsorbent surfaces. Finally, the optimized structures are used for further calculations (density of states, IV-curves) [178].

In ATK-VNL, by default, all geometry optimizations are performed under zero-stress conditions. It means that on the base of a single given value of target stress, the values of external pressure and internal stress tensor are interpreted. Then from these interpreted values, the stress of the system is calculated [179].

### **2.1.7 Graphene-based simulated structures for the detection of a wide range of molecules**

In this Ph.D. work, a wide range of organic/inorganic, toxic, and flammable compounds have been detected with graphene nano-sheets, graphene nanoribbons, and carbon nanotubes based novel devices. Phenol and methanol are flammable and toxic compounds [180-181]. These organic compounds can cause serious accidents in household and industrial environments. So, it is important to detect their presence. In **Paper E and F**, graphene nano-sheet and armchair graphene nanoribbon based devices have been simulated to detect the presence of phenol and methanol molecules, as shown in Fig. 20(a) and (b). In **Paper G**, highly flammable compounds; methane, and acetone have been detected with pristine graphene nano-sheet deposited over an intrinsic 4H-SiC substrate based device. The simulated structure has been shown in Fig. 20(c). Propane and butane are commonly used household and industrial gases that are highly flammable [182]. Their leakage detection is mandatory to avoid serious explosion accidents. In **Paper H**, a graphene armchair nanoribbon based device has been simulated to detect propane and butane gases, as shown in Fig. 20(d). In **Paper I**, a novel graphene nanoribbon based field-effect transistor has been simulated to detect propane and butane gases, as shown in Fig. 20(e). Moreover, benzene is a hazardous organic compound that causes vomiting, nausea, and dizziness in humans. Whereas, hydrogen- sulfide gas causes halitosis (bad breathing) and other health issues in humans [183-184]. Therefore, it is mandatory to detect these compounds. In **Paper J**, single-wall carbon nanotubes over an intrinsic 4H-SiC substrate have been numerically simulated to detect hydrogen-sulfide and benzene molecules, as shown in Fig. 20(f).

Moreover, in all graphene-based simulated devices, DOS, current-voltage curves, and photo-current curves (in some cases) have been numerically calculated. The change in IV-characteristics and photo-current curves have been used as signature signals for the detection of desired target molecules. All the simulations have been done in the high-performance computing (HPC) environment [121].

## **2.2 Results and discussion on simulated graphene-based gas sensors**

As discussed in sub-section 2.1.7, several graphene-based devices have been simulated for the detection of a wide range of hazardous and toxic organic/inorganic compounds. The change in electrical current, as well as photo-current in the proximity of the target molecules of the simulated devices, have been used as detection signals to detect their presence. The first goal of the results presented in this section is to prove that a wide

range of organic/inorganic compounds, even with very low concentrations (i.e. one or two molecules) can be detected with graphene-based materials. The change in electrical conductivity has been used to detect these foreign molecules to prove **Claim 3**. Whereas, the second target is to demonstrate the change in photo-current in the proximity of target molecules as a novel molecule detection mechanism [**Claim 4**]. These simulated structures and results have been discussed in detail in **Paper E, F, G, H, I, and J**.

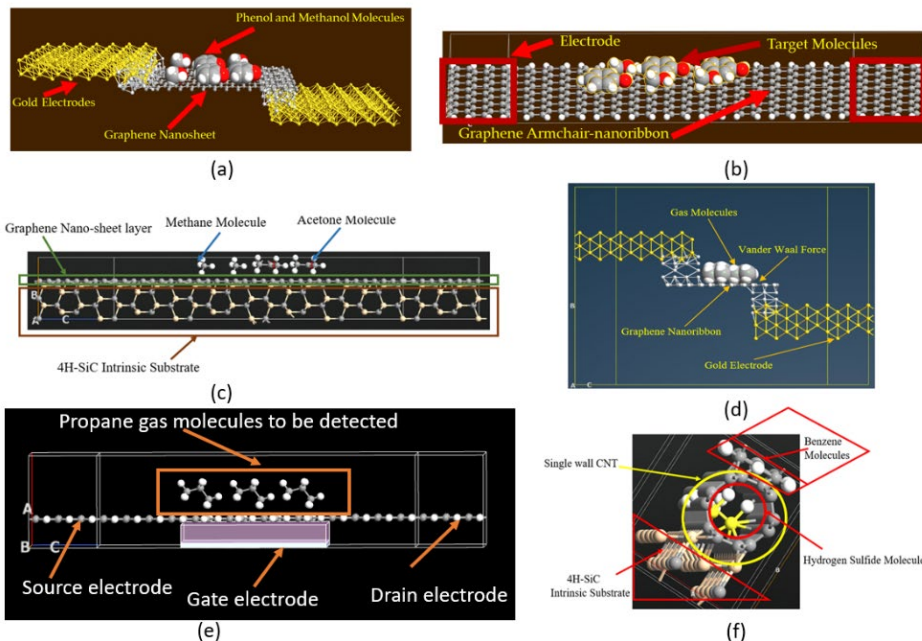


**Figure 20:** Simulated graphene-based gas sensors for the detection of a wide range of gases and organic/inorganic molecules in ATK-VNL software.

The change in electric current in all cases and changes in photo-current in some cases have been used as a detection signal for desired target gases/molecules.

As an example, some simulation results from **Paper I** are discussed in forth-coming subsections 2.2.1-3. In this article, a graphene nanoribbon based field-effect transistor has been simulated for the detection of propane and butane gases. The simulated structure is shown in Fig. 20(e). The DOS and IV-characteristics of the simulated device in the presence of target molecules have been calculated.

### 2.2.1 Geometry optimization of simulated graphene-based field-effect transistor

In **Paper I**, geometry optimization of the graphene-based FET sensor for the detection of propane and butane is done before calculation of DOS and IV-curves. Optimization of geometry is done by following the steps given in section 2.1.6. After geometry optimization, the **Viewer Tool** of ATK-VNL is used to ensure that Van der Waals forces are interacting between target molecules and graphene-based devices. The geometries of simulated structures are shown in Fig. 21 and 22.

### 2.2.2 Density of states of simulated graphene-based field-effect transistor (FET)

The simulated FET has been exposed to three propane, three butane molecules, and both propane & butane (i.e. four butane molecules and one propane molecule) simultaneously in three different experiments. Then the DOS for all three scenarios has been calculated,

as shown in Fig. 23. It can be observed in this figure that the influence of each type of target molecules on the DOS of the device is unique and different. Many new energy states have been added below and above the Fermi level by the adsorbed target gas molecules in each case. The change in DOS in each case has been compared to the simulated FET in the absence of any target molecules. This change in DOS will influence the electric current through the simulated FET.

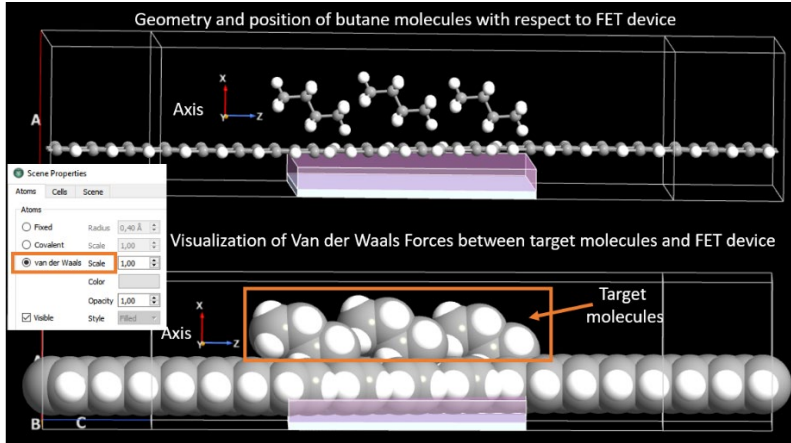


**Figure 21:** Geometry of graphene-based FET for the detection of butane molecules [185].

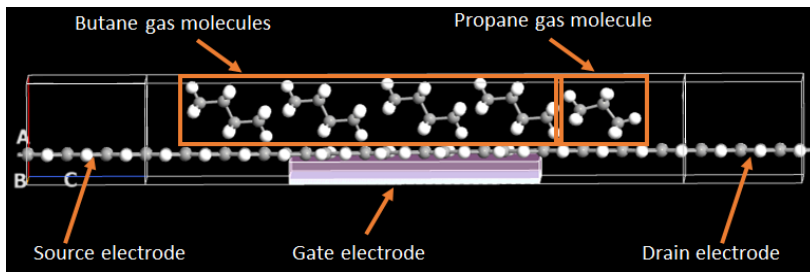


**Figure 22:** Geometry of graphene nanoribbon based field-effect transistor for the detection of propane and butane molecules [185].

### 2.2.3 IV-characteristics of simulated FET

The drain-to-source curves of simulated FET have been calculated at different gate voltages. The simulated device showed an n-channel depletion mode MOSFET like behavior in the absence of any target molecules at zero gate voltage, as shown in Fig. 24(a). After that, the simulated FET has been exposed to three propane, three butane molecules, and both propane & butane (i.e. four butane molecules and one propane molecule) simultaneously in three different experiments. Then, IV-characteristics of simulated FET have been calculated for all these scenarios at  $V_{gate} = -0.1, -0.3, -0.5V$ , as shown in Fig. 24(b), (c), (d).

The adsorbed foreign gas molecules behave as donors or acceptors of charge carriers for the graphene. Some adsorbed molecules at the graphene surface act like donors of charge carriers and increase the charge carrier's concentration. Ultimately, an increase in electric current in graphene-based devices is observed. Whereas, some adsorbed foreign molecules act like acceptors of charge carriers for graphene and decrease the

conductivity of graphene [186]. This change in electrical conductivity can be used as a detection signal to detect a wide range of organic/inorganic compounds and gas molecules. In resistive methods of graphene-based gas detectors, graphene can be considered as a resistive strip. The change in electrical current, in this case, is only a function of the applied external voltage.

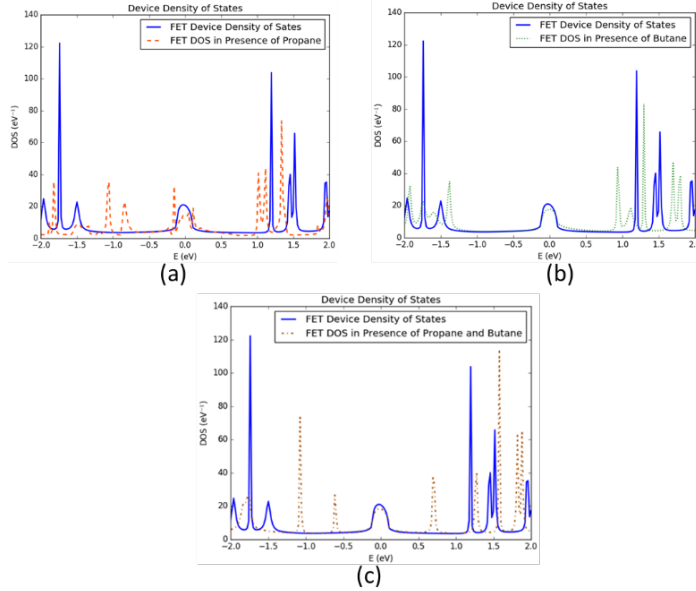


**Figure 23:** Change in the density of states (DOS) of simulated field-effect transistor in presence of (a) propane gas molecules; (b) butane gas molecules; (c) both propane and butane gas molecules [185].

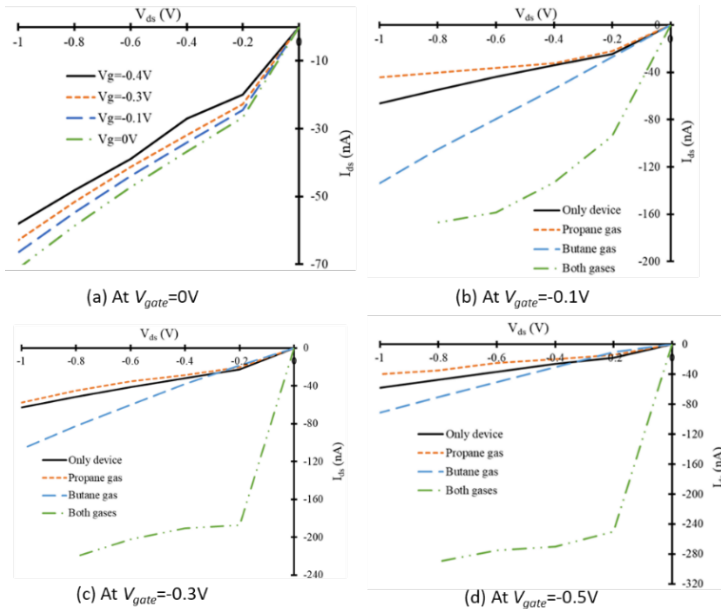


**Figure 24:**  $V_{ds}$  and  $I_{ds}$  curves of the simulated field-effect transistor in the presence propane and butane gases at (a)  $V_{gate}=0V$ ; (b)  $V_{gate}=-0.1V$ ; (c)  $V_{gate}=-0.3V$ ; (d)  $V_{gate}=-0.5V$  [185].

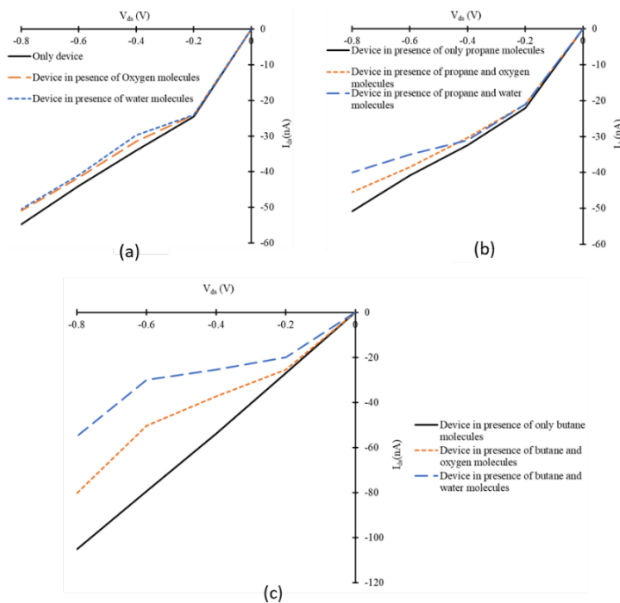


**Figure 25:**  $V_{ds}$  and  $I_{ds}$  curves of the simulated field-effect transistor at  $-0.1V$  gate voltage in the presence of (a) only water and oxygen molecules; (b) propane, water, and oxygen molecules; (c) butane, water and oxygen molecules [185].

Nevertheless, in FET based graphene sensors, the change in electric current ( $I_{ds}$ ) through the graphene channel is controlled by the gate voltage and hence could be more accurate. So, one has to realize the effect of gate voltage as well as drain-to-source voltage ( $V_{ds}$ ) on the IV-characteristics of the graphene-based FET sensor. The same working principle is used in this work to detect propane and butane gases with novel graphene-based FET devices.

The simulated FET device, in the absence of any target molecules, has been used as a reference device to compare the change in  $I_{ds}$  through the device after its exposure to the target gas molecules. The current range through the reference device is between  $-24$  nA to  $-66$  nA at  $V_{gate} = -0.1$  V and a fixed  $V_{ds}$ , as shown with a solid black line in Fig. 24(b). A decrease in  $I_{ds}$  has been observed in the simulated FET device at its exposure to propane gas molecules, at  $V_{gate} = -0.1$  V, as shown with the orange dotted line in Fig. 24(b). The current range, in this case, is between  $-22$ nA to  $-44$  nA, which is less than that of the reference device. It seems that propane molecules have behaved as acceptors of charge carriers for graphene-based FET device and reduced the charge carrier concentration in the device. Therefore, a decrease in current is observed at its exposure to propane gas molecules. A sufficient increase in  $I_{ds}$  is observed in the device at its exposure to butane gas molecules compared to that of the reference device under the same biased condition. The range of  $I_{ds}$ , in this case, is between  $-26$  nA to  $-134$  nA approximately, as shown with blue color dashed line in Fig. 24(b). Butane gas molecules have acted like donors of charge carriers for graphene and consequently, increased  $I_{ds}$  through FET device.

Furthermore, a dramatic increase in  $I_{ds}$  through FET has been observed at its simultaneous exposure to both butane and propane gas molecules. In this case, the range of  $I_{ds}$  is between  $-93$  nA to  $-167$  nA at  $V_{gate} = -0.1$  V, which is quite high compared to that of the reference device. The possible reason for this large increase in  $I_{ds}$  through

the device is due to the dominated donor like effect of four butane molecules compared to that of one propane molecule (which has acceptor like behavior), that are exposed to the device simultaneously in this experiment. This curve is shown with a dotted-dashed green colored line in Fig. 24(b). A similar trend of change in  $I_{ds}$  has been observed at  $V_{gate}=-0.3$  and  $-0.5$  at fixed  $V_{ds}$ , as shown in Fig. 24(c) and (d). A more detailed discussion on IV-characteristics can be found in **Paper I**.

Moreover, atmospheric species like oxygen, water molecules, and humidity may have a strong influence on the performance of the graphene-based gas sensors. They may mix with the desired target gases and affect the detectable change in current through the device. To realize this influence, oxygen and water molecules have been mixed with the desired target gases (i.e. propane and butane gases). Two oxygen molecules and two water molecules have been exposed to the simulated FET device in two individual experiments and change in  $I_{ds}$  through the FET is calculated at  $V_{gate}=-0.1V$ , as shown in Fig. 25(a). The simulation results revealed that the presence of water molecules reduced the  $I_{ds}$  through the FET device compared to that of the reference device, as shown with the blue-dashed line in Fig. 25(a). A similar effect of reduction of in  $I_{ds}$  is observed through the device at its exposure to oxygen molecules, as shown with the orange-dashed line in Fig. 25(a). After that, three propane molecules have been mixed with two water molecules and two oxygen molecules in two individual experiments. The influence of oxygen and water molecules mixed with propane molecules on the  $I_{ds}$  of the device is calculated. The simulation results revealed that the presence of oxygen and water molecules reduced the  $I_{ds}$  through the device compared to that of the device, which is exposed to only propane molecules, as shown in Fig. 25(b). Similarly, three butane molecules have been mixed with two water and two oxygen molecules in individual experiments. The simulation results showed a significant reduction in  $I_{ds}$  through the device in the presence of oxygen and water molecules compared to that of the device, which is merely exposed to the butane molecules, as shown in Fig. 25(c).

Moreover, it has been observed that the presence of atmospheric oxygen and water degraded the performance of simulated graphene-based FET devices in terms of detectable current for the desired target gases. Therefore, a careful calibration of a physically fabricated sensor is required to nullify the effect of these environmental gases on the actual reading of the device for desired target gases. Over time, atmospheric oxygen strongly reduces the conductivity of graphene-based sensors, which depends on the exposure time. Therefore, degraded performance may be expected for graphene-based sensors with a passage of time [187]. Similarly, the water content in the air also influences the electrical properties of the graphene. Therefore, a physically fabricated graphene-based sensor should be encapsulated well for stable operation [188-190].

In **Paper I**, a novel graphene nanoribbon based FET has been numerically analyzed to detect propane and butane gases. The change in  $I_{ds}$  at different gate voltages has been used as a detection signal. The effect of atmospheric species like water vapors and oxygen molecules on the performance of the simulated novel sensor has also been investigated. The simulated FET sensor exhibited an appreciable change in  $I_{ds}$  in presence of target gases. To the best of the author's knowledge, this kind of structure has not been reported in the literature for the detection of propane and butane gases. This paper proves **Claim 3** that has been made at the start of the thesis.

## 2.3 Validation of results of graphene-based simulated sensors (surfaces)

This Ph.D. work is completely simulation-based. At this time, no experimental results are available for comparison with the simulation results. Moreover, in physical sensors, the concentration of target gas molecules that are exposed to the gas sensor is given in terms of parts per million (ppm) for a specific time duration and the response of the sensors is observed [191-193]. In the simulator, the concentration of target gas molecules cannot be given in terms of ppm for a specific time duration. A very low concentration of target molecules (i.e. few molecules) has been exposed to the graphene-based simulated sensors in these simulations. It is very difficult to compare first-principles simulations with the experimental results already reported in the literature.

Furthermore, the purpose of these simulations is to investigate the effect of the adsorbed molecules on the electrical properties of graphene and CNT after their adsorption on graphene/CNT surfaces. In these simulations, the investigation is done after the adsorption of the target molecules on the surface of graphene. The pre-adsorption mechanisms of target molecules have not been investigated in these simulations. However, in graphene-based gas sensors, adsorption and desorption depend on the physisorption of target molecules on the graphene surface, their dispersion, and electrostatic interactions. Surface properties of adsorbent material and size, shape, and dipole moment of target molecules dictate the type of interactions. The surface area of adsorbent (e.g. graphene in this case) defines the potential of a material as a molecule detector. As graphene has a high surface area, therefore it is the best candidate for the adsorption of molecules having high polarizability. Surface modifications to enhance the specific surface area of adsorbent material improves its adsorption capability. At a given temperature, adsorption isotherms of adsorbed gas molecules are used to determine the quantity of adsorbed gas molecules. This adsorption isotherm is calculated with gravimetric or volumetric methods. Desorption/separation of specific gases is also evaluated by calculating isothermic adsorption values [194].

## 2.4 Conclusions from graphene-based gas sensors simulations

The simulation results showed a great potential of graphene-based structures for gas sensing applications. Different mechanisms are being used for the detection of gases and organic/inorganic molecules in graphene-based sensors as discussed before. In this work, the change in electrical conductivity due to the presence of adsorbed molecules has been used as a detection mechanism. The adsorbed gas molecules on the graphene surface act as donors or acceptors of charge carriers for graphene. Due to which charge transfer occurs between graphene and adsorbate molecules. When the relative position of the highest occupied molecular orbital (HOMO) of an adsorbed molecule is above the Dirac point of pristine graphene, then the charge is transferred from the adsorbed molecule to graphene. In this case, the adsorbed target molecule acts as a donor of charge carriers for graphene and alters the concentration of charge carriers in it. Consequently, an increase in electric current is observed in graphene at a specific voltage bias in the presence of adsorbed molecules. The molecules having their lowest unoccupied molecular orbital (LUMO) below the Fermi level of graphene act as acceptors of charge carriers. In this case, the transfer of charge occurs from graphene to adsorbed molecules. Consequently, the concentration of charge carriers in graphene is changed and ultimately a decrease in electric current is observed in it. Due to the above-mentioned reasons, adsorbed molecules on graphene act as acceptors or donors of charge carriers for it.

Consequently, a decrease or an increase in electric current is observed through the graphene after the adsorption of foreign gas molecules. Some times, the hybridization of adsorbate molecules of HOMO and LUMO with graphene is also a reason for charge transfer. Due to these complex overlapping of orbitals and interactions, it is very difficult to discuss the possible adsorption energies and interaction of different types of adsorbed gas molecules on graphene surfaces by just analyzing HOMO/LUMO of as adsorbed molecules. However, it is an obvious fact that the change in charge concentration and electric conductivity of graphene is due to the donor or acceptor like the behavior of adsorbate molecules. At the adsorption of target molecules, change in electric conductivity of graphene is the most feasible way to determine the behavior of adsorbed molecules (i.e. acceptors or donors). This mechanism has been used for the detection of gases/molecules in this Ph.D. For example, a significant change in electrical conductivity has been observed in graphene nano-sheets [Paper E, F, G], nano-ribbons [Paper F, H, I], and carbon nanotubes [Paper J] based simulated devices. In this Ph.D. work, change in photo-current is proposed as a novel molecule detection mechanism for graphene-based devices [Paper F, J]. This proposed mechanism can be used along with any state-of-the-art gas sensing mechanisms to improve the sensor accuracy and selectivity for the detection of very low concentration of gases.

However, due to some limitations of the used simulator in controlling the polarization of incident light and other optical parameters, high values of photo-current could not be achieved in this work. Since the generation of photo-current in carbon-based nano-materials also depends on the polarization of incident light and activation of hybrid plasmon-phonon coupling mode. Still, the potential of the proposed gas detection mechanism cannot be neglected. Because carbon-based nano-materials have been recognized as active photo-responsive material. Therefore, the proposed gas detection mechanism can be used in physically fabricated graphene-based gas sensors. In physically fabricated devices, the light-emitting diode can be used as an illumination source to obtain photo-current values and integrated with any state-of-the-art detection mechanism to get a more reliable device.

The following novel results have been achieved out of this part of Ph.D. work that also justifies the claims that are made at the start of the thesis:

1. It has been demonstrated that graphene-based devices (graphene surfaces) can be used for the detection of a wide range of hazardous and toxic compounds. The change in electrical current through graphene-based materials has been used as a detecting signal to detect their presence effectively. It also proves **Claim 3**, which has been made at the start of the thesis [Details in Papers D-J].
2. The change in photo-current has been proposed and demonstrated as a novel molecule detection mechanism for graphene-based molecule sensors. This mechanism can be integrated with any state-of-the-art molecule detection mechanism for improved accuracy and selectivity of the graphene-based sensors. In this way, **Claim 4** has been proved [Details in Papers F and J].

## 2.5 Challenges in the prospective physical fabrication of proposed gas/molecule sensors

There are still several challenges for real-time applications of graphene-based sensors. These challenges include reproducibility, selectivity, sensitivity, response/recovery time, and cost for a long period. Contaminations of the sensor surface may also affect its performance. Therefore, some methods must be adopted to eliminate contamination from the surface. Sensor fabrication methods also result in the randomness and deviation of results. For example, the disadvantage of the drop-casting method to develop nanosensors is the difficulty in controlling the distribution and layout of CNT. The uniform distribution of sensing material plays a crucial role in defining the performance of sensors. Replacing individual CNTs with a thin-film of CNT could solve this issue and the resultant device can give reproducible results. Therefore, advancement in graphene-based device fabrication techniques will overcome the hurdles in its commercialization and improve device performance as well [195].

In this Ph.D. work, graphene and CNT based gas/molecules sensors are simulated. Although CNT and graphene-based sensors are promising for the detection of very low concentrations of gases. In these simulations, the values of electric current are very small in some cases. This could be due to the low concentration (i.e. number of molecules) of target gases. Photo-current values are also extremely small in these simulated devices. It is difficult to measure such small current values in the physical environment. Selectivity and sensitivity of such devices can also be a challenge. The physical experiment will get more insight into the potential of these proposed graphene-based sensors for real-world applications.

## 2.6 Overview of publications related to the numerical simulations of graphene-based molecule detectors

This section of the thesis explains how this Ph.D. work helped in answering the research questions related to graphene-based sensors that were raised at the start of the thesis.

### Paper E

In this work, a nano-scale analysis of phenol and methanol detector based on pristine graphene nano-sheet has been accomplished. Phenol and methanol are toxic and flammable organic compounds that must be detected to avoid accidents in house-hold and industrial environments. The simulated device exhibited a significant change in the density of states and electrical conductivity in the proximity of phenol and methanol molecules. This change in conductivity is used as a detection signal to detect phenol and methanol molecules. The proposed device can be a prospective candidate for the physical development of graphene-based phenol and methanol detector (Answers to research questions 4-5).

### Paper F

This paper is an extended version of **Paper E**. In this paper additional simulations are done to detect phenol and methanol molecules with armchair graphene nanoribbon based device. A significant change in electrical conductivity and photo-current is observed in the proximity of the target molecules. The change in photo-current in the proximity of phenol and methanol molecules has been proposed as a novel molecule detection mechanism. This proposed mechanism can be used along

with any state-of-the-art molecule detection mechanism to improve the sensor accuracy and selectivity for desired target molecules (Answers to research questions **4-6**).

#### **Paper G**

In this paper, highly flammable organic compounds; methane and acetone have been detected with graphene nano-sheet deposited over an intrinsic 4H-SiC substrate. The nano-scale device is simulated in Quantumwise Atomistix Toolkit software. The change in electric current in the proximity of these target molecules is used as a detection mechanism. The goal of these simulations is to investigate the feasibility of prospective graphene nano-sheet based physical devices for the detection of acetone and methane molecules (Answers to research questions **4-5**).

#### **Paper H**

In this paper, a pristine armchair graphene nano-ribbon based device has been simulated to detect flammable house-hold gases like propane and butane. A considerable change in density of states and electrical current in the simulated graphene nano-ribbon based device has been observed in the presence of target molecules. Change in electric current is used as a gas detection mechanism for this simulated device (Answers to research questions **4-5**).

#### **Paper I**

In this paper, a novel graphene nano-ribbon based field-effect transistor is simulated for the detection of propane and butane gases. This nanoscale simulated device showed a significant change in IV-characteristics in the presence of adsorbed propane and butane molecules. This change in drain-to-source current in the presence of target molecules is used as a detection mechanism for the FET based device (Answers to research questions **4-5**).

#### **Paper J**

Inhaling of hydrogen-sulfide and benzene gases can cause serious health issues in humans. It is very important to detect their presence for public safety, health, industrial process control, and pollution control. In this paper, carbon nanotube over an intrinsic 4H-SiC substrate is used to detect the presence of these gases. Change in photo-current has been used as a novel gas detection mechanism in this simulated device. Change in electric current, as well as photo-current, can be used as a gas detection mechanism for this simulated device to improve the device selectivity and accuracy (Answers to research questions **4-6**).

## Limitations of DFT based Simulations

Although density functional (DFT) theory-based simulations are being extensively used in the field of chemistry, physics, and materials science research. Because of several simplifications made by DFT, it gives rise to some errors in the calculations. For example, the electron density distribution function of a system over space describes the ground state characteristics of a many-electron system. The exact density of electrons based on exact functional must be used to generate the correct energy of a system under study. The minimization of exact functional to generate exact energy and electron density of electrons is crucial for correct DFT calculations [196].

Hence, the accuracy of the DFT based calculation strongly depends on the exchange-correlation functional that describes the electron density of many-electron systems. DFT methods use several simplification and approximations to deal with the problems related to physics and predict the properties of the molecules. These simplifications and approximation in predicting the properties of molecules give rise to errors. Therefore, the optimization of exchange-correlation functionals is a key challenge to get accurate results from DFT calculations. Some major drawbacks of DFT calculation are miscalculations in the chemical reaction, the bandgap of materials, binding energies, and charge transfer mechanisms in a complex system of materials. The root cause of all these errors is the delocalization error of approximation of functionals (caused by Coulombic Forces between electrons that push them apart). Most of the DFT based calculations are unable to determine near-generate or degenerate states and breaking of chemical bonds. Therefore, DFT based calculation may suffer several errors that can even appear in the simplest systems. Efforts are being made to reduce these errors by minimizing delocalization errors [197].

## Limitations of SILVACO TCAD based Simulations

SILVACO TCAD is extensively used for modeling a wide range of power electronics devices based on SiC, GaN, and GaAs. Although the significance of TCAD based simulations cannot be neglected in the development of semiconductor devices. But the results obtained from these simulations sometimes are far away from real results. The accuracy of the results of these simulations is based on real experimental conditions and used physical models along with the material's parameters. These device simulations are based on Maxwell's equations. It is very important to use appropriate physical models for a simulated device to predict the experimental results. Mainly two approaches are used to improve the accuracy of TCAD based simulations to get the results close to the actual device. In the first approach, new physical models are developed based on more accurate physics for a specific device. Then these developed models are implemented in the SILVACO TCAD simulator but this solution is achieved at the cost of time and additional money. Therefore, this approach is mostly avoided. In the second approach, appropriate physical models are chosen and their parameters are adjusted to fit the real experimental parameters. But this process is also complex due to the following reasons:

- There are too many parameters related to each physical model and it is a complex task to optimize all of them
- All physical models for some processes like (defects formation, impurity, and stress generation) cannot be described well because some of them are still in the development phase
- Some parameters related to physical models are dependent on experimental equipment and actual experimental conditions
- It is not possible to realize all chemical and physical processes inside the simulated structure
- Experimental errors in the physical environment cannot be estimated in the simulator

Therefore, enormous sources of errors due to inappropriate physical models and material related parameters can be expected in TCAD based simulations. Such error can be minimized by accurate choice of used physical models and tuning of material's related parameter to get the results close to the actual device [198-199].

## Summary of conclusions of Ph.D. work

In this Ph.D. thesis, the characterization of SiC and graphene-based novel semiconductor structures are done. This Ph.D. dissertation is divided into two parts. The focus of the first part is to investigate the prospective physical fabrication of SiC-based heterostructures with a non-traditional technique known as diffusion bonding/welding. For this purpose, SiC-based heterostructures (diodes and LEDs) are numerically analyzed considering the diffusion bonding/welding approach and their electrical properties are investigated. All these simulations are done in SILVACO TCAD and QuantumWise Atomistix Toolkit softwares. In these simulations, different combinations of SiC polytypes itself, as well as with other semiconductor materials like Si and Ge are done successfully. These simulation results revealed valuable conclusions about the fabrication feasibility of SiC-based heterostructure diodes with the diffusion bonding technique. The results showed that theoretically, it is possible to develop SiC-based heterostructures with diffusion bonding approach. The physical fabrication of such devices with diffusion bonding will reduce the fabrication complexity and cost of the resultant devices.

In the second part of this Ph.D. work, numerical analysis of graphene-based novel gas sensing devices is done. The change in photocurrent in the presence of target gas molecules has been proposed as a novel gas/molecules detection mechanism along with the state-of-the-art mechanism (i.e. change in electric current). This novel molecule detection mechanism can be integrated with any other state-of-the-art molecule detection mechanism to improve the accuracy and selectivity for desired target molecules for graphene-based sensors. In this work, a wide range of toxic, hazardous, and flammable compounds are detected with graphene-based devices. All the simulations are done in QuantumWise Atomistix Toolkit software.

At the start of this Ph.D. thesis, the following research questions were raised:

1. Investigation of circumstances for the realization of SiC-based polytypic hetero-structure with direct bonding?
2. What are the main characteristics and the behavior of the structures realized with a direct bonding technique?
3. What would be the most advanced possible combinations of SiC-based polytypic heterostructures that could be realized?
4. Can graphene-based devices detect very low concentrations of target gases and compounds?
5. How the target molecules affect the conductivity of different graphene-based materials after adsorption on the graphene surface?
6. Can the changes in photocurrent in the proximity of target gases be used as a novel mechanism for gas detection?

The results of this Ph.D. work successfully answered the above-mentioned questions [Details are given in **Section 1.8** and **2.6**].

## Summary of claims

Below is the summary of claims about the novelty of this Ph.D. work. These claims correspond to the contributions **I** to **IV** that were mentioned at the start of this thesis.

**Claim 1:** It has been demonstrated with the help of simulations that theoretically it is possible to develop SiC-based polytypic heterostructure diodes with direct bonding technique. The direct bonding of wafers has been proposed for the very first time as a

prospective fabrication technique for SiC-based heterostructure devices. However, the physical bonding of SiC wafers with the diffusion welding/bonding technique is quite challenging due to the extreme hardness and ability of SiC wafers to resist high temperatures. Atomically flat surfaces of SiC wafers are required for sustainable adhesion of wafers at their interface. But it is very difficult to polish SiC wafers of such small dimensions (having a surface area of  $1 \times 1 \mu\text{m}^2$ ) due to the unavailability of the polishing disc of this small size. Therefore, catalytic etching has been proposed in this thesis for the polishing of wafer to get the atomically flat surface of wafers. Physical experiments are proposed to find out the diffusion welding parameters (i.e. pressure and temperature) at which wafers can be welded with each other without breakage. [Details in Papers **A-D** and **K**].

**Claim 2:** A suitable combination of constituent materials must be chosen to develop a heterostructure diode based on SiC. A considerable difference in electron affinities of the constituent materials is mandatory to avoid resistive behavior of the resultant device. So, the proper choice of the material plays a crucial role in defining the behavior of the devices. There must be a significant difference in electron affinities of constituent materials of heterostructures to create a potential barrier at their interface and get rectifying behavior. [Details in Papers **A-D**].

**Claim 3:** A large variety of organic/inorganic compounds and gases are detected with graphene-based devices in this Ph.D. work. Very low concentrations of target molecules (i.e. even one or two molecules) are detected with these graphene-based simulated devices. The presence of these adsorbed target molecules caused a considerable change in the electrical conductivity of the simulated devices. This change in electrical conductivity is used as a detection mechanism in the analyzed devices. Although, these simulation results revealed that the proposed graphene-based devices can be promising candidates for the detection of a wide range of hazardous/toxic gases and compounds. But the selectivity and sensitivity of proposed/simulated graphene-based devices can be challenging for their real-world applications due to small values of electric current. Therefore, physical experiments are required and proposed for the physical development of such gas sensors [Details in Paper **E-J**].

**Claim 4:** In this Ph.D. work, change in photo-current in the proximity of desired target molecules is proposed as a novel molecule detection mechanism for graphene-based gas sensors. The proposed mechanism has been demonstrated with the help of simulations where the change in photocurrent in the presence of desired target molecules is used as a molecule detection mechanism. In these simulated devices, measurable photo-current values are extremely small. The measurement of such small electric- and photo-current values can be challenging in the physical environment. Therefore, physical experiments are required to investigate the potential of the proposed molecule detection mechanism for graphene-based gas sensors [Details in Paper **F, J**].

## Prospective work

The future work includes the manufacturing of proposed SiC heterostructures with the diffusion bonding technique. These simulation results gave a good insight into the possibility of fabrication of different SiC-based heterostructures. The successful fabrication of these proposed structures with the diffusion bonding technique can be a breakthrough in SiC device fabrication technology. It will simplify the fabrication process of SiC-based heterostructures and significantly reduce the device fabrication cost and efforts. However, the possible defects and their effects on the electric properties of micro-scale SiC heterostructures considering the diffusion welding technique have not been investigated in this work. Prospective work related to SiC-based devices includes:

1. Numerical investigation of interface defects in micro-scale SiC heterostructures considering diffusion welding approach
2. Customization of physical models (i.e. impact ionization and tunneling models) for SILVACO TCAD to minimize the difference between nano- and micro-scale simulations in reverse bias regime
3. Investigation of optimized diffusion welding parameters for the fabrication of high electron mobility devices and LEDs using diffusion bonding technique

Whereas, the prospective work related to graphene-based devices includes:

1. Numerical investigations of different types of interactions between graphene surface and adsorbate molecules including the pre-adsorption phenomenon
2. Physical development of proposed sensors for the detection of a wide range of compounds and gases
3. Implementation and integration of proposed novel gas/molecule detection mechanism (i.e. changes in photocurrent) with any other state-of-the-art technique in physical graphene-based sensors

## References

- [1] G. T. Gebretsadik, "Power electronics: the hidden technology that makes the modern world run," 2009. [Online]. Available: <https://www.scribd.com/document/377377452/Course-Plan-Power-Electronics-2010-Semester-II> [Accessed: 11-Dec-2019].
- [2] D. K. Chy and M. Khaliluzzaman, "The Significance of Power Electronics Components on Sustainable Energy Sources," in Proc. 9th International Conference on Computing, Communication, and Networking Technologies, ICCCNT 2018, 2018, pp. 1–7.
- [3] J. Millan, P. Godignon, X. Perpina, A. Perez-Tomas, and J. Rebollo, "A survey of wide bandgap power semiconductor devices," *IEEE Trans. Power Electron.*, vol. 29, no. 5, pp. 2155–2163, 2014.
- [4] R. Singh and M. Pecht, "Opportunities and Challenges in Realizing the Full Potential of SiC Power Devices," *Ind. Electron.*, pp. 19–31, 2008.
- [5] K. Shenai, R.S. Scott and B. J. Baliga, "Optimum semiconductors for high power electronics," *IEEE Trans. Electron Devices*, vol. 36, no. 9, pp. 1811–1823, 1989.
- [6] P. Roussel, "SiC market and industry update," presented at the Int. SiC Power Electron. Appl. Workshop, ISICPEAW, Kista, Sweden, 2011.
- [7] J. Rąbkowski, D. Peftitsis, and H. P. Nee, "Silicon carbide power transistors: A new era in power electronics is initiated," *IEEE Ind. Electron. Mag.*, vol. 6, no. 2, pp. 17–26, 2012.
- [8] J. Millan, "Wide band-gap power semiconductor devices," in *IET Circuits, Devices & Systems*, vol. 1, no. 5, pp. 372–379, October 2007, doi: 10.1049/iet-cds:20070005.
- [9] X. She, A. Q. Huang, O. Lucia and B. Ozpineci, "Review of Silicon Carbide Power Devices and Their Applications," *IEEE Trans. Ind. Electron.*, vol. 64, no. 10, 2017.
- [10] C. Chen, F. Luo, and Y. Kang, "A Review of SiC Power Module Packaging: Layout, Material System and Integration," *CPSS Transaction On Power Electronics Applications*, vol.2, no.3, 2017.
- [11] H. A. Mantooth, M. D. Glover and P. Shepherd, "Wide Bandgap Technologies and Their Implications on Miniaturizing Power Electronic Systems," *IEEE Journal of Emerging and Selected Topics in Power Electronics*, vol. 2, no. 3, pp. 374–385, Sept. 2014, doi: 10.1109/JESTPE.2014.2313511.
- [12] J. Baliga, *Fundamentals of Power Semiconductor Devices*. New York: Springer, 2008.
- [13] W. Liu, "Electro-thermal simulations and measurements of silicon carbide power transistors," Ph.D. Thesis, KTH Royal Inst. Technol. Stockholm, Sweden, 2004.
- [14] D. A. Gajewski, S. H. Ryu, M. Das, B. Hull, J. Young, and J. W. Palmour, "Reliability performance of 1200 V and 1700 V 4H-SiC DMOSFETs for next generation power conversion applications," *Mater. Sci. Forum*, vol. 778–780, pp. 967–970, 2014.
- [15] L. C. Yu, G. T. Dunne, K. S. Matocha, K. P. Cheung, J. S. Suehle, and K. Sheng, "Reliability issues of SiC MOSFETs: A technology for high temperature environments," *IEEE Trans. Device Mater*, vol. 10, no. 4, pp. 418–426, 2010.
- [16] N. G. Wright, A. B. Horsfall, and K. Vassilevski, "Prospects for SiC electronics and sensors," *Mater. Today*, vol. 11, no. 1–2, pp. 16–21, 2008.

- [17] M. Östling, R. Ghandi and C. Zetterling, "SiC power devices – Present status, applications, and future perspective," in *IEEE 23rd International Symposium on Power Semiconductor Devices and ICs*, San Diego, CA, 2011, pp. 10–15, doi: 10.1109/ISPSD.2011.5890778.
- [18] L. F. S. Alves, R. C. M. Gomes, P. Lefrance, R. D. A. Pegado, P. Jeannin, B. A. Luciano and F. V. Rocha, "SiC Power Devices in Power Electronics: An Over-view," in Proc. Brazilian Power Electronics Conference (COBEP), Juiz de Fora, 2017, pp. 1–8, doi: 10.1109/COBEP.2017.8257396.
- [19] C. Chen, F. Luo, and Y. Kang, "A Review of SiC Power Module Packaging: Layout, Material System and Integration," *CPSS Transaction On Power Electronics Applications*, vol. 2, no. 3, 2017.
- [20] J. Rabkowski, D. Pefitsis and H. Nee, "Silicon Carbide Power Transistors: A New Era in Power Electronics Is Initiated," *IEEE Industrial Electronics Magazine*, vol. 6, no. 2, pp. 17–26, June 2012, doi: 10.1109/MIE.2012.2193291.
- [21] J. Millan, P. Godignon and D. Tournier, "Recent developments in SiC power devices and related technology," In Proc. 24th International Conference on Microelectronics (IEEE Cat. No.04TH8716), Nis, Serbia, 2004, pp. 23–30, vol. 1, doi: 10.1109/ICMEL.2004.1314551.
- [22] H. Qin, B. Zhao, X. Nie, J. Wen, and Y. Yan, "Overview of SiC power devices and its applications in power electronic converters," In Proc. IEEE 8th Conference on Industrial Electronics and Applications (ICIEA), Melbourne, VIC, 2013, pp. 466–471, doi: 10.1109/ICIEA.2013.6566414.
- [23] P. Friedrichs, "SiC power devices for industrial applications," In Proc. International Power Electronics Conference - ECCE ASIA -, Sapporo, 2010, pp. 3241–3248, doi: 10.1109/IPEC.2010.5543711.
- [24] L. Li, C. Li, Y. Cao and F. Wang, "Recent Progress of SiC Power Devices and Application," *IEEJ Trans.*, vol. 8, pp. 515–521, 2013.
- [25] M. Bakowski, "Roadmap for SiC Power Devices," *J. Telecommun. Inf. Technol.*, vol. 3, pp. 19–30, 2000.
- [26] X. Liu, S. Cheng, H. Liu, S. Hu, D. Zhang, and H. Ning, "A survey on gas sensing technology," *Sensors*, vol. 12, no. 7, pp. 9635–9665, 2012.
- [27] Y. Liu, J. Parisi, X. Sun, and Y. Lei, "Solid-state gas sensors for high temperature applications-a review," *J. Mater. Chem. A*, vol. 2, no. 26, pp. 9919–9943, 2014.
- [28] S. Capone, A. Forleo, L. Francioso, R. Rella, P. Siciliano, J. Spadavecchia, D. S. Presicce, A. M. Taurino, "Solid state gas sensors: state of the art and future activities," *J. Optoelectron. Adv. Mater.*, vol. 5, pp. 1335–1348, 2003.
- [29] P. T. Moseley, "Solid state gas sensors," *Meas. Sci. Technol.*, vol. 8, no. 3, pp. 223–237, 1997.
- [30] J. Kong, N. R. Franklin, C. Zhou, M. G. Chapline, S. Peng, K. Cho, and H. Dai "Nanotube molecular wires as chemical sensors," *Science*, vol. 287, no. 5453, pp. 622–625, 2000.
- [31] P. Dutta and P. M. Horn, "Low-frequency fluctuations in solids: 1/f noise," *Rev. Mod. Phys.*, vol. 53, no. 3, pp. 497–516, 1981.
- [32] G. Jiménez-Cadena, J. Riu, and F. X. Rius, "Gas sensors based on nanostructured materials," *Analyst*, vol. 132, no. 11, pp. 1083–1099, 2007.
- [33] F. Schedin, A. K. Geim, S. V. Morozov, E. W. Hill, P. Blake, M. I. Katsnelson, and K. S. Novoselov, "Detection of individual gas molecules adsorbed on graphene," *Nat. Mater.*, vol. 6, p. 652, 2007.

- [34] J. T. Robinson, F. K. Perkins, E. Snow, Z. Wei and P. E. Sheehan, "Reduced Graphene Oxide Molecular Sensors," *Nano Lett.*, vol. 8, pp. 3137–3140, 2008.
- [35] Y. Lu, B. R. Goldsmith, N. J. Kybert and A. T. C. Johnson, "DNA Decorated Graphene Chemical Sensors," *Appl. Phys. Lett.*, vol. 97, p. 83107, 2010.
- [36] E. Morales-Narazé and A. Merkoci, "Graphene Oxide as an Optical Biosensing Platform," *Adv. Mater.*, vol. 24, pp. 3298–3308, 2012.
- [37] S. S. Varghese, S. Lonkar, K. K. Singh, S. Swaminathan, and A. Abdala, "Recent Advances in graphene based gas sensors," *Sensors Actuators B: Chem.*, vol. 218, pp. 160–183, 2015.
- [38] W. Yuan and G. Shi, "Graphene-based gas sensors," *J. Mater. Chem. A.*, vol. 1, pp. 10078–10091, 2013.
- [39] M. Kumar, A. Laitinen, D. Cox, and P. J. Hakonen, "Ultra low 1/f noise in suspended bilayer graphene," *Appl. Phys. Lett.*, vol. 106, no. 26, pp. 2–7, 2015.
- [40] S. E. Saddow and A. Agarwal (Eds.), *Advances in Silicon Carbide Processing and Applications*. Norwood, Artech House, Inc., 2004.
- [41] H. Abderrazak, E. Selmane, and B. Hadj, "Silicon Carbide: Synthesis and Properties," in *Properties and Applications of Silicon Carbide*, R. Gerhardt, Eds. Croatia: InTech, 2011, pp. 361–389.
- [42] J. C. Phillips, *Bonds and Bands in Semiconductors*. New Jersey: Momentum Press, 2009.
- [43] Wikibands, "Polymorphs of Silicon carbide." [Online]. Available: [https://www.wikiwand.com/en/Polymorphs\\_of\\_silicon\\_carbide](https://www.wikiwand.com/en/Polymorphs_of_silicon_carbide). [Accessed: 12-Dec-2019].
- [44] B. Roul, M. Kumar, M. K. Rajpalke, T. N. Bhat, and S. B. Krupanidhi, "Binary group III-nitride based heterostructures: Band offsets and transport properties," *J. Phys. D: Appl. Phys.*, vol. 48, no. 42, 2015.
- [45] Z. I. Alferov, "The history and future of semiconductor heterostructures from the point of view of a Russian scientist," *Phys. Scr. T*, vol. 68, no. January, pp. 32–45, 1996.
- [46] N. G. Einspruch and W. R. Frensley *Heterostructures and Quantum Devices*. San Diego, CA.: Academic, 1994.
- [47] A. A. Lebedev, "Heterojunctions and superlattices based on silicon carbide," *Semicond. Sci. Technol.*, vol. 21, no. 6, pp. R17–R34, 2006.
- [48] Priya, "Estimation of Enhanced Breakdown Voltages in 3C-SiC Schottky Barrier Diode using Special Erfc Distribution Doping Profiles," M. S. thesis, Thapar University, India, 2013.
- [49] V. A. Gubanov and C. Y. Fong, "Doping in cubic silicon-carbide," *Appl. Phys. Lett.*, vol. 75, no. 1, p. 88, 1999.
- [50] Y. Zang, H. Chen, L. Li, Q. Lei, and J. Cho, "Preparation of SiC/SiNWs heterostructure on 4H-SiC(0001)," In Proc. IEEE International Conference on Electron Devices and Solid-State Circuits (EDSSC), Xi'an, China, 2019, pp. 1–2, doi: 10.1109/EDSSC.2019.8754462.
- [51] M. Ghosh and A. Acharyya, "Multiple Quantum Well IMPATT Sources based on Si<sup>~</sup>3C-SiC Heterostructures Operating at Millimeter-Wave and Terahertz Frequency Bands," in Proc. IEEE Electron Devices Kolkata Conference (EDKCON), Kolkata, India, 2018, pp. 103–105, doi: 10.1109/EDKCON.2018.8770499.

- [52] A. R. M. Faisal, T. Dinh, P. Tanner, H-P. Phan, K. Nguyen, E. W. Streed, and D. V. Dao, "Photoresponse of a Highly-Rectifying 3C-SiC/Si Heterostructure Under UV and Visible Illuminations," *IEEE Electron Device Letters*, vol. 39, no. 8, pp. 1219–1222, Aug. 2018, doi: 10.1109/LED.2018.2850757.
- [53] T. Nguyen *et al.*, "Ultra-Sensitive OPTO-Piezoresistive Sensors Utilising 3C-SiC/Si Heterostructures," in Proc. 20th International Conference on Solid-State Sensors, Actuators and Microsystems & Eurosensors XXXIII (TRANSDUCERS & EUROSENSORS XXXIII), Berlin, Germany, 2019, pp. 2057–2060, doi: 10.1109/TRANSDUCERS.2019.8808394]
- [54] U. S. Patankar, A. Koel, and T. Pardy, "Simulations of Wide Bandgap SiC N-N Heterostructure Diode," In Proc. IEEE International Conference on Consumer Electronics (ICCE), Las Vegas, NV, USA, 2020, pp. 1–4, doi: 10.1109/ICCE46568.2020.9043130],
- [55] L. Stuchlikova *et al.*, "DLTFS Study of Defect Distribution in InAlGaN/GaN/SiC HEMT Heterostructures," In Proc. 12th International Conference on Advanced Semiconductor Devices and Microsystems (ASDAM), Smolenice, 2018, pp. 1–4, doi: 10.1109/ASDAM.2018.8544477.
- [56] V. J. Gokhale, B. P. Downey, M. T. Hardy, E. N. Jin, J. A. Roussos, and D. J. Meyer, "Epitaxial Single-Crystal ScAlN on 4H-SiC for High-Velocity, Low-Loss SAW Devices," in Proc. IEEE 33rd International Conference on Micro Electro Mechanical Systems (MEMS), Vancouver, BC, Canada, 2020, pp. 1262–1265, doi: 10.1109/MEMS46641.2020.9056271.
- [57] A. S. Sokolov, C. Yu, E. Beam, X. Gu, Y. Obi and V. Harris, "AlN Interlayers Allow Robust Hexagonal Barium Ferrite Heteroepitaxy on 6H-SiC," in Proc. IEEE International Magnetics Conference (INTERMAG), Singapore, 2018, pp. 1–1, doi: 10.1109/INTMAG.2018.8508218. Jikai *et al.*
- [58] J. Xu, C. Wang, Q. Kang, S. Zhou, and Y. Tian, "Direct Heterogeneous Bonding of SiC to Si, SiO<sub>2</sub>, and Glass for High-Performance Power Electronics and Bio-MEMS," in Proc. IEEE 69th Electronic Components and Technology Conference (ECTC), Las Vegas, NV, USA, 2019, pp. 1266–1271, doi: 10.1109/ECTC.2019.00196.
- [59] C. Wang, J. Xu, S. Guo, Q. Kang, Y. Wang, Y. Wang and Y. Tian, "A Facile Method for Direct Bonding of single Crystalline SiC to Si, SiO<sub>2</sub>, and Glass using VUV Irradiation," *Appl. Surf. Sci.*, vol. 471, pp. 196–204, 2019. <https://doi.org/10.1016/j.apsusc.2018.11.239>.
- [60] J. Robertson, "High dielectric constant gate oxides for metal oxide Si transistors," *Reports Prog. Phys.*, vol. 69, no. 2, pp. 327–396, 2006.
- [61] S. M. Sze and K. K. Ng, *Physics of Semiconductor Devices*. John Wiley & Sons, Inc., 2006.
- [62] G. Margaritodo, "Electronic Structure of Semiconductor Heterojunctions," in *Heterojunctions in technology*, Kluwer Academic Publisher, 1988, p. 4.
- [63] S. Y. Davydov, "On the electron affinity of silicon carbide polytypes," *Semiconductors*, vol. 41, no. 6, pp. 696–698, 2007.
- [64] "Band Structure and Carrier Concentration of SiC." [Online]. Available: <http://www.ioffe.ru/SVA/NSM/Semicond/SiC/bandstr.html#carrier> concentration [Accessed: 13-Dec-2019].
- [65] K. Semmelroth, M. Krieger, G. Pensl, H. Nagasawa, R. Pusche, M. Hundhausen, L. Ley, M. Nerding and H. P. Strunk, "Growth of 3C-SiC bulk material by the modified Lely method," *Mater. Sci. Forum*, vol. 457–460, no. 1, pp. 151–154, 2004.

- [66] Dr. Yu. A. Vodakov, E. N. Mokhov, M. G. Ramm, and A. D. Roenkov, "Epitaxial growth of silicon carbide layers by sublimation sandwich method (I) growth kinetics in vacuum," *Cryst. Res. Technol.*, vol. 14, no. 6, pp. 729–740, 1979.
- [67] H. Matsunami and T. Kimoto, "Surface polarity dependence in step-controlled epitaxy: Progress in SiC epitaxy," *Diam. Relat. Mater.*, vol. 6, no. 10, pp. 1276–1281, 1997.
- [68] L. B. Rowland, R. S. Kern, S. Tanaka and R. F. Davis, "Gas-source molecular beam epitaxy of monocrystalline  $\beta$ -SiC on vicinal  $\alpha$ (6H)-SiC," *J. Mater. Res.*, vol. 8, no. 11, pp. 2753–2756, 1993.
- [69] J. A. Powell and H. A. Will, "Epitaxial growth of 6H SiC in the temperature range 1320–1390°C," *J. Appl. Phys.*, vol. 44, no. 11, pp. 5177–5178, 1973.
- [70] A. Bauer, J. Krausslich, B. Kocher, K. Geotz, A. Fissel and W. Richter "X-ray investigations of MBE-grown heteroepitaxial SiC layers on 6H – SiC substrates," *Mater. Sci. Eng. B.*, vol. 62, pp. 179–182, 1999.
- [71] A. A. Lebedev, A. M. Strel'chuk, D. V. Davydov, N. S. Savkina, A. S. Tregubova, A. N. Kuznetsov, V. A. Solov'ev, and N. K. Poletaev, "Electrical characteristics of p-3C-SiC/n-6H-SiC heterojunctions grown by sublimation epitaxy on 6H-SiC substrates," *Appl. Surf. Sci.*, vol. 184, no. 1–4, pp. 419–424, 2001.
- [72] A. A. Lebedev, G. N. Mosina, I. P. Nikitina, N. S. Savkina, L. M. Sorokin, and A. S. Tregubova, "Investigation of the structure of (p)3C-SiC-(n)6H-SiC heterojunctions," *Tech. Phys. Lett.*, vol. 27, no. 12, pp. 1052–1054, 2001.
- [73] A. Fissel, B. Schröter, U. Kaiser, and W. Richter, "Advances in the molecular-beam epitaxial growth of artificially layered heteropolytypic structures of SiC," *Appl. Phys. Lett.*, vol. 77, no. 15, pp. 2418–2420, 2000.
- [74] A. Fissel, U. Kaiser, J. Kraublich, K. Pfennighaus, B. Schroter, J. Schulz and W. Richter, "Epitaxial growth of SiC-heterostructures on  $\alpha$ -SiC(0001) by solid-source MBE," *Mater. Sci. Eng. B.*, vol. 61–62, pp. 139–142, 1999.
- [75] A. V. Semenov, A. V. Lopin, V. M. Puzikov, V. N. Baumer, and I. Dmitruk, "Fabrication of heterostructures based on layered nanocrystalline silicon carbide polytypes," *Semiconductors*, vol. 44, no. 6, pp. 816–823, 2010.
- [76] A. A. Lebedev, G. A. Oganessian, V. V. Kozlovski, I. A. Eliseyev, and P. V. Bulat, "Radiation defects in heterostructures 3C-SiC/4H-SiC," *Crystals*, vol. 9, no. 2, pp. 4–9, 2019.
- [77] D. V. Davydov, A.A. Lebedev, A. S. Tregubova, V. V. Kozlovski, A. N. Kuznetsov, and E. V. Bogdanova, "Investigation of 3C-SiC epitaxial layers grown by sublimation epitaxy," *Mater. Sci. Forum*, vol. 338, pp. 221–224, 2000.
- [78] A. A. Lebedev, V. V. Zelenin, P. L. Abramov, E. V. Bogdanova, S. P. Lebedev, D. K. Nel'son, B. S. Razbirin, M. P. Shcheglov, A. S. Tregubova, M. Suvajarvi, and R. Yakimova, "A study of thick 3C-SiC epitaxial layers grown on 6H-SiC substrates by sublimation epitaxy in vacuum," *Semiconductors*, vol. 41, no. 3, pp. 263–265, 2007.
- [79] V. Jokubavicius, G. R. Yazdi, R. Liljedahl, I. G. Ivanov, J. Sun, X. Liu, P. Schuh, M. Wilhelm, P. Wellmann, R. Yakimov and M. Syvajarvi, "Single domain 3C-SiC growth on off-oriented 4H-SiC Substrates," *Cryst. Growth Des.*, vol. 15, no. 6, pp. 2940–2947, 2015.
- [80] Merck, "Physical vapor deposition." [Online]. Available: <https://www.sigmaaldrich.com/materials-science/material-science-products.html?TablePage=108832720>. [Accessed: 14-Dec-2019].

- [81] M. Shenkin, O. Korolkov, T. Rang, and G. Rang, "Polytypic heterojunctions for wide bandgap semiconductor materials," *WIT Trans. Eng. Sci.*, vol. 90, pp. 273–282, 2015.
- [82] Rusnaldy, "Diffusion Bonding: An Advanced od material process," *ROTASI*, vol. 3, pp. 23–27, 2001.
- [83] Choyke, Wolfgang J., Matsunami, Hiroyuki, Pensl and Gerhard Eds., *Silicon Carbide : Recent Major Advances*. Springer Berlin Heidelberg, 2004.
- [84] A. Sahakyan, A. Koel, and T. Rang, "Non-destructive eddy current measurements for silicon carbide heterostructure analysis," *WIT Trans. Eng. Sci.*, vol. 116, pp. 49–60, 2017.
- [85] J. Toompu, N. Sleptsuk, R. Land, O. Korolkov, and T. Rang, "The measurement and tuning of SiC Diode Voltage Doubler represented as diffusion-welded stack," in Proc. 16th Biennial Baltic Electronics Conference (BEC), 2018.
- [86] N. Sleptsuk, O. Korolkov, J. Toompuu, P. Annus, and T. Rang, "Comparative characteristics of Diffusion Welded High Voltage Stacks and Connected in Series Schottky Diodes," in Proceedings of the 15th Biennial Baltic Electronics Conference (BEC), 2016.
- [87] O. Korolkov, V. Kozlovski, A. Lebedev, R. Land, N. Sleptsuk, J. Toompuu, and T. Rang, "SiC Schottky Diode Rectifier Represented as Diffusion Welded Stack," *Mater. Sci. Forum J.*, vol. 897, pp. 697–700, 2016.
- [88] A. Isohashi, P.V. Bui, D.Toh, S. Matsuyama, Y. Sano, K. Inagaki, Y. Morikawa and K. Yamauchi, "Chemical etching of silicon carbide in pure water by using platinum catalyst," *Appl. Phys. Lett.*, vol. 110, no. 20, 2017.
- [89] H. Kida, D.Toh, P.V. Bui, A. Isohashi, R. Ohnishi, S. Matsuyama, K. Yamauchi, and Y. Sano, "High efficiency planarization of SiC wafers by water-care(catalyst-referred etching) employing photoelectrochemical oxidation," *J. Mater. Sci. Forum*, vol. 963, pp. 525–529, 2019.
- [90] "SILVACO TCAD Software." [Online]. Available: <https://www.silvaco.com/products/tcad.html>. [Accessed: 16-Dec-2019].
- [91] S. Smidstrup, T. Markussen, P. Vanraeyveld, J. Wellendorff, J. Schneider, T. Gunst, B. Verstichel, D. Stradi, P. A. Khomyakov and U.G. Vej-Hansen, "QuantumATK: an integrated platform of electronic and atomic-scale modeling tools," *J. Phys. Condens. Mater.*, vol.32, 2020 .
- [92] A. Koel, "GaAs and SiC semiconductor materials based power structures: Static and dynamic behavior analysis," Ph.D. thesis, Tallinn University of Technology, Tallinn, Estonia, 2014
- [93] B. N. Pushpakaran and S. B. Bayne, *Modeling and Electrothermal simulation of SiC Power Devices using Silvaco ATLAS TCAD*. Singapore: World Scientific, 2019.
- [94] SILVACO, "Power device simulation" [Online]. Available: <https://silvaco.com/published-papers/power-device-simulation/> [Accessed: 26-May-2020].
- [95] Quantumwise, "Scientific Publications" [online]. Available: <https://docs.quantumwise.com/scientificpublications/scientificpublications.html> [Accessed: 26-May-2020]
- [96] Silvaco, Atlas User's Manual, CA: Silvaco, Inc., 2016. [E-Book] Available: <https://dynamic.silvaco.com/dynamicweb/jsp/downloads/DownloadManualsAction.do?req=silen-manuals&nm=atlas>.

- [97] M. Brandbyge, J.-L. Mozos, P. Ordejón, J. Taylor, and K. Stokbro, "Density-functional method for nonequilibrium electron transport," *Phys. Rev. B*, vol. 65, Mar 2002. doi:10.1103/PhysRevB.65.165401
- [98] J. M. Soler, E. Artacho, J. D. Gale, A. García, J. Junquera, P. Ordejón, and D. Sánchez-Portal, "The SIESTA Method for ab initio order-N materials simulation," *J. Phy. Condens. Matter.*, vol. 14, pp. 2745–2779, 2002.
- [99] Quantumwise, "Transmission coefficient" [online]. Available: <https://quantumwise.com/documents/manuals/ATK-2017/ReferenceManual/NEGF.html#transmission-coefficient>. [Accessed: 27-May-2020].
- [100] D. Stradi, U. Martinez, A. Blom, M. Brandbyge, and K. Stokbro. General atomistic approach for modeling metal-semiconductor interfaces using density functional theory and nonequilibrium green's function. *Phys. Rev. B*, 93:155302, Apr 2016. doi:10.1103/PhysRevB.93.155302
- [101] Quantumwise, "Transmission Spectrum" [online]. Available: <https://quantumwise.com/documents/manuals/ATK-2017/ReferenceManual/Types/TransmissionSpectrum/TransmissionSpectrum.html#transmissionspectrum-c>. [Accessed: 27-May-2020].
- [102] Quantumwise, "Transport calculation with QuantumwiseATK" [online]. Available: [https://docs.quantumwise.com/tutorials/atk\\_transport\\_calculations/atk\\_transport\\_calculations.html](https://docs.quantumwise.com/tutorials/atk_transport_calculations/atk_transport_calculations.html). [Accessed: 27-May-2020].
- [103] K. Stokbro, J. Taylor, M. Brandbyge, J.-L. Mozos and P. Ordejon, "Theoretical study of the nonlinear conductance of di-thiol benzene coupled to Au(1 1 1) surfaces via thiol and thiolate bonds," *Comput. Mater. Sci.*, vol. 22, pp. 151–160, 2003.
- [104] K. S. Thygesen and K. W. Jacobsen, "Molecular transport calculations with Wannier functions," *Chem. Phys.*, vol. 319, pp. 111–125, 2005.
- [105] V. Anisimov and Y. Izyumov, *Electronic Structure of Strongly Correlated Materials*. Berlin, Germany: Springer, 2010.
- [106] T. J. Giese and D. M. York, "Density-functional expansion methods: Evaluation of LDA, GGA, and meta-GGA Functionals and Different Integral Approximations," *J. Chem. Phys.*, vol. 133, 2010.
- [107] CASTEP, "Setting exchange- correlation functionals" [online] Available: <https://www.tcm.phy.cam.ac.uk/castep/documentation/WebHelp/content/modules/castep/tskcastepsetelecxc.htm#nlxc>.
- [108] M. D. Ganji and H. Kiyani, "Molecular simulation of efficient removal of H<sub>2</sub>S pollutant by cyclodextrine functionalized CNTs," *Sci. Rep.*, vol. 9, 2019],
- [109] J. Zhao, X. Liu, Z. Zhu, N. Wang, W. Sun, C. Chen, Z. He, "Molecular insight into the enhancement of benzene-carbon nanotube interactions by surface modification for drug delivery systems (DDS)," *Appl. Surf. Sci.*, vol. 416, pp. 757–765, 2017. <https://doi.org/10.1016/j.apsusc.2017.04.186>.
- [110] O. Leenaerts, B. Partoens and F. M. Peeters, "Adsorption of H<sub>2</sub>O, NH<sub>3</sub>. NO<sub>2</sub> and NO on graphene: A first principles study," *Phys. Rev. B.*, vol. 77, 2008.
- [111] A. K. Manna and S. K. Pati, "Tunning the electronic structure of graphene by molecular charge transfer: a computational study," *Chem. Asian. J.*, vol. 4, 2009.
- [112] M. Schlipf and F. Gygi, "Optimization algorithm for generation of ONCV pseudopotential," *Comput. Phys. Commun.*, vol. 196, pp. 36–44, 2015.
- [113] Y. Hinuma, H. Hayashi, Y. Kumagai, I. Tanaka, and F. Oba, "Comparison of approximation in density functional theory calculations: Energetic and structure of binary oxides," *Phys. Rev. B*, Vol. 96, 2017.

- [114] Lindefelt, "Equations for electrical and electrothermal simulation of anisotropic semiconductors," *J. Appl. Phys*, vol. 76, pp. 4164–4167, 1994.
- [115] M. Lades and G. Wachutka "Extended Anisotropic Mobility Model Applied to 4H/6HSiC Devices," in Proc. IEEE SISPAD, 1997, pp. 169–171.
- [116] D. M. Caughey and R. E. Thomas, "Carrier Mobilities in Silicon Empirically Related to Doping and Field," in Proc. IEEE 55, 1967, pp. 2192–2193.
- [117] Choo and S. C., "Theory of Forward-Biased Diffused Junction P-L-N Rectifier -- Part 1: Exact Numerical Solutions," *IEEE Trans on Electron Devices*, vol. 8, no. 19, pp. 954–966, 1972.
- [118] H. Rashid, A. Koel, T. Rang, R. Gähwiler, M. Grosberg, and R. Jõemaa "Nanoscale And Microscale Simulations Of NN-Junction Heterostructures Of 3C-4H Silicon Carbide," *WIT Transactions on Engineering Sciences*, vol. 116, June, pp. 235–248, 2017.
- [119] "Transport calculation with Quantumwise ATK." [Online]. Available: [https://docs.quantumatk.com/tutorials/atk\\_transport\\_calculations/atk\\_transport\\_calculations.html](https://docs.quantumatk.com/tutorials/atk_transport_calculations/atk_transport_calculations.html) [Accessed: 16-Dec-2019].
- [120] QuantumWise User Manual, "DFT: LCAO Calculator." [Online]. Available: <https://docs.quantumatk.com/manual/DFTLCAO.html> [Accessed: 14-Oct-2019].
- [121] "High Performance Computing." [Online]. Available: <https://www.ttu.ee/support-structure/it-services/services-4/high-performance-computing-2/> [Accessed: 14-oct-2019].
- [122] Quantumwise, "Advanced device relaxation-manual workflow" [online]. Available: [https://docs.quantumatk.com/tutorials/optimize\\_device\\_configuration/optimize\\_device\\_configuration.html](https://docs.quantumatk.com/tutorials/optimize_device_configuration/optimize_device_configuration.html) [Accessed June 17, 2020].
- [123] M. Haroon Rashid, A. Koel, and T. Rang, "Nano and microscale simulations of the Si/4H-SiC and Si/3C-SiC NN-heterojunction diodes," *Mater. Sci. Forum*, vol. 963, pp. 357–361, 2019.
- [124] M. H. Rashid, A. Koel, T. Rang, "Simulations of heterostructures based on 3C-4H and 6H-4H silicon carbide polytypes," *Mater. Sci. Forum*, vol. 924, pp. 302–305, 2018.
- [125] M. H. Rashid, A. Koel, and T. Rang, "Nano- and Micro-scale Simulations of Ge/3C-SiC and Ge/4H-SiC NN-heterojunction Diodes," *Mater. Sci. Forum*, vol. 1004, pp. 490–496, 2020.
- [126] M. H. Rashid, A. Koel, and T. Rang, "Effects of the inclusion of armchair graphene nanoribbons on the electrical conduction properties of NN-heterojunction 4H-6H/SiC diodes," *Mater. Sci. Forum*, vol. 962, pp. 29–35, 2019.
- [127] S. Tanuma and C. Powell and D. R. Pen, "Calculations of Electron Inelastic Mean Free Paths," *Surf. interface Anal.*, vol. 21, p. 165, 1993.
- [128] V. Zeghbrock, "Carrier Drift: Surface Scattering," in *Principles of Semiconductor Devices*, 2007.
- [129] C. Calvin, "Mechanisms of Carrier Scattering," in *Modern Semiconductor Devices for Integrated Circuits*, Prentice-Hall, 2009, p. 4041.
- [130] M. J. Allen, V. C. Tung, and R. B. Kaner, "Honeycomb carbon: A review of graphene," *Chem. Rev.*, vol. 110, no. 1, pp. 132–145, 2010.
- [131] K. S. Novoselov, A. K. Geim, S. V. Morozov, D. Jiang, S. V. Dubonos, I. V. Grigorieva, and A. A. Firsov, "Electric field effect in atomically thin carbon films," *Science*, vol. 306, no. 5696, pp. 666–669, 2004.

- [132] E. Bourgeat-Lami, J. Faucheu, and A. Noël, "Latex routes to graphene-based nanocomposites," *Polym. Chem.*, vol. 6, no. 30, pp. 5323–5357, 2015.
- [133] X. Yu, H. Cheng, M. Zhang, Y. Zhao, L. Qu, and G. Shi, "Graphene based smart materials," *Nat. Rev. Mater.*, vol. 2, 2017.
- [134] "Graphene electronic cloud." [Online]. Available: <https://www.pinterest.com/pin/36802921940380640/> [Accessed: 19-Dec-2019].
- [135] F. Schedin, A. K. Geim, S. V. Morozov, E. W. Hill, P. Blake, M. I. Katsnelson, and K. S. Novoselov, "Detection of individual gas molecules adsorbed on graphene," *Nat. Mater.*, vol. 6, pp. 652–655, 2007.
- [136] R. Purohit, K. Purohit, S. Rana, R. S. Rana, and V. Patel, "Carbon Nanotubes and Their Growth Methods," in *Procedia Materials Science*, 2014, vol. 6, no. Icmpc, pp. 716–728.
- [137] N. A. Poklonski, E. F. Kislyakov, S. A. Vyrko, O. N. Bubel, and S. V. Ratkevich, "Electronic band structure and magnetic states of zigzag graphene nanoribbons: quantum chemical calculations," *J. Nanophotonics*, vol. 6, no. 1, p. 61712, 2012.
- [138] F. J. Owens, "Electronic and magnetic properties of armchair and zigzag graphene nanoribbons," *J. Chem. Phys.*, vol. 128, no. 19, 2008.
- [139] S. Joshi, V. D. Bhatt, H. Wu, M. Becherer, and P. Lugli, "Flexible lactate and glucose sensors using electrolyte-gated carbon nanotube field effect transistor for non-invasive real-time monitoring," *IEEE Sensors J.*, vol. 17, no. 14, pp. 4315–4321, 2017.
- [140] S. M. Hosseini-Golgoob, F. Salimi, A. Saberhari and S. Rahbarpour, "Comparison of information content of temporal response of chemoresistive gas sensor under three different temperature modulation regimes for gas detection of different feature reduction methods," *J. Phys.*, vol. 939, no. 1, 2017.
- [141] R. Ramamoorthy, P. K. Dutta, and S. A. Akbar, "Oxygen sensors : Materials, methods , designs," *Mater. Sci., J.* vol. 8, pp. 4271–4282, 2003.
- [142] J. R. Macdonald, *Impedance Spectroscopy: Emphasizing Solid Materials and Systems*. New York: John Wiley & Sons, 1987.
- [143] C. O. Park, S. A. Akbar, and W. Weppner, "Ceramic electrolytes and electrochemical sensors," *J. Mater. Sci.*, vol. 38, no. 23, pp. 4639–4660, 2003.
- [144] G. Korotcenkov, "Gas response control through structural and chemical modification of metal oxide films: State of the art and approaches," *Sensors Actuators, B: Chem.*, vol. 107, no. 1, pp. 209–232, 2005.
- [145] T. Purkait, G. Singh, M. Singh, D. Kumar, and R. S. Dey, "Large area few-layer graphene with scalable preparation from waste biomass for high-performance supercapacitor," *Scientific Reports*, vol.7, no.115239, 2017.
- [146] U. K. Sur, "Graphene: A Rising Star on the Horizon of Materials Science," *Int. J. Electrochem.*, vol. 2012, pp. 1–12, 2012.
- [147] W. Yuan and G. Shi, "Graphene-based gas sensors," *J. Mater. Chem. A*, vol. 1, no. 35, pp. 10078–10091, 2013.
- [148] W. Yuan and G. Shi, "Graphene-based gas sensors," *J. Mater. Chem. A*, vol. 1, 2013.
- [149] K. S. Novoselov, A. K. Geim, S. V. Morozov, D. Jiang, Y. Zhang, S. V. Dubonos, I. V. Grigorieva and A. A. Firsov, "Electric Field Effect in Atomically Thin Carbon Films Supplementary," *Science*, vol. 306, no. 5696, pp. 666–669, 2004.
- [150] K. R. Ratinac, W. Yang, S. P. Ringer, and F. Braet, "Toward ubiquitous environmental gas sensors - Capitalizing on the promise of graphene," *Environ. Sci. Technol.*, vol. 44, no. 4, pp. 1167–1176, 2010.

- [151] M. A. Stolyarov, G. Liu, S. L. Rumyantsev, M. Shur, and A. A. Balandin, "Suppression of  $1/f$  noise in near-ballistic  $h$ -BN-graphene- $h$ -BN heterostructure field-effect transistors," *Appl. Phys. Lett.*, vol. 107, no. 2, 2015.
- [152] F. Schedin, A. K. Geim, S. V. Morozov, E. W. Hill, P. Blake, M. I. Katsnelson and K. S. Novoselvo, "Detection of Individual Gas Molecules Adsorbed on Graphene," *Nat. Mater.*, vol. 6, pp. 652–655, 2007.
- [153] R. Pearce, T. Iakimov, M. Andersson, L. Hultman, A. L. Spetz, and R. Yakimova, "Epitaxially grown graphene based gas sensors for ultra sensitive  $\text{NO}_2$  detection," *Sensors Actuators, B Chem.*, vol. 155, no. 2, pp. 451–455, 2011.
- [154] R. Bogue, "Recent developments in MEMS sensors: A review of applications, markets, and technologies," *Sens. Rev.*, vol. 33, no. 4, pp. 300–304, 2013.
- [155] Y. Ohno, K. Maehashi and K. Matsumoto, "Chemical and biological sensing applications based on graphene field-effect transistors," *Biosens. Bioelectron.*, vol. 26, pp. 1727–1730, 2010.
- [156] Y-C. Syu, W-E. Hsu and C-T. Lin, "Review—Field effect transistor biosensing: Devices and clinical application," *ECS J. Solid-State Sci. and Tech.*, vol. 7, pp. Q3196–Q3207, 2018.
- [157] N. R. E. Labortary, "Solar Spectra." [Online]. Available: <https://www.nrel.gov/grid/solar-resource/spectra.html> [Accessed:25-Dec-2019].
- [158] M. Freitag, Y. Martin, J. A. Misewich, R. Martel, and P. Avouris, "Photoconductivity of single carbon nanotubes," *Nano Lett.*, vol. 3, no. 8, pp. 1067–1071, 2003.
- [159] K. Balasubramanian, Y. Fan, M. Burghard, and K. Kern, "Photoelectronic transport imaging of individual semiconducting carbon nanotubes," *Appl. Phys. Lett.*, vol. 84, no. 13, pp. 2400–2402, 2004.
- [160] M. Freitag, T. Low, W. Zhu, H. Yan, F. Xia, and P. Avouris, "Photocurrent in graphene harnessed by tunable intrinsic plasmons," *Nat. Commun.*, vol. 4, pp. 1–8, 2013.
- [161] A. L. Falk, K-C. Chiu, D. B. Farmer, Q. Cao, J. Tersoff, Y-H. Lee, P. Avouris, and S-J. Han, "Coherent Plasmon and Phonon-Plasmon Resonances in Carbon Nanotubes," *Phys. Rev. Lett.*, vol. 118, no. 25, pp. 2–7, 2017.
- [162] T. Pichler, M. Knupfer, M. S. Golden, J. Fink, A. Rinzler, and R. E. Smalley, "Localized and Delocalized Electronic States in Single-Wall Carbon Nanotubes," *Phys. Rev. Lett.*, vol. 80, pp. 4729–4732, 1998.
- [163] M. Ohfuchi and Y. Miyamoto, "Optical properties of oxidized single-wall carbon nanotubes," *Carbon*, vol. 114, pp. 418–423, 2017.
- [164] A. Puzder, A. J. Williamson, F. A. Reboledo and G. Galli, "Structural stability and optical properties of nanomaterials with reconstructed surfaces," *Phys. Rev. Lett.*, vol. 91, pp. 1–4, 2003.
- [165] K. Bubke, H. Gnewuch and M. Hempstead, "Optical anisotropy of dispersed carbon nanotubes induced by an electric field," *Appl. Phys. Lett.*, vol. 71, pp. 1906–1908, 1997.
- [166] F. Xia, T. Mueller, Y. Lin, A. Valdes-Garcia, and P. Avouris, "Ultrafast graphene photodetector," *Nat. Nanotechnol.*, vol. 4, pp. 839–843, 2009.
- [167] F. F. Hu, H. Y. Tang, C. J. Tan, H. Y. Ye, X. P. Chen, and G. Q. Zhang, "Nitrogen dioxide gas sensor based on monolayer SnS: A first-principle study," *IEEE Electron Device Lett.*, vol. 38, no. 7, pp. 983–986, 2017.
- [168] H. Song, X. Li, P. Cui, S. Guo, W. Liu, and X. Wang, "Sensitivity investigation for the dependence of monolayer and stacking graphene  $\text{NH}_3$  gas sensor," *Diam. Relat. Mater.*, vol. 73, pp. 56–61, 2017.

- [169] N. Harada and S. Sato, "Electronic properties of NH<sub>4</sub>-adsorbed graphene nanoribbon as a promising candidate for a gas sensor," *AIP Adv.*, vol. 6, no. 5, 2016.
- [170] S. J. Ray, "Single atom impurity in a single molecular transistor," *J. Appl. Phys.*, vol. 116, no. 15, pp. 1–6, 2014.
- [171] X. L. Wei, Y. P. Chen, W. L. Liu, and J. X. Zhong, "Enhanced gas sensor based on nitrogen-vacancy graphene nanoribbons," *Phys. Lett. Sect. A Gen. At. Solid State Phys.*, vol. 376, no. 4, pp. 559–562, 2012.
- [172] J. Chen, Y. Hu, and H. Guo; "First-principles analysis of photocurrent in graphene PN junctions," *Phys. Rev. B*, vol. 85, 2012.
- [173] L. Zhang, K. Gong, J. Chen, L. Liu, Y. Zhu, D. Xiao, and H. Guo, "Generation and transport of valley-polarized current in transition-metal dichalcogenides," *Phys. Rev. B*, vol. 90, 2014.
- [174] L. E. Henrickson, "Nonequilibrium photocurrent modeling in resonant tunneling photodetectors," *J. Appl Phys.*, vol.91, no.10, pp. 6273–6281, 2002.
- [175] M. Palsgaard, T. Markussen, T. Gunst, M. Brandbyge, and K. Stokbro, "Efficient first-principles calculation of phonon-assisted photocurrent in large-scale solar-cell devices," *Phys. Rev. Appl.*, vol. 10, 2018.
- [176] Quantumwise, "Simple carbon nanotube device" [Online]. Available: [https://docs.quantumatk.com/tutorials/quantumatk\\_cnt\\_device/quantumatk\\_cnt\\_device.html](https://docs.quantumatk.com/tutorials/quantumatk_cnt_device/quantumatk_cnt_device.html) [Accessed: 12-june-2020].
- [177] Quantumwise, "Building a graphene nanoribbon device" [Online]. Available: [https://docs.quantumatk.com/tutorials/intro\\_quantumatk3/intro\\_quantumatk3.html#introduction-quantumatk3](https://docs.quantumatk.com/tutorials/intro_quantumatk3/intro_quantumatk3.html#introduction-quantumatk3) [Accessed: 12-june-2020].
- [178] Quantumwise, "Gemetry optimization: CO/Pd(100)" [Online]. Available: [https://docs.quantumwise.com/tutorials/geometry\\_optimization/geometry\\_optimization.html](https://docs.quantumwise.com/tutorials/geometry_optimization/geometry_optimization.html) [Accessed: 12-June-2020].
- [179] Quantumwise, "OptimizeGeometry" [Online]. Available: <https://docs.quantumatk.com/manual/Types/OptimizeGeometry/OptimizeGeometry.html> [Accessed: 12-June-2020].
- [180] The National Institute for Occupational Safety and Health (NIOSH), "Phenol" [Online]. Available: <https://www.cdc.gov/niosh/topics/phenol/> [Accessed: 3-Jan-2020].
- [181] The National Institute for Occupational Safety and Health (NIOSH), "Methyl Alcohol (methanol)" [Online]. Available: <https://www.cdc.gov/niosh/topics/methyl-alcohol/> [Accessed: 3-Jan-2020].
- [182] THE GAS COMPANY, "PROPANE VS. BUTANE" [Online]. Available: <https://www.thegascompany.ie/content/117-what-is-the-difference-between-propane-gas-vs-butane-gas> [Accessed: 4-Jan-2020].
- [183] A. Tangerman and E. G. Winkel, "Extra-oral halitosis: An overview," *J. Breath Res.*, vol. 4, no. 1, 2010.
- [184] K-I. Choi, H. J. Kim, Y. C. Kang, and J. H. Lee, "Ultrasensitive and ultrasensitive detection of H<sub>2</sub>S in highly humid atmosphere using CuO-loaded SnO<sub>2</sub> hollow spheres for real-time diagnosis of halitosis," *Sensors Actuators, B Chem.*, vol. 194, pp. 371–376, 2014.
- [185] M. H. Rashid and A. Koel and T. Rang, "Simulations of Graphene Nanoribbon Field Effect Transistor for the Detection of Propane and Butane Gases: A First Principles Study," *Nanomaterials*, vol. 10, no. 98, 2020.

- [186] F. Yavari and N. Koratkar, "Graphene-based chemical sensors," *J. Phys. Chem. Lett.*, vol. 3, no. 13, pp. 1746–1753, 2012.
- [187] B. Bekdüz, L. Kampermann, W. Mertin, C. Punckt, I. A. Aksay, and G. Bacher, "Influence of atmospheric species on the electrical properties of functionalized graphene sheets," *RSC Adv.*, vol. 8, no. 73, pp. 42073–42079, 2018.
- [188] C. Melios, A. Centeno, A. Zurutuza, V. Panchal, C. E. Giusca, S. Spencer, S. Ravi, P. Silva, and O. Kazakova, "Effects of humidity on the electronic properties of graphene prepared by chemical vapour deposition," *Carbon N. Y.*, vol. 103, pp. 273–280, 2016.
- [189] "What Effect Does Humidity Have on Graphene Sensors?" [Online]. Available: <https://www.azosensors.com/article.aspx?ArticleID=1323> [Accessed: 04-Jan-2020].
- [190] Y. Yao, X. Chen, J. Zhu, B. Zeng, Z. Wu, and X. Li, "The effect of ambient humidity on the electrical properties of graphene oxide films," *Nanoscale Res. Lett.*, vol. 7, pp. 2–19, 2012.
- [191] I. F. Rivera, R. K. Joshi, and J. Wang, "Graphene-based ultra-sensitive gas sensors," in *Proc. of IEEE Sensors*, 2010, pp. 1534–1537.
- [192] M. Yang, Y. Wang, L. Dong, Z. Xu, Y. Liu, N. Hu, E. S. kong, J. Zhao, and C. Peng "Gas Sensors Based on Chemically Reduced Holey Graphene Oxide Thin Films," *Nanoscale Res. Lett.*, vol. 14, no. 1, pp. 1–8, 2019.
- [193] T. Wang, D. Huang, Z. Yang, S. Xu, G. He, X. Li, N. Hu, G. Yin, D. He and L. Zhang "A Review on Graphene-Based Gas/Vapor Sensors with Unique Properties and Potential Applications," *Nano-Micro Lett.*, vol. 8, no. 2, pp. 95–119, 2016.
- [194] S. Gadipeli and Z. X. Guo, "Graphene-based materials: synthesis and gas sorption, storage and separation," *Prog. Mater. Sci.*, vol. 69, 2015.
- [195] S. Mao, G. Lu, and J. Chen, "Nanocarbon-based gas sensors: progress and challenges," *J. Matre. Chem. A.*, vol. 2, pp. 5573–5579, 2014.
- [196] M.G. Medvedev, I. S. Bushmarinov, J. Sun, J. P. Perdew, and K. A. Lyssenko, "Density Functional Theory is Straying from The Path towards Exact Functional," *Sci.*, vol. 355, no. 6320, pp. 49–52, 2017.
- [197] A. J. Cohen, P. Mori-Sanchez, and W. Yang, "Insights into Current Limitations of Density Functional Theory," *Sci.* vol. 321, no. 5890, pp. 792–794, 2008.
- [198] I. Lysenko, D. Zykov, S. Ishutkin, and R. Meshcheryakov, "The use of TCAD in technology simulations for increasing the efficiency of semiconductor manufacturing," In *Proc. AIP Conference*, 2016 <https://doi.org/10.1063/1.4964592>.
- [199] V. Velayudhan, "TCAD study of interface traps-related variability in ultra-scales MOSFETs," Ph.D. thesis, Universidad Autonoma de Barcelona, Spain, 2016.

## **Acknowledgements**

I would like to say special thanks to my Ph.D. supervisors, Professor Toomas Rang, and Dr. Ants Koel for their support and encouragement during my study period. They were always available to guide me in my research activities. Their appreciation always kept me motivated and helped me to excel in my research abilities. They transformed me from an ordinary student to a good researcher. I am also thankful to our IT manager Fredrick Rang, who was always willing to solve any IT related issues on priority bases. I would say that it was the best time of my life to study and stay in Estonia.

Finally, I express my heartiest gratitude to the Estonian Research Council for financial support of my Ph.D. project as this research was supported by the Estonian Research Council through Research Projects PUT1435 and IUT1911, and by the Horizon 2020 ERA-chair grant “Cognitive Electronics COEL H2020-WIDESPREAD-2014-2” (agreement number 668995; project TTU code VFP15051).

## Abstract

### Characterization of Silicon Carbide (SiC) and Graphene-Based Novel Semiconductor Devices

This Ph.D. work contains the numerical simulations of Silicon carbide (SiC) and graphene-based devices for power electronics and gas sensing applications, respectively. SiC-based heterostructures have gained an important place in the semiconductors research field. Heterostructure is a junction between two different semiconductor materials having different band gaps. The discontinuity at the heterojunction interface gives rise to several interesting electronic properties in the resultant devices. One can customize the electronic properties of such devices by choosing appropriate constituent semiconductor materials. These structures are best suitable for fast switching and high frequency digital electronic applications in harsh environments. During the past few decades, SiC (a wide bandgap semiconductor) has gained significant importance for a wide range of high power, high temperature, and high-frequency power electronics application. SiC exists in more than 200 different crystalline forms; polytypes. Some of these polytypes, like 3C-SiC, 4H-SiC, and 6H-SiC have very attractive physical and electronic properties. Heterostructures based on these polytypes are being used as power electronic diodes, transistors, light-emitting diodes, and sensors. So far, epitaxial growth techniques have been considered as the most well-known techniques with predictable results for the fabrication of SiC-based heterostructures. However, these state-of-the-art techniques are complicated, expensive, and a high level of expertise is required to handle the related fabrication equipment. Even with this high cost and complicated process, the resultant heterostructures may have defects in them (like stacking faults, point defects, etc.). Such types of defects degrade the device performance.

So, in the first part of this Ph.D. work, a novel technique called direct bonding (diffusion welding) has been proposed for the fabrication of SiC heterostructure devices. This technique is cheap and requires fewer efforts for the fabrication of proposed devices. The prospective fabrication of SiC heterostructures with this proposed technique will reduce the complexity of the fabrication process and cost. The resultant device may have better performance compared to that of fabricated with state-of-the-art epitaxial growth techniques. In this Ph.D. work, micro- and nano-scale simulations of SiC-based hetero-structures are done with SILVACO TCAD and QuantumWise Atomistix Toolkit (ATK-VNL) Software packages, respectively. These simulation results gave a detailed insight into which materials combinations would be the best for the physical development of SiC heterostructure devices. These results revealed that theoretically, it is possible to develop SiC-based heterostructures with the diffusion bonding technique. However, there must be a significant difference in the electron affinity values of the constituent materials to get the rectifying behavior of the resultant device. Otherwise, the device will be nothing but an expensive resistor due to a low energy band-offset at the junction interface.

In the second part of this research work, simulations of graphene-based novel devices for the detection of a wide range of toxic, flammable, and hazardous compounds like phenol, methanol, methane, acetone, propane, butane, benzene and hydrogen-sulfide are performed with a nanoscale semiconductor device simulator; QuantumWise Atomistix Toolkit (ATK-VNL). Graphene has emerged as a potential candidate for future nano-electronics applications due to its exceptional and extraordinary chemical, optical,

electrical, and mechanical properties. Graphene-based sensors have gained significant importance for a wide range of sensing applications like the detection of biomolecules, chemicals, and gas molecules. In the presence of the target molecules, change in electric current through the devices is used as a molecule detection mechanism for these simulated sensors. In this work, the change in photocurrent in graphene-based devices in the presence of adsorbed target molecules is proposed as a novel molecule detection mechanism. The proposed molecules detection mechanism (change in photocurrent) can be integrated with any other state-of-the-art mechanisms to improve the sensor accuracy and selectivity for desired target molecules. In this work, graphene nanoribbon, nano-sheets, and carbon nanotubes based devices are simulated for the detection of the molecules mentioned above. These simulation results showed a considerable change in the electric current and photocurrent through graphene-based simulated devices, even in very low concentrations of target molecules (one or two molecules).

## Lühikokkuvõte

### Ränikarbiidil (SiC) ja grafeenil põhinevate uudsete pooljuhtstruktuuride karakteriseerimine

Käesolev doktoritöö sisaldab ränikarbiidil (SiC) ja grafeenil põhinevate pooljuhtseadiste numbrilisi simulatsioone jõuelektroonika ja gaaside detektorite rakenduste jaoks. SiC-põhised heterostruktuurid on pooljuhtide uurimisvaldkonnas hõivanud olulise koha. Heterostruktuur sisaldab üht- või mitut siiret erineva keelutsooni laiusega pooljuhtmaterjalide vahel. Katkematu materjalide üleminek heterosiirdes võimaldab saadud seadistes realiseerida unikaalseid elektroonilisi omadusi. Selliste seadiste elektroonilisi omadusi saab kohandada, valides sobivad pooljuhtmaterjalid. Heterostruktuurid sobivad kõige paremini kiireks ümberlülitamiseks ja digitaalsete kõrgsageduslike rakenduste jaoks karmides keskkondades. Viimase paarikümne aasta jooksul on SiC (laia keelutsooniga pooljuht) omandanud märkimisväärse tähtsuse rakenduste jaoks, mis eeldavad suurt võimsust, kõrge temperatuuri taluvust ja tööd kõrgsagedusliku toitelektronika aladel. SiC esineb enam kui 200 erineval polütüüpsel kristalsel kujul. Mõnedel neist polütüüpidest, näiteks 3C-SiC, 4H-SiC ja 6H-SiC, on väga atraktiivsed füüsikalised ja elektroonilised omadused ning nad on sobivad (korratavad) tööstuslikes protsessides. Nendel polütüüpidel põhinevaid heterostruktuure kasutatakse elektrooniliste diodide, transistoride, valgusdiodide ja anduritena. Siiani on epitaktsiaalse kasvu tehnoloogiaid peetud kõige sobivamateks meetoditeks, millel on prognoositavad tulemused SiC-põhiste heterostruktuuride valmistamiseks. Need tehnoloogiaid on keerulised, kallid (kõrgetemperatuursed) ja vajavad tootmiseseadmete käsitsemiseks kõrgetasemelist asjatundlikkust. Isegi selle kõrge hinna ja keeruka protsessi korral võivad toodetavatel heterostruktuuridel tekkida defektid (näiteks virnade defektid, punktdefektid jne). Seda tüüpi defektid halvendavad seadme jõudlust, vähendavad lubatud piirparameetreid või muudavad kasutuse hoopis võimatuks..

Käesoleva doktoritöö esimeses osas analüüsitakse SiC heterostruktuuriseadmete valmistamiseks difusioonkeevituse niššitehnoloogiat. See tehnoloogia on võrreldes teistega odav ja on vähenõudlikum (ruumi puhtus, pindade eeltöötlus) kavandatud seadiste valmistamiseks. SiC-heterostruktuuride valmistamine viidatud tehnoloogiaga vähendab valmistamisprotsessi keerukust ja kulusid. Saadud pooljuhtseadis võib olla analoogilise jõudlusega võrreldes tipptasemel epitaktsiaalse kasvu tehnikaga. Käesoleva töö SiC-põhiste hetero-struktuuride mikro- ja nanomõõtmete simulatsioonid tehakse vastavalt tarkvarapakettidega SILVACO TCAD ja QuantumWise Atomistix Toolkit (ATK-VNL). Need simulatsioonitulemused annavad üksikasjaliku ülevaate sellest, millised materjalide kombinatsioonid oleksid SiC heterostruktuuriseadmete loomiseks parimad. Need tulemused näitavad, et teoreetiliselt on difusioonkeevituse tehnoloogiaga võimalik välja töötada SiC-põhised heterostruktuurid. Tulemuseks oleva seadise alaldava käitumise saamiseks peab koostisosade elektronide afiinsusväärtustes olema oluline erinevus. Vastasel juhul ei ole seade muud kui kallis takisti, kuna materjalide siirde fermi nivoode erinevus on väike.

Käesoleva uurimistöö teises osas on simuleeritud grafeenil põhinevaid uudseid seadiseid erinevate toksiliste, tuleohtlike ja keemiliselt agressiivsete ühendite, nagu fenool, metanool, metaan, atsetoon, propaan, butaan, benseen ja vesiniksulfiid, avastamiseks. Simulatsioonid on läbi viidud nanomõõtmeliste pooljuhtmaterjalide simulaatoriga QuantumWise Atomistix Toolkit (ATK-VNL). Grafeen on oma erakordsete

keemiliste, optiliste, elektriliste ja mehaaniliste omaduste tõttu tõusnud potentsiaalseks kandidaadiks tulevastele nanoelektronika rakendustele. Grafeenipõhised andurid on omandanud märkimisväärse tähtsuse paljude sensorsete rakenduste jaoks, näiteks biomolekulide, kemikaalide ja gaasimolekulide tuvastamiseks. Sihtmolekulide abil kasutatakse nende andurite molekuli tuvastamise mehhanismina seadises toimuvat elektrivoolu muutust. Käesolevas töös uuritakse uudse molekuli tuvastamise mehhanismina fotovoolu muutumist grafeenil põhinevates seadistes, adsorbeeritud sihtmolekulide toimel. Kavandatud molekulide tuvastamise mehhanismi (fotovoolu muutus) saab integreerida mistahes muu tiptasemel meetodiga, et parandada anduri täpsust ja selektiivsust soovitud sihtmolekulide suhtes. Käesolevas töös on simuleeritud ülalnimetatud molekulide tuvastamiseks grafeeni nanoriba, nanolehed ja nanotorudel põhinevaid seadiseid. Simulatsioonitulemused näitavad märkimisväärset muutust elektrivoolus ja fotovoolus läbi grafeenil põhineva simuleeritud seadise isegi sihtmolekulide väga madalates kontsentratsioonides (üks-kaks molekuli).



## Appendix A

**M. H. Rashid**, A. Koel and T. Rang

“Simulations of heterostructures based on 3C-4H and 6H-4H silicon carbide polytypes,” *Mater. Sci. Forum*, vol. 924, pp. 302–305, 2018. **(ETIS 1.1)**



## Simulations of Heterostructures Based on 3C-4H and 6H-4H Silicon Carbide Polytypes

M. Haroon Rashid<sup>a</sup>, Ants Koel<sup>b\*</sup> and Toomas Rang<sup>c</sup>

Thomas Johann Seebeck Department of Electronics, Tallinn University of Technology,  
Ehitajate tee 5, 19086, Tallinn, Estonia.

<sup>a</sup>murash@ttu.ee, <sup>b</sup>ants.koel@ttu.ee, <sup>c</sup>toomas.rang@ttu.ee

**Keywords:** polytypes, heterostructures, direct bonding, 3C-SiC, 4H-SiC, 6H-SiC

**Abstract.** In the last decade, silicon carbide (SiC) has gained a remarkable position among wide bandgap semiconductors due to its high temperature, high frequency, and high power electronics applications. SiC heterostructures, based on the most prominent polytypes like 3C-SiC, 4H-SiC and 6H-SiC, exhibit distinctive electrical and physical properties that make them promising candidates for high performance optoelectronic applications. The results of simulations of nn-junction 3C-4H/SiC and 6H-4H/SiC heterostructures, at the nanoscale and microscale, are presented in this paper. Nanoscale devices are simulated with QuantumWise Atomistix Toolkit (ATK) software, and microscale devices are simulated with Silvaco TCAD software. Current-voltage (IV) characteristics of nanoscale and microscale simulated devices are compared and discussed. The effects of non-ideal bonding at the heterojunction interface due to lattice misplacements (axial displacement of bonded wafers) are studied using the ATK simulator. These simulations lay the groundwork for the experiments, which are targeted to produce either a photovoltaic device or a light-emitting diode (working in the ultraviolet or terahertz spectra), by direct bonding of SiC polytypes.

### Introduction

Silicon carbide (SiC) has achieved a conspicuous rank among wide bandgap semiconductors for its high temperature and high power optoelectronics applications. Heterojunction electronic devices fabricated from the most well-studied polytypes like 3C-SiC, 4H-SiC and 6H-SiC exhibit superior physical and electrical behavior [1, 2]. The performance of these devices can be customized by modifying the energy band profiles of the constituent SiC polytypes. SiC heterostructures fabricated by direct bonding can significantly simplify device production and offer new optoelectronic properties. The direct bonding of SiC polytypes is extremely challenging due to their stability and hardness, even at elevated temperatures [3]. Currently, the most promising techniques with predicted results and stable yield for growing epilayers of SiC polytypes for the fabrication of electronic devices have been chemical vapour deposition (CVD), liquid-phase epitaxy (LPE) and molecular beam epitaxy (MBE) [4].

### Methodology

Microscale simulations of heterostructures are conducted with the Silvaco TCAD software toolkit, which includes a microscale semiconductor device simulator that solves the basic set of semiconductor equations. Nanoscale simulations are carried out with the QuantumWise Atomistix Toolkit (ATK) with the Virtual Nanolab (VNL) user interface package. ATK includes several models for the electronic properties of quantum systems, of which the density functional theory (DFT) is used for our simulations. The mathematical model used by the ATK-DFT calculator is described in [5]. Donor doping concentrations in 3C-SiC, 4H-SiC and 6H-SiC are chosen as  $10^{18} \text{ cm}^{-3}$  for all polytypes and simulations are conducted to ensure low breakdown voltage in the reverse-biased regime. In the microscale device models, the thickness of each polytype layer is set at 300 nm, and default ohmic contacts are assumed as electrodes. The geometry of a microscale simulated device is shown in Fig. 1(a). Suitable inbuilt recombination, generation and mobility models are used in these microscale simulations. The ATK Builder view of a nanoscale simulated



## Appendix B

M. H. Rashid, A. Koel and T. Rang

“Nano and microscale simulations of the Si/4H-SiC and Si/3C-SiC NN-heterojunction diodes,” *Mater. Sci. Forum*, vol. 963, pp. 357–361, 2019. (ETIS 1.1)



## Nano and Micro-Scale Simulations of Si/4H-SiC and Si/3C-SiC NN-Heterojunction Diodes

M. Haroon Rashid<sup>a\*</sup>, Ants Koel<sup>b</sup> and Toomas Rang<sup>c</sup>

Thomas Johann Seebeck Department of Electronics, Tallinn University of Technology, Ehitajate tee 5, 19086, Tallinn, Estonia.

<sup>a</sup>haroonrashid199@gmail.com, <sup>b</sup>ants.koel@ttu.ee, <sup>c</sup>toomas.rang@ttu.ee

**Keywords:** diffusion welding, diodes, heterojunction, direct bonding, 3C-SiC, 4H-SiC, Silicon

**Abstract.** In the last decades, silicon carbide (SiC) based heterostructures have gained a remarkable place in research field due to their exceptional properties. These properties make SiC highly suitable for high temperature, high frequency, and high power electronics applications. The most prominent polytypes (among 200 types) of SiC like 3C-SiC, 4H-SiC and 6H-SiC, have distinctive electrical and physical attributes that make them promising candidates for high performance optoelectronic applications. Silicon (Si) also has been accepted as a promising material for wide range of electronic, optical and optoelectronic applications. Heterostructures fabricated by the direct bonding of SiC polytype and Si may have interesting physical and electrical attributes. In this paper, micro and nano-scale simulations of the nn-heterostructures of Si/4H-SiC and Si/3C-SiC have been done with Silvaco TCAD and QuantumWise Atomistix Toolkit (ATK) softwares respectively. Voltage-current density characteristics of the nanoscale and microscale simulated devices are computed and discussed. In nanoscale devices, the effects of defects due to lattice misplacements (axial displacement of bonded wafers) are also studied. These simulations are the preparation for our future experiments, which are targeted to produce either a high electron mobility diode or a light emitting diode, by direct bonding (diffusion welding) of SiC polytypes.

### Introduction

Silicon carbide (SiC) has gained a conspicuous rank in modern technology for fabrication of electronic devices due to its many exceptional electrical and physical properties. In nature, SiC exist in several crystalline forms, called polytypes that differ from each other due to their stacking sequences [1]. The wide bandgap semiconductors like SiC exhibit better physical properties in comparison to the conventional semiconductor materials (Si, GaAs) for high temperature and high frequency power electronics applications [2]. Nowadays heterostructures are considered as an essential building blocks of the modern analog and digital electronic devices. The discontinuity at the heterojunction interface of the electronic devices gives rise to several useful electrical attributes [3]. The integration of SiC with Silicon (Si) may give rise to interesting electrical attributes in the resultant devices. Such type of typical pn-heterojunction devices have been fabricated and reported in the literature [4]. The fabrication of SiC heterostructures by direct bonding of wafers (which is extremely difficult due to high stability of SiC) can significantly simplify device production and offer new optoelectronic properties [5]. The most well studied technology used for the fabrication of heterostructures of SiC and related materials with predictable results is the epitaxial growth [6]. We proposed one of the rarely used technique for the fabrication of heterostructures called direct bonding (diffusion welding) of the wafers. In this article nano and microscale simulations of the above mentioned materials have been done. The voltage-current density curves of the simulated devices are calculated and discussed.

### Methodology

In nanoscale simulations, Silicon is (100)-oriented and 3C-SiC is (111)-oriented for Si/3C-SiC nn-heterojunction diode. Whereas in Si/4H-SiC diode, Si is (100)-oriented and 4H-SiC is (0001)-oriented. N-type Si has been joined with n-type 3C-SiC and 4H-SiC separately in above mentioned orientations to build two different heterostructure diodes. In the nanoscale simulated devices, SiC



## Appendix C

M. H. Rashid, A. Koel and T. Rang

“Nano- and Micro-scale Simulations of Ge/3C-SiC and Ge/4H-SiC NN-heterojunction Diodes,” *Mater. Sci. Forum*, vol. 1004, pp. 490–496, 2020. (ETIS 1.1)



## Nano- and Micro-Scale Simulations of Ge/3C-SiC and Ge/4H-SiC NN-Heterojunction Diodes

M. Haroon Rashid<sup>a\*</sup>, Ants Koel<sup>b</sup> and Toomas Rang<sup>c</sup>

Thomas Johann Seebeck Department of Electronics, Tallinn University of Technology,  
Ehitajate tee 5, 19086, Tallinn, Estonia

<sup>a</sup>haroonrashid199@gmail.com, <sup>b</sup>ants.koel@ttu.ee, <sup>c</sup>toomas.rang@ttu.ee

**Keywords:** silicon carbide, heterostructures, diffusion bonding, 3C-SiC, 4H-SiC, germanium

**Abstract.** During the last decade, silicon carbide (SiC) and its heterostructures with other semiconductors have gained a significant importance for wide range of electronics applications. These structures are highly suitable for high frequency and high power applications in extremely high temperature environments. SiC exists in more than 200 different polycrystalline forms, called polytypes. Among these 200 types, the most prominent polytypes with exceptional physical and electrical attributes are 3C-SiC, 4H-SiC and 6H-SiC. Heterostructures of these SiC polytypes with other conventional semiconductors (like Si, Ge) can give rise to interesting electronic characteristics. In this article, Germanium (Ge) has been used to make heterostructures with 3C-SiC and 4H-SiC using a novel technique called diffusion welding. Microscale and nanoscale simulations of *nn*-heterojunction of Ge/3C-SiC and Ge/4H-SiC have been done. Microscale devices have been simulated with a commercially available semiconductor device simulator tool called Silvaco TCAD. Whereas nanoscale devices have been simulated with QuantumWise Atomistix Toolkit (ATK) software package. Current-voltage (IV) curves of all simulated devices have been calculated and compared. In nanoscale device, the effects of defects on IV-characteristics due to non-ideal bonding (lattice misplacement) at heterojunction interface have been analyzed. Our simulation results reveal that the proposed heterostructure devices with diffusion welding of wafers are theoretically possible. These simulations are the preparations of our near future physical experiments targeted to fabricate SiC based heterostructure devices using diffusion bonding technique.

### Introduction

Semiconductor hetero-structures are one of the most essential component of the modern solid-state devices. Heterostructures are being used widely in almost every electronic device like light-emitting diodes (LEDs), bipolar junction transistors, and telecommunication applications [1]. The motion of the charge carriers and states can be precisely controlled in the heterostructure devices at design stage by choosing appropriate semiconductor materials. Heterostructure device performance can be improved due to the control on energy band profile during the design phase [2]. In recent years, Silicon carbide (a wide bandgap semiconductor material) has gained significant importance for the fabrication of heterostructures devices. SiC exists in several crystalline forms called polytypes. Each polytype exhibits unique electrical and physical properties [3]. SiC has high thermal conductivity and chemical tolerance. That is why SiC based electronic devices are highly suitable for high temperature electronic applications [4].



## Appendix D

M. H. Rashid, A. Koel and T. Rang

“Effects of the inclusion of armchair graphene nanoribbons on the electrical conduction properties of NN-heterojunction 4H-6H/SiC diodes,” *Mater. Sci. Forum*, vol. 962, pp. 29–35, 2019. **(ETIS 1.1)**



# Effects of the Inclusion of Armchair Graphene Nanoribbons on the Electrical Conduction Properties of NN-Heterojunction 4H-6H/SiC Diodes

Muhammad Haroon Rashid<sup>1,a</sup>, Ants Koel<sup>1,b</sup> and Toomas Rang<sup>1,c</sup>

<sup>1</sup>Thomas Johan Seebeck Department of Electronics, Tallinn University of Technology  
Ehitajate tee 5, 12616 Tallinn, Estonia

<sup>a</sup>haroonrashid199@gmail.com, <sup>b</sup>ants.koel@ttu.ee, <sup>c</sup>toomas.rang@ttu.ee

**Keywords:** heterostructure, heterojunction, armchair graphene, nanoribbon, 4H-SiC, 6H-SiC

**Abstract.** In recent years, graphene has sparked the interest of researchers due to its promising electrical and physical attributes. These attributes make it highly suitable to develop electronic devices with ultra-high mobility of charge carriers. Meanwhile silicon carbide (SiC), a wide bandgap semiconductor material, is being used for high temperature optoelectronic applications. SiC has more than 250 different crystalline forms, these are called polytypes. Some of these polytypes (such as 4H-SiC, 6H-SiC and 3C-SiC) have exceptional physical and electrical properties. Electronic devices which have SiC and graphene as their constituent materials may combine the outstanding attributes of both materials. This article attempts to simulate electronic devices having SiC and graphene as their constituent materials. For this purpose, simulations of a novel nn-heterojunction 4H-6H/SiC diodes with the inclusion of an armchair nanoribbon layer have been carried out. All of the simulations have been run using QuantumWise Atomistix Toolkit (ATK) software, which is an atomic scale electronic device simulator. The density of the states, charge carrier densities and current-voltage curves of the simulated devices have been computed. The simulation results showed a significant improvement in the electrical conduction properties of nn-heterojunction 4H-6H/SiC diodes after the inclusion of the armchair graphene nanoribbons. These simulations provide the groundwork for our future experiments, which will be targeted on fabricating high mobility diodes and/or field effect transistors.

## Introduction

In recent years, graphene ( a monolayer packed into a 2D honeycomb lattice) has gained the intension of research scientists due to its several appealing properties for electronic applications [1]. Graphene has a great potential to be used in the advanced technological applications. It has exceptional electronic attributes that make it highly suitable for electronic, optoelectronic and biomedical applications [2]. Graphene has high mobility of charge carriers, optical transparency and mechanical flexibility. The high mobility of charge carriers in graphene makes it highly suitable for high frequency electronic applications [3]. Furthermore, graphene nanoribbons (GNRs) have been accepted as unique conjugated polymers. Their band gap can be tuned depending on the application requirements. The electronic features of the GNRs are determined by their edge structure and the width. Depending on the edge termination pattern, GNRs are divided into armchair graphene nanoribbons (AGNRs) and zigzag graphene nanoribbons (ZGNRs) [4]. Graphene nanoribbons can be obtained by the unzipping of carbon nanotubes (CNTs). The unzipping pattern of CNT defines the edge shape of the nanoribbons [5]. The armchair edge graphene nanoribbons and zigzag edge graphene nanoribbons, are shown in Fig. 1(a) and (b) [6]. The trend of the change in the band gap of the armchair and zigzag nanoribbons decreases gradually with an increase in the number of carbon atoms, as shown in Fig. 1 (c) and (d) [7].

Graphene is being used for the fabrication of field effect transistors, radio frequency devices, transparent electrodes and sensors [8]. Recently single layer graphene has been synthesized by using various types of precursors and catalysts of transition metals [9]. Epitaxial growth of graphene over SiC substrates has been accepted as the most suitable method to obtain graphene crystals with good electronic and physical properties for the fabrication of electronic devices.



## Appendix E

**M. H. Rashid**, A. Koel and T. Rang

“Phenol and methanol detector based on pristine graphene nano-sheet: A first principles study,” In Proc. Baltic Electronic Conference, Tallinn, Estonia, October 8–10, 2018. **(ETIS 3.1)**



# Phenol and Methanol Detector Based on Pristine Graphene Nano-sheet: A First Principles Study

M. Haroon Rashid<sup>1</sup>, Ants Koel<sup>1</sup>, and Toomas Rang<sup>1</sup>

<sup>1</sup>Thomas Johann Seebeck Department of Electronics, Tallinn, Estonia, email: [haroonrashid199@gmail.com](mailto:haroonrashid199@gmail.com)

**Abstract**—Over the last decade graphene and its derivatives have stimulated the interest of researchers due to their extraordinary electrical, optical and chemical properties. Graphene has emerged as a potential candidate for electronic sensors and optical sensors applications. The purpose of the work presented in this article is to contribute in this novel field by simulating graphene nano-sheet based sensor to detect phenol and methanol molecules. QuantumWise Atomistix Toolkit (ATK) software has been used to carry out the sensor simulations. A significant change in the density of states and conductivity of the graphene have been noticed in the proximity of the target molecules. This change in the conductivity of graphene nano-sheet has been used as a detection signal. These simulations lay the groundwork for our physical experiments, which are targeted to produce a cheap sensor.

## I. INTRODUCTION

Graphene, a monoatomic thick allotrope of carbon has gained a significance importance in the research field due to its exceptional electronic, optical, thermal and mechanical properties. It has sparked the interest of researchers to investigate this exotic material for future electronic applications [1]. In a graphene planar sheet,  $sp^2$ -bonded carbon atoms are closely packed into a honeycomb crystal lattice. It can be categorized by number of stacks of atomically thin carbon layers ranging from single layer to multi-layers. Intrinsic graphene is a zero-gap semiconductor material with inherently low Johnson noise [2].

Moreover, the electronic structure of graphene is explained by tight-binding approach [3]. The possibility of band gap tuning of graphene makes it an exceptional material for electronic applications [4]. It also has an exceptional high mobility of electrons at room temperature and low resistivity at low temperatures [5]. The mobility of charge carriers in graphene remains ballistic upto  $0.3\mu\text{m}$  length at 300 K. Every carbon atom in graphene contributes to provide a large surface area per unit volume and helps to enhance the exposure to the foreign particles [6]. This combination of distinctive electrical attributes and low noise makes it a suitable candidate for electronic sensor applications. The presence of adsorbed molecules in the proximity of graphene alter its conductivity. Adsorbed molecules act as donors or acceptor for the graphene and consequently change its conductivity. This change can be used as a signature for the detection of specific organic/inorganic molecules [1, 7].

Since, phenol and methanol are toxic and flammable organic compounds [8, 9], it is important to detect their presence to avoid accidents. In this article, simulations of graphene nano-sheet based phenol and methanol detector have been done. These simulations are the groundwork for the experiments, which are targeted to fabricate a novel and low cost sensor for the detection of phenol and methanol molecules.

## II. METHODOLOGY

### A. QuantumWise Atomistix Toolkit (ATK) Software

Nano-scale simulations of the graphene based sensor have been done with the ATK software. Its graphical user interface, Virtual NanoLab (VNL) has been used to simulate graphene nano-sheet based sensor for the detection of phenol and methanol molecules.  $38\text{ \AA}$  long graphene nano-sheet has been used with gold electrodes deposited at its both edges as shown in Fig. 1. Six molecules of phenol, six molecules of methanol and three-three molecules of both compounds interacting under Van der Waals Forces with graphene sheet have been used in three individual experiments to detect their presence. The presence of the target molecules changes the electrical conductivity of the graphene nano-sheet. This change in the conductivity has been used as a detection signal to detect phenol and methanol molecules [6]. A voltage bias has been applied at the gold electrodes of the structure shown in Fig. 1 and four different current-voltage curves have been calculated for four different scenarios (phenol, methanol, phenol and methanol both, only nano-sheet).

### B. ATK-Density Functional Theory (ATK-DFT) Calculator

ATK software computes electronic properties of the nano materials using a wide range of atomic-scale computational methods such as quantum-mechanical computational methods and classical empirical potentials methods [10]. For our simulations, ATK-DFT calculator [11] has been used. These simulations have been run on high performance computing (HPC) machine having total 232 nodes with 2xIntel Xeon E5-2630L processor and 1 Tera-byte (TB) of operating RAM. 8-cores of HPC have been used for running each job (python code-file). Each IV-curve has been computed by HPC in approximately one week. ATK-DFT calculator models the electronic properties of the quantum systems using a linear combination of atomic orbitals. In self consistent calculations of Kohn-Sham equations, density matrix is the key parameter. This electron density function then defines the effective potential. The effective potential is used to obtain Kohn-Sham

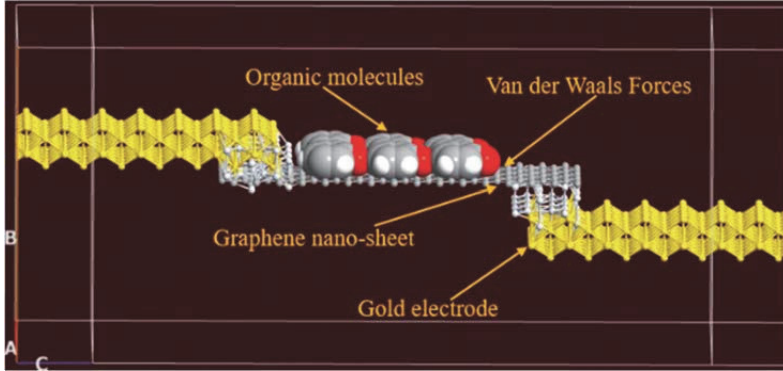


Fig. 1. Simulated structure of graphene nano-sheet based phenol and methanol sensor.

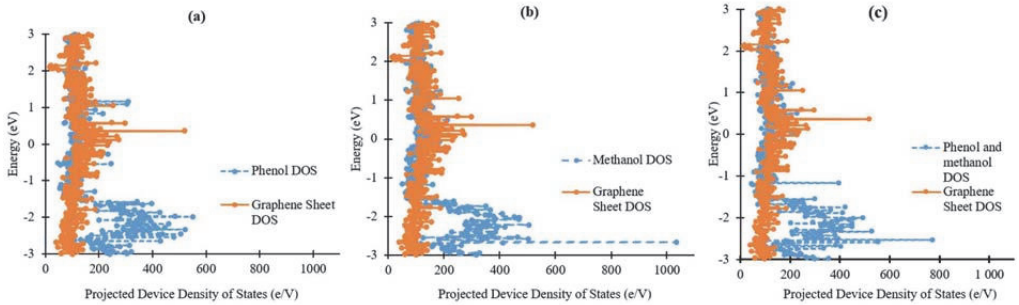


Fig. 2. Change in the projected device density of states of graphene based sensor in the proximity of (a) only phenol molecules; (c) only methanol molecules; (d) both phenol and methanol molecules

Hamiltonian:

$$H_{I_{electron}} = -\frac{\hbar^2}{2m} \nabla^2 + V^{eff}[n](r) \quad (1)$$

In (1), the first term indicates the kinetic energy of the electron and second term is the potential energy of the electron moving in the field produced by other electrons in the presence of external applied field. Eigenfunctions of the Kohn-Sham Hamiltonian are calculated by solving one electron Schrödinger equation. In this equation the electrons have been written in terms of the total electron density and given by  $n=n(r)$ . In next step Kohn-Sham equations are solved and for this, a one-electron Schrödinger equation is solved to get the one-electron eigenfunctions of the Kohn-Sham Hamiltonian ( $\Psi_\alpha$ ),

$$H_{I_{electron}} \Psi_\alpha(r) = \epsilon_\alpha \Psi_\alpha(r) \quad (2)$$

Eq. (2) is called a Kohn-Sham equation within DFT. In the next step this equation is solved by expanding the eigenfunctions  $\Psi_\alpha$ ,

$$\Psi_\alpha(r) = \sum_i c_{\alpha i} \phi_i(r) \quad (3)$$

Now, the differential equations can be written as a matrix equation to determine the expansion coefficients,  $C_{\alpha i}$ :

$$\sum_j H_{ij} c_{ij} = \epsilon_\alpha \sum_j S_{ij} c_{\alpha j} \quad (4)$$

In Eq. (4),  $H_{ij}$  represents Hamiltonian matrix and  $S_{ij}$  represents the overlap matrix. The next target is to obtain the electron density of a many-electron system and this is given by the eigenstates of the Kohn-Sham Hamiltonian, thus:

$$n(r) = \sum_\alpha f_\alpha |\Psi_\alpha(r)|^2 \quad (5)$$

Where in Eq. (5),  $f_\alpha$  is the occupation level that has been denoted by  $\alpha$ . In final step, the electron density function is given by the density matrix as:

$$n(r) = \sum_{ij} D_{ij} \phi_i(r) \phi_j(r) \quad (6)$$

Then from the eigen states of the many electron system, electron density is calculated. Electron density matrix can be given by:

$$D_{ij} = \sum_\alpha f_\alpha C_{\alpha i}^* C_{\alpha j} \quad (7)$$

In (7),  $D_{ij}$  is density matrix,  $f_\alpha$  is the occupation of the energy level denoted by  $\alpha$ , where  $C_{\alpha i}^*$  and  $C_{\alpha j}$  are basis set expansion coefficients.

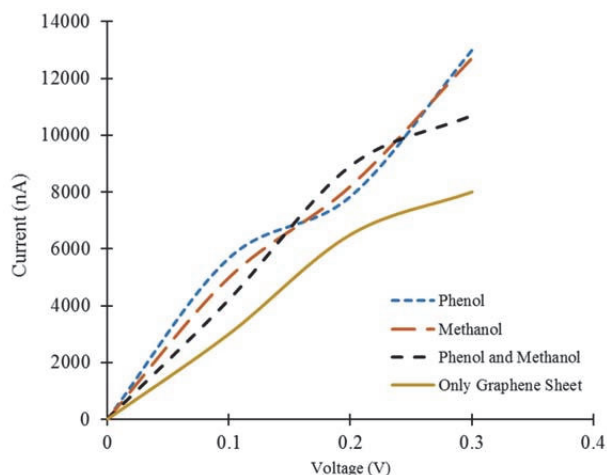


Fig. 3. Current-voltage (IV) curves of the simulated device in the proximity of target molecules.

### III. RESULTS AND DISCUSSION

This section contains a detailed discussion on the simulation results. The projected density of the states (PDDOS) of the device and IV-curves have been calculated and discussed in this section. The simulation results showed a noticeable change in the PDDOS of the device in the presence of phenol and methanol molecules as shown in Fig. 2. The density of the states have been calculated for the energy range of -3 to +3 eV. The presence of phenol and methanol molecules has introduced many new energy states in the graphene nano-sheet as shown in Fig. 2. Many sharp peaks have been introduced in the graphene by the adsorption of phenol molecules as shown in Fig. 2(a). These peaks can be observed in the energy range of -1.5 to -3 eV. The maximum magnitude of these states approaches to approximately 580 e/V in the proximity of phenol molecules as shown in Fig. 2(a).

Similarly the analysis of the PDDOS of the simulated device reveals that many new energy states have been introduced by the methanol molecules as shown in Fig. 2(b). A comparison of the PDDOS of Fig. 2(a) and (b) reveals that the energy states introduced by phenol molecules are different from those of methanol molecules. A high peak of PDDOS of magnitude about 1000 e/V at energy level of approximately at -2.5 eV can be seen in the proximity of methanol molecules in Fig. 2 (b).

Furthermore, under the joint influence of phenol and methanol molecules, the change in the density of the states is different as compared to the change in PDDOS caused by phenol and methanol molecules separately. In Fig. 2(c), many new energy states can be observed in the PDDOS of the graphene based device that do not exist in the graphs of Fig. 2(a) and (b). So, this change in the density of the states in all three cases will definitely influence the total electric current flowing through the device. Consequently, three different current-voltage (IV) curves have been obtained due to the

presence of phenol, methanol and both compounds. DC bias voltages are applied at the electrodes of the simulated device (Fig. 1) and change in electric current is measured. Four different IV-curves are obtained for four different cases. The IV-curves of the simulated device in the presence of phenol, methanol and both molecules (target molecules) are shown in Fig. 3.

It can be observed in Fig. 3 that the presence of the target molecules has increased the current through the graphene based device. Each IV-curve of Fig. 3 is different for different target molecules. The device showed a resistive behavior is almost all the cases. When there was no target molecules in the proximity of graphene sheet, the value of the current varied from 3000 nA to 8000 nA. Since the presence of phenol and methanol molecules introduces new energy states in the graphene nano-sheet, therefore an increase in the current through the device has been observed.

In the presence of phenol molecules, the electric current varies from approximately 5670 nA to 13000 nA as shown in Fig. 3. At each bias voltage the value of the electric current is distinct in the presence of phenol molecules. Similarly the presence of methanol molecules changes the current from approximately 4986 nA to 12700 nA. The proximity of both phenol and methanol molecules changes the current through the device between 4200 nA to 13224 nA as shown in Fig. 3.

A change in the electrical conductivity of graphene based device has been observed due to the presence of adsorbed molecules of these organic compounds. These molecules act as donor or acceptor to change the conductivity of the graphene [6]. They either change the number of charge carriers or their mobility in the graphene sheet. This change in conductivity is specific to the interacting molecules and can be used to detect these molecules. The results of our simulated device showed that the target molecules increased the current through the device. The possible reason could be a change in the number of

charge carries or their mobility through the graphene nano-sheet.

#### IV. CONCLUSION

The results of the simulations revealed a change in the density of the states and conductivity of the graphene in the presence of phenol and methanol molecules. This change in density of the states and conductivity is specific to the target molecules. It means that for different molecules, the density of the states and conductivity is affected differently. This change in the conductivity of the device has been used to detect the target molecules successfully. The simulated results showed an increase in the electric current through the device in the presence of target molecules.

However the difference in the electric current for all four cases is not so large. But this could be due to less concentration of the phenol and methanol molecules. In these simulations a limited number of target molecules have been detected to reduce the computational time of the simulator. Although further investigations are required before physical fabrication of the device to deal with the challenge of selectivity of graphene to detect specific molecules. For this purpose more than one detection mechanisms (change in optical and electrical properties) may be used simultaneously to improve the device reliability.

#### ACKNOWLEDGMENT

This research was supported by the Estonian Research Council through the Institutional Research Project IUT19-11, by the Estonian Research Council through the Institutional Research Project PUT1435, and by the Horizon 2020 ERA-chair Grant "Cognitive Electronics COEL" —H2020-WIDESPREAD-2014-2 (Agreement number: 668995; project TTU code VFP15051).

#### REFERENCES

- [1] V. Singh, D. Joung, L. Zhai, S. Das, S. I. Khondaker, and S. Seal, "Graphene based materials: Past, present and future," *Prog. Mater. Sci.*, vol. 56, no. 8, pp. 1178–1271, 2011.
- [2] W. Choi, I. Lahiri, R. Seelaboyina, and Y. S. Kang, "Synthesis of graphene and its applications: A review," *Crit. Rev. Solid State Mater. Sci.*, vol. 35, no. 1, pp. 52–71, 2010.
- [3] J. Wang, S. Deng, and Z. Liu, "The rare two-dimensional materials with Dirac Cones," *Natl. Sci. Rev.*, vol. 2, no.1, pp.22-39, 2015.
- [4] Y. Zhang, T. Tang, C. Girit, and Z. Hao, "Direct observation of widely tunable bandgap in bilayer graphene," *Nat. Lett.*, vol.459, pp.820-823, 2009.
- [5] M. S. Artilles, C. S. Rout, and T. S. Fisher, "Graphene-based hybrid materials and devices for biosensing," *Adv. Drug Deliv. Rev.*, vol. 63, no. 14–15, pp. 1352–1360, 2011.
- [6] F. Yavari, and N. Koratkar, "Graphene-based chemical sensors," *J. Phys. Chem. Lett.*, vol.3, pp.1746-1753, 2012.
- [7] Y. H. Zhang et al., "Improving gas sensing properties of graphene by introducing dopants and defects: A first-principles study," *Nanotechnology*, vol. 20, no. 18, 2009.
- [8] International Chemical Safety Cards- The National Institute for Occupational Safety and Health, "PHENOL." Internet: [www.cdc.gov/niosh/ipcsneng/neng0070.html](http://www.cdc.gov/niosh/ipcsneng/neng0070.html), July 22, 2015 [May 10, 2018]
- [9] International Chemical Safety Cards- The National Institute for Occupational Safety and Health, "METHANOL: Systemic Agent." Internet: [www.cdc.gov/niosh/ipcsneng/neng0070.html](http://www.cdc.gov/niosh/ipcsneng/neng0070.html), Nov. 9, 2017 [May 12, 2018]
- [10] "Atomic Scale Computational Methods." Internet: <https://quantumwise.com/products/features>, Updated 2017 [May 14, 2018]
- [11] "ATK-DFT" Internet: <https://docs.quantumwise.com/manuals/ATKDFT.html>, Updated 2017 [May 22, 2018]

## Appendix F

**M. H. Rashid**, A. Koel and T. Rang

“First Principles Simulations of Phenol and Methanol Detector Based on Pristine Graphene Nanosheet and Armchair Graphene Nanoribbons,” *Sensors Journal*, vol. 19, no. 2713, June, pp. 1–14, 2019. **(ETIS 1.1)**





Article

# First Principles Simulations of Phenol and Methanol Detector Based on Pristine Graphene Nanosheet and Armchair Graphene Nanoribbons

Muhammad Haroon Rashid <sup>\*</sup>, Ants Koel and Toomas Rang

Thomas Johan Seebeck Department of Electronics, Tallinn University of Technology, Ehitajate tee 5, 12616 Tallinn, Estonia; ants.koel@taltech.ee (A.K.); toomas.rang@taltech.ee (T.R.)

\* Correspondence: haroonrashid199@gmail.com; Tel.: +372-53912599

Received: 24 April 2019; Accepted: 13 June 2019; Published: 18 June 2019



**Abstract:** Over the last decade graphene based electronic devices have attracted the interest of researchers due to their exceptional chemical, electrical and optical properties. Graphene is very sensitive to any physical changes in its surrounding environment and, inherently, has very low electronic noise. This property of graphene makes it a suitable candidate for sensor applications. The purpose of the work presented in this article is to demonstrate the ability of graphene derivatives to detect toxic organic compounds like phenol and methanol. A novel method for the detection of organic compounds (phenol and methanol) has been introduced in this article. In this method, a change in the photocurrent, as well as electric current, have been used as detection signals to improve the sensor accuracy and selectivity for specific target molecules. A nanoscale electronic device simulator, Quantumwise Atomistix Toolkit (ATK), has been used to simulate graphene nanosheet and armchair graphene nanoribbon based sensors. Devices density of states (DOS), current–voltage curves and photocurrent curves have been calculated with the ATK simulator. In the proximity of target molecules, a significant change in DOS, electric current and photocurrent have been observed. The simulated graphene based structures can be converted into physical sensors to obtain a low cost, small sized, integrated sensing device.

**Keywords:** graphene; graphene nanosheet; armchair graphene nanoribbon; phenol; methanol; detector; photocurrent

## 1. Introduction

In modern society, the development of a cheap, portable and reliable gas sensor for domestic and industrial environments is of utmost importance. Industrial environment monitoring, for the health and safety of the workforce, demands highly reliable sensors for the detection of toxic compounds [1]. The demand for gas sensors has been increased with the development of the internet of things (IoT). The applications of these sensors include the chemical industry [2,3], food quality assessment [4,5] and the agricultural sector [6,7]. Graphene is a promising candidate for modern gas sensor applications due to its good conductivity [8], good light transmittance [9] and good thermal conductivity [10]. At room temperature, the mobility of charge carriers in graphene remains ballistic for the length of 0.3  $\mu\text{m}$ . A large surface area to volume ratio allows graphene to be exposed to the target molecules more effectively [11]. Inherently, graphene has a very low electronic noise [12], which makes it an astonishing material to detect gases and other related organic compounds. Graphene nanosheet has  $\text{sp}^2$  bonded carbon atoms that are tightly packed to give a honeycomb lattice structure. Graphene can be categorized from a single layer to several stacks of single layers called multilayers. It is mostly known as a zero-gap semiconductor, whose band gap can be tailored according to the application

requirement [13,14]. Single layer of graphene (SLG) has numerous unique attributes, especially its band structure. SLG exhibits ambipolar properties (charges can be alternated between electrons and holes based on applied voltages) [15]. All the above-mentioned properties make graphene highly suitable for gas sensor applications.

A wide range of graphene-based devices are being investigated for the detection of organic compounds and gases. Several advancements in the technology have revolutionized the field of graphene-based sensors and devices. Recently, laser induced graphene paper (LIGP) has emerged as a promising candidate to detect liquids and antibacterial media [16]. Graphite nanoplatelet thin film fiber sensors, with very high sensitivity, have also been fabricated to detect stress/strain and failure of the host composite material [17]. Graphene like materials have been developed to detect volatile organic compounds [18]. Graphene-based flexible, and wearable, gas sensors have been fabricated to detect a wide range of gases and organic chemicals [19].

Moreover, graphene-based gas and organic compound detectors have different working principles. They may include resistive method, micro-electro-mechanical systems (mems) method and field effect transistors (FET) methods. Most of the commercial gas sensors use the resistive method to detect foreign gas particles. The conductivity of the graphene changes with the change in the gas concentration in the environment [20]. The presence of the gas can be measured as a function of change in conductivity of graphene [21]. In FET based devices, drain to source current changes in the presence of the adsorbed target molecules [22,23]. In the case of quality sensitive gas sensors, the operating frequency of the device changes in the presence of a target gas or organic compound [24]. The working principle of the first reported graphene-based gas sensors was also based on the resistive method [12]. That sensor was capable of detecting individual gas and volatile organic molecules. The resistive method based graphene sensors can be easily developed. The absorbed gas, and volatile organic molecules, interact with the graphene surface and change its conductivity by changing the charge carrier concentration. This method provides a high sensitivity to the sensor and even very low concentrations of gases/organic vapors can be detected [25]. The resistive method is being widely used to fabricate sensors to detect gases and organic/inorganic compounds [12].

Furthermore, graphene has a unique electronic band structure that is different from semiconductors, insulators and conductors. It has a conical band structure above and below the Fermi level. These conical band structures are called Dirac cones [26]. Graphene sheets and ribbons have different electronic attributes from each other. Even the electronic properties of armchair and zigzag nanoribbons are dissimilar. Depending on the termination pattern of the edge of the ribbons, their electronic properties change. The bandgap of armchair graphene nanoribbons (AGNRs) changes with the increase in the number of carbon atoms in the ribbon. This bandgap decreases gradually from 3 to 0.75 eV as the number of carbon atoms increases from 20 to 65 atoms, approximately. Whereas, this change for zigzag nanoribbons, is different from AGNRs. For an even number of electrons in the carbon atoms, the change in the bandgap is different compared to that of an odd number of electrons in the carbon atoms. For both cases, the bandgap gradually decreases with an increase in the number of carbon atoms. Doping of boron and nitrogen may be the reason for this change in the bandgap, which changes the ionization energy of the ribbons [27]. Graphene monolayer 2D crystals are fabricated on a large scale by chemical vapor deposition (CVD) [28], and epitaxial growth, on SiC substrates. However, pristine graphene, obtained from these methods, is a gapless semiconductor that limits its applications in nanoelectronics. Theoretical and experimental studies have demonstrated the change in the properties of these nanoribbons compared to those of 2D crystals [29]. Graphene nanoribbons (GNRs) and nanosheets are being used for gas sensor applications [30,31].

Phenol and methanol are toxic and flammable organic compounds that are harmful to human health so it is essential to detect their presence in domestic and industrial environments to avoid serious accidents [32,33]. In this article, phenol and methanol molecules have been detected by using pristine graphene nanosheet and AGNRs. The reason for using pristine graphene for the detection of phenol and methanol is its better response and low detection limit. Even a change by a single atom

can be detected. Although graphene-based metal oxide semiconductor sensors are being widely used, but they have a short lifetime, poor selectivity and a high operating temperature [34]. Most of the graphene-based sensors detect the target molecules by a change in its conductivity [20]. The same principle has been used in our work to detect phenol and methanol molecules. This article is an extension to our previously published work [35].

In that paper [35], phenol and methanol molecules have been detected by a change in electric current through a graphene nanosheet. In the current article, a novel mechanism for the detection of phenol and methanol molecules, to improve the sensor selectivity for these target molecules, is proposed. This novel method introduces the change in photocurrent through AGNRs in the proximity of these target molecules. The simulation results demonstrate a significant change in the density of states (DOS), electric current (through graphene nanosheet and AGNRs) and photocurrent (through AGNRs) in the presence of target molecules. These changes in the above-mentioned parameters can be used as the detection signals to develop a physical sensor, based on the graphene nanosheet or AGNR, over a suitable substrate like SiC. The purpose of these simulations is to access the feasibility of graphene nanosheet, or AGNR, based sensors for the detection of phenol and methanol molecules before physical fabrication.

## 2. Materials and Methods

Phenol and methanol molecules have been detected with two types of devices. First, graphene nanosheet based structures, with gold electrodes, have been used to detect target molecules, as shown in Figure 1. Secondly, graphene armchair nanoribbon-based structures have been used to detect phenol and methanol molecules. These simulations have been conducted in a nanoscale semiconductor device simulator using, Quantumwise Atomistix Toolkit (ATK), which has a graphical user interface, called Virtual nano lab (VNL), that allows the simulation of a variety of nanoscale devices. This complete software package, with the graphical user interface, is called ATK-VNL. More details about the used simulator will be given in the next section.

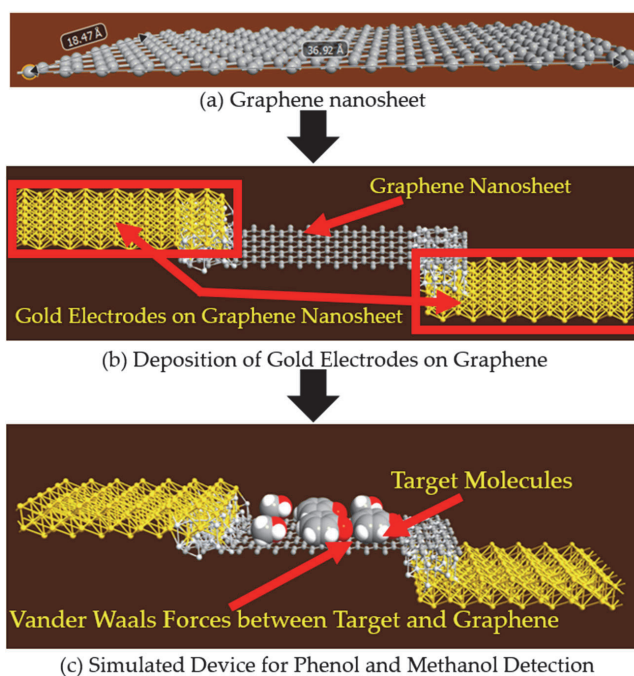


**Figure 1.** Schematic of the simulated graphene nanosheet based phenol and methanol detector.

### 2.1. Graphene Nanosheet for the Detection of Phenol and Methanol Molecules

In our previously published work [35], graphene nanosheet based structures were used to detect the presence of phenol and methanol molecules. In this study the schematic of the simulated structure is shown in Figure 1. This graphene nanosheet has an approximate length of 37 Å and width of 18 Å, and is simulated with the ATK-VNL, as shown in Figure 1a. In the next step, gold electrodes have been deposited at both edges of the graphene nanosheet, as shown in Figure 1b. In step three, phenol and methanol molecules have been exposed to the surface of the simulated device to detect their presence. Van der Waals forces are acting between the target molecules and the graphene nanosheet, as the target molecules are only a few Angstroms above the surface of the graphene sheet, as shown in Figure 1c.

During the characterization of the simulated device, DC bias voltage is applied to the gold electrodes of the simulated device. Current–voltage (IV) curves have been calculated for four different scenarios: In the absence of target molecules, in the presence of only four phenol molecules, in the presence of only four methanol molecules and in the presence of both molecules (two-phenol and two-methanol molecules). For the same scenarios, four different DOS have also been calculated under zero-bias conditions.

### 2.2. Armchair Graphene Nanoribbon (AGNR) for the Detection of Phenol and Methanol Molecules

This simulated structure is an extension to our previously published work [35]. Termination of infinite graphene layers into finite structures results into two types of nanoribbons [36]. Depending on the termination sequence of the edge, they are categorized into armchair and zigzag nanoribbons, as shown in Figure 2.

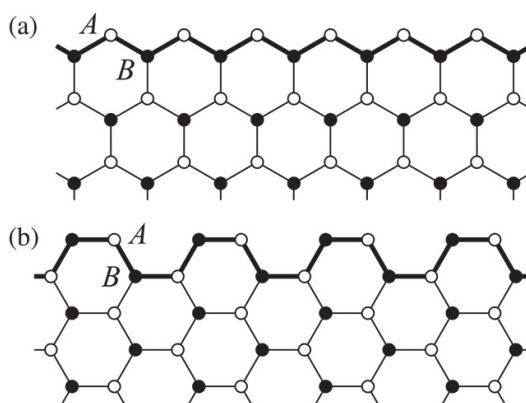
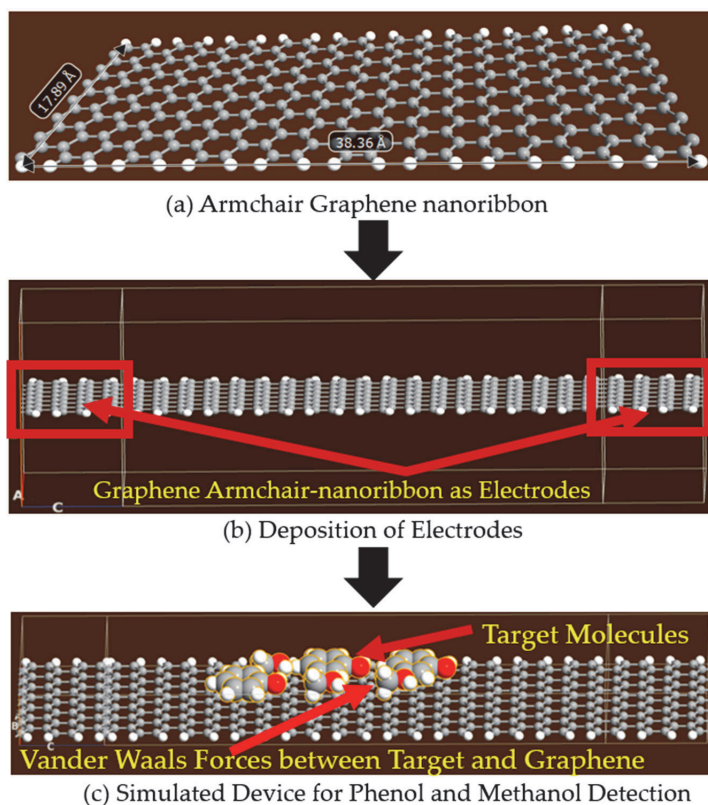


Figure 2. (a) Zigzag graphene nanoribbon; (b) armchair graphene nanoribbon [36].

In Figure 2b, the structure of an armchair graphene nanoribbon is shown. In the simulations, AGNR based structures have been used to detect the presence of phenol and methanol molecules, as shown in Figure 3. Armchair graphene nanoribbons, with width (armchair edge side) of approximately 37 Å and with length (repetition pattern side) of 18 Å, have been simulated with ATK-VNL, as shown in Figure 3a. In the next step, AGNR itself has been chosen as the electrodes (shown within red rectangles) to avoid any Schottky barrier formation at the electrodes, as shown in Figure 3b. This approach reduces the computational time as well. Finally, phenol and methanol molecules have been exposed to the simulated structure, as shown in Figure 3c. The same process described in Section 2.1 has been repeated for the characterization of this device. Device DOS, IV-curves and photocurrent curves have been calculated for four different scenarios.



**Figure 3.** Schematic of the simulated armchair graphene nanoribbon-based phenol and methanol detector.

### 2.3. Methodology for Simulated Graphene Nanosheet and Armchair Graphene Nanoribbon Based Devices

For the simulations of the structures described in Sections 2.1 and 2.2, an atomic scale semiconductor device simulator, Quantumwise Atomistix Toolkit (ATK) has been used. ATK has a graphical user interface called Virtual Nanolab (VNL). The ATK-VNL software package models the electronic properties of the quantum systems [37]. This software package has different types of in-built calculators that use different methodologies to compute the electronic parameters of the simulated devices. For these simulations, the inbuilt ATK-DFT calculator [38] together with a high-power computing (HPC) environment [39] has been used.

This HPC has 232 computing machines with 1024 GB of total memory. With eight computing nodes, each IV-curve took about one week to calculate in HPC for these experiments. ATK-VNL follows a workflow to simulate electronic devices. In this workflow, first of all the structure of the device is formed using the ATK builder tool, then this simulated structure is sent to the script generator tool that generates the python file. During the script generation, an inbuilt calculator is added into the simulated structure with the desired parameters to be analyzed. The script contains a simulated device, new calculator and density of states (to be analyzed). Finally, the script has been generated as a script.py file. The python code, generated by the scripser can be customized by using the custom scripser tool of ATK-VNL. In the last step, this generated script is run in the job manager. The script can be run on the local machine or on a remote high-power computing machine. After the execution of the job, the output file is obtained (for example, script.nc or script.hdf5). Finally, the results are viewed in

the viewer tab. The ATK-DFT in-built calculator was used for the simulations with K-point sampling of  $K_A = 5$ ,  $K_B = 5$  and  $K_C = 50$ .

### 3. Results and Discussions

This section has been divided into two subsections, as two types of devices have been simulated. The density of states (DOS) and IV-curves have been calculated for graphene nanosheet and AGNR based devices.

#### 3.1. Density of States and Current–voltage Characteristics Analysis of the Graphene Nanosheet Based Device

In Figure 4, the projected device density of states (PDDOS) in the presence of phenol, methanol and both phenol and methanol molecules have been shown. In Figure 4a, a noticeable change in the PDDOS of the device could be seen in the presence of phenol molecules (blue lines) compared to that of in the absence of target molecules (orange lines). Exposure of the device to the phenol molecules had introduced many new energy states below the Fermi energy level. At energies  $-1$  to  $-3$  eV, new energy states with higher values could be observed, compared to the device in the absence of target molecules. This change would definitely affect the current through the graphene nanosheet based device. The effect of methanol molecules on the PDDOS was totally different, as compared to the previous case, as shown in Figure 4b. Many sharp energy states could be observed, below the Fermi level, in the presence of methanol molecules only. These energy states were different from those introduced by phenol molecules.

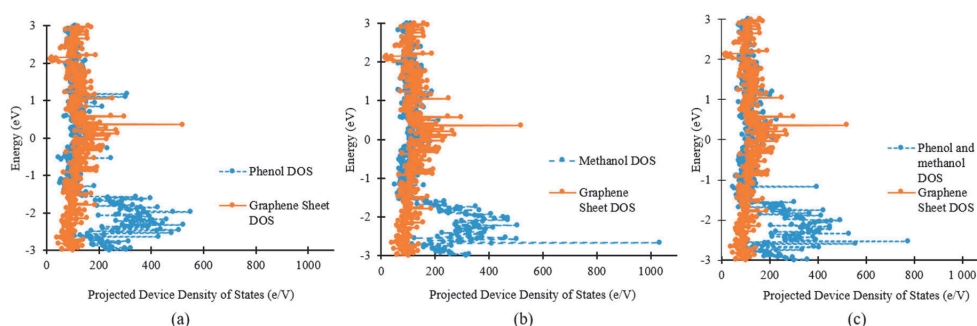


**Figure 4.** Change in density of states of graphene nanosheet based device in the presence of (a) only phenol molecules; (b) only methanol molecules; (c) both phenol and methanol molecules.

In the third scenario (Figure 4c), both phenol and methanol molecules were exposed to the graphene nanosheet based device. The change in the PDDOS in this case was totally different from the last two scenarios i.e., Figure 4a,b. Many new energy states could be observed between  $-2$  to  $-3$  eV in the presence of both phenol and methanol molecules, in Figure 4c. These new states will consequently change the electric current through the device.

Figure 5 shows four different IV-curves for four different cases for the simulated device i.e., in the absence of target molecules, in the presence of phenol molecules, in the presence of methanol molecules and in the presence of both phenol and methanol molecules. An increase in the current for the device was observed in the presence of methanol, phenol and both phenol and methanol molecules. The adsorbed target molecules work as acceptors, or donors, for the graphene and change its conductivity [11,40,41]. Adsorbed target molecules were responsible for the change in the charge carrier's concentration in the graphene nanosheet. If these molecules act as donors for graphene, then they increase its conductivity. Alternatively, the adsorbed molecules reduce the electrical conductivity of graphene if they are acting as acceptors [42]. The simulation results shown in Figure 5 reveal that the target molecules were acting as donors for the graphene nanosheet and changing the concentration of charge carriers in it, but this change in the concentration of charge carriers and conductivity was

dissimilar for the different adsorbed molecules (i.e., phenol, methanol and both phenol and methanol molecules).

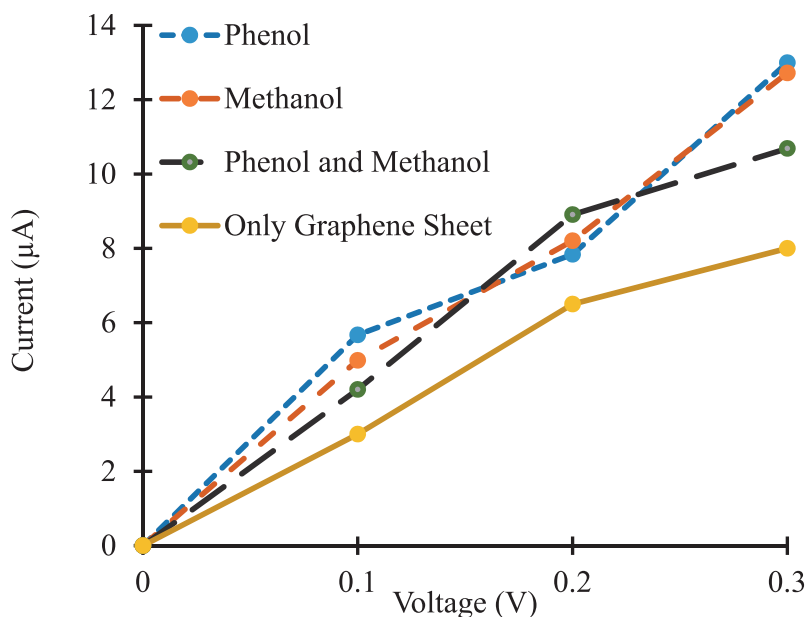


**Figure 5.** Current–voltage (IV) curves of graphene nanosheet based simulated device in the proximity of phenol and methanol as target molecules.

Moreover, the difference in the electric current values is not very significant for different target molecules in the simulations. This could be due to a lesser concentration of target molecules that are exposed to the graphene nanosheet. The concentration of target molecules has been kept low (four molecules in each case) to minimize the computational time of the simulations. Even with this lesser concentration of target molecules, each IV-curve took more than one week to calculate in HPC. This difference in current values would be more obvious with an increased concentration of target molecules.

### 3.2. Density of States and Current–Voltage Characteristics Analysis of Armchair Graphene Nanoribbon Based Device

In another set of experiments, armchair graphene nanoribbon (AGNR) of approximately the same dimensions as the graphene nanosheet (dimensions are given in Figures 1 and 3) were used for the detection of phenol and methanol molecules. The device density of states (DOS), IV-curves and photocurrent curves were calculated for the same target molecules. The purpose of detecting the same target molecules with AGNR was to analyze which graphene-based material was more sensitive and suitable for the development of a physical sensor. In Figure 6, energy vs. density of states was shown on logarithmic scales. In the magnified view (right image) of Figure 6, it can be clearly seen that the DOS of AGNR (dark blue dotted line), in the absence of target molecules, was significantly different from all other three DOS curves. In Figure 6, the green dotted line, red dotted line and solid greenish blue line are representing the DOS of the device in the proximity of methanol, phenol and both methanol and phenol molecules, respectively (also see the legend). It can be observed in Figure 6 that in the presence of methanol molecules, the abrupt spikes in energy states were not present between energy levels of  $10^{-2}$  to  $10^{-1}$  eV, as compared to that of the device in the absence of target molecules.

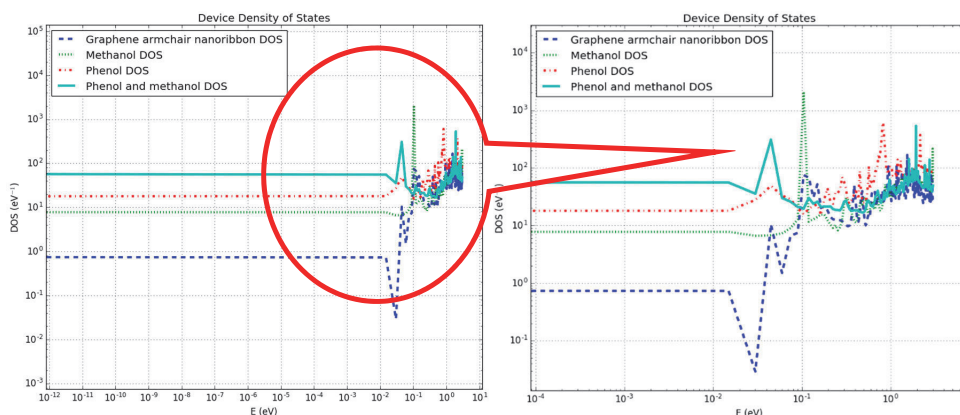


**Figure 6.** Change in density of states of an armchair graphene nanoribbon-based device in the proximity of target molecules where the x- and y-axis are in logarithmic scales (Right figure is a magnified view of left figure).

Moreover, the comparison of energy states for the rest of the energy window between the device in the absence of target molecules and the device in the presence of methanol shows that they were different from each other. The presence of methanol molecules had changed the DOS of the pristine AGNR. This figure shows that DOS curves of the AGNR based device in the presence of only phenol, and both phenol and methanol, molecules had changed the energy states differently. This change in DOS of the device would definitely influence the electric current through the device in the proximity of these target molecules.

Furthermore, Figure 7 shows the change in IV-curves of AGNR based device in the presence of phenol, methanol and both phenol and methanol molecules as target molecules. Simulation results reveal that in the absence of target molecules, a very low current in the range of  $10^{-20}$  to  $10^{-19}$   $\mu\text{A}$  flowed through the device, as shown in Figure 7 (curve 1). Exposure of the AGNR based device to both phenol and methanol molecules resulted in an increase in the electric current through the device. The range of the electric current through the device in this case was of  $10^{-14}$  to  $10^{-13}$   $\mu\text{A}$ , as shown in Figure 7 (curve 2). The influence of the phenol and methanol molecules seemed to be like donors of charge carriers for AGNR, due to which an increase in the electric current, with reference to curve 1, was observed in the presence of both phenol and methanol molecules.

Furthermore, it was observed that the exposure of an AGNR based device to phenol molecules only, significantly increased the flow of the electric current through the device as shown in Figure 7 (curve 3). Phenol molecules may have acted as donors of charge carriers for AGNR, due to which a significant increase in the electric current through the device, with reference to curves 1 and 2, was observed, as shown in Figure 7. The range of current in this case was between 1.325 to 5.788  $\mu\text{A}$  approximately. A similar increase in current through the device was observed in the presence of only methanol molecules. In this case, methanol molecules might have acted like donors for AGNR but the range of current was between 2.131 to 9.323  $\mu\text{A}$  approximately, as shown in Figure 7 (curve 4).

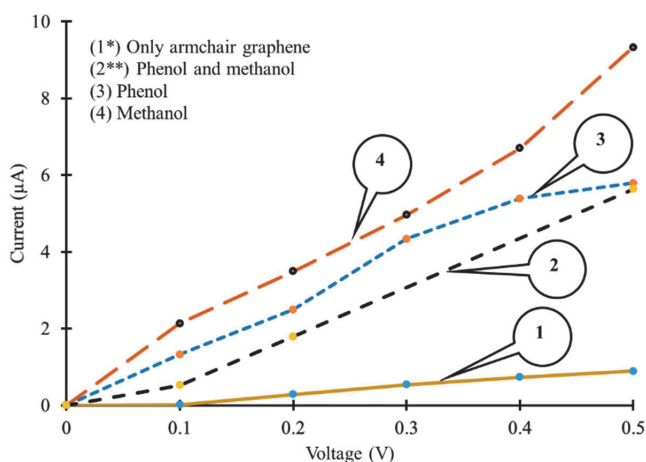


**Figure 7.** Current–voltage (IV) curves of armchair graphene nanoribbon based simulated device (1\*) without target molecules (current axis  $\times 10^{-18}$  to get actual values); (2\*\*) with phenol and methanol molecules (current axis  $\times 10^{-13}$  to get actual values); (3) with phenol molecules; (4) with methanol molecules.

#### PhotoCurrent Analysis of an Armchair Graphene Nanoribbon Based Device in the Proximity of Different Target Molecules

In order to improve the sensor reliability and selectivity for specific target molecules, more than one detection mechanism can be used. In Section 3.2, the change in electric current in the presence of target molecules was used as a signature to detect them. In this sub-section, change in the photocurrent in the presence of target molecules was used as a detection signal, along with a change in electric current, to enhance the device selectivity for specific molecules. The AGNR based device has been illuminated by AM1.5 solar spectrum obtained from [43], where AM1.5 stands for the air mass coefficient that is used to characterize the performance of solar cells, for terrestrial power-generating panels, under standardized conditions. In these simulations, photon energies have been kept between 0 to 3 eV and the resultant photocurrent was calculated. Generation of a photocurrent in AGNR was observed under the above-mentioned illumination conditions in the simulator. This kind of first principles simulation has been reported in the literature for solar cell devices [44]. The same principle was implied for the AGNR sensor.

During the physical characterization process, the AGNR based device could be exposed to an artificial light source (a light bulb or LED) to generate a photocurrent. Then the change in photocurrent, in the presence of different target molecules, could be used as a signature signal to detect specific molecules. The AGNR based device was illuminated with photons, having energies between 0 to 3 eV, and the change in photocurrent was calculated for different target molecules, as shown in Figure 8.

Moreover, the results show that with an increase in photon energies, the generation of photocurrent also increases, but the change in photocurrent, for different target molecules, was dissimilar, as shown in Figure 8. During the physical characterization of the graphene-based sensor, the change in the electric current, as well as the photocurrent, can be used as detection signals. Afterwards, these signals can be fed to, and stored in, a micro-controller as a signature signal for the detection of a specific target. Finally, an inbuilt light source can be installed for the illumination of the AGNR to get a photocurrent in a physically fabricated device.

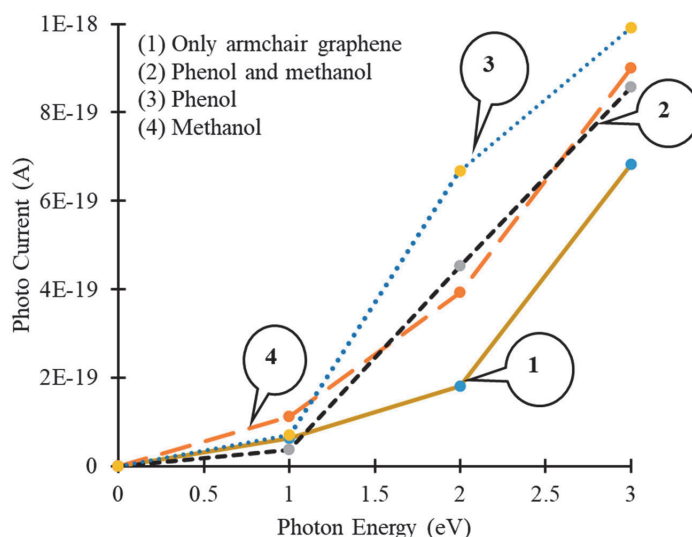


**Figure 8.** Photon energy vs. photocurrent curves of an armchair graphene nanoribbon device (1) without target molecules; (2) with phenol and methanol molecules; (3) with phenol molecules and (4) with methanol molecules.

However, a very low photocurrent has been observed during the simulations in AGNR as shown in Figure 8. The simulation of light absorption in a single layer of graphene, is still a key challenge, although graphene based optoelectronic devices, with high internal quantum efficiencies, have been reported for physically fabricated devices. Due to the dissimilarities of the behavior of traditional semiconductors and graphene, in the generation and transportation of charge carriers, high-bandwidth and high internal quantum efficiency values have been reported for graphene based experimental devices [45], but it is not an easy task to reproduce the same results, by simulations, due to limitations of the available simulators in relation to the material's parameters and other complex phenomena. Hot carriers play a crucial role in the generation of photocurrents in optoelectronic devices, but the mechanism involved in this process has not been fully determined yet [46]. The key challenge is to resolve the differences, between the theoretical material properties and the experimental results, to achieve more accurate simulation-based results.

However, with heavy chemical doping, the absorption in a single layer of graphene can be increased physically up to 40%. The generation of a photocurrent also depends on the interaction of graphene plasmons with surface polar phonons of insulating substrates, like SiO<sub>2</sub>. This hybrid plasmon–phonon mode, between graphene plasmons and its substrate's polar phonons, can be excited in the mid-infrared region under s-polarization. In this interaction, the phonon's and electron's temperature are raised and this increased temperature changes the electrical conductivity and increases the photocurrent in graphene. Due to the limitations of the simulator in controlling the polarization of photons and the activation of the plasmon-phonon coupling mode (in the case of using an insulating substrate for AGNR), high values of photocurrent could not be achieved in the simulations. However, in physically fabricated graphene-based devices, high photocurrents can be achieved by tuning intrinsic plasmons and activating the hybrid plasmon–phonon mode [47].

Moreover, we are planning to conduct experiments based on differential measurements to study the effect of light on the generation of photocurrents in graphene-based devices. In these experiments two graphene strips will be placed in parallel within a controlled environment. In the experimental setup, one strip will be illuminated with a suitable light source and the other one will be kept in darkness. After that, the differential signal will be acquired from these two graphene strips with

the help of a locally developed amplifier [48] to get rid of noise and acquire the information signal (photocurrent).

Pristine graphene nanosheet and AGNRs were used to detect phenol and methanol molecules in our simulations. However, in practice, it is not possible to avoid defects in the large-scale fabrication process of graphene-based devices. Defects in graphene change its electronic properties. Sometimes, defects can contribute to the introduction of beneficial effects in graphene-based devices that can be utilized for different device applications. More significant effects of defects are self-heating and a degraded performance of the device [49].

#### 4. Conclusions

The purpose of the work that has been presented in this article is to access the feasibility of the graphene nanosheet and armchair graphene nanoribbon to detect phenol and methanol molecules prior to the physical fabrication of a sensor. The simulation results showed that both phenol and methanol could be detected with a graphene nanosheet and armchair nanoribbons, but the sensitivity of a graphene nanosheet is very low for the detection of the desired target molecules. The change in the electric current of the graphene nanosheet is very small in the presence of phenol and methanol as target molecules. In a low concentration of these target molecules, it is very difficult to differentiate between the presence of phenol, methanol and both phenol and methanol molecules. Whereas, the selectivity and sensitivity of armchair graphene nanoribbon, to detect phenol and methanol molecules, is better than the graphene nanosheet. A significant difference between the IV-curves of AGNR based device has been observed in the presence of phenol and methanol as target molecules. Furthermore, a change in the photocurrent through AGNR, in the presence of the above-mentioned target molecules, was also calculated, although, the values of the photo generated current were very small in the simulated devices. By controlling the polarization of photons and activating the plasmon-photon coupling mode (after selecting a suitable insulating substrate for AGNR), higher values of photocurrent could be physically achieved. In order to improve the sensor selectivity and accuracy, changes in the electric current, as well as the photocurrent, are suggested as signature signals for the detection of phenol and methanol molecules. These simulations revealed that AGNR is a better choice for the detection of phenol and methanol molecules as the change in IV-curves, in the presence of target molecules, is more obvious as compared to that of graphene nanosheet. The future intention is to develop a physical sensor based on AGNR to detect phenol and methanol molecules. Changes in the electric current and photocurrent, in the presence of specific target molecules, will be used as a detection signal for the AGNR based physical sensor.

**Author Contributions:** M.H.R. and A.K. conceived the idea. M.H.R. performed the simulations and drafted the article. A.K. and T.R. reviewed the article and managed funding of the project.

**Funding:** This research was supported by the Estonian Research Council through Research Projects PUT 1435, IUT 1911 and by the Horizon 2020 ERA-chair grant “Cognitive Electronics COEL H2020-WIDESPREAD-2014-2” (agreement number 668995; project TTU code VFP15051).

**Acknowledgments:** Authors would like to acknowledge the courtesy of Nikolai A. Poklonski and SPIE publishers to give copyright permission to reprint a figure from article Poklonski, N.A.; Kislyakov, E.F.; Vyrko, S.A.; Bubel', O.N.; Ratkevich, S.V.; Electronic band structure and magnetic states of zigzag graphene nanoribbons: quantum chemical calculations. *J. Nanophotonics* **2012**, *6*, 61712, DOI:10.1117/1.JNP.6.061712.

**Conflicts of Interest:** The authors declare no conflict of interests.

#### References

1. Andre, R.S.; Mercante, L.A.; Facure, M.H.; Mattoso, L.H.C. Enhanced and selective ammonia detection. *Appl. Surf. Sci.* **2019**, *473*, 133–140. [[CrossRef](#)]
2. Costa, S.; Ferreira, J.; Silveira, C.; Costa, C. Integrating health on air quality assessment—Review report on health risks of two major European outdoor air pollutants: PM and NO<sub>2</sub>. *J. Toxicol. Environ. Heal. Part B Crit. Rev.* **2014**, *17*, 307–340. [[CrossRef](#)] [[PubMed](#)]

3. Chatterjee, S.G.; Chatterjee, S.; Ray, A.K.; Chakraborty, A.K. Graphene-metal oxide nanohybrids for toxic gas sensor: A review. *Sens. Actuators B Chem.* **2015**, *221*, 1170–1181. [[CrossRef](#)]
4. Hong, X.; Wang, J.; Hai, Z. Discrimination and prediction of multiple beef freshness indexes based on electronic nose. *Sens. Actuators B Chem.* **2012**, *161*, 381–389. [[CrossRef](#)]
5. Wei, Z.; Wang, J.; Jin, W. Evaluation of varieties of set yogurts and their physical properties using a voltammetric electronic tongue based on various potential waveforms. *Sens. Actuators B Chem.* **2013**, *177*, 684–694. [[CrossRef](#)]
6. Zhang, H.; Wang, J.; Ye, S.; Chang, M. Application of electronic nose and statistical analysis to predict quality indices of peach. *Food Bioprocess Technol.* **2012**, *5*, 65–72. [[CrossRef](#)]
7. Wei, Z.; Wang, J. Tracing floral and geographical origins of honeys by potentiometric and voltammetric electronic tongue. *Comput. Electron. Agric.* **2014**, *108*, 112–122. [[CrossRef](#)]
8. Marinho, B.; Ghislandi, M.; Tkalya, E.; Koning, C.E.; de With, G. Electrical conductivity of compacts of graphene, multi-wall carbon nanotubes, carbon black, and graphite powder. *Powder Technol.* **2012**, *221*, 351–358. [[CrossRef](#)]
9. Wright, A.R.; Xu, X.G.; Cao, J.C.; Zhang, C. Strong nonlinear optical response of graphene in the terahertz regime. *Appl. Phys. Lett.* **2009**, *95*, 93–96. [[CrossRef](#)]
10. Chai, G.; Chen, Q. Characterisation study of the thermal conductivity of carbon nanotube copper nanocomposites. *J. Compos. Mater.* **2010**, *44*, 2863–2873. [[CrossRef](#)]
11. Yavari, F.; Koratkar, N. Graphene-based chemical sensors. *J. Phys. Chem. Lett.* **2012**, *3*, 1746–1753. [[CrossRef](#)] [[PubMed](#)]
12. Schedin, F.; Geim, A.K.; Morozov, S.V.; Hill, E.W.; Blake, P.; Katsnelson, M.I.; Novoselov, K.S. Detection of individual gas molecules adsorbed on graphene. *Nat. Mater.* **2007**, *6*, 652–655. [[CrossRef](#)] [[PubMed](#)]
13. Choi, W.; Lahiri, I.; Seelaboyina, R.; Kang, Y.S. Synthesis of graphene and its applications: A review. *Crit. Rev. Solid State Mater. Sci.* **2010**, *35*, 52–71. [[CrossRef](#)]
14. Zhang, Y.; Tang, T.; Girit, C.; Hao, Z.; Martin, M.C.; Zettl, A.; Crommie, M.F.; Shen, Y.R.; Wang, F. Direct observation of a widely tunable bandgap in bilayer graphene. *Nature* **2009**, *459*, 820–823. [[CrossRef](#)] [[PubMed](#)]
15. Novoselov, K.S.; Geim, A.K.; Morozov, S.V.; Jiang, D.; Zhang, Y.; Dubonos, S.V.; Grigorieva, I.V.; Firsov, A.A. Electric field effect in atomically thin carbon films. *Science* **2004**, *306*, 666–669. [[CrossRef](#)] [[PubMed](#)]
16. Wang, Y.; Wang, Y.; Zhang, P.; Liu, F.; Luo, S. Laser-induced freestanding graphene papers: A new route of scalable fabrication with tunable morphologies and properties for multifunctional devices and structures. *Nano Micro Small* **2018**, *14*. [[CrossRef](#)] [[PubMed](#)]
17. Luo, S.; Liu, T. Graphite Nanoplatelet enabled embeddable fibre sensor for in-situ curing monitoring and structural health monitoring of polymeric composites. *Appl. Mater. Interfaces* **2014**, *6*, 9314–9320. [[CrossRef](#)]
18. Brigida, A.; Alfe, M.; Gargiulo, V.; Polichetti, T.; Massera, E.; Miglietta, M.; Francia, G.D. A new chemical sensing material for ethanol detection: Graphene-like film. In Proceedings of the 3rd National Conference on Sensors, Rome, Italy, 23–25 February 2016.
19. Eric, S.; Meyya, M.; Hari, S.N. Flexible graphene-based wearable gas and chemical sensors. *ACS Appl. Mater. Interfaces* **2017**, *9*, 34544–34586.
20. Pearce, R.; Iakimov, T. Epitaxially grown graphene based gas sensors for ultra sensitive NO<sub>2</sub>, detection. *Sens. Actuators B Chem.* **2010**, *155*, 451–455. [[CrossRef](#)]
21. Sun, F.; Xu, S. Application of graphene material in gas-sensor. *J. South China Norm. Univ.* **2013**, *6*, 93–98.
22. Ohno, Y.; Maehashi, K. Chemical and biological sensing applications based on graphene field-effect transistors. *Biosens. Bioelectron.* **2010**, *26*, 1727–1730. [[CrossRef](#)] [[PubMed](#)]
23. Syu, Y.-C.; Hsu, W.-E.; Lin, C.-T. Review—Field effect transistor biosensing: Devices and clinical application. *ECS J. Solid-State SC.* **2018**, *7*, Q3196–Q3207. [[CrossRef](#)]
24. Arsat, R.; Breedon, M. Graphene-like nano-sheets for surface acoustic wave gas sensor applications. *Chem. Phys. Lett.* **2009**, *467*, 344–347. [[CrossRef](#)]
25. Lin, Y.M.; Avouris, P. Strong suppression of electrical noise in bi-layer graphene nanodevices. *Nano Lett.* **2008**, *8*, 2119–2125. [[CrossRef](#)] [[PubMed](#)]
26. Condensed Concepts. Available online: <http://condensedconcepts.blogspot.com/2015/08/conical-intersections-vs-dirac-cones.html> (accessed on 1 February 2019).

27. Owens, F.J. Electronic and magnetic properties of armchair and zigzag graphene nanoribbons. *J. Chem. Phys.* **2008**, *128*. [[CrossRef](#)]
28. Sukang Bae, X.X.; Kim, H.; Lee, Y. Roll-to-roll production of 30-inch graphene films for transparent electrodes. *Nat. Nanotechnol.* **2010**, *5*, 574–578.
29. Paupitz, R.; Autreto, P.A.; Legoas, S.B.; Srinivasan, S.G.; Van Duin, A.C.; Galvao, D.S. Graphene to fluorographene and fluorographane: A theoretical study. *Nanotechnology* **2013**, *24*. [[CrossRef](#)]
30. Pajoohepour, N.; Rezaei, M.; Hajian, A.; Afkhami, A.; Sillanpää, M.; Arduini, F.; Bagheri, H. Protein templated Au-Pt nanoclusters-graphene nanoribbons as a high-performance sensing layer for the electrochemical determination of diazinon. *Sens. Actuators B Chem.* **2018**, *275*, 180–189. [[CrossRef](#)]
31. Yan, P.; Jiang, D.; Li, H.; Bao, J.; Xu, Li.; Qian, J.; Chen, C.; Xia, J. BiPO<sub>4</sub> nanocrystal/BiOCl nanosheet heterojunction as the basis for a photoelectrochemical 4-chlorophenol sensor. *Sens. Actuators B Chem.* **2018**, *279*, 466–475. [[CrossRef](#)]
32. Budavari, S. *The Merck Index: An Encyclopedia of Chemical, Drugs, and Biologicals*; Merck: Hoboken, NJ, USA, 1996.
33. Methanol. Available online: [www.ilo.org/dyn/icsc/showcard.display?p\\_lang=en&p\\_card\\_id=0057&p\\_version=2](http://www.ilo.org/dyn/icsc/showcard.display?p_lang=en&p_card_id=0057&p_version=2) (accessed on 15 February 2019).
34. Tian, W.; Liu, X.; Yu, W. Research progress of gas sensor based on graphene and its derivatives: A review. *Appl. Sci.* **2018**, *8*, 1118. [[CrossRef](#)]
35. Rashid, M.H.; Koel, A.; Rang, T. Phenol and methanol detector based on pristine graphene nano-sheet: A first principles study. In Proceedings of the 16th Biennial Baltic Electronics Conference, Tallinn, Estonia, 8–10 October 2018.
36. Poklonski, N.A.; Kislyakov, E.F.; Vyrko, S.A.; Bubel, O.N.; Ratkevich, S.V. Electronic band structure and magnetic states of zigzag graphene nanoribbons: Quantum chemical calculations. *J. Nanophotonics* **2012**, *6*, 61712. [[CrossRef](#)]
37. Atomic-scale Modelling for Semiconductor & Materials Research. Available online: [www.synopsys.com/silicon/quantumatk.html](http://www.synopsys.com/silicon/quantumatk.html) (accessed on 28 February 2019).
38. ATK-DFT. Available online: <https://docs.quantumwise.com/v2017/manuals/ATKDFT.html> (accessed on 1 March 2019).
39. High Power Computing. Available online: <https://www.ttu.ee/support-structure/it-services/services-4/high-performance-computing-2/> (accessed on 13 March 2019).
40. Dau, T.N.N.; Vu, V.H.; Cao, T.T.; Nguyen, V.C.; Ly, C.T.; Tran, D.L.; Pham, T.T.N.; Loc, N.T.; Piro, B.; Vu, T.T. In-situ electrochemically deposited Fe<sub>3</sub>O<sub>4</sub> nanoparticles onto graphene nanosheets as amperometric amplifier for electrochemical biosensing applications. *Sens. Actuators B Chem.* **2019**, *283*, 52–60. [[CrossRef](#)]
41. Zhang, H.F.; Wu, D.P.; Ning, X.J. Atomistic mechanism for graphene based gaseous sensor working. *Appl. Surf. Sci.* **2019**, *470*, 448–453. [[CrossRef](#)]
42. Ni, J.; Yang, N.; Liang, Q.; Jiang, J.; Meng, R.; Huang, Y.; Chen, X. Gas adsorption on graphene with different layers: A first-principles study. In Proceedings of the 16th International Conference on Electronic Packaging Technology, Changsha, China, 11–14 August 2015.
43. National Renewable Energy Laboratory (N.R.E. Lab.). Solar Spectra. Available online: <https://www.nrel.gov/grid/solar-resource/spectra.html> (accessed on 2 April 2019).
44. Palsgaard, M.; Markussen, T.; Gunst, T.; Brandbyge, M.; Stokbro, K. Efficient first principles calculation of phonon-assisted photocurrent in large-scale solar-cell devices. *Phys. Rev. Appl.* **2018**, *10*, 1–5. [[CrossRef](#)]
45. Xia, F.; Mueller, T.; Lin, Y.; Valdes-Garcia, A.; Avouris, P. Ultrafast graphene photodetector. *Nat. Nanotechnol.* **2009**, *4*, 839–843. [[CrossRef](#)] [[PubMed](#)]
46. Gabor, N.M.; Song, J.C.W.; Ma, Q.; Nair, N.L.; Taychatanapat, T.; Watanabe, K.; Taniguchi, T.; Levitov, L.S.; Jarillo-Herrero, P. Hot Carrier-Assisted Intrinsic Photoresponse in graphene. *Science* **2011**, *334*, 648–651. [[CrossRef](#)] [[PubMed](#)]
47. Freitag, M.; Low, T.; Zhu, W.; Yan, H.; Xia, F.; Avouris, P. Photocurrent in graphene harnessed by tunable intrinsic plasmons. *Nat. Commun.* **2013**, *4*, 1–8. [[CrossRef](#)]

48. Ojarand, J.; Min, M.; Koel, A. Multichannel electrical impedance spectroscopy analyser with microfluidic sensors. *Sensors* **2019**, *19*. [[CrossRef](#)]
49. Halder, S.; Amorim, R.G.; Sanyal, B.; Scheicher, R.H.; Rocha, A. Energetic stability, STM fingerprints and electronic transport properties of defects in graphene and silicone. *RSC Adv.* **2016**, *6*, 6702–6708. [[CrossRef](#)]



© 2019 by the authors. Licensee MDPI, Basel, Switzerland. This article is an open access article distributed under the terms and conditions of the Creative Commons Attribution (CC BY) license (<http://creativecommons.org/licenses/by/4.0/>).

## Appendix G

H. Rashid, A. Koel and T. Rang

“Simulations of methane and acetone detector based on pristine graphene nano-sheet over intrinsic 4H-SiC substrate,” in Proc. 19<sup>th</sup> IEEE Nano Conference, Macau, China, July 22–26, 2019. **(ETIS 3.1)**



# Simulations of Methane and Acetone Detector Based on Pristine Graphene Nano-sheet Over Intrinsic 4H-SiC Substrate

M. Haroon Rashid<sup>1</sup>, Ants Koel<sup>1</sup>, and Toomas Rang<sup>1</sup>

<sup>1</sup>Thomas Johann Seebeck Department of Electronics, Tallinn, Estonia, email: [haroonrashid199@gmail.com](mailto:haroonrashid199@gmail.com)

**Abstract** — Nowadays graphene and its derivatives have gained the interest of researchers due to their exceptional optical, electrical and chemical attributes. They have emerged as potential candidates for electronics and optoelectronics sensor applications. Graphene is highly sensitive to any physical change in its surrounding environment that makes it a suitable candidate for sensing a large variety of organic and inorganic molecules. Volatile and flammable organic compounds like acetone and methane can lead to fatal accidents in domestic and industrial environments. In this article, nanoscale simulations of graphene nano-sheet based methane and acetone detector have been done. Intrinsic 4H-SiC has been used as a substrate for graphene nano-sheet. These simulations have been carried out in QuantumWise Atomistix Toolkit (ATK) software that is an atomic scale semiconductor device simulator. A noticeable change in the density of states (DOS) and electrical conductivity through the device has been observed in the presence of target molecules. This change in electrical conductivity through this nano-scale device can be used as a detection signal for methane and acetone molecules to develop a physical sensor.

## I. INTRODUCTION

Graphene based gas sensors have shown a great potential for the detection of the adsorbed molecules with high sensitivity and fast response on graphene surface. The adsorbed molecules change the electrical conductivity of graphene sheets [1]. Gas sensors based on pristine graphene nano-sheets have faster response time compared to that one with defects [2]. Further, graphene has inherently low Johnson noise [3, 4].

The combination of above mentioned physical and electrical attributes makes graphene a highly sensitive material. Hence, it can be used in a variety of electronics, optoelectronics and biochemical devices applications [5]. Acetone [6] and methane [7] are highly flammable organic compounds. Most common mining accidents are caused due to the explosion of methane and dust gases. These explosions results in loss of several human lives each year [7]. Therefore, monitoring of these organic compounds is critical in domestic and industrial environments to avoid accidents.

Density functional theory (DFT) is being used extensively to study the behavior of graphene based gas sensors [8]. In this

paper, we also used DFT method to study the graphene nano-sheet over intrinsic SiC substrate based methane and acetone sensor. Density of states (DOS) and electric current of device have been calculated in the presence and absence of target molecules.

## II. METHODOLOGY

### A. QuantumWise Atomistix Toolkit (ATK) Software

Nano-scale simulations of graphene based methane and acetone sensor have been done with the ATK software. Pristine graphene nano-sheet has been deposited over intrinsic 4H-SiC substrate cut in (0001)-orientation by using graphical user interface, Virtual NanoLab (VNL) of ATK software package. The simulated device is a quasi-two dimensional structure. The main length of the devices is approximately 60Å including electrodes as shown in Fig. 1. In this device, semiconductor material itself has been used as electrode to avoid Schottky barrier formation at electrodes. Three molecules of methane, three molecules of acetone and two-two molecules of both compounds have been detected in three different experiments. These target molecules of organic compounds are interacting under Van der Waals Forces with graphene sheet deposited over intrinsic 4H-SiC substrate. Change in electric current through the device in the proximity of target molecules has been used as a detection signal to detect these organic molecules [9]. A DC voltage bias has been applied at the electrodes of the structure shown in Fig. 1. Four different current-voltage curves have been calculated for four different scenarios (only device without target molecules, only methane molecules, only acetone molecules and both methane and acetone molecules).

### B. ATK-Density Functional Theory (ATK-DFT) Calculator

ATK software uses density functional theory (DFT) to compute the electronic properties of wide range of nano-scale semiconductor devices [10]. ATK software has an in-built ATK-DFT calculator that has been used for our simulations of graphene-based sensor. All these simulations have been run on high performance computing (HPC) environment having total 232 nodes and 1TB of operating random access memory (RAM). Each IV-curve has been calculated by using eight cores of HPC in approximately one week. ATK-DFT calculator [11] can model quantum systems by using a linear combination of atomic orbitals. Where, density matrix is the key parameter in Kohn-Sham equations.

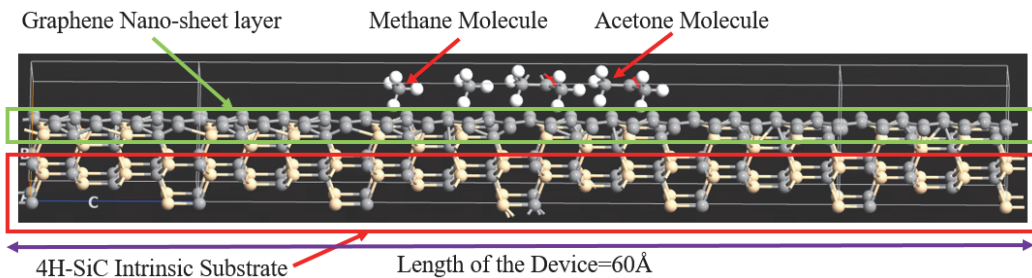


Fig. 1. Simulated structure of graphene nanosheet based methane and acetone sensor.

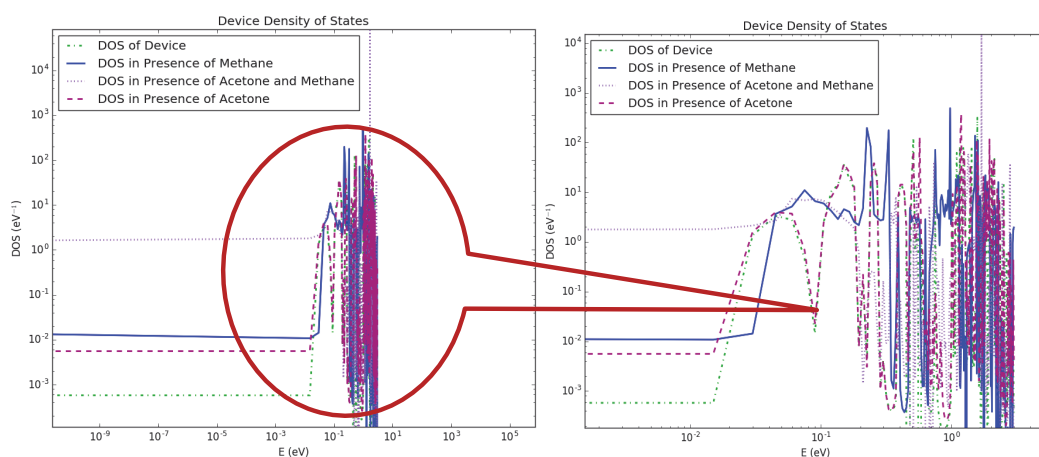


Fig. 2. A comparison of density of states of sensor in the presence of target molecules with logarithmic scales (where right figure is magnified view of left figure).

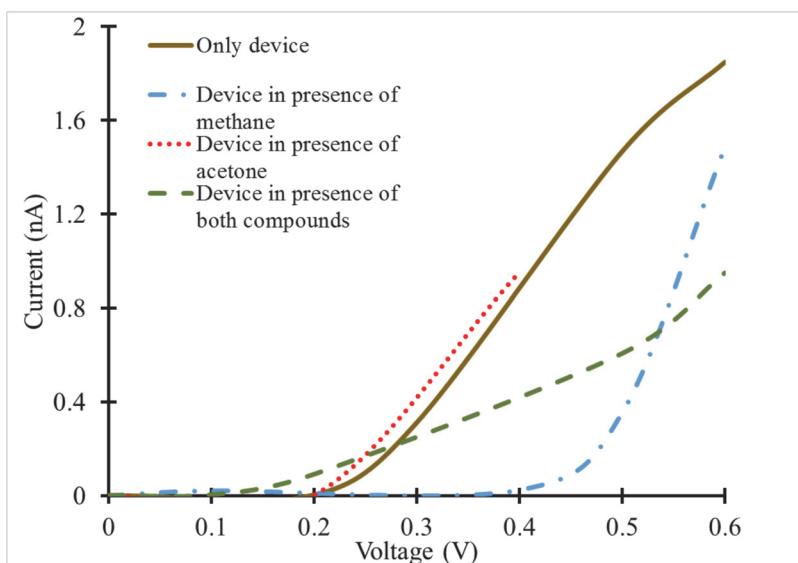


Fig. 3. Current-voltage (IV) curves of the simulated device in the presence of target molecule

Then, this electron density function is used to define the effective potential. In the next step, this effective potential is used to get Kohn-Sham Hamiltonian:

$$H_{Ielectron} = -\frac{\hbar^2}{2m}\nabla^2 + V^{eff}[n](r) \quad (1)$$

In (1), the first and second terms indicate the kinetic energy and the potential energy of the moving electron in the presence of external applied electric field respectively. After that, one electron Schrödinger equation is used to calculate the Eigenfunctions of Kohn-Sham Hamiltonian. Finally, a one-electron Schrödinger equation is used to get the one-electron Eigenfunctions of the Kohn-Sham Hamiltonian ( $\Psi_\alpha$ ),

$$H_{Ielectron}\Psi_\alpha(r) = \varepsilon_\alpha\Psi_\alpha(r) \quad (2)$$

In the next step (2) is solved by expanding the Eigenfunctions  $\Psi_\alpha$ ,

$$\Psi_\alpha(r) = \sum_i c_{\alpha i}\phi_i(r) \quad (3)$$

Now, a matrix equation can be written to determine the expansion coefficients,  $C_{\alpha i}$ :

$$\sum_j H_{ij}c_{ij} = \varepsilon_\alpha \sum_j S_{ij}c_{\alpha j} \quad (4)$$

In (4),  $H_{ij}$  denotes Hamiltonian matrix and  $S_{ij}$  denotes the overlap matrix. In the next step, the electron density of a many-electron system is given by the eigenstates of the Kohn-Sham Hamiltonian, thus:

$$n(r) = \sum_\alpha f_\alpha |\psi_\alpha(r)|^2 \quad (5)$$

Where in (5),  $f_\alpha$  represents the occupation level that has been denoted by  $\alpha$ . In final step, density matrix is calculated:

$$n(r) = \sum_{ij} D_{ij}\phi_i(r)\phi_j(r) \quad (6)$$

Then from the Eigen states of the many electron system, electron density is calculated. Electron density matrix can be given by:

$$D_{ij} = \sum_\alpha f_\alpha C_{\alpha i}^* C_{\alpha j} \quad (7)$$

In (7),  $D_{ij}$  denotes density matrix,  $f_\alpha$  represents the occupation of the energy level denoted by  $\alpha$ , where  $C_{\alpha i}^*$  and  $C_{\alpha j}$  are basis set expansion coefficients.

### III. RESULTS AND DISCUSSION

This section contains a detailed discussion on the simulation results. The density of the states (DOS) and IV-curves of the simulated device have been calculated for four different cases (only device in the absence of target molecules, in the presence of methane molecules, in the presence of acetone molecules and in the presence of both methane & acetone molecules). The comparison of density of states as a function of energy has been shown in Fig. 2. A Logarithmic scale has been used for X and Y-axis to fit all the values of DOS in one graph.

X-axis shows the energy values in eV for DOS graph and Y-axis shows the density of states at different energy levels. DOS of the device in the absence of any target molecules is given by Green dotted line in Fig. 2. This DOS of the device demonstrates a constant value as we move along the energy axis from  $10^{-9}$  to  $10^{-3}$  eV. Above energy level of  $10^{-1}$  many energy states in the form of abrupt spikes can be observed within a narrow region, as shown in Fig. 2.

After this, the device was exposed to only three methane molecules and DOS was calculated. In the presence of methane molecules, a change in DOS can be observed (blue solid line) compared to that of the device in the absence of target molecules. The position of energy states has been shifted approximately from  $10^{-3}$  to  $10^{-2}$  eV $^{-1}$  between the energy window of approximately  $10^{-9}$  to  $10^{-3}$  eV compared to that of the device in the absence of target molecules, as shown in Fig. 2 (Dark blue line). Many new energy states have been added by the methane molecules in the form of abrupt spikes between energy values of  $10^{-1}$  to  $10^1$  eV, as shown in Fig. 2.

Similarly, the change in DOS can be observed in the presence of both acetone and methane molecules. A significant shift in DOS (light pink dotted line) from  $10^{-3}$  to  $10^0$  eV $^{-1}$  can be noticed between energy values of  $10^{-9}$  to  $10^{-3}$  approximately compared to that of the reference device (green dotted line), as shown in Fig. 2. Many sharp spikes in the DOS of the device can be observed as we move above energy level of  $10^{-3}$  eV (light pink dotted line) in Fig. 2. The trend of change in the DOS of the device in the presence of both acetone and methane molecules is more obvious as compared to the previous two cases. Several new energy states have been added below and above fermi levels. These spikes can be observed in enlarged view of Fig. 2 (right graph).

Finally, DOS have been calculated by exposing the device to acetone molecules. The DOS has been shown with dark red dotted line in Fig. 2. In this case, the change in DOS (dark red dotted line) is almost similar to the reference device (green dotted line). The graphs shown in Fig. 2 demonstrate a small change in DOS of the device in the presence of these target molecules. The possible reason of this small change in DOS can be the low concentration of target molecules that are exposed to the device. The reason of keeping this concentration so low is to minimize the computation time. More significant change in DOS can be experienced by increasing the length of the device to increase the exposure area and then increasing the concentration of target molecules.

Furthermore, in another set of experiments current-voltage curves have been calculated for the above-mentioned four scenarios. Four different curves have been shown in Fig. 3. Adsorbed foreign molecules act as donors or acceptors for graphene. If they act like donors, then an increase the conductivity of graphene is observed. Whereas when they behave as acceptors for graphene, a decrease in conductivity of graphene is observed [12]. This change in conductivity is being used as a detection signal to detect a wide range of organic/inorganic and gas molecules. The same principle has been used in our simulations to detect the presence of methane and acetone molecules.

In the presence of methane molecules, a decrease in electric current has been observed when compared to the device in the absence of target molecules. Electric current starts to flow through the graphene-based device at 0.4 V in the presence of adsorbed methane molecules, as shown in Fig. 3. The influence of adsorbed methane molecules seems like acceptors for graphene, due to which a decrease in electric current has been observed in graphene-based device. In the presence of both acetone and methane as target, same trend of decrease in electric current has been observed as compared to the device in the absence of target. The device starts to conduct electric current at 0.1 V, as shown in Fig. 3. The joint influence of adsorbed methane and acetone molecules seems like acceptor. Due to which a decrease in electric current has been observed, as shown in Fig. 3.

Moreover, in the presence of acetone as target molecules, a slight increase in electric current has been observed as compared to the device in the absence of target molecules. The influence of adsorbed acetone molecules seems like donors of charge carriers for graphene-based device. Due to which an increase in electric current has been observed, as shown in Fig. 3. Exposure of simulated device to different target molecules have influenced the electric current through the device differently.

#### IV. CONCLUSION

Our simulations results demonstrated a change in the density of the states and conductivity of the graphene in the presence of acetone and methane as target molecules. Although, the change in electric current in the presence of target molecules is more obvious as compared to that of DOS. However, the change in DOS of the device in the presence of target molecules is not so significant in our simulations. The possible reason is less concentration of acetone and methane molecules that are exposed to the sensor. A remarkable change in DOS and electric current through the device can be observed by increasing the dimensions of the device to increase exposure area. However, this increment will also increase the computation time even in high power computing environment.

Moreover, the purpose of these simulations is to access the feasibility of graphene for the detection of acetone and methane molecules in real world. Our near future intension is to develop a physical sensor based on graphene. During real world application of this physical device, the presence of other gases will also be a challenge in the selectivity of the sensor. To overcome this problem our future research goal is to add change in photocurrent as an additional mechanism to detect the desired target molecules with more accuracy. For this reason intrinsic 4H-SiC has been used as a substrate in our simulations. Because in generation of photocurrent, the interaction between graphene plasmons and substrate's surface polar phonons plays an important role. Our next objective is to study the effect of intrinsic 4H-SiC on the generation of photocurrent in this sensor.

#### ACKNOWLEDGMENT

This research was supported by the Estonian Research Council through Research Projects PUT 1435, IUT 1911 and

by the Horizon 2020 ERA-chair grant "Cognitive Electronics COEL H2020-WIDESPREAD-2014-2" (agreement number 668995; project TTU code VFP15051).

#### REFERENCES

- [1] J. Kong, N. R. Franklin, C. Zhou, M. G. Chapline, S. Peng, and K. Cho, "Nanotube molecular wires as chemical sensors," *Science* 28 Jan., p.622-625. 2000.  
<https://doi.org/10.1126/science.287.5453.622>.
- [2] F. Ricciardella, S. Vollebregt, T. Polichetti, M. Miscuglio, B. Alfano, and M. L. M. Iglietta, "Effects of graphene defects on gas sensing properties towards NO<sub>2</sub> detection," *Nanoscale*, pp.6085–6093, 2017  
<https://doi.org/10.1039/c7nr01120b>.
- [3] W. Choi, I. Lahiri, R. Seelaboyina, and Y. S. Kang, "Synthesis of graphene and its applications: A review," *Crit. Rev. Solid State Mater. Sci.*, vol. 35, no. 1, pp. 52–71, 2010.
- [4] Y. H. Zhang et al., "Improving gas sensing properties of graphene by introducing dopants and defects: A first-principles study," *Nanotechnology*, vol. 20, no. 18, 2009.
- [5] R. Shepard, S. Shepard, and M. Smeu, "Ab initio investigation into the physical physisorption of noble gases on graphene," *Surface Science*, vol. 682, pp.38-42, 2019.
- [6] "Acetone MSDS,"  
Internet: <https://hazard.com/msds/mf/baker/baker/files/a0446.htm>, April 21, 1998 [Jan. 28, 2019]
- [7] P. Dozolme, "Common mining accidents,"  
Internet: <https://www.thebalancesmb.com/most-common-accidents-occurring-in-the-mining-industry-2367335>, Jan. 14, 2019 [Jan. 28, 2019]
- [8] Mo. Y. et al., "Acetone adsorption to (BeO)<sub>12</sub>, (MgO)<sub>12</sub> and (ZnO)<sub>12</sub> nanoparticles and their graphene composites: A density functional theory (DFT) study," *Applied Surface Science*, vol.469, pp. 962-973, 2019
- [9] F. Yavari, and N. Koratkar, "Graphene-based chemical sensors," *J. Phys. Chem. Lett.*, vol.3, pp.1746-1753, 2012.
- [10] "Atomic Scale Computational Methods." Internet:  
<https://quantumwise.com/products/features>, Updated 2017 [Jan 31, 2019]
- [11] "ATK-DFT" Internet:  
<https://docs.quantumwise.com/v2017/manuals/ATKDFT.html>, Updated 2017 [Feb. 8, 2019]
- [12] J. Ni, N. Yang, Q. Liang, J. Jiang, R. Meng, and Y. Huang, "Gas adsorption on graphene with different layers: A first-principles study," In Proc. of 16<sup>th</sup> International Conference on Electronic Packaging, 2015.

## Appendix H

H. Rashid, A. Koel and T. Rang

“Simulations of Propane and Butane Gas Sensor Based on Pristine Armchair Graphene Nanoribbon,” in Proc. of International Conference on Smart Engineering Materials, Romania, March 2017. **(ETIS 3.1)**



PAPER • OPEN ACCESS

## Simulations of Propane and Butane Gas Sensor Based on Pristine Armchair Graphene Nanoribbon

To cite this article: Haroon Rashid *et al* 2018 *IOP Conf. Ser.: Mater. Sci. Eng.* **362** 012001

View the [article online](#) for updates and enhancements.

### Related content

- [Band Gap Calculations of Bilayer Graphene and Bilayer Armchair Graphene Nanoribbon](#)  
E. Sustini, Khairurrijal, F. A. Noor et al.
- [Selective scattering in a zigzag graphene nanoribbon](#)  
Jun Nakabayashi and Susumu Kurihara
- [A new approach to model sensitivity of graphene-based gas sensors](#)  
Mahdiar Ghadiry, Razali Ismail, Bahareh Naraghi et al.

# Simulations of Propane and Butane Gas Sensor Based on Pristine Armchair Graphene Nanoribbon

Haroon Rashid<sup>1</sup>, Ants Koel<sup>2</sup> and Toomas Rang<sup>3</sup>

1 Ph.D Student at Thomas Johan Seebeck Department of Electronics, Tallinn University of Technology, Estonia

2 Associate Professor at Thomas Johan Seebeck Department of Electronics, Tallinn University of Technology, Estonia

3 Professor at Thomas Johan Seebeck Department of Electronics, Tallinn University of Technology, Estonia

E-mail: haroonrashid199@gmail.com

**Abstract.** Over the last decade graphene and its derivatives have gained a remarkable place in research field. As silicon technology is approaching to its geometrical limits so there is a need of alternate that can replace it. Graphene has emerged as a potential candidate for future nano-electronics applications due to its exceptional and extraordinary chemical, optical, electrical and mechanical properties. Graphene based sensors have gained significance for a wide range of sensing applications like detection of biomolecules, chemicals and gas molecules. It can be easily used to make electrical contacts and manipulate them according to the requirements as compared to the other nanomaterials. The intention of the work presented in this article is to contribute in this field by simulating a novel and cheap graphene nanoribbon sensor for the household gas leakage detection. QuantumWise Atomistix (ATK) software is used for the simulations of propane and butane gas sensor. Projected device density of the states (PDDOS) and the transmission spectrum of the device in the proximity of gas molecules are calculated and discussed. The change in the electric current through the device in the presence of the gas molecules is used as a gas detection mechanism for the simulated sensor.

## 1. Introduction

The discovery of graphene has quickly sparked the interest of researchers due to its tremendous promising and unique attributes. The exceptional properties and nontoxic nature of graphene are making it a potential candidates for future electronics applications [1]. Graphene is a single layer of carbon atoms having thickness of 0.35-1.6 nm with a honeycomb lattice structure of sp<sup>2</sup>-bonded carbon atoms. It is a two dimensional material with Dirac cones. In graphene lattice, C-C bond length is 1.42 Å and the lattice constant is 2.46 Å. The electronic structure of graphene can be explained by tight-binding approach [2]. Graphene is so called a zero-gap semiconductor [3] which has the possibility to tune its band gap [1]. The unique band structure of graphene give rise to exceptional high electron mobility. It has been reported that the charge carrier transport in the graphene remains ballistic up to 0.3 μm at 300 K. It is highly sensitive to any chemical change in its surrounding environment. Every carbon atom in graphene provides the greatest surface per unit volume and makes mobility of the charge carriers highly sensitive to the adsorbed molecules. Another interesting quality of graphene is its intrinsically low electrical noise due to high quality of crystal lattice. This property makes it highly suitable for ultra high sensitive chemical detection applications [4].



Graphene is being used for high frequency electronic application, field effect transistors, and transparent conductors. Recently graphene based biological and chemical sensor has gained significant importance [5]. Graphene is also emerging as a potential candidate for sensor applications in nano-electronics. Graphene is being used for the detection of gases, biomolecules and heavy metal ions. The adsorption and desorption of gas molecules change the conductivity of the graphene. These gas molecules act as acceptors or donors when they approach the graphene and ultimately they change the conductance of the graphene. The change in the electrical conductance of the graphene nanoribbon is taken as a detection signal for the gas molecules. Molecules of different gases affect the conductance of the graphene differently. So a large number of gases can be detected by using graphene [6]. In this paper pristine armchair graphene nanoribbon based sensor has been simulated for the detection of household alkane group gases like propane ( $C_3H_8$ ) and butane ( $C_4H_{10}$ ). To the best of author's knowledge only one closest reference [7] has been found that deals with the usage of the nanotubes for the detection of natural gases that are detected in this paper. In the presence of these gases, change in current through the armchair nanoribbon has been used as a gas detection signal. These simulations are to estimate the device behaviour before physical fabrication experiments of household gas leakage detection sensor.

### 1.1. Graphene nanoribbons

Different synthetic techniques are being used to synthesize a versatile family of graphene based materials with distinct properties. Graphene nanoribbons belong to the graphene materials family that are highly suitable for sensor applications. The electronic properties of the graphene nanoribbons change from semiconductors to spin-polarized half metals. Graphene nanoribbons are obtained from the unzipping of carbon nanotubes (CNTs) [8]. Depending on the termination pattern of the edge, graphene nanoribbons are divided into two types: armchair edge graphene nanoribbon (AGNR) and zigzag edge graphene nanoribbon (ZGNR). GNRs tend to repeat their geometric sequence to form periodic structures as shown in figure 1 [3].

It has been reported that the bandgap of GNRs changes with the number of carbon atoms constituted by them. It means that the electronic and the magnetic properties of nanoribbons are a function of the length of the ribbons. The bandgap of armchair nanoribbons gradually decreases as the number of carbon atoms increase in the ribbon as shown in figure 2(a). The bandgap of zigzag nanoribbon also tends to decrease gradually for odd and even number of carbon atoms differently in the ribbon as shown in figure 2(b) [9].

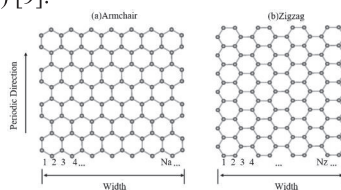


Figure 1. Armchair and zigzag graphene nanoribbons.

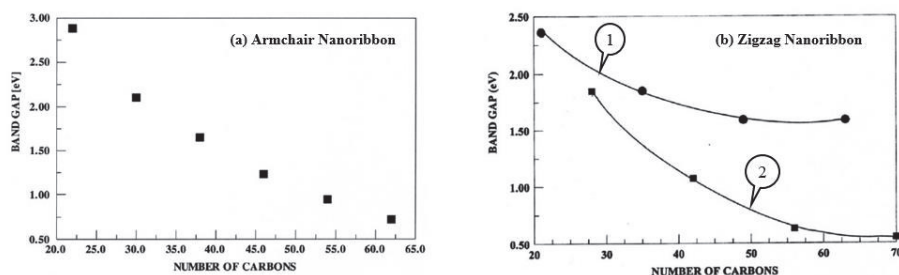


Figure 2. Plots of bandgap energies vs number of carbon atoms for armchair and zigzag graphene nanoribbons where curve 1 is for odd and 2 is for even number of electrons.

Many theoretical studies such as density functional theory (DFT), tight-binding calculations and many-electron Green's function approach have been done for the investigation of the electronic properties of the graphene nanoribbons. Most of the theoretical studies have been done by using DFT calculations method [3]. In order to enhance the sensing capabilities of graphene, usually it is functionalized by a functional group. Mostly hydroxyl (-OH) and carboxylic (-COOH) groups are used as functional groups for the graphene. In addition, many kinds of chemical moieties such as hydroxyl or alkyl groups can be introduced onto graphene surfaces by adding oxidizing agents. Furthermore, amino groups (-NH<sub>2</sub>) and sulfonate (-SO<sub>3</sub>) groups can also be introduced into the graphene. These functional groups act as a chemical handlers to graft different polymers and proteins by creating covalent bonds with them. Hence, in this manner the sensing capabilities of the graphene is increased by covalent bonding [5]. In spite of the stability and the effectivity of covalent strategies, this method is avoided. Because, it unavoidably changes the inherent electronic properties of the graphene by converting sp<sup>2</sup> hybridization of carbon atoms to sp<sup>3</sup> hybridization. So, in order to preserve the intrinsic electronic properties of the graphene; non-covalent modifications to graphene are commonly used [5].

## 2. Methodology

QuantumWise Atomistix (ATK) software package has been used for the simulations of the gas sensor based on pristine armchair graphene nanoribbon. ATK software package has a graphical user interface called virtual nano lab (VNL). VNL has been used to simulate the structure of graphene based nano sensor as shown in figure 3.

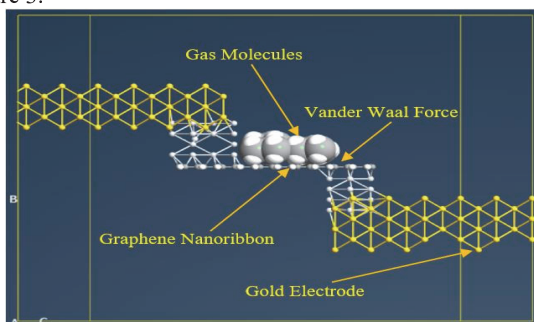


Figure 3. Simulated structure of armchair graphene Nanoribbon based propane and butane gas sensor.

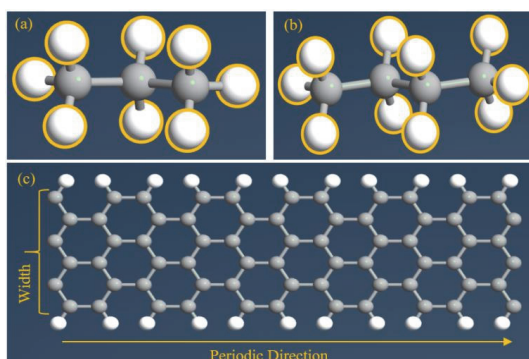


Figure 4. Simulated structure of (a) propane; (b) butane; (c) armchair graphene nanoribbon in ATK.

The Gas molecules are interacting with the armchair graphene nanoribbon by Van der Waal Forces in these simulations. Whereas gold electrodes have been deposited on the nanoribbon for

characterization of the sensor by applying external voltages. In order to reduce computational time in the simulator; four molecules of the propane gas, four molecules of the butane gas, and two-two molecules of both propane and butane gases are detected by the graphene nanoribbons in three individual experiments. The length of armchair graphene nanoribbon in the simulated device along the periodic direction is 21.31 Å and width is 8.05 Å in figure 4(c). The white balls indicate hydrogen atoms and black balls represent carbon atoms in figure 4(a), (b) and (c).

### 2.1. Calculation methodology of the ATK-DFT calculator

ATK software has different types of inbuilt calculators to solve Schrödinger equation. ATK-DFT calculator has been used for the simulations presented in this paper. Mathematical formalism [10] used by the ATK-DFT calculator has been explained in this subsection. ATK is a nano-level device simulator that is used to model open and closed systems within the domain of the density functional theory (DFT). Density matrix is the key parameter for the calculations of the Kohn-Sham equations. This density matrix defines the electron density. A non-equilibrium Green's Function (NEGF) is used to calculate the density matrix for open system. Whereas for closed systems diagonalisation of the Kohn-Sham Hamiltonian equation is used to calculate the density matrix. The effective potential set up by the electron density is given by the Hartree, the external potential and the exchange correlation. Then effective potential is used to get the Kohn-Sham Hamiltonian. Electronic structure of a system can be given by one-electron Kohn-Sham Hamiltonian as follows:

$$H1e = -\frac{\hbar^2}{2m}\nabla^2 + V^{eff}[n](r) \quad (1)$$

In equation (1), the first term indicates the kinetic energy of electron whereas the second term indicates the potential energy of electrons moving in the electrical field created by the external potential. Total electron density can be given by,  $n = n(r)$ . After this one-electron Schrödinger equation is solved to get the eigen-functions of the Kohn-Sham Hamiltonian as:

$$H1e\Psi_\alpha(r) = \varepsilon_\alpha\Psi_\alpha(r) \quad (2)$$

Equation (2) is called a Kohn-Sham equation with the density functional theory (DFT). This is solved by expanding eigen-functions in a set of basis function,  $\Phi_i$ :

$$\Psi_\alpha(r) = \sum_i c_{\alpha i} \Phi_i(r) \quad (3)$$

Now the differential equation can be represented as a matrix equation to determine the expansion coefficients,  $c_{\alpha i}$ :

$$\sum_j H_{ij}c_{\alpha j} = \varepsilon_\alpha \sum_j S_{ij}c_{\alpha j} \quad (4)$$

In equation (4), the Hamiltonian matrix  $H_{ij}$  and the overlap matrix  $S_{ij}$  are given by the multiple integrals with respect to the electron coordinates. Now finally the electron density of many-electron system can be given by the eigenstates of the Kohn-Sham Hamiltonian, thus:

$$n(r) = \sum_\alpha f_\alpha |\Psi_\alpha(r)|^2 \quad (5)$$

In equation (5),  $f_\alpha$  is the occupation of level which has been denoted by  $\alpha$ . Then finally the electron density can be given in terms of the density matrix as follows:

$$n(r) = \sum_{ij} D_{ij}\Phi_i(r)\Phi_j(r) \quad (6)$$

## 3. Results and discussion

This section contains the results and discussion of the simulations of gas sensor. The transmission spectrum and projected density of states of the device at zero bias condition are given and discussed. Furthermore, the graphs for the change in the current through the device in the proximity of the propane and the butane gases are also discussed in this section.

### 3.1. Projected density of the states of the device

The projected density of the states (PDOS) versus energy of the graphene nanoribbon based gas sensor is shown in figure 5. It can be clearly observed from these plots that many energy states are available to be occupied below and above the fermi level. The Projected density of the states are indicating the presence of many energy states around the fermi level. Comparison of the density of the states (DOS) with respect to corresponding energy values of the device reveals a considerable difference in DOS.

Figure 5(a) is the density of the state of the sensor in the absence of any gas while (b) is the DOS in the presence of the propane gas. It can be seen in figure 5(a) that there are three sharp peaks appearing at the energy levels of approximately 1.2 eV, 1.7 eV and 2.4 eV. Whereas in figure 5(b) the presence of propane gas has influenced the DOS of the device. Hence, there is only one sharp peak is appearing at the energy level of 1.2eV in this graph as compared to figure 5(a).

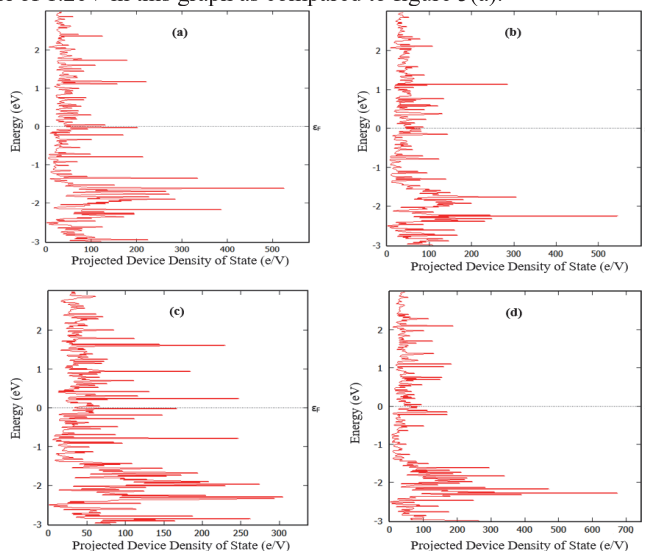


Figure 5. Projected density of the states of the simulated sensor vs. energy where (a) graphene sensor without gas; (b) sensor with propane gas; (c) sensor with the butane; (d) sensor with propane and butane gas.

Comparison of the DOS of the device in the presence of butane gas in figure 5(c) with the sensor in the absence of gas in figure 5(a) reveals that a lots of energy states have been added by the butane gas. Many sharp peaks of the density can be seen above and below the fermi level as compared to figure 5 (a) and (b). Finally the density of the states of the device under the joint influence of the propane and the butane gases are shown in figure 1(d). It can be observed in this graph that the energy states have been modified differently as compared to figure 1(b) and (c). These modifications in the density of the states by these gases have a strong influence on the electrical conduction properties of graphene based gas sensor.

### 3.2. Transmission spectrum of the device

Transmission spectrum of the device is calculated to analyse the contribution of different energy levels in the total transmission of the charge carriers through the device [11]. The plots of the transmission as a function of the energy are shown in figure 6 and 7. It can be seen in figure 6 that for the same energy levels, the value of the transmission is different for the different gases. In the absence of any gas at energy level of  $E = -1.32$  eV, the value of transmission is 0.606 for the sensor as shown in figure 6(a). Whereas for the same energy level, the value of the transmission for the device in the proximity of the propane gas is 0.0046, as shown in figure 6(b).

Similarly in figure 6(c); the value of transmission as a function of the same energy level is 0.00034 in the presence of butane gas. This value of transmission is quite different from the values that are shown in figure 6 (a) and (b). At  $E = -1.32$  eV, in the presence of the propane and the butane gases the transmission value is 0.0486 as shown in figure 6(d). So, it is clear from these results that the presence of different gases alters the value of the transmission of the charge carrier through the device for the same energy levels.

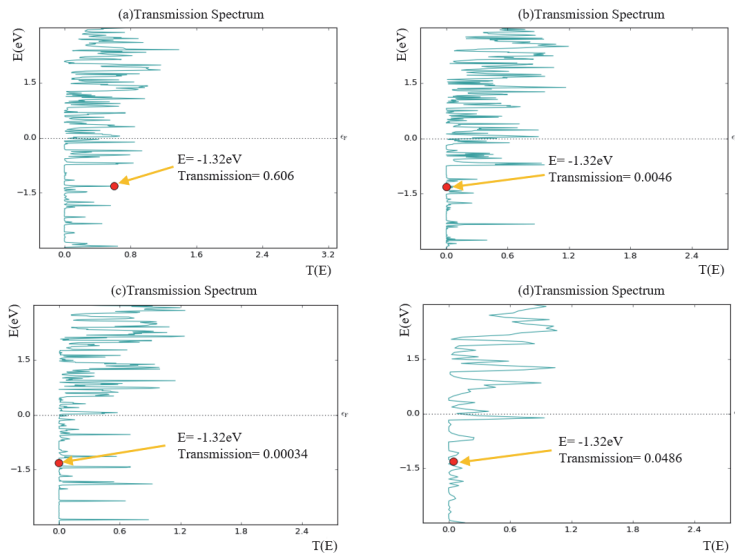


Figure 6. Transmission spectrum as a function of energy of simulated sensor at different energy levels (a) in the absence of gas; (b) with propane gas; (c) with the butane gas; (d) with the propane and butane gas.

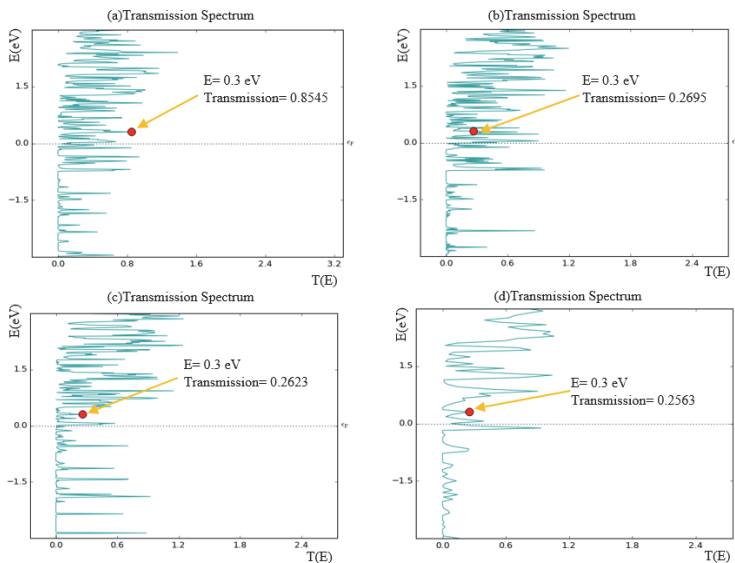


Figure 7. Transmission spectrum as a function of energy of simulated sensor at different energy levels (a) in the absence of gas; (b) with the propane gas; (c) with the butane gas; (d) with propane and butane gas.

Furthermore, the transmission spectrum at different energy levels of the same device in the presence of the same gases is also presented in figure 7. It can be observed in figure 7 (a) that at energy level  $E = 0.3$  eV, the value of transmission is 0.8545 in the absence of any gas. While, for the same energy level for the propane gas the value of transmission is 0.2695 in figure 7(b). For the same energy level, in the presence of the butane gas transmission is 0.2623 as shown in figure 7(c). Whereas

the transmission is 0.2563 at the same energy level in the presence of the butane and the propane gases as shown in figure 7(d).

### 3.3. Current-voltage curves of the device

The electrical conductivity of the majority of the graphene based gas sensors changes in the presence of foreign gas molecules. This change in the conductivity is used as a gas detection mechanism in the graphene based gas sensors [4]. The same principle has been used to develop the propane and the butane gas sensor based on the armchair graphene nanoribbon in our simulations. DC bias voltages are applied at the electrodes of the simulated sensor to obtain the current-voltage (IV) curves. These simulations are done in the absence of any gas, in the presence of the propane gas, in the presence of the butane gas and in the presence of both propane & butane gases to obtain different IV-curves. These IV-curves are shown in figure 8. The Curve 1 in figure 8 is representing the current through the simulated device when there was no gas in the proximity of the sensor. It can be observed that the device is showing almost resistive behaviour in all cases. Curve 1 is revealing that the device starts to conduct immediately even at a very low bias voltage. In the absence of any gas, the IV-curve of the device is almost linear with the high current flowing through the device.

Curve 2 in figure 8 is obtained in the presence of the propane gas molecules. It can be observed in this curve that the presence of the propane gas molecules has reduced the current through the device as compared to curve 1. The adsorbed gas molecules act as donors or acceptors for the graphene and change its conductivity [4]. Graphene shows ultrahigh sensitivity in the presence of the foreign gases because the pristine graphene is inherently a low noise material. The presence of gases near the graphene introduce electrical noise and disturbs its electronic cloud. As the conductivity of the charge carriers through the device depends on the number of charge carriers and their mobility. So, the presence of the propane gas may have changed the number of the charge carriers or their mobility in the graphene nanoribbon. Due to which Curve 2 is showing a decrease in current through the device. The change in charge carriers concentration, changes the current through the device and acts as a governing mechanism for the conductivity of the device [4, 5].

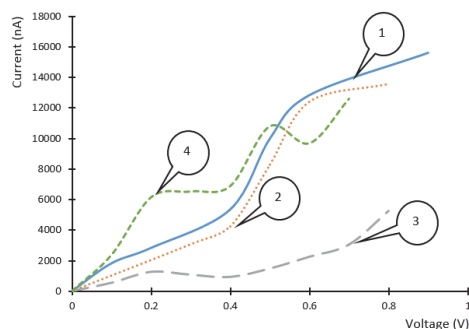


Figure 8. Current-voltage curves of simulated armchair graphene Nanoribbon based gas sensor where curve (1) in the absence of gas; (2) with propane gas; (3) with butane gas; (4) with propane and butane gas.

Furthermore, in the presence of the butane gas a significant reduction in the current through the sensor is observed as shown in Curve 3 in figure 8. The possible reason of this reduction in the current can be the decrease in the number of the majority charge carriers and their scattering by the butane gas molecules [8]. An interesting behaviour of IV-curve is observed in Curve 4 in figure 8 when the both propane & butane gases were in the proximity of the device. It can be observed from this curve that the current through the device has increased significantly. In addition to the electric current, the nonlinearities in this IV-curve 4 are also increased. The reason of this increase in the electric current up to a certain voltage level and then decrease could be due to the joint influence of the scattering process provoked by these both gases.

#### 4. Conclusion

The objective of the current work is to simulate the graphene nanoribbon based sensor for the leakage detection of household gases and estimate device behaviour before physical fabrication. The nanoscale simulations of the gas sensor are done successfully with the QuantumWise Atomistix software. The results of these simulations revealed that the graphene is highly sensitive to the change in its surrounding environment. The presence of the gases in the proximity of the graphene device strongly influenced its density of the states, the transmission spectrum and the electric current, when propane and butane gases were in its proximity. The reasons of this change in the conductivity are an increase or decrease in the charge carriers and/or their mobility caused by the adsorbed gas molecules on the surface of graphene. A decrease in the current through the sensor is observed when propane and butane gases are interacting with it individually. But when both gases are interacting simultaneously with the graphene, an increase in the current and the nonlinearities are observed. This change in the conductivity through the device can be used as a gas detection signal for sensor applications. Although the graphene is a potential candidate for sensor applications in future electronics, but there are still a large number of technical challenges that need to be addressed. These challenges are the selectivity of graphene to detect the specific gases, reliability and the cost of the device. Further investigations are required to improve the performance of our simulated graphene based gas sensor. For this purpose, more than one detection mechanisms can be used simultaneously (i.e. change in optical and electrical properties) to avoid errors in the sensor readings due to the contamination of undesired particles and the effect of the temperature in the sensing environment.

#### References

- [1] Zhang Y *et al.* Direct observation of a widely tunable bandgap in bilayer graphene 2009 *Nature* **459** 820-23
- [2] Wang J Deng S and Liu Z The rare two-dimensional materials with Dirac cones 2015 *Natl. Sci. Rev.* **2** 22-39
- [3] Khan E Li Z and Yang J *Physics and Applications of Graphene – Theory* (InTech) pp 332-348
- [4] Yavari F Koratkar N Graphene based chemical sensors 2012 *J. Phys. Chem. Lett.* **3** 1746-53
- [5] Liu Y Dong X and Chen P Biological and chemical sensors based on graphene materials 2012 *Chem. Soc. Rev.* **41** 2283-2307
- [6] Kuila T Bose S Khanra P Mishra A K Kim N H and Lee J H Recent advances in graphene-based biosensors 2011 *Biosens. Bioelectron.* **26** 4637-48
- [7] Keshtkar S Rashidi A Kooti M Development of tin dioxide quantum dots/multi-walled carbon Nanotubes and tin dioxide quantum dots/carbon nanohorns nanohybrids as low temperatures Natural gas sensors 2017 *Cera. Intl* **43** 14326-1433
- [8] Erol O Uyan I Hatip M Yilmaz C Tekinay AB and Guler O Recent advances in bioactive 1D and 2D carbon nanomaterials for biomedical applications 2016 *Nanomed.* 1-22
- [9] Owens F J Electronic and magnetic properties of armchair and zigzag graphene nanoribbons 2008 *J. Chem. Phys.* **126**
- [10] QuantumWise User Manual: ATK-DFT Calculator. Internet: <https://docs.quantumwise.com/manuals/ATKDFT.html> [Nov. 20, 2017]
- [11] QuantumWise User Manual: ATK Transport Calculations. Internet: [https://docs.quantumwise.com/tutorials/atk\\_transport\\_calculations/atk\\_transport\\_calculations.html](https://docs.quantumwise.com/tutorials/atk_transport_calculations/atk_transport_calculations.html) [Nov. 24, 2017]

#### Acknowledgments

This research was supported by the Estonian Research Council through the Institutional Research Project IUT19-11, by the Estonian Research Council through the Institutional Research Project PUT1435, and by the Horizon 2020 ERA-chair Grant “Cognitive Electronics COEL” —H2020-WIDESPREAD-2014-2 (Agreement number: 668995; project TTU code VFP15051).



## Appendix I

H. Rashid, A. Koel and T. Rang

“Simulations of Graphene Nanoribbon Field Effect Transistor for the Detection of Propane and Butane Gases: A First Principles Study,” *Nanomaterials*, vol. 10, no. 98, 2020. **(ETIS 1.1)**





Article

# Simulations of Graphene Nanoribbon Field Effect Transistor for the Detection of Propane and Butane Gases: A First Principles Study

Muhammad Haroon Rashid <sup>\*</sup>, Ants Koel and Toomas Rang

Thomas Johan Seebeck Department of Electronics, Tallinn University of Technology, Ehitajate tee 5, 12616 Tallinn, Estonia; ants.koel@ttu.ee (A.K.); toomas.rang@ttu.ee (T.R.)

\* Correspondence: murash@ttu.ee; Tel.: +372-5391-2599

Received: 7 December 2019; Accepted: 30 December 2019; Published: 3 January 2020



**Abstract:** During the last few years graphene has emerged as a potential candidate for electronics and optoelectronics applications due to its several salient features. Graphene is a smart material that responds to any physical change in its surrounding environment. Graphene has a very low intrinsic electronic noise and it can detect even a single gas molecule in its proximity. This property of graphene makes it a suitable and promising candidate to detect a large variety of organic/inorganic chemicals and gases. Typical solid state gas sensors usually require high operating temperature and they cannot detect very low concentrations of gases efficiently due to intrinsic noise caused by thermal motion of charge carriers at high temperatures. They also have low resolution and stability issues of their constituent materials (such as electrolytes, electrodes, and sensing material itself) in harsh environments. It accelerates the need for development of robust, highly sensitive and efficient gas sensors with low operating temperature. Graphene and its derivatives could be a prospective replacement of these solid-state sensors due to their better electronic attributes for moderate temperature applications. The presence of extremely low intrinsic noise in graphene makes it highly suitable to detect a very low concentration of organic/inorganic compounds (even a single molecule can be detected with graphene). In this article, we simulated a novel graphene nanoribbon based field effect transistor (FET) and used it to detect propane and butane gases. These are flammable household/industrial gases that must be detected to avoid serious accidents. The effects of atmospheric oxygen and humidity have also been studied by mixing oxygen and water molecules with desired target gases (propane and butane). The change in source-to-drain current of FET in the proximity of the target gases has been used as a detection signal. Our simulated FET device showed a noticeable change in density of states and IV-characteristics in the presence of target gas molecules. Nanoscale simulations of FET based gas sensors have been done in Quantumwise Atomistix Toolkit (ATK). ATK is a commercially available nanoscale semiconductor device simulator that is used to model a large variety of nanoscale devices. Our proposed device can be converted into a physical device to get a low cost and small sized integrated gas sensor.

**Keywords:** field effect transistor; graphene nanoribbon; propane; butane; gas sensor; detector; oxygen; humidity; water; nitrogen; carbon dioxide

## 1. Introduction

Gas sensing has been a critical subject for a wide range of applications such as medical, industrial environment, military and aerospace applications. The presence of hazardous and toxic gases may lead to some serious accidents in industrial as well as household environments. There must be some tool to detect the presence of these gases effectively [1,2]. The ultimate goal of gas detection is to obtain high

level of sensitivity with high resolution. The presence of very low concentration of desired gases should be detected. However, such high resolution of gas sensor has not been achieved even with solid-state gas sensors [3–5]. The main reason of low resolution of these sensors are defects and abrupt fluctuations due to the thermal motion of charge carriers [6], which lead to the creation of noise in these device. Due to this noise, the detection of individual molecules becomes very difficult. Solid-state gas sensors can be categorized into different groups depending on the base of their working principle. The most common categories of such sensors are resistive type sensors, semiconductor gas sensors, impedance type gas sensors (based on alternating current measurements) and electrolyte based gas sensors. The resistive type solid-state gas sensors are the most commonly used gas sensors because their working principle is simple and they have low fabrication cost. The resistance of the constituent semiconductor material changes due to its interaction with target gas. The reason of change in electrical resistance is the transfer of charge carriers between target gas and semiconductor material [7]. In impedance based gas sensors, the frequency response of the device changes in response to the target gas molecules [8]. Whereas, in solid-state electrolyte based gas sensors, the ionic conductivity of the electrolyte changes due to the transportation of holes or electrons from the desired target gas molecules. This change in ionic conductivity is used as a detection signal. Amperometric and potentiometric gas sensors are included in this category [9]. Solid-state gas sensors are very crucial to monitor and control the emission of toxic and hazardous gases. However, they also have some limitations in terms of selectivity, long term stability, sensitivity and reproducibility. The long term stability of electrodes, sensing materials, electrolyte and substrates of solid-state sensors are open challenges. It is also a big challenge to obtain a reliable and accurate reading at high temperatures with such sensors. Due to these reasons, the analysis of desired gases at lower temperature is being done in industries to avoid the issues of inaccuracy and durability of the devices [10].

Although, with an increase in the demand of gas sensors, still there is a need to develop robust, highly sensitive and reversible sensors that work at low temperatures. Gas sensors based on conventional semiconductor materials usually require high operating temperatures. In order to cope with these issues, several efforts are being made to modify the shape and orientations of such materials [11]. Nanomaterials are the promising candidates for the development of gas sensors with low operating temperature and low power consumption. It has been considered that nanomaterials can be used efficiently to detect a large variety of organic/inorganic molecules. The main parameter that dictates the sensitivity of a gas sensing material is its surface-to-volume ratio, which is quite high for nanostructures. This high surface-to-volume ratio allows nanomaterials to adsorb the detectable target molecules effectively and make them suitable candidates to develop efficient gas sensors [12]. In order to overcome the issues found in conventional solid-state gas sensors, graphene has emerged as an exciting and promising candidate to detect a wide range of organic and inorganic materials including gases more efficiently. Extraordinary electronic attributes of graphene and its derivatives make them a promising candidate to replace solid-state gas sensors [13–15].

Graphene based gas and inorganic/organic molecule detectors detect the presence of these molecules with different mechanisms. The most popular detection mechanisms are the resistive method, field effect transistors (FET) method and micro-electromechanical system (MEMS) based method. In the resistive method, the change in electrical conductivity in the presence of target molecules is used as a detection signal [16]. In FET based gas detectors, the change in drain-to-source current at some gate voltage is used as a signature to detect the presence of foreign adsorbed particles [17,18]. MEMS based gas sensors have low power consumption, small size, fast response and high sensitivity [19]. In MEMS based sensors, electrical and mechanical components are integrated in the form of a chip. The mechanical component of this sensor converts any physical change in the surrounding into electrical signal [20].

Graphene based field effect transistor (FET) can be a potential candidate to detect the presence of a wide range of chemicals, toxic compounds, biomolecules and gases with better sensitivity compared to that of solid-state sensors. The sensitivity range of these graphene based FETs usually range from

parts per billion (ppb) to parts per million (ppm) [21–23]. Typically, the gate electrode controls the flow of electric current through FET based gas sensors. Actually, the adsorption of foreign gas molecules and organic compounds effect the concentration of the charge carriers through the graphene layer and consequently the current through the device changes at some gate voltage. Some gas molecules act as donors of charge carriers for graphene and increase the electric current through the device after adsorption. Whereas, some foreign gas molecules act as acceptor for the graphene layer and they reduce the current through the device. This change in electric current is used as a detection signal for gases and other organic/inorganic compounds [24,25]. Even the fluctuation of the conductance can be used as a detection signal [26].

Moreover, propane and butane are the most commonly used fuel for household/industrial environments [27]. These are flammable and toxic gases [28]. In order to avoid fatal explosion accidents, the leakage of these gases in the environment must be detected. Different material processing techniques are used to obtain graphene-based materials like carbon nano-sheets, carbon nanoribbons, and carbon nanotubes with exceptional electronic attributes. Recently, graphene nanoribbons (GNRs) have attracted the interest of researchers due to their distinct electronic properties. GNRs are promising candidate as building blocks of next generation electronics devices [29]. Carbon nanotubes (CNTs) are unzipped with different techniques to get GNRs [30]. Graphene nanoribbon based FETs have very interesting electrical properties that change with the width and direction of the constituent nanoribbons [29,31]. First principles simulations of graphene based FETs to study the doping effects on the IV-characteristics have been reported in the literature [29,32]. Graphene based FET devices and sensors have also been reported in the literature [33–35].

In this article, we simulated a novel FET device based on graphene nanoribbons with nanoscale semiconductor device simulator, Quantumwise Atomistix Toolkit (ATK). This simulated device has been used to detect the presence of propane and butane gases. The change in electric current through FET device at different gate voltages in the presence of these gases has been used as a detection mechanism. To the best of our knowledge, this type of device has not been reported in the literature for the detection of propane and butane gases.

## 2. Materials and Methods

The simulations of GNR based FET for the detection of propane and butane gases have been carried out with Quantumwise Atomistix Toolkit (ATK) software package. Graphical user interface of ATK is called Virtual Nano Lab (VNL). ATK-VNL allows atomic scale modeling of nano-systems. This software uses several in-built calculators to solve and calculate transportation properties of quantum systems. Density functional theory (DFT) calculator has been used for the simulations of our proposed device in ATK-VNL. The work flow and mathematical formalism used by ATK-DFT has been given in [36]. All these simulations have been run in a high performance computing environment (HPC) [37]. This HPC has 232 high power computing machines. Each machine has 24 processing units and 48 GB of internal memory. Density of states (DOS) and IV-curves of simulated device in the presence of propane and butane gases have been calculated using eight computing nodes of HPC. With eight computing nodes of HPC, each IV-curve took around more than one week to calculate. A brief description of used materials have been given in the next subsection below.

### *Graphene Armchair and Zigzag Nanoribbons*

The constituent materials of simulated graphene field effect transistor are armchair graphene nanoribbons (AGNR) and zigzag graphene nanoribbons (ZGNR). The termination pattern of the edge of these structures defines the type of nanoribbon either armchair edge or zigzag edge, as shown in Figure 1 [38]. The structure shown in Figure 1a is zigzag nanoribbon because the termination edge forms a zigzag pattern. Whereas, the structure shown in Figure 1b is armchair nanoribbon because the termination edge forms an armchair pattern. The bandgap of armchair and zigzag nanoribbons change with an increase or decrease in number of carbon atoms in the ribbons [39]. The bandgap of

AGNR decreases with an increase in number of carbon atoms in its structure. The bandgap of AGNRs decreases from 3 to 0.75 eV with an increase in number of carbon atoms from 20 to 65 in its ribbon. Whereas, change in bandgap for ZGNR with an increase in number of carbon atoms is different for even and odd number of electrons in its structure. For both cases the bandgap decreases gradually with an increase in number of atoms [39]. GNRs provides perfect interfaces to make junctions at atomic levels. Generally, due to small contact areas, it is very difficult to avoid high contact resistance between metal electrodes and molecular devices. So, this problem could be solved by using metallic GNRs which can be directly connected to the circuits [29].

Furthermore, the two probe model of GNR based FET has been simulated by using AGNR and ZGNR in ATK-VNL. The builder tool of ATK-VNL is used to simulate FET. All the details have been given in next lines. First of all, the central region of the device have been simulated. The central region of FET consists of AGNR. AGNR with width of four atoms has been created using Nanoribbon Plugin Tool of ATK Software. Afterwards, this GNR has been extended 5 times along C-axis (the repetition pattern) as shown in Figure 2. Whereas A, B and C vectors have been shown in each figure. In the next step, ZGNR has been created with the same plug in tool. However, this time zigzag nanoribbon consists of six atoms, as shown in Figure 3. After creating this ZGNR, its structure has been repeated along C-axis four times and then a copy of this structure has been made. These two structures will be used to form electrodes of FET by connecting them to the central region of the device.

After that, the next step is to join the central region (Figure 2) with the electrodes (Figure 3) to form a z-shaped structure. For this purpose, armchair graphene nanoribbon has been rotated by 30 degrees along X-axis (the axis have been shown in the upright position of Figures 2 and 3, as shown in Figure 4a). Now, AGNR is ready to be joined with ZGNR (electrodes). The next step is to merge ZGNR with AGNR to form a z-shaped structure, as shown in Figure 4b. After merging these cells, we get a z-shaped structure in which AGNR is in the center (central region) whereas ZGNRs are on the left and right side of this structures. These ZGNRs form the source and drain electrodes of FET, as shown in Figure 4c. In the next step, dielectric material and gate electrode have been deposited on this structure to get FET device, as shown in Figure 4d. The permittivity of the dielectric material has been chosen as  $4\epsilon_0$  and a very thin metallic layer has been deposited on it to form a gate electrode of field effect transistor. The lengths of source and drain electrodes are approximately 7 Å. In next step, three molecules of propane, three molecules of butane and both propane & butane (four molecules of butane and one molecule of propane) have been exposed to the FET device in three different experiments, as shown in Figure 4e. In order to add the influence of atmospheric gases and humidity, oxygen and water molecules have been mixed with the desired target gases (propane and butane). Two oxygen molecules and two water molecules have been exposed to the device, as shown in Figure 4f. In the simulated device, these molecules have also been mixed with propane and butane target gases in two different experiments.

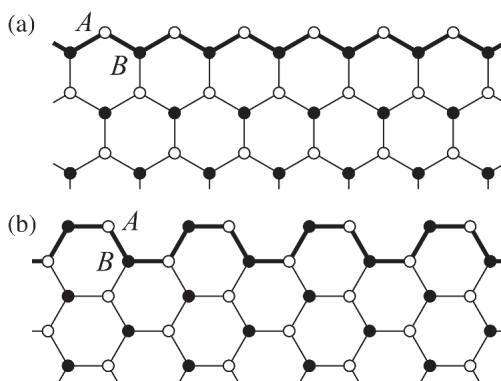


**Figure 1.** Schematic of (a) zigzag graphene nanoribbon; (b) armchair graphene nanoribbon reproduced from [38] with permission from SPIE publishers, 2012.

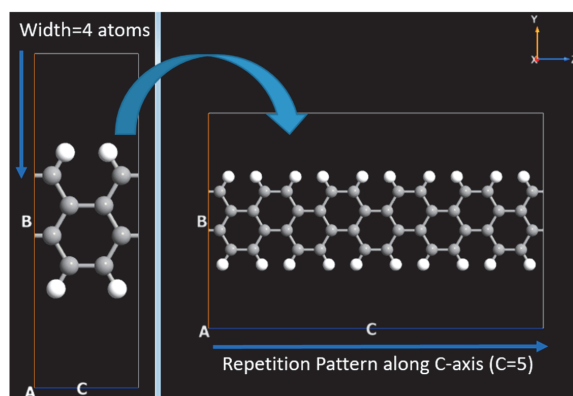


Figure 2. Simulation of armchair graphene nanoribbon for the central region of Field Effect Transistor.

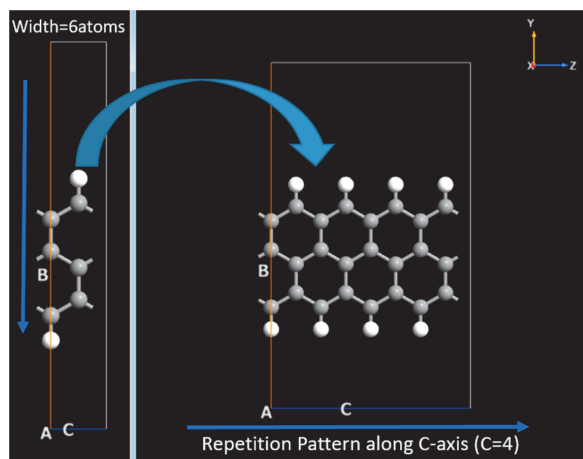
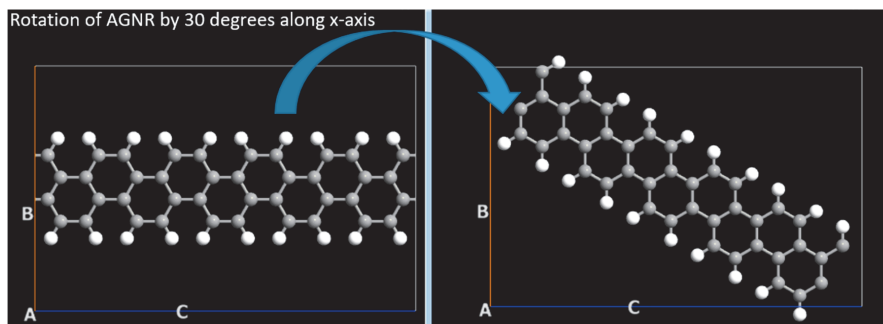


Figure 3. Simulation of zigzag graphene nanoribbons for electrodes of Field Effect Transistor.



(a)

Figure 4. Cont.

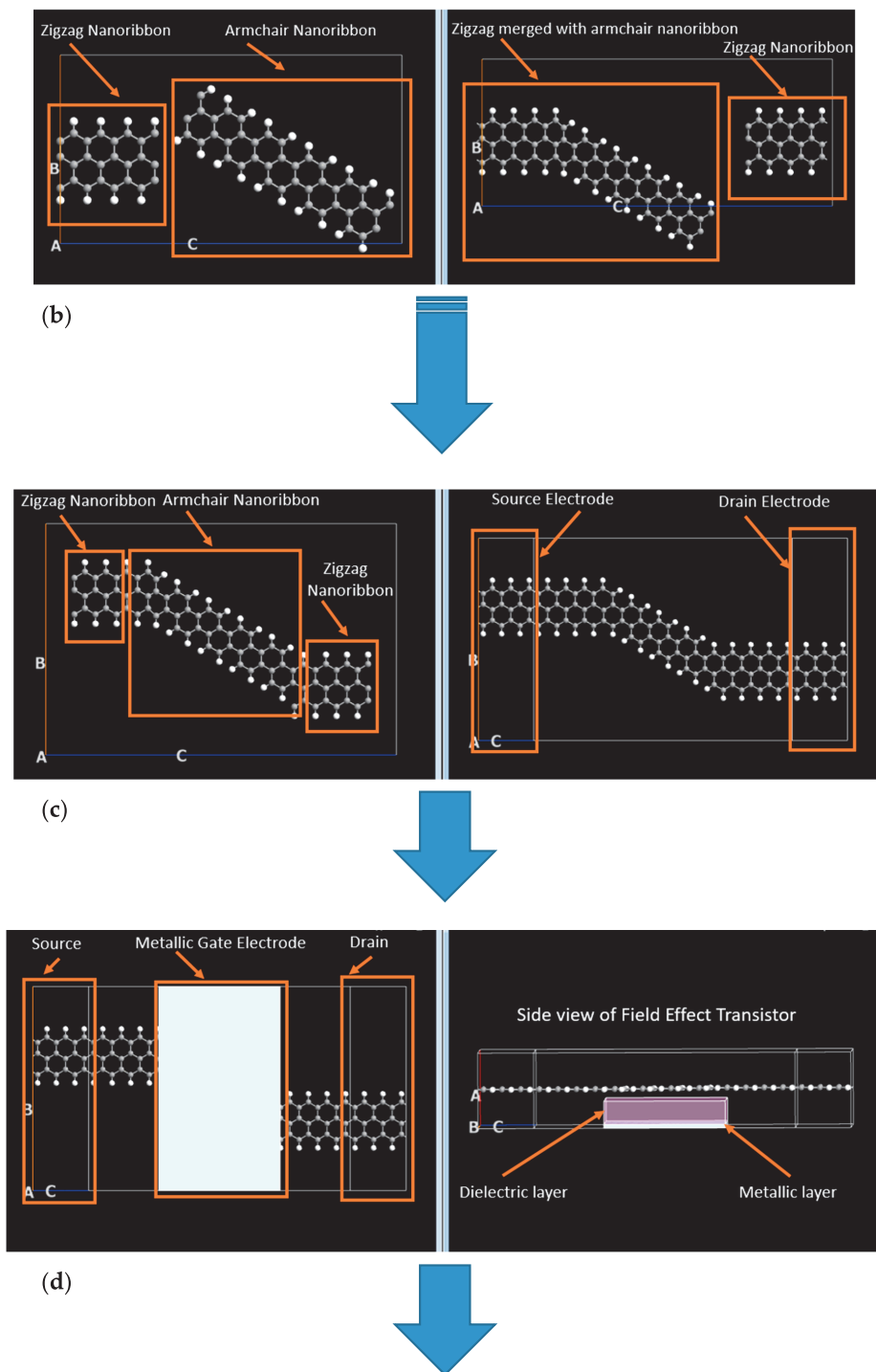
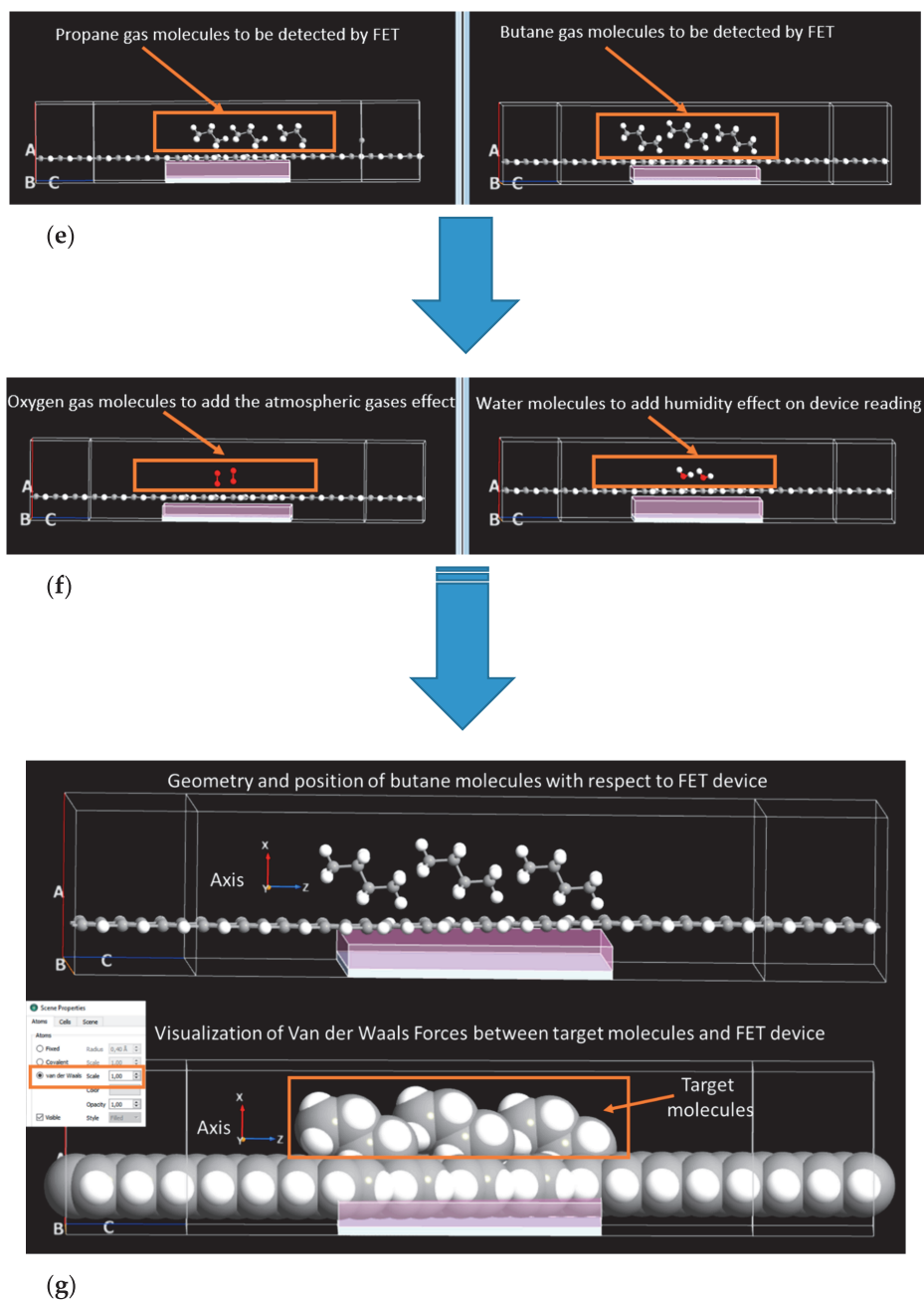


Figure 4. Cont.



**Figure 4.** Simulation steps for graphene zigzag and armchair nanoribbon based field effect transistor for the detection of propane and butane gases under the influence of atmospheric oxygen and humidity.

Furthermore, an in-built Merger Tool of ATK-VNL has been used to expose the target molecules (i.e., propane, butane, oxygen, water molecules) to the simulated FET device (Figure 4d). ATK-VNL has an inbuilt Move Tool that is used to move (in  $X$ ,  $Y$ ,  $Z$  coordinates) the target molecules with respect to

the simulated FET device. The position and geometry of each butane molecule along with X, Y, Z axis have been shown as an example in Figure 4g. It can be seen in this figure that the geometry of all butane molecules are almost identical to each other with respect to the FET device. Similar atoms (oxygen atoms in case of butane molecules) of all target molecules are facing to the FET device. The same procedure has been adopted for exposing other target molecules to the simulated FET device. All target molecules have been kept at an optimal distance of few Angstroms to the FET device, ensuring that Van der Waals Forces are acting between target molecules and FET device. Graphical user interface of ATK-VNL software has been used to confirm that Van der Waals Forces are acting between target molecules and FET device, as shown in Figure 4g. A more comprehensive detail about simulating graphene nanoribbon based FET in ATK-VNL can be found at this reference [40]. The reason of choosing this small number of gas molecules in these simulations is to reduce the computation time in HPC environment. The change in density of states (DOS) and IV-characteristics of FET have been calculated in the presence of propane and butane as target molecules.

### 3. Results and Discussion

In this section, the results obtained from simulations have been presented and discussed in detail. The DOS and IV-characteristics of simulated FET based sensor have been calculated.

#### 3.1. Density of States of Simulated Graphene Nanoribbon Field Effect Transistor Device

A significant and distinct change in the DOS of FET device have been observed in the presence of different target gas molecules. A comparison of DOS of simulated FET device in the absence of any target gas molecules and in the presence of three propane gas molecules has been shown in Figure 5a. It can be observed that many new energy states have been introduced by propane gas molecules both above and below the fermi level of the device compared to that of the reference simulated device (without any target gas), as shown in Figure 5a. Many new energy spikes can be observed at energy levels of  $-1.8$ ,  $-1.2$ ,  $-0.8$ ,  $1.0$  and  $1.3$  eV in FET device in the presence of propane gas.

Furthermore, the presence of three butane gas molecules affected DOS of FET differently compared to that of propane gas molecules, as shown in Figure 5b. Many new energy states can be observed at energy levels of  $-1.9$ ,  $-1.4$ ,  $0.9$ ,  $1.6$  and  $1.8$  eV, approximately. These energy states were not present in the presence of propane molecules. Similarly, a distinct change in DOS can be observed in the device when it is exposed to both propane and butane gas molecules simultaneously, as shown in Figure 5c. It can be observed that the presence of both gases introduced new energy states in FET device. New energy spikes can be observed at energy levels of  $-1.1$ ,  $-0.6$ ,  $0.6$ ,  $1.3$ ,  $1.6$ ,  $1.8$  and  $1.9$  eV approximately, as shown in Figure 5c.

#### 3.2. Current-Voltage Characteristics of Simulated Graphene Nanoribbon Field Effect Transistor Device in Presence of Only Propane and Butane Molecules

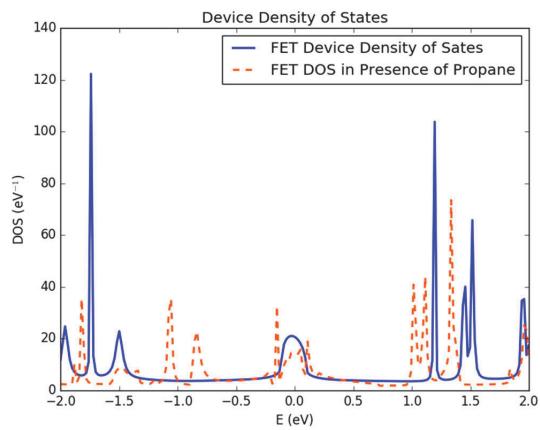
Drain to source current ( $I_{ds}$ ) and voltage ( $V_{ds}$ ) curves of simulated FET have been calculated for different applied gate voltages. The simulated device (in absence of any target gas molecules) showed depletion mode MOSFET like behavior. A decrease in  $I_{ds}$  versus  $V_{ds}$  has been observed with an increase in negative gate to source voltage ( $V_{gs}$ ), as shown in Figure 6. The same IV-curves for the gate voltages of  $-0.1$ ,  $-0.3$  and  $-0.5$  V have been calculated in the presence of three propane molecules, three butane molecules and both gases (four molecules of butane and one molecule of propane) in three different experiments. In the presence of target gas molecules, a significant change in IV-curves of FET device has been observed for the same voltage biased conditions compared to that of the device in the absence of target gas molecules. This change in IV-characteristics can be used as a detection signal to detect the presence of propane and butane gases.

In our previously published work [31], we used purely resistive method based on pristine AGNR to detect propane and butane gases. However, in this article, we used FET based device in which the electric current not merely depends on applied bias voltage ( $V_{ds}$ ), but also on gate voltage. The adsorbed

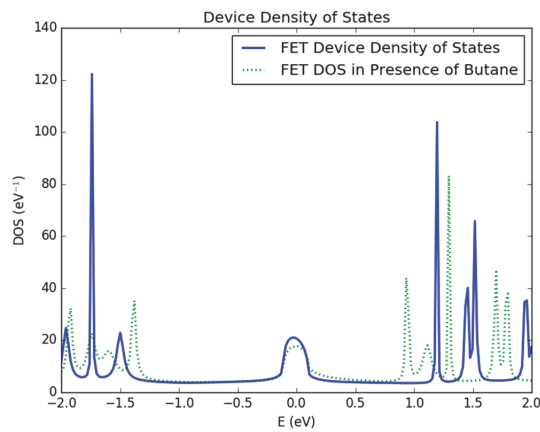
target gas molecules act as donors or acceptors of charge carriers for the graphene. If they act as donors, they change (increase) the concentration of charge carriers in graphene. Consequently, the electric current through the graphene based device increases in the presence of adsorbed target molecules under same bias condition. When the foreign target molecules behave like acceptors of charge carriers, they decrease the current through the graphene based device [41]. In resistive methods of graphene based gas detectors, it is comparatively easy to realize this change in conductivity of graphene. Because in such type of devices, graphene behaves like a resistive strip which is only a function of external applied voltage. Nevertheless, in FET based graphene sensors, the change in charge carriers through the graphene channel is also a function of gate voltage and hence could be more accurate. So one has to keep in mind the effect of gate voltage as well as  $V_{ds}$  on the IV-characteristics of FET based sensor.

Furthermore, our simulated device exhibited a considerable change in IV-characteristics in the presence of the target gases. The reference FET device showed a current range between  $-24$  nA to  $-66$  nA at  $V_{gate} = -0.1$  V and at a fixed  $V_{ds}$ , shown with a solid black line in Figure 7. A decrease in  $I_{ds}$  has been observed in the presence of propane as a target gas, at  $V_{gate} = -0.1$  V, as shown with orange dotted line in Figure 7. The current range of FET based device in the presence of propane target is between  $-22$  nA to  $-44$  nA, which is less than that of reference device. It seems that propane molecules may have acted like acceptors of charge carriers for graphene and reduced the charge carrier concentration in the device. Consequently, a decrease in current has been observed in the presence of propane molecules. The device showed a sufficient increase in  $I_{ds}$  in presence of butane gas molecules compared to that of reference device. The range of the  $I_{ds}$  is between  $-26$  nA to  $-134$  nA approximately in the presence of butane gas, shown with blue color dashed line in Figure 7. It seems that butane molecules may have acted like donors of charge carriers for graphene and increased the charge carrier concentration in the device. Consequently, an increase in current has been observed in the presence of butane molecules. A dramatic increase in  $I_{ds}$  has been observed when FET device is exposed to four butane and one propane gas molecules simultaneously. The range of  $I_{ds}$  in this case is between  $-93$  nA to  $-167$  nA at  $V_{gate} = -0.1$  V, which is quite high compared to that of the reference device. This high amount of current through the device may be due to the donor like dominated effect of four butane molecules compared to that of one propane molecule (acceptor like behavior), which are exposed to the device simultaneously. This curve has been shown with a dotted-dashed green colored line in Figure 7.

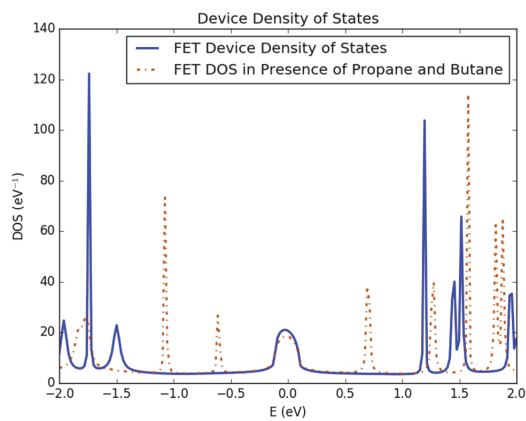
However, an increase in negative bias gate voltage reduced the overall  $I_{ds}$  through reference FET, as it is a depletion mode n-channel FET. A similar trend of increase and decrease in  $I_{ds}$  at  $V_{gate} = -0.3$  V for the same  $V_{ds}$  has been observed with respect to the reference FET device, as shown in Figure 8. In presence of propane gas molecules a decrease in  $I_{ds}$  at this  $V_{gate}$  has been observed compared to that of reference FET. The range of  $I_{ds}$  in this case is between  $-20$  nA to  $-57$  nA, approximately. Whereas butane gas increased the  $I_{ds}$  compared to that of reference FET and the range of current is between  $-18$  nA to  $-106$  nA. The simultaneous presence of both gases increased the  $I_{ds}$  in similar manner that is observed in previous cases. The range of electric current under this bias condition is between  $-187$  nA to  $-220$  nA, which is quite high compared to that of the device at  $V_{gate} = -0.1$  V, as shown in Figure 8. Finally, the IV-characteristics of the device have been calculated at  $V_{gate} = -0.5$  V, as shown in Figure 9. It also exhibited a similar trend but with different current ranges compared to that of the previously discussed cases.



(a)



(b)



(c)

**Figure 5.** Change in density of states (DOS) of simulated filed effect transistor in presence of (a) propane gas molecules; (b) butane gas molecules; (c) both propane and butane gas molecules.

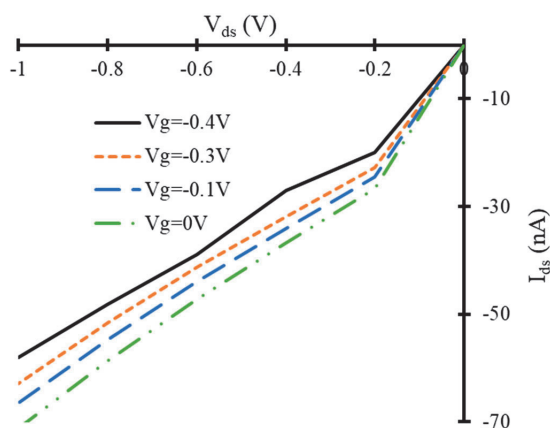


**Figure 6.**  $V_{ds}$  versus  $I_{ds}$  curves of simulated field effect transistor at different gate voltages in the absence of target gas molecules.

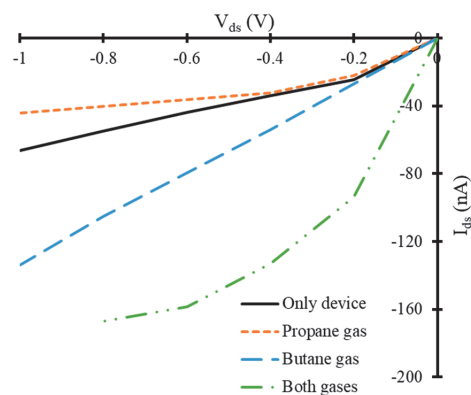


**Figure 7.**  $V_{ds}$  versus  $I_{ds}$  curves of simulated field effect transistor at  $-0.1$  V gate voltage in the presence of target gas molecules.

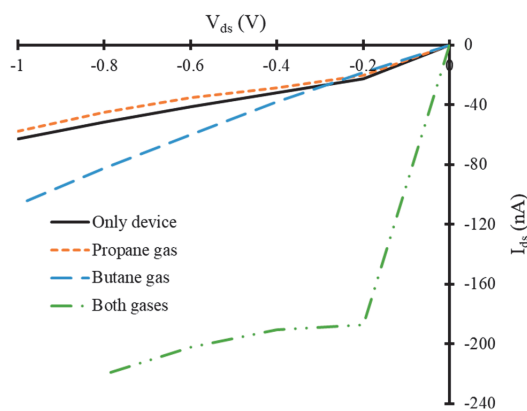


**Figure 8.**  $V_{ds}$  versus  $I_{ds}$  curves of simulated field effect transistor at  $-0.3$  V gate voltage in the presence of target gas molecules.

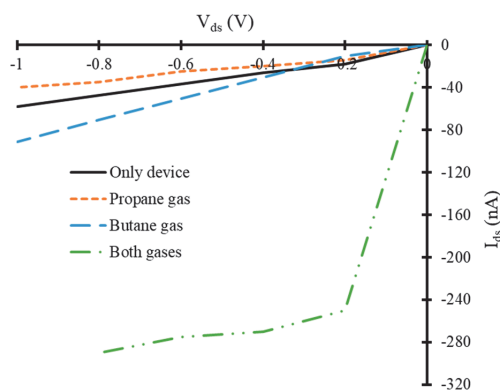


**Figure 9.**  $V_{ds}$  versus  $I_{ds}$  curves of simulated field effect transistor at  $-0.5$  V gate voltage in the presence of target gas molecules.

### 3.3. Influence of Oxygen and Water Molecules on the Current-voltage Characteristics of Simulated Graphene Nanoribbon Field Effect Transistor

In Section 3.2, the simulated graphene based FET device is exposed to only propane and butane molecules in a controlled environment, where the influence of the atmospheric species like oxygen, carbon dioxide, water vapors and humidity have been neglected. The purpose of the work presented in this article is to access the feasibility of the simulated device for the detection of propane and butane gases. But for real-time application of such device, the influence of other atmospheric parameters cannot be ignored. Therefore, we also studied the effect of oxygen and water molecules on IV-characteristics of simulated structure. For this purpose, additional simulations have been done. In two different experiments, the simulated FET has been exposed to only two oxygen molecules and only two water molecules. In third and fourth experiment, three propane molecules have been detected in the presence of two water molecules and two oxygen molecules individually. In fifth and sixth experiment, three butane molecules have been detected in the presence of two water molecules and two oxygen molecules individually. The IV-curves of simulated device at  $V_{gate} = -0.1$  and fixed  $V_{ds}$  have been calculated. A slight decrease in  $I_{ds}$  of the simulated FET has been observed in the presence of two oxygen molecules, as shown in Figure 10a. At exposure to two water molecules, the FET device also exhibited a decrease in source-drain current, as shown in Figure 10a. In case of exposure to two water molecules, the decrease in current of device is more compared to that of the oxygen molecules. Similarly, a decrease in  $I_{ds}$  has been observed, when water and oxygen molecules are mixed with propane gas molecules, as shown in Figure 10b. At the exposure of the device to butane molecules mixed with water molecules simultaneously, the device showed a decrease in  $I_{ds}$ , as shown in Figure 10c. Whereas, a similar effect on  $I_{ds}$  has been observed in the presence of mixture of butane and oxygen molecules, as shown in Figure 10c.

The presence of both oxygen and water molecules degraded the device performance in terms of reduction of detectable current for propane and butane gases. A careful calibration of such physical sensor is required to nullify the environmental effects on the actual reading of the device in the presence of desired target molecules. The presence of oxygen content in the atmosphere has a strong influence on the electrical properties of graphene. The oxygen content of the air strongly affects the electrical resistance of graphene which depends on the exposure time. The electrical conductance of graphene reduces with passage of time at its exposure to the oxygen content of the air. Therefore, the change in device performance may be expected as exposure time increases [42]. Similarly, the presence of water content in the air also has an effect on the electrical properties of the graphene as water molecules act as p-type dopant for graphene and change its electronic properties. Therefore, the device should be encapsulated for stable operation [43–45].

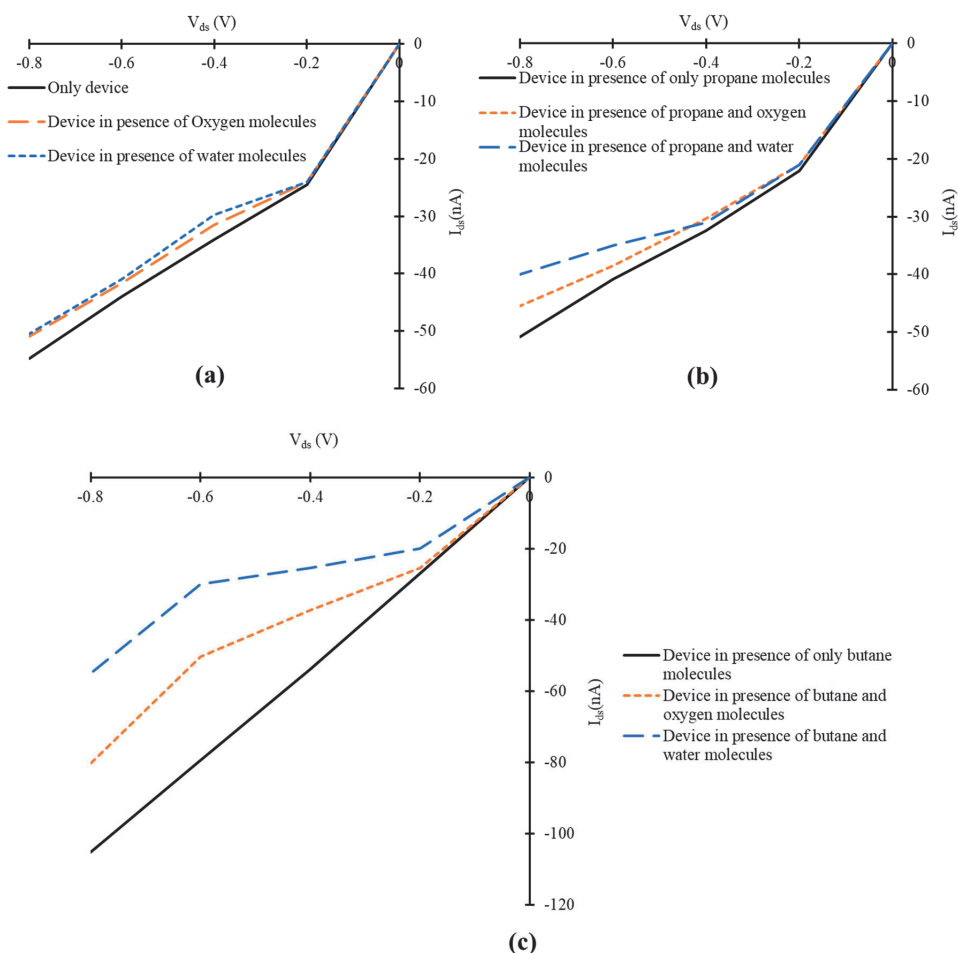


**Figure 10.**  $V_{ds}$  versus  $I_{ds}$  curves of simulated field effect transistor at  $-0.1$  V gate voltage in the presence of (a) only water and oxygen molecules; (b) propane, water and oxygen molecules; (c) butane, water and oxygen molecules.

Moreover, in ambient atmospheric conditions, the effect of nitrogen ( $N_2$ ) and carbon dioxide ( $CO_2$ ) on the electrical conduction properties of graphene based sensors are negligible. Whereas, water molecules have strong influence on the conductivity of graphene. The considerable response of graphene to the water molecules makes it highly suitable for humidity sensor applications [46]. Therefore,  $N_2$  and  $CO_2$  gases have not been considered in these simulations. The purpose of these simulations is to investigate the feasibility of simulated FET device for the detection of solely propane and butane molecules for household and industrial environments. However, the concentration of methane ( $CH_4$ ) gas is increasing day by day due to green house effect. Several efforts have been done for the development of  $CH_4$  gas sensors [47–58]. The detection of  $CH_4$  with our proposed device for climatic and household applications can be considered as future work. These simulation results are convincing in terms of the ranges of detectable electric current values. In our previous work [31], the differentiation between electric current values in the presence of the these target gases was difficult for each individual gas and the combination of both gases. In current work, the behavior of FET device and current values are more obvious. However, the trend of increase or decrease of current values in IV-curves for both devices shows a conflict. The possible reason of this conflict could be the

involvement of the effect of gate voltage and addition of zigzag nanoribbons as electrodes for the FET device that was absent in our previously simulated device [31]. The physical fabrication of this type of device could be challenging due to the handling and processing of nanoribbons at atomic level. In near future, as the graphene technology will evolve, the physical fabrication of such type of devices will be possible.

#### 4. Conclusions

The goal of the work that has been presented in this article is to access the potential of graphene nanoribbon based FET for the detection of propane and butane gases. Armchair graphene nanoribbons and zigzag nanoribbon have been used to develop FET device. In the absence of any target gas molecules, the IV-characteristics of the simulated device are similar to n-channel depletion mode FET. In the proximity of target gas molecules, a change in source-to-drain current of FET at different gate voltages has been observed. This change is distinct for each specific target gas i.e., propane and butane. Our simulated FET device also exhibited a noticeable change in the density of states in the proximity of these target gases. The change in source-to-drain current of FET in the presence of target gas molecules has been used as a detection signal for the leakage detection of these gases. The influence of atmospheric factors like the presence of water and oxygen molecules on the proposed device have also been investigated. It has been observed that the presence of these molecules also affected the IV-characteristics of the device. A careful calibration of such physically fabricated device is required to nullify the effect of atmospheric factors and get the correct reading for desired target gases. Our proposed device could be a promising candidate to replace conventional solid-state gas sensors due to its exceptional electronic properties and compact size. Theoretically, it is possible to simulate such type of FET sensors. However, the physical fabrication of these kind of device could be a challenge due to extremely small dimensions of graphene nanoribbons that make it difficult to handle at atomic levels. Moreover, during physical fabrication of our proposed FET, there is a need of some suitable substrate like SiC or Si for the deposition of graphene. Our nearest future intension is to develop graphene based FET device for the detection of propane and butane gases.

**Author Contributions:** M.H.R. and A.K. conceived the idea. M.H.R. performed the simulations and drafted the article. A.K. and T.R. reviewed the article and managed funding of the project. All authors have read and agreed to the published version of the manuscript.

**Funding:** This research was supported by the Estonian Research Council through Research Projects PUT 1435, IUT 1911 and by the Horizon 2020 ERA-chair grant “Cognitive Electronics COEL H2020-WIDESPREAD-2014-2” (agreement number 668995; project TTU code VFP15051).

**Acknowledgments:** Authors would like to acknowledge the courtesy of Poklonski, N.A. and SPIE publishers to give copyright permission to reprint a figure from article Poklonski, N.A.; Kislyakov, E.F.; Vyrko, S.A.; Bubeľ, O.N.; Ratkevich, S.V.; Electronic band structure and magnetic states of zigzag graphene nanoribbons: quantum chemical calculations. *J. Nanophotonics* **2012** Volume 6, 61712. doi:10.1117/1.JNP.6.061712.

**Conflicts of Interest:** The authors declare no conflict of interest.

#### References

1. Joshi, S.; Bhatt, V.D.; Wu, H.; Becherer, M.; Lugli, P. Flexible lactate and glucose sensors using electrolyte-gated carbon nanotube field effect transistor for non-invasive real-time monitoring. *IEEE Sens. J.* **2017**, *17*, 4315–4321. [[CrossRef](#)]
2. Hosseini-Golgoos, S.M.; Salimi, F.; Saberhari, A.; Rahbarpour, S. Comparison of information content of temporal response of chemoresistive gas sensor under three different temperature modulation regimes for gas detection of different feature reduction methods. *J. Phys.* **2017**, *939*, 012005. [[CrossRef](#)]
3. Moseley, P.T. Solid state gas sensors. *Meas. Sci. Technol.* **1997**, *8*, 223–237. [[CrossRef](#)]
4. Simonetta, C.; Forleo, A.; Francioso, L.; Rella, R.; Siciliano, P.; Spadavecchia, J.; Presicce, D.S.; Taurino, A.M.; Forleo, D.A. Solid state gas sensors: State of the art and future activities. *J. Optoelectron. Adv. Mater.* **2003**, *5*, 1335–1348.

5. Kong, J.; Franklin, N.R.; Zhou, C.; Chapline, M.G.; Peng, S.; Cho, K.; Dai, H. Nanotube molecular wires as chemical sensors. *Science* **2000**, *287*, 622–625. [CrossRef] [PubMed]
6. Dutta, P.; Horn, P.M. Low-frequency fluctuations in solids: 1/f noise. *Rev. Mod. Phys.* **1981**, *53*, 497–516. [CrossRef]
7. Ramamoorthy, R.; Dutta, P.K.; Akbar, S.A. Oxygen sensors: Materials, methods, designs and applications. *J. Mater. Sci.* **2003**, *38*, 4271–4282. [CrossRef]
8. Macdonald, J.R. *Impedance Spectroscopy: Emphasizing Solid Materials and Systems*; John Wiley & Sons: New York, NY, USA, 1987.
9. Park, C.O.; Akbar, S.A.; Weppner, W. Ceramic electrolytes and electrochemical sensors. *J. Mater. Sci.* **2003**, *38*, 4639–4660. [CrossRef]
10. Liu, Y.; Parisi, J.; Sun, X.; Lei, Y. Solid-state gas sensors for high temperature applications—a review. *J. Mater. Chem. A* **2014**, *2*, 9919–9943. [CrossRef]
11. Korotcenkov, G. Gas response control through structural and chemical modification of metal oxide films: State of the art and approaches. *Sens. Actuators B Chem.* **2005**, *107*, 209–232. [CrossRef]
12. Jiménez-Cadena, G.; Riu, J.; Rius, F.X. Gas sensors based on nanostructured materials. *Analyst* **2007**, *132*, 1083–1099.
13. Schedin, F.; Geim, A.K.; Morozov, S.V.; Hill, E.W.; Blake, P.; Katsnelson, M.I. Detection of individual gas molecules adsorbed on graphene. *Nat. Mater.* **2007**, *6*, 652–655. [CrossRef] [PubMed]
14. Robinson, J.T.; Perkins, F.K.; Snow, E.S.; Wei, Z.; Sheehan, P.E. Reduced Graphene Oxide Molecular Sensors. *Nano Lett.* **2008**, *8*, 3137–3140. [CrossRef] [PubMed]
15. Lu, Y.; Goldsmith, B.R.; Kybert, N.J.; Johnson, A.T.C. DNA Decorated Graphene Chemical Sensors. *Appl. Phys. Lett.* **2010**, *97*, 83107. [CrossRef]
16. Pearce, R.; Iakimov, T.; Andersson, M.; Hultman, L.; Spetz, A.L.; Yakimova, R. Epitaxially grown graphene based gas sensors for ultra sensitive NO<sub>2</sub> detection. *Sens. Actuators B Chem.* **2011**, *155*, 451–455. [CrossRef]
17. Ohno, K.; Maehashi, K.; Matsumoto, K. Chemical and biological sensing applications based on graphene field-effect transistors. *Biosens. Bioelectron.* **2010**, *26*, 1727–1730. [CrossRef]
18. Syu, Y.-C.; Hsu, W.-E.; Lin, C.-T. Review—Field effect transistor biosensing: Devices and clinical application. *ECS J. Solid State Sci. Technol.* **2018**, *7*, Q3196–Q3207. [CrossRef]
19. Lee, J.; Kim, J.; Im, J.P.; Lim, S.Y.; Kwon, J.Y.; Lee, S.M.; Moon, S.E. MEMS-based NO<sub>2</sub> gas sensor using ZnO nano-rods for low-power IoT application. *J. Korean Phys. Soc.* **2017**, *70*, 924–928. [CrossRef]
20. Bogue, R. Recent developments in MEMS sensors: A review of applications, markets and technologies. *Sens. Rev.* **2013**, *33*, 300–304. [CrossRef]
21. Morales-Narvaez, E.; Merkoci, A. Graphene oxide as an optical biosensing platform. *Adv. Mater.* **2012**, *24*, 3298–3308. [CrossRef]
22. Varghese, S.S.; Lonkar, S.; Singh, K.K.; Swaminathan, S.; Abdala, A. Recent Advances in graphene based gas sensors. *Sens. Actuators B Chem.* **2015**, *218*, 160–183. [CrossRef]
23. Yuan, W.; Shi, G. Graphene-based gas sensors. *J. Mater. Chem. A* **2013**, *1*, 10078–10091. [CrossRef]
24. Latif, U.; Dickert, F.L. Graphene hybrid materials in gas sensing applications. *Sensors* **2015**, *15*, 30504–30524. [CrossRef] [PubMed]
25. Korotcenkov, G. Metal oxides for solid-state gas sensors: What determines our choice. *Mater. Sci. Eng. B* **2007**, *139*, 1–13. [CrossRef]
26. Rumyantsev, S.; Liu, G.; Potyrailo, R.A.; Balandin, A.A.; Shur, M.S. Selective sensing of individual gases using graphene devices. *IEEE Sens. J.* **2013**, *13*, 2818–2822. [CrossRef]
27. Natgaz. Propane vs. Butane. Available online: <http://www.natgaz.com.lb/all-about-gaz/propane-vs-butane> (accessed on 10 September 2019).
28. National Research Council USA. Butane: Acute exposure guide levels. In *Acute Exposure Guideline Levels for Selected Airborne Chemicals*; National Academies Press (US): Washington, DC, USA, 2012; Volume 12. Available online: <https://www.ncbi.nlm.nih.gov/books/NBK201460/olome12> (accessed on 10 September 2019).
29. Yan, Q.; Huang, B.; Yu, J.; Zheng, F.; Zang, J.; Wu, J.; Gu, B.; Liu, F.; Duan, W. Intrinsic current-voltage characteristics of graphene nanoribbon transistors and effect of edge doping. *Nano Lett.* **2007**, *7*, 1469–1473. [CrossRef]

30. Erol, O.; Uyan, I.; Hatip, M.; Yilmaz, C.; Tekinay, A.B.; Guler, M.O. Recent advances in bioactive 1D and 2D carbon nanomaterials for biomedical applications. *Nanomed. Nanotechnol. Biol. Med.* **2018**, *14*, 2433–2454. [[CrossRef](#)]
31. Rashid, M.H.; Koel, A.; Rang, T. Simulations of propane and butane gas sensor based on pristine armchair graphene nanoribbon. In Proceedings of the IOP Conference Series: Materials Science and Engineering, Bucharest, Romania, 7–9 March 2018; Volume 362.
32. Narendar, V.; Gupta, S.K.; Saxena, S. First principle study of doped graphene for FET applications. *Silicon* **2019**, *11*, 277–286. [[CrossRef](#)]
33. Siddique, S.; Mukhtar, H. Probing the performance of glucose oxidase treated graphene-based field effect transistors. *J. Nanosci. Nanotechnol.* **2019**, *19*, 7442–7446. [[CrossRef](#)]
34. Hasan, N.; Hou, B.; Radadia, A.D. Ion sensing with solution-gated graphene field-effect sensors in the frequency domain. *IEEE Sens. J.* **2019**, *19*, 8758–8766. [[CrossRef](#)]
35. Tsang, D.K.H.; Lieberthal, T.J.; Watts, C.; Dunlop, E.L.; Ramadan, S.; Hernandez, A.E.D.R.; Klien, N. Chemically functionalised graphene FET biosensor for the label-free sensing of exosomes. *Sci. Rep.* **2019**, *9*, 1–10.
36. QuantumWise User Manual, ATK-DFT Calculator. Available online: <https://docs.quantumwise.com/v2017/manuals/ATKDFT.html> (accessed on 14 October 2019).
37. High Performance Computing. Available online: <https://www.ttu.ee/support-structure/it-services/services-4/high-performance-computing-2/> (accessed on 15 October 2019).
38. Poklonski, N.A.; Kislyakov, E.F.; Vyrko, S.A.; Bubel', O.N.; Ratkevich, S.V. Electronic band structure and magnetic states of zigzag graphene nanoribbons: Quantum chemical calculations. *J. Nanophotonics* **2012**, *6*, 61712. [[CrossRef](#)]
39. Owens, F.J. Electronic and magnetic properties of armchair and zigzag graphene nanoribbons. *J. Chem. Phys.* **2008**, *128*, 194701. [[CrossRef](#)] [[PubMed](#)]
40. QuantumWise, Building a Graphene Nanoribbon Transistor. Available online: [https://docs.quantumwise.com/v2017/tutorials/vnl\\_graphene\\_transistor/vnl\\_graphene\\_transistor.html](https://docs.quantumwise.com/v2017/tutorials/vnl_graphene_transistor/vnl_graphene_transistor.html) (accessed on 16 October 2019).
41. Yavari, F.; Koratkar, N. Graphene-based chemical sensors. *J. Phys. Chem. Lett.* **2012**, *3*, 1746–1753. [[CrossRef](#)]
42. Bekduz, B.; Kampermann, L.; Mertin, W.; Punckt, C.; Aksay, I.A.; Bacher, G. Influence of the atmospheric species on the electrical properties of functionalized graphene sheets. *RSC Adv.* **2018**, *8*, 42073–42079. [[CrossRef](#)]
43. Melios, C.; Centeno, A.; Zurutuza, A.; Panchal, V.; Giusca, C.E.; Spencer, S.; Silva, S.R.P.; Kazakova, O. Effects of humidity on the electronic properties of graphene prepared by chemical vapour deposition. *Carbon* **2016**, *103*, 273–280. [[CrossRef](#)]
44. What Effect Does Humidity Have on Graphene Sensors? Available online: <https://www.azosensors.com/article.aspx?ArticleID=1323> (accessed on 3 December 2019).
45. Yao, Y.; Chen, X.; Zhu, J.; Zeng, B.; Wu, Z.; Li, X. The effect of ambient humidity on the electrical properties of graphene oxide films. *Nanoscale Res. Lett.* **2012**, *7*, 363. [[CrossRef](#)] [[PubMed](#)]
46. Smith, A.D.; Elgammal, K.; Fan, X.; Lemme, M.C.; Delin, A.; Rasander, M.; Bergqvist, L.; Schroder, S.; Fischer, A.C.; Niklaus, F.; et al. Graphene-based CO<sub>2</sub> sensing and its cross-sensitivity with humidity. *RSC Adv.* **2017**, *7*, 22329–22339. [[CrossRef](#)]
47. Eugster, W.; Kling, G.W. Performance of low-cost methane sensor for ambient concentration measurements in preliminary studies. *Atmos. Meas. Tech.* **2012**, *5*, 1925–1934. [[CrossRef](#)]
48. Tao, C.; Li, X.; Yang, J.; Shi, Y. Optical fiber sensing element based on luminescence quenching of silica nanowires modified with cryptophane-A for the detection of methane. *Sens. Actuators B Chem.* **2011**, *156*, 553–558. [[CrossRef](#)]
49. Wu, Z.; Chen, X.; Zhu, S.; Zhou, Z.; Yao, Y.; Quan, W.; Liu, B. Room Temperature Methane Sensor Based on Graphene Nanosheets/Polyaniline Nanocomposite Thin Film. *IEEE Sens.* **2013**, *13*, 777–782. [[CrossRef](#)]
50. Roy, S.; Sarkar, C.K.; Bhattacharyya, P. A highly sensitive methane sensor with nickel alloy microheater on micromachined Si substrate. *Solid State Electron.* **2012**, *76*, 84–90. [[CrossRef](#)]
51. Haridas, D.; Gupta, V. Enhanced response characteristics of SnO<sub>2</sub> thin film based sensors loaded with Pd clusters for methane detection. *Sens. Actuators B Chem.* **2012**, *166*, 156–164. [[CrossRef](#)]

52. Prasad, A.K.; Amirthapandian, S.; Dhara, S.; Dash, S.; Murali, N.; Tyagi, A.K. Novel single phase vanadium dioxide nanostructured films for methane sensing near room temperature. *Sens. Actuators B Chem.* **2014**, *191*, 252–256. [[CrossRef](#)]
53. Vuong, N.M.; Hieu, N.M.; Hieu, H.N.; Yi, H.; Kim, D.; Han, Y.S.; Kim, M. Ni<sub>2</sub>O<sub>3</sub>-decorated SnO<sub>2</sub> particulate films for methane gas sensors. *Sens. Actuators B Chem.* **2014**, *192*, 327–333. [[CrossRef](#)]
54. Gong, G.; Zhu, H. Development of highly sensitive sensor system for methane utilizing cataluminescence. *Luminescence* **2015**, *31*, 183–189. [[CrossRef](#)]
55. Zhang, Y.N.; Zhao, Y.; Wang, Q. Measurement of methane concentration with cryptophane E infiltrated photonic crystal microcavity. *Sens. Actuators B Chem.* **2015**, *209*, 431–437. [[CrossRef](#)]
56. Yang, D.; Yang, N.; Ni, J.; Xiao, J.; Jiang, J.; Liang, Q.; Ren, T.; Chen, X. First-principles approach to design and evaluation of graphene as methane sensors. *Mater. Des.* **2017**, *119*, 401. [[CrossRef](#)]
57. Humayun, M.T.; Divan, R.; Stan, L.; Rosenmann, D.; Gosztola, D.; Paul, L.G.; Solomon, A.; Paprotny, I. Ubiquitous low-cost functionalized multi-walled carbon nanotube sensors for distributed methane leak detection. *IEEE Sens. J.* **2016**, *16*, 8692–8699. [[CrossRef](#)]
58. Humayun, M.T.; Divan, R.; Liu, Y.; Gundel, L.; Solomon, P.; Paprotny, I. Novel chemoresistive CH<sub>4</sub> sensor with 10 ppm sensitivity based on multiwalled carbon nanotubes functionalized with SnO<sub>2</sub> nanocrystals. *J. Vac. Sci. Technol. A Vac. Surf. Films* **2016**, *34*, 01A131. [[CrossRef](#)]



© 2020 by the authors. Licensee MDPI, Basel, Switzerland. This article is an open access article distributed under the terms and conditions of the Creative Commons Attribution (CC BY) license (<http://creativecommons.org/licenses/by/4.0/>).



## Appendix J

H. Rashid, A. Koel, T. Rang and M. H. Ziko

“Simulations of Benzene and Hydrogen-sulfide Gas Detector based on Single Walled Carbon Nanotube over Intrinsic 4H-SiC Substrate,” *Micromachines*, vol. 11, 2020. **(Published in ETIS 1.1)**





Article

# Simulations of Benzene and Hydrogen-Sulfide Gas Detector Based on Single-Walled Carbon Nanotube over Intrinsic 4H-SiC Substrate

Muhammad Haroon Rashid <sup>\*</sup>, Ants Koel , Toomas Rang and Mehadi Hasan Ziko

Thomas Johan Seebeck Department of Electronics, Tallinn University of Technology, Ehitajate tee 5, 12616 Tallinn, Estonia; ants.koel@ttu.ee (A.K.); toomas.rang@ttu.ee (T.R.); Mehadi.Ziko@taltech.ee (M.H.Z.)

\* Correspondence: murash@ttu.ee; Tel.: +372-5391-2599

Received: 3 March 2020; Accepted: 23 April 2020; Published: 26 April 2020



**Abstract:** Carbon nanotubes (CNTs)-based sensors have gained significant importance due to their tremendous electrical and physical attributes. CNT-based gas sensors have high sensitivity, stability, and fast response time compared to that of solid-state sensors. On exposure to a large variety of organic and inorganic compounds, the conductivity of CNT changes. This change in electrical conductivity is being used as a detection signal to detect different target molecules. Hydrogen-sulfide and benzene are hazardous gases that can cause serious health issues in humans. Therefore, it is mandatory to detect their presence in industrial and household environments. In this article, we simulated CNT-based benzene and hydrogen-sulfide sensor with a nanoscale semiconductor device simulator—Quantumwise Atomistix Toolkit (ATK). The change in the device density of states, electric current, and photocurrent in the presence of target molecules have been calculated. The change in photocurrent in the presence of target molecules has been proposed as a novel detection mechanism to improve the sensor selectivity and accuracy. This change in photocurrent as well as electric current in the presence of target molecules can be used simultaneously as detection signals. Our intension in the future is to physically fabricate this simulated device and use photocurrent as well as electric current as detection mechanisms.

**Keywords:** carbon nanotube; benzene; hydrogen sulfide; sensor; detector; photocurrent; 4H-SiC

## 1. Introduction

The detection of hazardous biochemicals and gases in industrial and household environments have been a great concern. It is very significant to monitor the emission of such gases for environmental pollution control, industrial process controls, public safety, and health. The demand for the development of miniature and portable gas sensors is increasing day by day. Nanomaterials, especially one-dimensional nanomaterials like carbon nanotubes, nanoribbons and nanowires, are promising candidates to replace the conventional solid-state sensors due to their exceptional physical and electrical attributes. These materials have great adsorption capabilities and are hence very suitable to adsorb and detect a wide range of gases [1]. Carbon nanotubes (CNTs) were discovered by Iijima in 1991 [2]. Since their discovery, CNT has attracted the attention of researchers due to their exceptional electrical, mechanical, and thermal attributes that make them highly suitable for real-life applications. CNTs are promising candidates for a wide range of applications such as supercapacitors, flexible heaters, medical devices, sensors, nano-electronics, power storage batteries, electricity transmission, automobiles, and light emitting displays [3–8].

Furthermore, the transition of electronic cloud distribution in CNT from uniform to asymmetric circular clouds around its cylindrical structure (creating a  $\pi$ -electrons clouds) makes it highly suitable

for electrochemical reactions [9]. CNTs are made up of tiny covalently bonded carbon atoms. They may be in a single layer of carbon atoms (single wall CNT/SWCNT) or multiple layers of carbon atoms (multi wall CNT/MWCNT) [2,10]. The most popular techniques to synthesize carbon nanotubes are chemical vapor deposition, arc discharge, and laser ablation [11–15]. Carbon nanotubes show a unique diversity in their electronic behavior. The chirality and diameter of nanotubes dictate the behavior of CNTs. They may show metallic nature or semiconducting nature [16,17]. Semiconducting SWCNTs change their bandgap inversely with their diameter [18]. CNTs are totally made of surface atoms that make them ideal candidates for the detection of chemicals and gases. The most commonly used mechanism in CNT-based sensors to detect foreign particles is the resistive method. In this method, the resistance of CNT changes after the adsorption of gas or chemical molecules. CNT-based field effect transistors also work on the same principle, except that the current through the channel is controlled by the gate voltage [19].

Moreover, in this article, we used the resistive method to detect hydrogen sulfide ( $H_2S$ ) and benzene with SWCNT.  $H_2S$  can be found in abundance in natural gas, sulphur hot springs, and volcanic soil. This gas has bad effect on lungs and respiratory system of humans. It can diffuse into human lungs while inhaling.  $H_2S$  can cause serious damage to human nervous system and eyes [20]. Inhaling of this gas causes halitosis (bad breathing) in humans. A very low concentration of about 0.1 to 0.5 ppm of  $H_2S$  can cause halitosis in humans [21]. Thus, this fact makes it very important to detect this gas even at very low concentrations. Usually, the chromatography technique [18] is used to detect and diagnose halitosis in humans. However, this technique is time consuming and expensive. Nanomaterials based sensors are very promising candidates for the replacement of the chromatography technique due to their small size and low cost [22].

Furthermore, benzene is another hazardous gas and the major sources of benzene are petroleum products, automobile exhaust, building materials, and industrial discharges [23]. It can cause nausea, cough, vomiting, and dizziness in humans. Benzene can enter into a human's body through inhaling [24–26]. Therefore, detection of benzene in industrial as well as household environments is mandatory. Conventional solid-state gas sensors are not so accurate to detect a very low concentration of such gases and require high operating temperature [27–30]. CNTs have emerged as promising candidates to cope with the challenges of selectivity, accuracy, and sensitivity to detect a wide range of organic/inorganic molecules.

In this article, SWCNT over intrinsic 4H-SiC substrate has been used to detect  $H_2S$  and benzene molecules. A novel method (change in photocurrent) has been added along with the existing one (change in electric current) to improve the device accuracy to detect  $H_2S$  and benzene molecules. The work presented in this article is totally computational-based. All the simulations have been done in a nanoscale semiconductor device simulator—Quantumwise Atomistix Toolkit.

## 2. Materials and Methods

In this section, comprehensive details about the used materials and simulated devices have been given. All the simulations have been done in a nanoscale electronic device simulator, Quantumwise Atomistix Toolkit (ATK) (QuantumWise, Copenhagen, Denmark). This software package has an inbuilt graphical user interface called Virtual nanolab (VNL). The complete software package ATK-VNL allows the users to model a large variety of nanoscale electronic devices. We simulated SWCNT and deposited it on intrinsic 4H-SiC substrate to detect  $H_2S$  and benzene molecules.

### 2.1. Carbon Nanotube over Intrinsic 4H-SiC Substrate for the Detection of Hydrogen Sulfide and Benzene Molecules

The constituent materials of the simulated sensor are SWCNT and intrinsic 4H-SiC substrate. SWCNT has been deposited on intrinsic (0001)-oriented 4H-SiC substrate in the ATK-VNL builder tool. In the first step, an inbuilt CNT plugin tool of ATK-VNL software has used to insert the basic structure of CNT, as shown in left image of Figure 1a. Afterward, this basic structure of CNT has been repeated along C-axis to form 50Å long SWCNT, as shown in Figure 1a. In the second step, 4H-SiC has

been cut along (0001)-orientation to form a substrate for CNT. After that, CNT has been deposited on this quasi 2-dimensional intrinsic 4H-SiC substrate, as shown in Figure 1b. In the third step, this simulated structure has been converted into device by defining electrodes and central region of the device, as shown in Figure 1c.

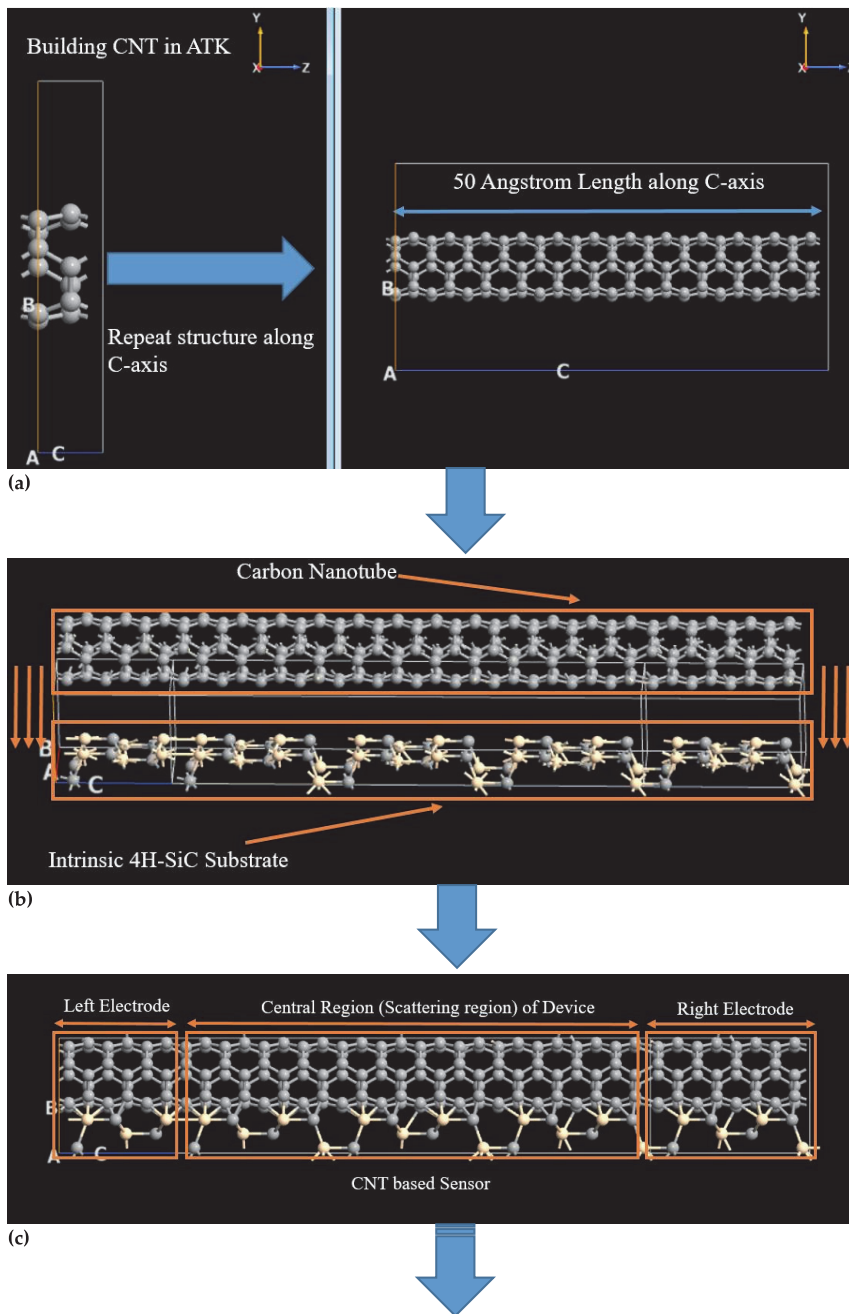
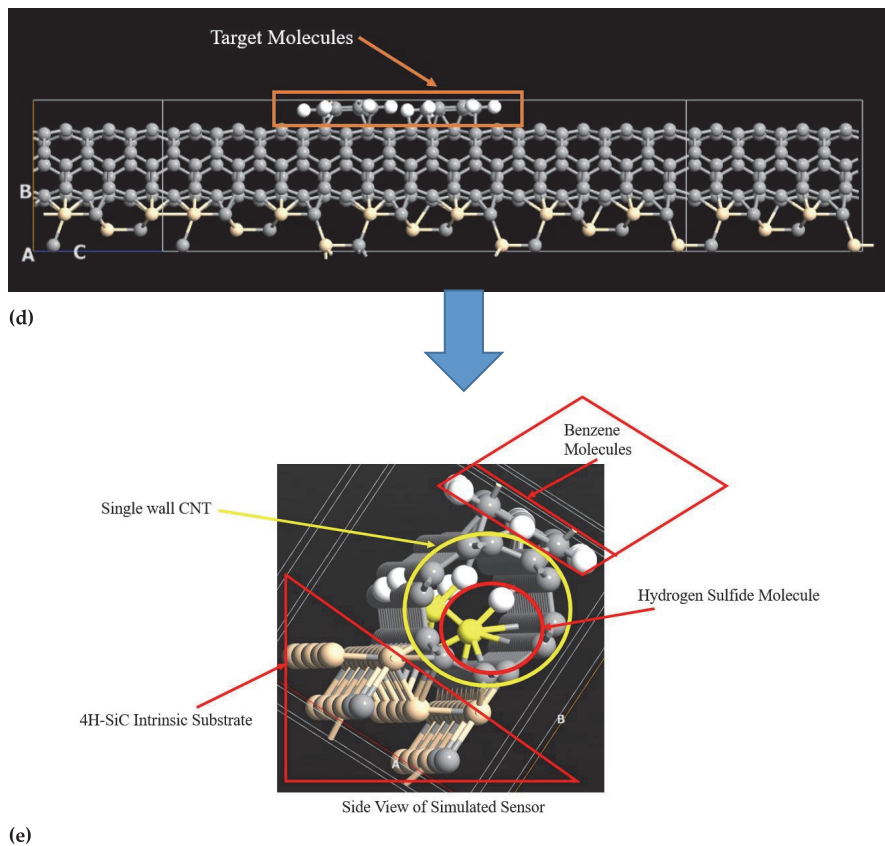


Figure 1. Cont.



**Figure 1.** Simulation of single-wall carbon nanotube-based hydrogen-sulfide and benzene detector in Quantumwise Atomistix Toolkit Software.

Rather than depositing metal electrodes, CNT itself has been used as electrodes to avoid Schottky barrier formation at electrodes and reduce computational time in the simulator. Now, this structure is a CNT-based device that can be used to detect desired target molecules. In the fourth step, the simulated device has been exposed to the target molecules to detect their presence, as shown in Figure 1d. This device has been exposed to two benzene, two hydrogen-sulfide molecules individually, and four  $\text{H}_2\text{S}$  and two benzene molecules simultaneously in three different experiments. A magnified 3-dimensional side-view of the simulated sensor has been shown in Figure 1e. In this view, SWCNT over intrinsic 4H-SiC substrate has been exposed to hydrogen-sulfide and benzene molecules simultaneously to detect their presence. In physical CNT-based sensors, the target gas molecules can stick to the surface of CNT as well as penetrate into the CNT. CNT having open ends allows the penetration of target molecules into its internal areas. This penetration of target molecule into CNT results in an increase in the sensitivity of the sensor. That is why, the penetration of gas molecules into CNT has also been realized in these simulations, as shown in Figure 1e [31]. The device density of the states (DOS), electric current, and photocurrent have been calculated for four different scenarios, i.e., in the absence of any target, in the presence of only benzene molecules, in the presence of only hydrogen-sulfide molecules, and in the presence of both benzene and hydrogen-sulfide molecules.

## 2.2. Methodology for Simulated Carbon Nanotube Based Benzene and Hydrogen Sulfide Sensor

All the simulations have been done in a nanoscale semiconductor device simulator, Quantumwise Atomistix Toolkit (ATK). ATK has an inbuilt graphical user interface called Virtual Nanolab (VNL). The ATK-VNL software package allows the users to model the electronic properties of a wide range of organic and inorganic quantum devices [32]. This software is also being used for the simulations of wide range of gas sensors [33–37]. This software has several inbuilt calculators to calculate a wide range of electronic properties of the simulated nanostructures. We used ATK-DFT calculator [38] to compute the electronic properties of our simulated CNT-based benzene and hydrogen-sulfide sensor. ATK-VNL software follows a workflow for the simulations of nanoscale devices. This schematic of this workflow has been shown in Figure 2. In step-1, Builder Tool is used to simulate the desired structure. This tool is a graphical user interface of the software package. In step-2, the simulated structure is transferred to the Scripter Tool. At this stage, an inbuilt calculator and the parameters to be analyzed are added to form a Python code-based script file, as shown in Figure 2. In step-3, the Python code-based script file can be modified and edited by using the Custom Scripter and Editor Tools. In step-4, this Python file is forwarded to the Jobs Tool for execution, as shown in Figure 2. This simulated code can be run at local computing machines or remotely available high-power computing machines. We used remotely available high-power computing (HPC) machines [39] for our simulations. This HPC uses 232 high power computing machines that have 1024 GB of total memory. We used 8-computing nodes to calculate DOS,  $I$ - $V$  curves, and photocurrent for our simulated devices. It took about two weeks to calculate each  $I$ - $V$  curve and photocurrent curve in HPC. The K-point sampling values used in ATK-DFT calculator are  $K_a = 5$ ,  $K_b = 5$ , and  $K_c = 50$  for each calculation. Finally, the simulation results were viewed with the Viewer Tool of ATK-VNL Software. A more comprehensive detail of the workflow used by ATK-VNL can be found at this reference [40]. ATK-DFT calculator has been used for the calculation of DOS,  $I$ - $V$  curves, and photocurrent curves for our simulated devices. Basis Set and Exchange Correlation specifications are shown in Figure 2b.

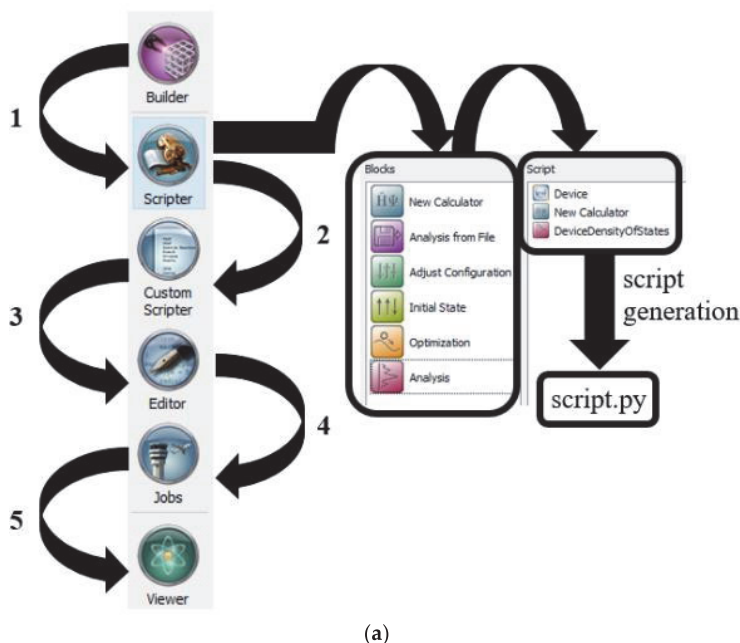
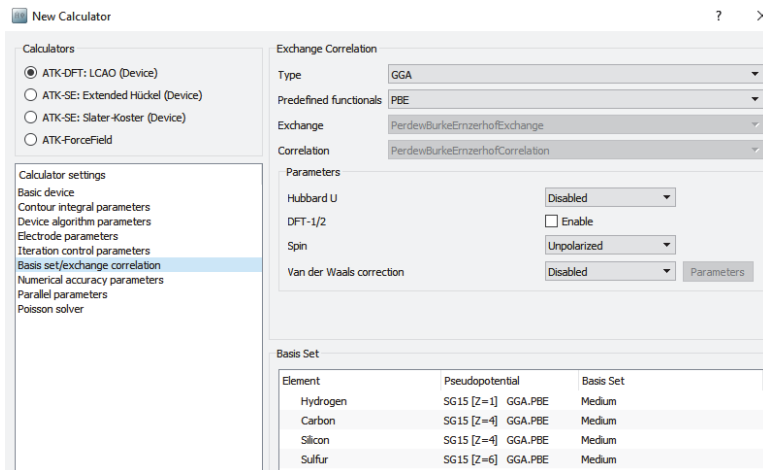


Figure 2. Cont.



(b)

**Figure 2.** (a) Workflow of ATK-VNL software package for the simulation of nanoscale devices; (b) Basis set and exchange correlation details for the simulated devices.

### 3. Results and Discussions

In this section, the density of states (DOS),  $I$ - $V$  curves, and photocurrent curves of the simulated device have been presented and discussed in detail.

#### 3.1. Density of States and Current-Voltage Characteristics Analysis of CNT-Based Device

The DOS of simulated CNT and 4H-SiC substrate have been calculated individually before depositing CNT over 4H-SiC substrate. Then, density of states of only CNT, only 4H-SiC substrate and CNT over 4H-SiC have been compared with each other, as shown in Figure 3a. In this figure, DOS of simulated CNT and intrinsic 4H-SiC have been shown with red and green curves, respectively. Whereas, the DOS of CNT after depositing it over intrinsic 4H-SiC substrate has been shown with a blue curve in Figure 3a. The change in DOS after depositing CNT over 4H-SiC substrate compared to that of only CNT and only 4H-SiC substrate can be observed in Figure 3a.

Moreover, the simulated device shown in Figure 1c has been used as a reference device (in the absence of any target molecules). Later on, this device was exposed to benzene and hydrogen-sulfide target molecules and change in DOS and  $I$ - $V$  curves were compared with this reference device. In Figure 3b, DOS of CNT-based sensor in the absence of any target molecules has been compared to that of in the presence of two  $H_2S$  molecules. It can be observed in the figure that many new energy states have been added in DOS of the device in the presence of  $H_2S$  gas. Many new sharp energy peaks can be observed in DOS of the device at energy levels of  $-2.7$ ,  $-2.3$ ,  $-2.2$ ,  $-0.8$ ,  $0.9$ ,  $1.1$ ,  $1.7$ , and  $2.5$  eV approximately in the presence of  $H_2S$  gas. These new energy states are not present in the device before its exposure to the target gas, as shown in Figure 3b. Furthermore, a comparison of DOS of the reference device with device in the proximity of two benzene molecules has been shown in Figure 3c. It can be seen in this figure that many new energy states have been added into DOS of the device by the benzene molecules. The new energy states can be viewed at energy levels of  $-2.3$ ,  $-2.1$ ,  $-1.9$ ,  $-1.7$ ,  $-1.6$ ,  $-1.4$ ,  $-1.2$ ,  $-1.1$ ,  $-1$ , and  $1.8$  eV approximately. These new energy states will definitely influence the conductivity of the device in the presence of benzene molecules.

Similarly, a comparison of DOS of the reference device with the device in the presence of both hydrogen-sulfide and benzene molecules has been made in Figure 3d. The device has been exposed to two benzene and four  $H_2S$  molecules. It can be observed in this figure that the joint influence of  $H_2S$

and benzene on DOS is very different and unique compared to that of the device in the presence of only H<sub>2</sub>S gas. Many new energy peaks have been introduced by H<sub>2</sub>S and benzene in the DOS of the device. These new energy peaks can be observed at energy levels of  $-2.1$ ,  $-1.8$ ,  $-1.7$ ,  $-1.6$ , and  $0.4$  eV in the DOS of the device in presence of both H<sub>2</sub>S and benzene molecules in Figure 3d. These energy states were not present in the reference device.

The *I-V* characteristics of the simulated device have been calculated for four different scenarios, i.e., in the absence of target molecules, in the presence of only benzene target molecules, in presence of only H<sub>2</sub>S target molecules, in the presence of both benzene and H<sub>2</sub>S target molecules simultaneously. These *I-V* curves have been shown in Figure 4. The simulation results revealed that the influence of each target molecule on electric current of the simulated CNT-based device is unique and different. CNTs exhibit a significant change in electric current at the exposure to a wide range of organic/inorganic molecules. The response time of CNT-based sensors is very fast [41,42]. This change in electrical conductivity is used as a detection mechanism to detect foreign adsorbed molecules [43,44].

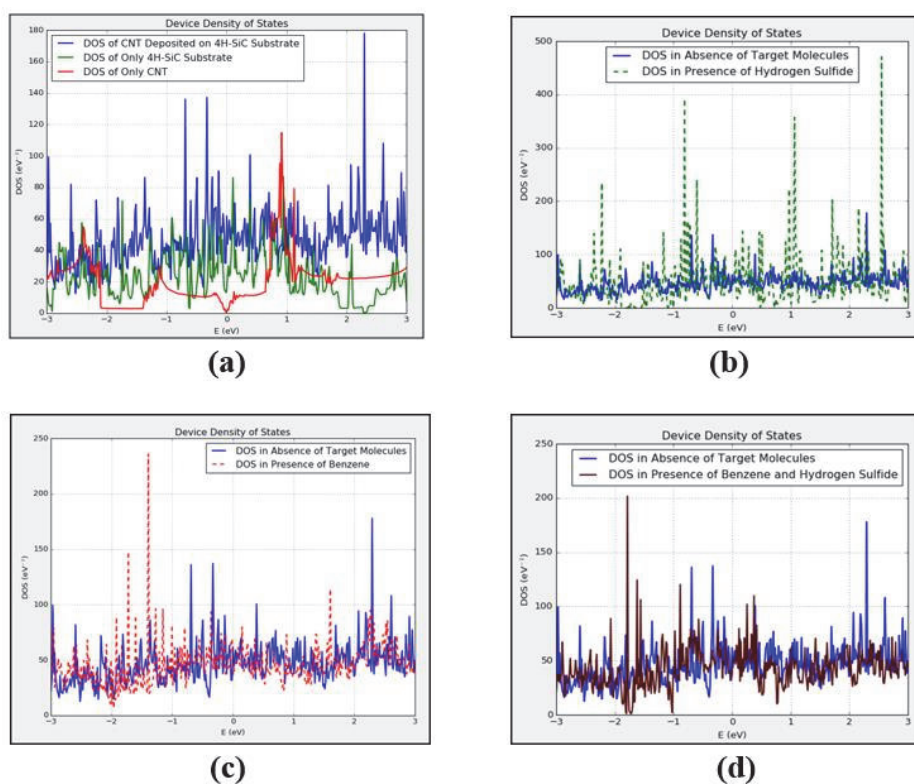


**Figure 3.** Density of states (DOS) of (a) only carbon nanotube-based device; (b) device in presence of only hydrogen-sulfide molecules; (c) device in presence of only benzene molecules; (d) device in presence of both hydrogen-sulfide and benzene molecules.

In this subsection, the change in electric current in the presence of benzene and H<sub>2</sub>S as target molecules has been presented. The simulated device in the absence of any target molecules has been used as a reference device to observe and compare the change in electric current in the presence of target molecules. A voltage bias of 0 to 1 V has been applied at the electrodes of the simulated device and *I-V* characteristics have been calculated, as shown in Figure 4. The reference device exhibited a current in the range of 0 to 9.2 pA approximately, as shown with the solid black line in Figure 4.

After that, the device was exposed to two  $H_2S$  molecules and change in current has been calculated. It has been observed that exposure of the device to  $H_2S$  gas molecules increased the electric current through the device compared to that of reference device. The range of current in this case is between 0 to 9.9 pA for the same voltage bias condition, as shown with the orange dotted line in Figure 4. Actually, the adsorbed target molecules act as acceptor or donor for CNT. If they act as donor of charge carriers, they increase the charge carrier's concentration. Consequently, the conductivity of CNT increases after the adsorption of such molecules. On the other hand, if adsorbed molecules act as acceptors of charge carriers, they reduce the electrical conductivity through CNT [42]. It seems that  $H_2S$  gas molecules act as donors of charge carriers for CNT. Due to which they increase the electric current through CNT after adsorption.

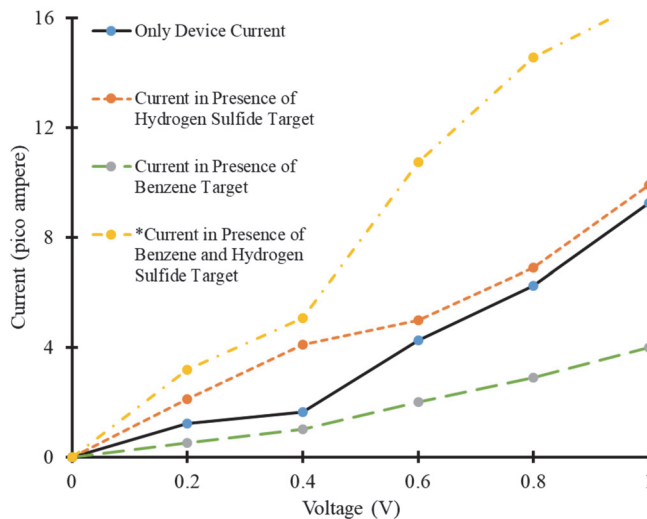


**Figure 4.** Current-voltage ( $I$ - $V$ ) curves of carbon nanotube based simulated device in the proximity of benzene and hydrogen-sulfide as target molecules (\*multiply current axis with  $10^6$  to get the exact value of current in pico ampere for benzene and hydrogen-sulfide target curve).

Furthermore, the reference device is exposed to two benzene molecules and change in current has been calculated. The device showed a decrease in electric current at its exposure to benzene molecules compared to that of the reference device, as shown with the green dashed line in Figure 4. The range of the current is between 0 to 4 pA for the same voltage bias condition. Benzene molecules may have acted like acceptors of charge carriers for CNT. Consequently, they reduced the electric current through the CNT, as shown in Figure 4. Whereas, the device exhibited a very high current at its exposure to two benzene and four  $H_2S$  molecules simultaneously. The range of the current in this case is between 0 to 16.678 mA, approximately. The possible reason of this high current could be the presence of more  $H_2S$  gas molecules (which act like donors) compared to that of benzene molecules (which act like acceptor). Consequently, the overall effect of change in charge carrier concentration in CNT is dominated by  $H_2S$  and a large increase in current is observed. The joint influence of both target molecules on electric current is unique and different from the last two cases.

Moreover, electron densities of the simulated device have been calculated to investigate the reason of very large values of electric current through the device at its exposure to both benzene and hydrogen-sulfide molecules simultaneously. At bias voltage of 0.6 V, electron densities have been calculated for all the previously discussed scenarios (in presence of different target molecules). It has been observed that the joint influence of the benzene and hydrogen-sulfide target molecules on the

electron density of the device is very strong compared to that of all other cases. At the exposure to benzene and hydrogen-sulfide molecules, high electron density/ $\text{\AA}^3$  has been observed, as shown in Figure 5b. In all other scenarios, the values of electron densities/ $\text{\AA}^3$  are quite low and approximately in the same range that have been shown in Figure 5a. That is why in all other cases the change in current values are quite low.

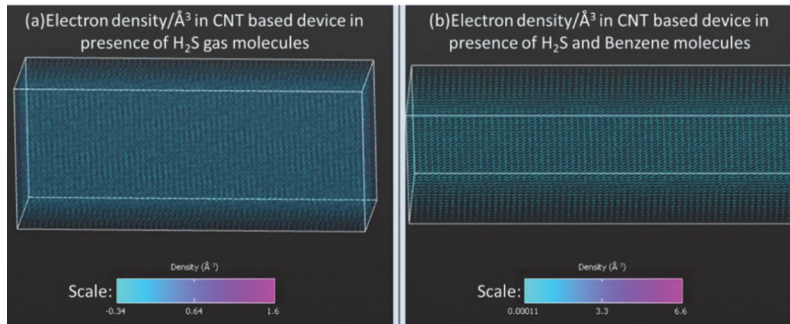


**Figure 5.** Electron density/ $\text{\AA}^3$  of simulated device in presence of (a) only  $\text{H}_2\text{S}$  gas molecules; (b) both  $\text{H}_2\text{S}$  and benzene molecules.

Furthermore, in the physical environment the influence of the presence of other gases like hydrogen, oxygen, carbon dioxide, and humidity cannot be neglected. In the simulator, a controlled environment has been used to detect benzene and hydrogen-sulfide gases. In physically fabricated device, a careful calibration is required of to get the actual change in electric current in the presence of only desired gases. For this purpose, the physical device can be first exposed to only desired gases in a controlled environment and change in current is measured. Then, the same device is exposed to the target gases in the physical environment for real-time detection of gases. The difference in electric currents in controlled and uncontrolled environment can be used to get the actual values of current for the detection of desired gases.

### 3.2. Photocurrent Analysis of Carbon Nanotube Based Benzene and Hydrogen Sulfide Detector

In this article, we proposed a novel additional mechanism (change in photocurrent) to be added with the conventional chemical detection mechanism (change in electric current) to improve device selectivity and accuracy for the detection of desired target molecules. The simulated CNT-based sensor has been illuminated by AM1.5 solar spectrum [45] in the presence of benzene and  $\text{H}_2\text{S}$  targets. The change in photocurrent in the presence of these targets has been measured and compared to that of the device in the absence of target molecules.

However, we could not achieve significant values of photocurrent for our simulated device due to some limitations of the simulator (in controlling polarization of incident light and other related parameters). The generation of photocurrent in CNT is also dependent upon the polarization of incident light [46,47]. CNT has been accepted as an active photo-responsive material. It has several optical attributes like ultraviolet absorption, polarization selectivity, and infrared absorption [48–51]. It is possible to use this mechanism of change in photocurrent as an additional mechanism along with the conventional techniques to improve the device selectivity and accuracy. In our simulations, we bombard the photons having energy values between 0 to 5 eV on CNT to generate photocurrent. In physical device, a light emitting diode can be used as a light source to illuminate CNT and change in photocurrent as well as electric current in the presence of different target molecules can be measured.

Moreover, photocurrent versus photon energy has been shown in Figure 6. It can be observed that the magnitudes of photo-generated current are different for different target molecules. In all cases, an increase in photocurrent with an increase in photon energy has been observed, as shown

in Figure 6. The values of photocurrent in the device in absence of target molecules are between 0 to 0.028 fA. Whereas, the range of photo-generated current in the presence of two benzene target molecules is between 0 to 0.0035 fA, as shown with a green dashed line in Figure 6. In the presence of two H<sub>2</sub>S molecules, the range of photo-generated current is between 0 to 0.0007 fA, as shown with the orange dashed line in Figure 6. The highest values of photocurrent was observed when the device was exposed to two benzene and four H<sub>2</sub>S molecules simultaneously. The range of photo-generated current in this case is between 0 to 0.03 fA, as shown with the yellow dotted-dashed line in Figure 6. Although, all these values of photo-generated current are quite low. Still, these values can be extracted and used to detect gas targets in the physical device.

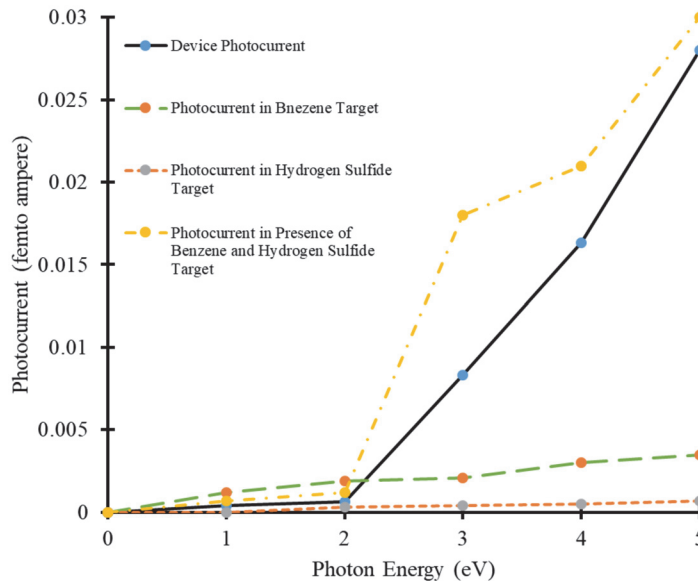


**Figure 6.** Photon energy vs. photocurrent curves of carbon nanotube-based device in presence of benzene and hydrogen-sulfide target molecules.

Furthermore, the purpose of using intrinsic 4H-SiC substrate for CNT is to investigate the influence of SiC substrate on the generation of photocurrent in a physical device. Because generation of photocurrent is also influenced by the plasmon-phonon interaction of graphene and insulated substrates. Plasmon-phonon mode can be excited in graphene-based devices in the mid-infrared region under s-polarization. This interaction increases the overall temperature of interacting phonons and electrons and results in an increase in photo-generated current in graphene-based devices [52,53]. But as mentioned above, due to some limitation of simulator in controlling polarization of incident light, high values of photo-generated current could not be achieved in the presented work. In the near future, we want to investigate this plasmon-phonon coupling mode in case of SiC substrate in a physically fabricated device.

We next intend to create the physical fabrication of this simulated device and implement both detection mechanisms in that device. Our plan is to use a locally developed amplifier [54] to remove noise signal and extract the correct values of photocurrents from the CNT-based sensor. In this experiment, two strips of this same CNT-based devices will be placed parallel to each other. One device will be kept in dark condition while the other one will be illuminated with a light source. Both signals will be fed to the amplifier to detect the change in photocurrent and get rid of noise signal.

#### 4. Conclusions

The purpose of the work presented in this article is to access the feasibility of CNT as a benzene and hydrogen-sulfide molecule detector and introduce a new gas detection mechanism. Carbon nanotube (CNT)-based molecule detectors could be promising candidates to replace conventional solid-state sensors due to their small size, better sensitivity, low operating temperature, and low cost. In this article, nanoscale simulations of CNT-based benzene and hydrogen-sulfide sensors have been done. Single-wall CNT has been deposited on intrinsic 4H-SiC substrate to form a sensor. The change in density of states (DOS), electric current, and photocurrent have been calculated for the simulated carbon nanotube-based sensor. A significant change in DOS, electric current, and photocurrent in the presence of benzene and hydrogen-sulfide molecules have been observed. A novel molecule detection mechanism (change in photocurrent) along with the state-of-the-art molecule detection mechanism (change in electric current) for CNT-based sensors have been proposed to improve the sensor selectivity and accuracy. The simulation results revealed that different target molecules affected the DOS, electric conductivity, and photoconductivity of the device uniquely. This change in electric current as well as photocurrent in the presence of different target molecules can be used simultaneously to detect their presence effectively. Although due to some limitation of the simulator in controlling the polarization of incident light and other related parameters, high values of photocurrent could not be achieved. Still, CNT has been recognized an exciting material for photo detection applications. We next intend to physically fabricate this simulated device and implement our proposed molecule detection mechanism in that device.

**Author Contributions:** M.H.R. and A.K. conceived the idea. M.H.R. performed the simulations. M.H.R. and M.H.Z. drafted the article. A.K. and T.R. reviewed the article and managed funding of the project. All authors have read and agreed to the published version of the manuscript.

**Funding:** This research was supported by the Estonian Research Council through Research Projects PUT 1435, IUT 1911, by the Horizon 2020 ERA-chair grant “Cognitive Electronics COEL H2020-WIDESPREAD-2014-2” (agreement number 668995; project TTU code VFP15051) and by ETAg grant PRG620.

**Conflicts of Interest:** The authors declare no conflicts of interest.

#### References

1. Kolmakov, A.; Moskovits, M. Chemical sensing and catalysis by one-dimensional metal-oxide nanostructures. *Annu. Rev. Mater. Res.* **2004**, *34*, 151–180. [[CrossRef](#)]
2. Iijima, S. Helical microtubules of graphitic carbon. *Nature* **1991**, *354*, 56–58.
3. Ajayan, P.M.; Zhou, O.Z. Applications of carbon nanotubes. In *Carbon Nanotubes Topics in Applied Physics*; Springer: Berlin, Germany, 2001; Volume 80, pp. 391–425.
4. Baughman, R.H.; Zakhidov, A.A.; Heer, W.A.D. Carbon nanotubes—The route toward applications. *Science* **2002**, *297*, 787–792. [[CrossRef](#)] [[PubMed](#)]
5. Dresselhaus, M.S.; Dai, H. Carbon nanotubes: Continued innovations and challenges. *Adv. Carbon Nanotub.* **2004**, *29*, 237–243. [[CrossRef](#)]
6. Dai, H. Carbon nanotubes: Opportunities and challenges. *Surf. Sci.* **2002**, *500*, 218–241. [[CrossRef](#)]
7. Tran, T.Q.; Lee, J.K.Y.; Chinnappan, A.; Jayathilaka, W.A.D.M.; Ji, D.; Kumar, V.V.; Ramakrishna, S. Strong, lightweight, and highly conductive CNT/Au/Cu wires from sputtering and electroplating methods. *J. Mater. Sci. Tech.* **2020**, *40*, 99–106. [[CrossRef](#)]
8. Duong, H.M.; Myint, S.M.; Tran, T.Q.; Le, D.K. Post-spinning treatment to carbon nano fibers. In *Carbon Nanotubes Fibers and Yarn*; WOODHEAD Publishing: Cambridge, UK, 2020.
9. Meyyappan, M. *Carbon Nanotubes: Science and Applications*; CRC Press: Washington, DC, USA, 2004.
10. Harris, P.J.F. *Carbon Naotube Science*; Cambridge university Press: Cambridge, UK, 2010.
11. Antisari, M.V.; Marazzi, R.; Krsmanovic, R. Synthesis of multiwall carbon nanotubes by electric arc discharge in liquid environments. *Carbon* **2003**, *41*, 2393–2401. [[CrossRef](#)]
12. Arepalli, S. Laser ablation process for single-walled carbon nanotube production. *Nanosci. Nanotechnol.* **2004**, *4*, 317–325. [[CrossRef](#)]

13. Braidy, N.; El Khakani, M.A.; Botton, G.A. Carbon nanotubular structures synthesis by means of ultraviolet laser ablation. *J. Mater. Res.* **2002**, *17*, 2189–2192. [[CrossRef](#)]
14. Choi, Y.C.; Bae, D.J.; Lee, Y.H.; Lee, B.S. Growth of carbon nanotubes by microwave plasma-enhanced chemical vapor deposition at low temperature. *J. Vac. Sci. Technol.* **2000**, *18*, 1862–1868. [[CrossRef](#)]
15. Ajayan, P.M.; Ebbesen, T.W. Large-scale synthesis of carbon nanotubes. *Nature* **1992**, *358*, 220–222.
16. Treacy, M.M.J.; Ebbesen, T.W.; Gibson, J.M. Exceptionally high Young's modulus observed for individual carbon nanotubes. *Nature* **1996**, *381*, 678–680. [[CrossRef](#)]
17. Zhu, W.Z.; Wang, F.; Wang, T.; Sun, L.; Wang, Z. Chirality dependence of the thermal conductivity of carbon nanotubes. *Nanotechnology* **2004**, *15*, 936–939.
18. Dresselhaus, M.S.; Dresselhaus, G.; Eklund, P.C. *Science of Fullerenes and Carbon Nanotubes*; Academic Press: San Diego, CA, USA, 1996. [[CrossRef](#)]
19. Martel, R.; Schmidt, T.; Shea, H.R.; Hertel, T.; Avouris, P. Single- and multi-wall carbon nanotube field-effect transistors. *Appl. Phys. Lett.* **1998**, *73*, 2447–2449. [[CrossRef](#)]
20. Choi, K.I.; Kim, H.J.; Kang, Y.C.; Lee, J.H. Ultrasensitive and ultrasensitive detection of H<sub>2</sub>S in highly humid atmosphere using CuO-loaded SnO<sub>2</sub> hollow spheres for real-time diagnosis of halitosis. *Sens. Actuators B Chem.* **2014**, *194*, 371–376. [[CrossRef](#)]
21. Tangerman, A.; Winkel, E.G. Extra-oral halitosis: An overview. *J. Breath Res.* **2010**, *4*, 017003. [[CrossRef](#)]
22. Konvalina, G.; Haick, H. Sensors for breath testing: From nanomaterials to comprehensive disease detection. *Acc. Chem. Res.* **2014**, *47*, 66–76. [[CrossRef](#)]
23. Exposure to Benzene: A Major Public Health Concern (World Health Organization). Available online: <https://www.who.int/ipcs/features/benzene.pdf> (accessed on 17 April 2020).
24. Oberlin, A.; Endo, M.; Koyama, T. Filamentous growth of carbon through benzene decomposition. *J. Cryst. Growth* **1976**, *32*, 335–349. [[CrossRef](#)]
25. Collins, J.J.; Lineker, G.A. A review and meta-analysis of formaldehyde exposure and leukemia. *Regul. Toxicol. Pharmacol.* **2004**, *40*, 81–91. [[CrossRef](#)]
26. Seo, H.; Jung, S.; Jeon, S. Detection of formaldehyde vapor using mercaptophenol-coated piezoresistive cantilevers. *Sens. Actuators B Chem.* **2007**, *126*, 522–526. [[CrossRef](#)]
27. Zhang, Y.M.; Lin, Y.T.; Chen, J.L.; Zhang, J.; Zhu, Z.Q.; Liu, Q.J. A high sensitivity gas sensor for formaldehyde based on silver doped lanthanum ferrite. *Sens. Actuators B Chem.* **2014**, *190*, 171–176. [[CrossRef](#)]
28. Gu, C.; Xu, X.; Huang, J.; Wang, W.; Sun, Y.; Liu, J. Porous flower-like SnO<sub>2</sub> nanostructures as sensitive gas sensors for volatile organic compounds detection. *Sens. Actuators B Chem.* **2012**, *174*, 31–38. [[CrossRef](#)]
29. Xu, K.; Zeng, D.; Tian, S.; Zhang, S.; Xie, C. Hierarchical porous SnO<sub>2</sub> micro-rods topologically transferred from tin oxalate for fast response sensors to trace formaldehyde. *Sens. Actuators B Chem.* **2014**, *190*, 585–592. [[CrossRef](#)]
30. Li, Y.; Chen, N.; Deng, D.; Xing, X.; Xiao, X.; Wang, Y. Formaldehyde detection: SnO<sub>2</sub> microspheres for formaldehyde gas sensor with high sensitivity, fast response/recovery and good selectivity. *Sens. Actuators B Chem.* **2017**, *238*, 264–273. [[CrossRef](#)]
31. Barkaline, V.A.; Chashynski, A.S. Adsorption properties of carbon nanotubes from molecular dynamic viewpoint. *Rev. Adv. Mater. Sci.* **2009**, *20*, 21–27.
32. Atomic-Scale Modelling for Semiconductor & Materials Research. Available online: <https://www.synopsys.com/silicon/quantumatk.html> (accessed on 1 November 2019).
33. Hu, F.-F.; Tang, H.-Y.; Tan, C.-J.; Ye, H.-Y.; Chen, X.-P.; Zhang, G.-Q. Nitrogen dioxide gas sensor based in monolayer SnS: A first principles study. *IEEE Electron Device Lett.* **2017**, *38*, 983–986. [[CrossRef](#)]
34. Song, H.; Li, X.; Cui, P.; Guo, S.; Liu, W.; Wang, X. Sensitivity investigation for the dependence of monolayer and stacking graphene NH<sub>3</sub> gas sensor. *Diam. Relat. Mater.* **2017**, *73*, 56–61. [[CrossRef](#)]
35. Harada, N.; Sato, S. Electron properties of NH<sub>4</sub> adsorbed graphene nanoribbon as a promising candidate for gas sensor. *AIP Adv.* **2016**, *6*, 055023.
36. Nahlik, J.; Voves, J.; Laposa, A.; Kroutil, J. The study of graphene gas sensor. *Key Eng. Mater.* **2014**, *605*, 495–498. [[CrossRef](#)]
37. Ruixue, D.; Yintang, Y.; Lianxi, L. Working of a SiC nanotube NO<sub>2</sub> gas sensor. *J. Semicond.* **2009**, *30*, 114010. [[CrossRef](#)]
38. QuantumWise User Manual, “ATK-DFT Calculator”. Available online: <https://docs.quantumwise.com/v2017/manuals/ATKDFT.html> (accessed on 18 November 2019).

39. High Performance Computing. Available online: <https://www.ttu.ee/support-structure/it-services/services-4/high-performance-computing-2/> (accessed on 5 November 2019).
40. VNL Tasks and Workflow. Available online: <https://docs.quantumwise.com/v2017/tutorials/vnl.html> (accessed on 10 November 2019).
41. Wang, Y.; Yeow, T.W. A review of carbon nanotube-based gas sensors. *J. Sens.* **2009**, *2009*, 24. [[CrossRef](#)]
42. Zaporotskova, I.V.; Boroznina, N.P.; Parkhomenko, Y.N.; Kozhitov, L.V. Carbon nanotubes: Sensor properties. A review. *Mod. Electron. Mater.* **2016**, *2*, 95–105. [[CrossRef](#)]
43. Sinha, N.; Ma, J.; Yeow, J.T. Carbon nanotube-based sensors. *J. Nanosci. Nanotechnol.* **2006**, *6*, 573–590. [[CrossRef](#)]
44. Schroeder, V.; Savagatrup, S.; He, M.; Lin, S.; Swager, T.M. Carbon Nanotube Chemical Sensors. *Chem Rev.* **2019**, *119*, 599–663. [[CrossRef](#)] [[PubMed](#)]
45. National Renewable Energy Laboratory-Solar Spectra. Available online: <https://www.nrel.gov/grid/solar-resource/spectra.html> (accessed on 15 November 2019).
46. Freitag, M.; Martin, Y.; Misewich, J.A.; Martel, R.; Avouris, P.H. Photoconductivity of single carbon nanotubes. *Nano Lett.* **2003**, *3*, 1067–1071. [[CrossRef](#)]
47. Balasubramanian, K.; Fan, Y.; Burghard, M.; Kern, K. Photoelectronic transport imaging of individual semiconducting carbon nanotubes. *Appl. Phys. Lett.* **2004**, *8*, 2400. [[CrossRef](#)]
48. Pichler, T.; Knupfer, M.; Golden, M.S.; Fink, J.; Rinzler, A.; Smalley, R.E. Localized and delocalized electronic states in single-wall carbon nanotubes. *Phys. Rev. Lett.* **1998**, *80*, 4729–4732. [[CrossRef](#)]
49. Ohfuchi, M.; Miyamoto, Y. Optical properties of oxidized single-wall carbon nanotubes. *Carbon* **2017**, *114*, 418–423. [[CrossRef](#)]
50. Puzder, A.; Williamson, A.; Reboredo, F.A.; Galli, G. Structural stability and optical properties of nanomaterials with reconstructed surfaces. *Phys. Rev. Lett.* **2003**, *91*, 1–4. [[CrossRef](#)]
51. Bubke, K.; Gnewuch, H.; Hempstead, M. Optical anisotropy of dispersed carbon nanotubes induced by an electric field. *Appl. Phys. Lett.* **1997**, *71*, 1906–1908. [[CrossRef](#)]
52. Freitag, M.; Low, T.; Zhu, W.; Yan, H.; Xia, F.; Avouris, P. Photocurrent in graphene harnessed by tunable intrinsic plasmons. *Nat. Commun.* **2013**, *4*, 1–8. [[CrossRef](#)] [[PubMed](#)]
53. Falk, A.L.; Chiu, K.-C.; Farmer, D.B.; Cao, Q.; Tersoff, J.; Lee, Y.-S.; Avouris, P.; Han, S.-J. Coherent plasmon and phonon-plasmon resonances in carbon nanotubes. *Phys. Rev. Lett.* **2017**, *118*, 257401–257406. [[CrossRef](#)] [[PubMed](#)]
54. Ojarand, J.; Min, M.; Koel, A. Multichannel electrical impedance spectroscopy analyzer with microfluidic Sensors. *Sensors* **2019**, *19*, 1891. [[CrossRef](#)] [[PubMed](#)]



© 2020 by the authors. Licensee MDPI, Basel, Switzerland. This article is an open access article distributed under the terms and conditions of the Creative Commons Attribution (CC BY) license (<http://creativecommons.org/licenses/by/4.0/>).



## Appendix K

H. Rashid, A. Koel, T. Rang and H. Mehmood

“Modelling and Simulations of 4H-SiC/6H-SiC/4H-SiC Double Hetero-structure Single Quantum-well Light Emitting Diode,” *Materials*, 2020. **(Under-review in ETIS 1.1)**



## **Abstract “Paper K”**

During the last decade, Silicon carbide (SiC) has emerged as an exceptional material for high temperature and high frequency electronics and optoelectronics applications. SiC exists in more than 200 different crystallographic forms, called polytypes. The most distinguished polytypes of SiC are 3C-SiC, 4H-SiC and 6H-SiC due to their tremendous physical and electrical properties. In this article, simulations of a novel structure of light emitting diode (LED) based on a unique combination of 4H-SiC and 6H-SiC have been done by considering a novel material joining technique, called diffusion welding/bonding. Single quantum well (SQW), edge emitting SiC based LED has been simulated with a commercially available semiconductor device simulator, SILVACO TCAD. Current-voltage characteristics, luminous power and power spectral density of simulated LED have been calculated. Our proposed LED device exhibited promising results in terms of luminous power efficiency and external quantum efficiency (EQE). The device achieved luminous efficiency of 25% and EQE of 16.43%, which are quite good for a SQW LED. This type of edge emitting LED is used in fiber optic communication links as light source. Our proposed LED structure can be customized by choosing appropriate materials of different bandgaps to get the light emission spectrum in desired wavelength range. Physical fabrication of this LED by direct bonding of SiC-SiC wafers will improve the device performance and reduce the fabrication cost.

# Curriculum vitae

## Personal data

Name: Muhammad Haroon Rashid  
Date of birth: 15.04.1990  
Place of birth: Pakistan  
Citizenship: Pakistan

## Contact data

Address: Akadeemia Tee 5, Tallinn, Estonia.  
Phone: +37253912599  
E-mail: haroonrashid199@gmail.com

## Education

Educational Institution	Year	Degree
Tallinn University of Technology, Estonia	2016–2021	Ph.D., Electronic and Telecommunication
Ghulam Ishaq Khan Institute of Engineering Sciences and Technology, KPK, Pakistan	2013–2015	MS in Electronics Engineering
The University of Faisalabad, Pakistan	2009–2013	BS in Electrical Engineering (Specialization in Electronics)

## Language competence

Urdu: Native  
English: Fluent

## Professional employment

June 2015 to November 2016: Lecturer at School of Electrical Engineering, The University of Faisalabad, Pakistan

## Elulookirjeldus

### Isikuandmed

Nimi: Muhammad Haroon Rashid  
Sünniaeg: 15.04.1990  
Sünnikoht: Pakistan  
Kodakondsus: Pakistani

### Kontaktandmed

Adress: Akadeemia Tee 5, Tallinn, Estonia  
Telefon: +37253912599  
E-post: haroonrashid199@gmail.com

### Hariduskäik

Haridusasutus Tallinna Tehnikaülikool	Aasta 2016–2021	Haridus PhD, elektroonika ja telekommunikatsioon
Inseneriteaduste ja Tehnoloogia Instituut, KPK, Pakistan	2013–2015	Magister, elektroonikatehnika
The University of Faisalabad, Pakistan	2009–2013	Bakalaureus, elektroonikatehnika

### Keelteoskus

Urdu keel: emakeel  
Inglise keel: kõrgtase

### Teenistuskäik

Juuni 2015–Detsember 2016: õppejõud, elektrotehnika kool, Faisalabadi Ülikool, Pakistan

ISSN 2585-6901 (PDF)  
ISBN 978-9949-83-659-8 (PDF)